Investigating Flow over an Airfoil at Low Reynolds Numbers Using Novel Time-Resolved Surface Pressure Measurements

by

Ryan J. Gerakopulos

A thesis
presented to the University of Waterloo
in fulfillment of the
thesis requirement for the degree of
Master of Applied Science
in
Mechanical Engineering

Waterloo, Ontario, Canada, 2011

I hereby declare that I am the sole author of this thesis. This is a true copy of the thesis, including any required final revisions, as accepted by my examiners.

I understand that my thesis may be made electronically available to the public.

Abstract

An aluminum NACA 0018 airfoil testbed was constructed with 95 static pressure taps and 25 embedded microphones to enable novel time-resolved measurements of surface pressure. The main objective of this investigation is to utilize time-resolved surface pressure measurements to estimate salient flow characteristics in the separated flow region over the upper surface of an airfoil. The flow development over the airfoil was examined using hot wire anemometry and mean surface pressure for a range of Reynolds numbers from $80x10^3$ to $200x10^3$ and angles of attack from 0° to 18°. For these parameters, laminar boundary layer separation takes place on the upper surface and two flow regimes occur: (i) separation is followed by flow reattachment, so that a separation bubble forms and (ii) separation occurs without subsequent reattachment. Measurements of velocity and mean surface pressure were used to characterize the separated flow region and its effect on airfoil performance using the lift coefficient. In addition, the transition process and the evolution of disturbances were examined. The lift curve characteristics were found to be linked to the rate of change of the separation, transition, and reattachment locations with the angle of attack. For both flow regimes, transition was observed in the separated shear layer. Specifically, the amplification of disturbances within a band of frequencies in the separated shear layer resulted in laminar to turbulent transition. Validation of time-resolved surface pressure measurements was performed for $Re_c = 100x10^3$ at $\alpha = 8°$ and $\alpha = 12°$, corresponding to regimes of flow separation with and without reattachment, respectively. A comparative analysis of simultaneous velocity and time-resolved surface pressure measurements showed that the characteristics and development of velocity fluctuations associated with disturbances in the separated shear layer can be extracted from time-resolved surface pressure measurements. Specifically, within the separated flow region, the amplitude of periodic oscillations in the surface pressure signal associated with disturbances in the separated shear layer grew in the streamwise direction. In addition, the frequency at the spectral peak of the amplified disturbances in the separated shear layer was identified. Based on the results of the validation analysis, time-resolved surface pressure measurement analysis techniques were applied for a Reynolds number range from $60x10^3$ to $130x10^3$ and angles of attack from 6° to 16°. Within the separated flow region, the streamwise growth of surface pressure fluctuations is distinctly different depending on the flow regime. Specifically, within the separation bubble, the RMS surface pressure fluctuations increase in the streamwise direction and reach a peak just upstream of the reattachment location. The observed trend is in agreement with that observed for other separating-reattaching flows on geometries such as the forward and backward facing step and splitter plate with fence. In contrast to the separation bubble formation, when the separated shear layer fails to reattach to the airfoil surface, RMS surface pressure fluctuations increase in the streamwise direction with no maximum and the amplitude is significantly lower than those observed in the separation bubble. Surface pressure signals were further examined to identify the frequency, convective velocity, and spanwise uniformity of disturbances in the separated shear layer. Specifically, for both flow regimes, the fundamental frequency and corresponding Strouhal number exhibit a power-law dependency on the Reynolds number. Based on the available data for which velocity

measurements were obtained in the separated flow region, the convective velocity matched the mean velocity at the wall-normal distance corresponding to the maximum turbulence intensity. A distinct increase in the convective velocity of disturbances in the separated shear layer was found when the airfoil was stalled in comparison to that found in the separation bubble. From statistical analysis of surface pressure signals in the spanwise direction, it was found that disturbances are strongly two-dimensional in the laminar portion of the separated shear layer and become three-dimensional through the transition process.

Acknowledgements

I'd like to thank my supervisor, Serhiy Yarusevych, for providing your technical expertise, editorial services, and guidance during this project.

To my fellow graduate student, Michael Bishop. It has been a pleasure to work with such a talented, hardworking, and passionate teammate. The diversity of your skills and professionalism is admirable. My research is a success because of your mentorship and your effort to modernize the wind tunnel facility. For all of this, I will always be grateful.

Michael Boutilier, thank you for your insight, companionship, and perseverance during the testing phase of this project, which was filled with excitement and hardships. I am truly appreciative of all your help collecting data and for your assistance in developing a methodology for boundary layer measurements.

I would also like to thank the student machine shop supervisors, John Potzold and Kwai Chan, for truly teaching me the art of machine design. John, your advice and training was instrumental in helping me develop the experimental setup. Your fearless attitude is commendable and I am grateful for your mentorship.

Thanks to the engineering machine shop personnel, especially Rick Forgett and John Bolt. Your willingness to collaborate was critical for creating such a complex experimental setup. Rick, the long days and nights you put in fabricating the airfoil with such quality were much appreciated.

I would also like to thank the departmental electronics technicians, Neil Griffett and Andy Barber. Neil, your superior electronics expertise was absolutely vital for the developing the sensor amplification bus.

To my fellow graduate students, Adam McPhee, Stephen Orlando, and Adam Bale. Thank you all for your help and advice during the sensor evaluation and calibration phase. Adam McPhee, thank you for your unconditional advice on the sensor technology and selection.

To my other fellow graduate students Christopher Morton, Sina Kheirkhah, and Drew Gertz. Thank you for your willingness to always provide a helping hand.

Finally, I would like to thank the Natural Sciences and Engineering Research Council of Canada, the University of Waterloo, and Bombardier Aerospace for their financial support and interest in this research project.

Dedication

This thesis is dedicated to my parents Nick and Violet and my brother Stephen. Thank you for your unconditional love, support, and encouragement throughout my academic career. I am forever grateful to have such an understanding and compassionate family.

Table of Contents

List of Figures

List of Tables

Nomenclature

AR	aspect ratio
b	model span [m]
c	airfoil chord [m]
C_l	airfoil lift coefficient, L/(qSc)
C_p	surface pressure coefficient based on mean (static) pressure, $(P-P_o)/ (0.5\rho U_o^2)$
d	height of airfoil projected on vertical plane [m]
D	diameter of circular cylinder [m]
DAQ	data acquisition system (used interchangeably with data acquisition card)
E_{pp}	normalized energy spectrum of p
E_{uu}	normalized energy spectrum of u
f	frequency [Hz]
f_o	fundamental frequency [Hz]
FFT	fast Fourier transform
l,h,s	length, height, and span of test section [m]
L	airfoil lift [N]
p	fluctuating pressure on airfoil surface [Pa]
p'	RMS fluctuating pressure on airfoil surface [Pa]
P	mean (static) pressure on airfoil surface [Pa]
P_o	free-stream static pressure [Pa]
q	dynamic pressure, $0.5\rho U_o^2$ [Pa]
R	reattachment location
$R(\tau)$	cross-correlation function $[m^2/s^2]$
Re_c	Reynolds number based on chord length, U_0c/ν
Re_D	Reynolds number based on cylinder diameter, U_0D/ν
RMS	Root Mean Square
S	microphone sensitivity [mV/Pa]
St_o	Strouhal number based on f_o, f_od/U_0
T	transition location
T_u	turbulence intensity

U	streamwise mean velocity [m/s]
U_c	convection velocity [m/s]
U_e	streamwise velocity at edge of boundary layer [m/s]
U_o	free-stream velocity in x direction [m/s]
u	streamwise fluctuating velocity component [m/s]
u'	RMS of fluctuating streamwise velocity component [m/s]
u_f'	RMS of bandpass filtered u at a y/c location corresponding to u_{max}'/U_o [m/s]
u'/U_o	turbulence intensity (u_{max}'/U_o corresponds to maximum turbulence intensity)
x, y, z	streamwise, vertical, and spanwise coordinates, respectively [m]
α	angle of attack [deg]
θ_c	positive angle measured from stagnation point of cylinder [deg]
Γ	coherence function
φ	cross-spectrum function
ρ	density of air [kg/m^3]
$\rho(\tau)$	cross-correlation coefficient function
τ	time lag [s]
ν	kinematic viscosity of air [m^2/s]
$d( )/d\alpha$	rate of change of ( ) with angle of attack

1 Introduction

1.1 The Need for a Field-Applicable Flow Diagnostics System

A wide range of engineering devices employ airfoils operating at relatively low chord Reynolds numbers. Specifically, airfoil performance in the chord Reynolds number range from 10^4 to 10^6 is of interest for such applications as small-to-medium scale wind turbines and unmanned aerial vehicles (e.g., Carmichael, 1981; Raghunathan & Ombaka, 1986; Tangler & Somers, 1995; Mueller & DeLaurier, 2003). In this Reynolds number range, the laminar boundary layer on the upper surface of an airfoil is susceptible to separation, even at low angles of attack. When laminar separation occurs, the evolution of the separated shear layer has a strong influence on the entire flow field. For Reynolds number greater than approximately $50x10^3$, the separated shear layer undergoes laminar-to-turbulent transition over the airfoil surface (Brendel & Mueller, 1990). If the separated shear layer reattaches to the airfoil surface, an enclosed region of recirculating fluid is formed adjacent to the airfoil surface, referred to as a transitional separation bubble, and a narrow wake is formed behind the airfoil (Fig. 1.1). When a separation bubble forms on an airfoil surface for Reynolds numbers below about $300x10^3$, the separation bubble may occupy upwards of 15% of the chord (Brendel & Mueller, 1988). Conversely, the separated shear layer may fail to reattach to the airfoil surface and a wide wake is formed behind the airfoil (Fig. 1.2). Independent of the flow regime, flow separation usually has a detrimental effect on airfoil performance and may also contribute to undesirable noise generation. Thus, knowledge of the existence and extent of the separated flow region is vital in low Reynolds number airfoil design and performance assessment.

Detailed experimental studies have been conducted in order to advance understanding of separated shear layer development in transitional separation bubbles. Such studies examined separation bubbles on a flat plate induced by an adverse pressure gradient (e.g., Gaster, 1967; Horton, 1967; Watmuff, 1999; Häggmark, 2000) and on an airfoil surface (e.g., Boiko et al., 1989, 2002; Dovgal et al., 1994; Brendel & Mueller, 1988, 1990; Yarusevych et al., 2006, 2009, Burgmann et al., 2006, 2007; Burgmann & Schröder, 2008). Several theoretical models and criteria to predict the characteristics of transitional separation bubbles (e.g., van Ingen, 1965; Gaster, 1967; Horton, 1967; Roberts, 1980; Gleyzes et al., 1985) have been derived, but they are heavily reliant on empirical correlations and often lead to inaccurate predictions (Weibust et al., 1987; Malkiel & Mayle, 1996; Jones et al., 2008).

Computational studies employing Direct Numerical Simulation (DNS) are capable of fully resolving laminar-to-turbulent transition in the separated shear layer (e.g., Jones et al., 2008). Several computational studies have been designed to model transitional separation bubbles generated on a flat plate (e.g., Rist & Maucher, 1994, 2002; Alam & Sandham, 2000; Spalart & Strelets, 2000; Marxen et al., 2004; Marxen & Rist, 2005, 2010; McAuliffe & Yaras, 2010). However, since studies employing DNS are computationally intensive, only a few comprehensive studies have been performed for a full airfoil configuration (Jones et al., 2008, 2010). Thus, high quality experimental data remains essential for validating theoretical and computational models and advancing knowledge of separated shear layer development over an airfoil surface.

Such experimental techniques as flow visualization, static (mean) surface pressure, hot wire anemometry, laser Doppler anemometry (LDA), and particle image velocimetry (PIV) have been utilized to characterize the separated flow region over an airfoil (e.g., Tani,

1964; Brendel & Mueller, 1988, 1990; Lang et al., 2004; Burgmann et al., 2006, 2007; Burgmann & Schröder, 2008; Yarusevych et al., 2006, 2009). However, these techniques are either not field-applicable or not capable of time-resolved single-point and/or multi-point measurements. Since the separated flow region over an airfoil surface is highly unsteady, multi-point time-resolved measurements are essential to resolve spatial and temporal characteristics of the separated flow region. In addition, a field-applicable measurement system may be utilized for online flow diagnostics and/or active flow control. Thus, there is a need for a field-applicable measurement system that is capable of multi-point time-resolved measurements over an airfoil surface in a low Reynolds number flow.

A technique involving embedded pressure sensors may be a viable solution that is field-applicable and configurable for multi-point time-resolved measurements. Early studies in the 1950s have demonstrated that a microphone embedded in an aircraft surface can detect pressure fluctuations within boundary layers and characterize noise emission in flight (e.g., Mull & Algranti, 1956; McLeod & Jordan, 1958). Additionally, wind tunnel studies have demonstrated that flow structures responsible for noise emission from flaps and slats (e.g., Choudhari et al., 2002) and from the trailing-edge of an airfoil (e.g., Paterson et al., 1973; Brooks & Hodgson, 1981) can be detected using surface embedded microphones. In contrast, only a few studies employed measurements of fluctuating surface pressure to characterize the separated flow region on an airfoil operating at low Reynolds numbers (e.g., Weibust et al., 1987; Yarusevych et al., 2008). In these studies, only single-point measurements of fluctuating surface pressure were performed. These studies are likely limited because of the complexity of separated shear layer development over an airfoil surface at low Reynolds numbers. On the other hand, extensive studies involving single-point and multi-point measurements of fluctuating surface pressure have been performed for simple geometries

involving separating-reattaching flows. Specifically, time-resolved surface pressure measurements have been employed to characterize a separation bubble for a blunt-faced splitter plate (BFSP) (e.g., Kiya & Sasaki, 1983; Cherry et al., 1984), a backward-facing step (BFS) (e.g., Driver et al., 1987; Farabee & Casarella, 1986; Lee & Sung, 2001; Hudy et al., 2007), and a splitter plate with fence (SPF) (e.g., Hudy et al., 2003). Additionally, for the case of boundary layer separated without subsequent reattachment, measurements of fluctuating surface pressure have been utilized in several previous studies on a circular cylinder (e.g., Norberg, 1986, 2003; Norberg & Sundén, 1987). Collectively, these studies performed for simple geometries are relevant since they examine both flow regimes of separation with and without reattachment with laminar-to-turbulent transition occurring in the separated shear layer for some cases (namely, BFSP, SPF, and circular cylinder).

This thesis is focused on: (i) developing an airfoil testbed with an array of microphones embedded in the airfoil surface and (ii) utilizing the microphone array to obtain novel measurements of time-resolved fluctuating surface pressure to estimate salient flow characteristics within the separated flow region on an airfoil surface at low Reynolds numbers.

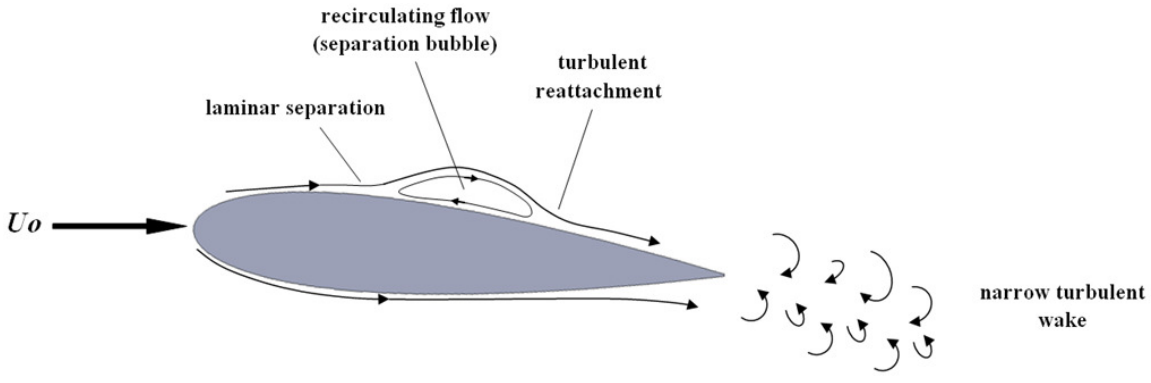

Figure 1.1: Flow separation with subsequent reattachment.

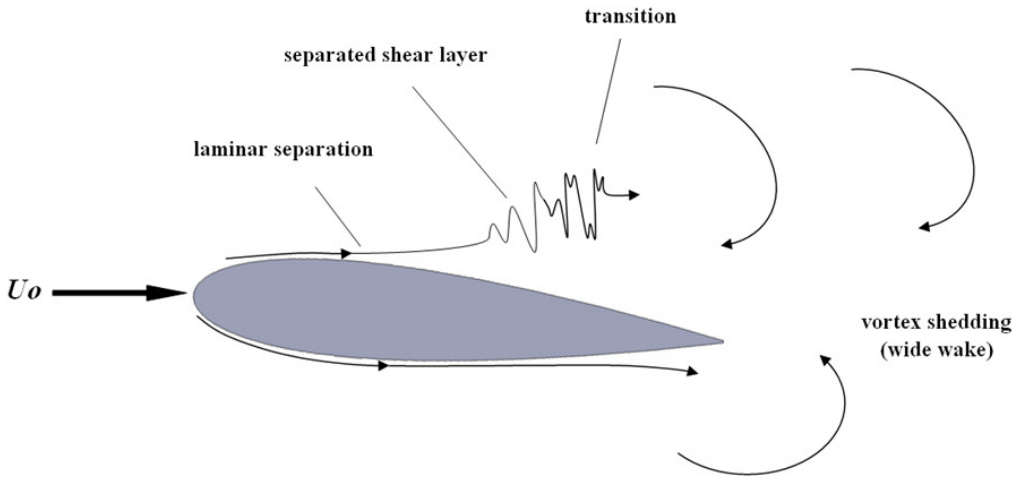

Figure 1.2: Flow separation without subsequent reattachment.

1.2 Flow Regimes

1.2.1 Time-Averaged Transitional Separation Bubble

A number of previous studies have examined the structure of the two-dimensional time-averaged transitional separation bubble, which will simply be referred to as *separation bubble* or *bubble*. Some of the earliest investigations were performed by Crabtree (1959), Tani (1964), Gaster (1967), and Horton (1968). For airfoils operating at low Reynolds numbers, the laminar boundary layer often separates from the upper surface due to an adverse pressure gradient. The conventional physical model of the separation bubble sketched by Horton (1968) is shown in Fig. 1.3. The dead air region, bounded between the dividing streamline and the airfoil surface in Fig. 1.3, is characterized zero velocity (e.g., LeBlanc et al., 1987; Brendel & Mueller, 1988). Downstream of separation, the separated shear layer contained between the mean dividing streamline and the boundary layer edge moves away from the surface. Laminar-to-turbulent transition in the separated shear layer

occurs at a location near the maximum vertical displacement of the separated shear layer (Brendel & Mueller, 1990). A region of unsteady flow is characterized by a reverse flow vortex and reattachment of the separated shear layer. Additionally, a turbulent boundary layer develops downstream of reattachment.

As described by Tani (1964), a distinctive characteristic of a separation bubble is the region of nearly constant static surface pressure downstream of separation through the dead air region. The transition location is associated with a sudden surface pressure recovery following the region of constant surface pressure (Tani, 1964). O'Meara & Mueller (1987) proposed that the reattachment location can be identified as the location downstream of the transition point where a rapid decrease in the rate of surface pressure recovery is observed.

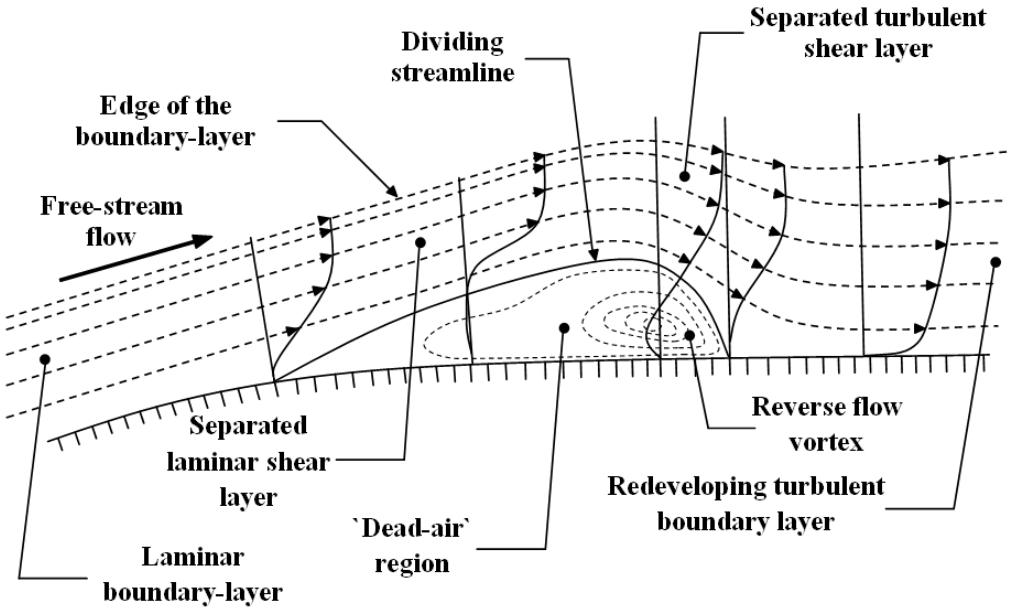

Figure 1.3: Time-averaged structure of a two-dimensional separation bubble (reproduced from Horton, 1968).

1.2.2 Characteristics of the Separated Flow Region

Two distinct types of separation bubbles can form on the surface of an airfoil at low Reynolds numbers, namely, a *short separation bubble* and a *long separation bubble* (Fig. 1.4a). A short separation bubble may occupy upwards of 15% of the airfoil chord (Brendel & Mueller, 1990), while a long separation bubble may occupy the entire chord (Tani, 1964). As shown in Fig. 1.4b, short and long separation bubbles have distinctly different effects on the pressure distribution. For instance, a short separation bubble is associated with a sharp suction peak with a magnitude that is diminished relative to the inviscid flow. Downstream of the suction peak, a region of constant pressure occupies a few percent of the chord. Following a sudden increase in the pressure, the pressure distribution over the remainder of the airfoil returns to the inviscid flow. For a long separation bubble, the suction peak is broad, the magnitude is reduced relative to the inviscid flow, and the subsequent region of constant pressure extends over almost the entire length of the chord. If the length of the separation bubble terminates before the trailing-edge as shown in Fig. 1.4b, then the pressure increases and returns to the inviscid flow distribution.

Three distinct types of airfoil stall at low Reynolds numbers were first identified by Jones (1933, 1934) and later correlated to boundary layer characteristics by McCullough & Gault (1951). A *trailing-edge stall* is associated with an upstream movement of the turbulent separation point from the trailing-edge of an airfoil with an increase in the angle of attack. At higher angles of attack, a strong adverse pressure gradient may cause separation to occur in the laminar boundary layer, followed by laminar-to-turbulent transition in the separated shear layer and subsequent reattachment, forming a separation bubble. A further increase in the angle of attack or decrease in Reynolds number may cause another two types of stall. A l*eading-edge stall* occurs if the separated shear layer fails to reattach to the surface, forming a

wide wake behind the airfoil. This type of stall will also be referred to as bubble bursting. Such a stall is abrupt and results in a deterioration of airfoil performance, signified by a sharp decrease in lift and an increase in drag (Tani, 1964). Alternatively, a *thin-airfoil stall* occurs when the separated shear-layer extends over the airfoil surface and reattaches downstream near the trailing-edge, forming a long separation bubble which occupies upwards of the entire chord length (Tani, 1964). Thus, a change in the pressure distribution from a short separation bubble to a long separation bubble similar to that observed in Fig. 1.4 would indicate a thin-airfoil stall. Conversely, when the shear-layer fails to reattach to the airfoil surface and a leading-edge stall occurs, a region of constant pressure extends from separation to the trailing-edge (Tani, 1964).

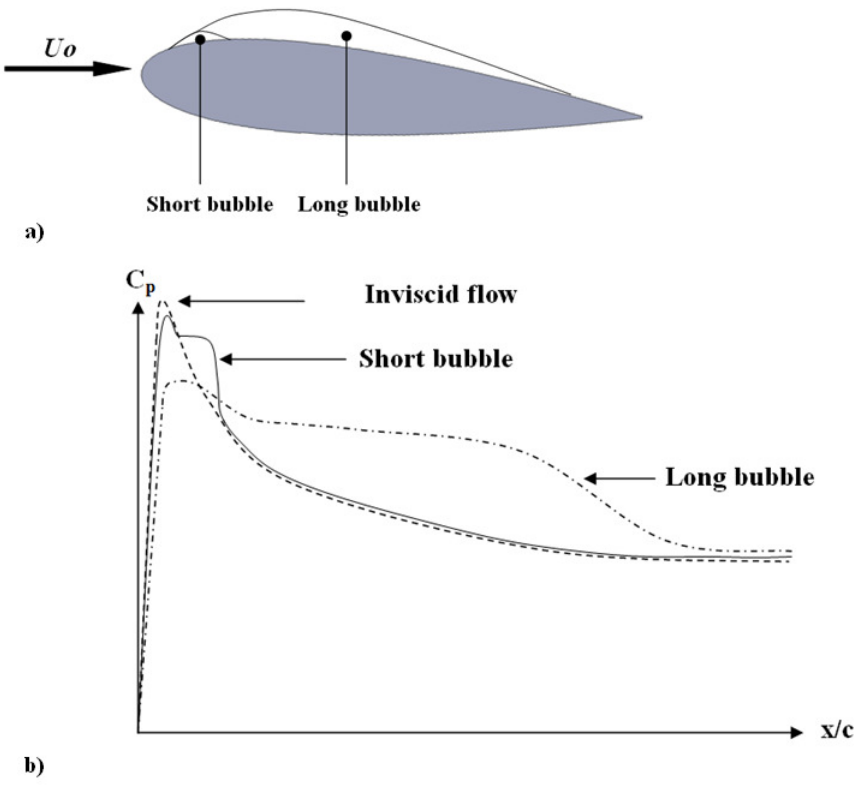

Figure 1.4: a) Short and long separation bubbles on the upper surface of an airfoil and b) effect of the separation bubble on the pressure distribution (images reproduced from Malkiel & Mayle, 1996).

Performance characteristics such as lift and drag exhibit hysteresis loops as a consequence of stalling (e.g., Mueller, 1985; Hsiao et al., 1989; Hoffmann, 1990). When a stall is induced by increasing the angle of attack and/or decreasing the Reynolds number, causing the bubble to burst, the separation bubble may not reform upon restoring the pre-stall angle of attack and/or Reynolds number. Such hysteresis in performance characteristics is observed since the pressure distributions and wake are significantly affected by a flow regime change as a consequence of stalling.

The topological structure of a separation bubble may differ from the time-averaged structure described in §1.2.1 if the bubble is induced by a strong adverse pressure gradient. In a time-resolved sense, a steady bubble may develop initially, but unsteadiness may develop within the bubble, causing it to periodically split into two distinct cells, shedding the latter cell downstream as a vortical structure (e.g., Pauley et al., 1990; Lin & Pauley, 1996; and Wilson & Pauley, 1998). From a comparative analysis of pressure distributions for time-averaged steady and unsteady bubbles, Pauley et al. (1990) observed that the time-averaged unsteady bubble with vortex shedding was short, while the time-averaged steady bubble was long with a length, on the average, approximately twice that of the short bubble. Therefore, the authors concluded that unsteady and steady separation bubbles are time-averaged short and long separation bubbles, respectively.

1.3 Flow Transition

The separated flow region over an airfoil has characteristics similar to an attached boundary layer, a free shear layer, or a hybrid of the latter two. In the separated flow region,

disturbances associated with a band of frequencies are amplified in the streamwise direction, centered at the fundamental frequency (e.g., Dovgal et al., 1994). The subsequent discussions highlight the characteristics of laminar-to-turbulent transition in an attached boundary layer, free shear layer, and separation bubble, respectively.

1.3.1 Attached Boundary Layer and Free Shear Layer

One of the first experiments to investigate laminar-to-turbulent transition in an attached boundary layer on a flat plate was reported by Shubauer & Skramstad (1948). The authors observed that, for a small-amplitude disturbance environment (i.e., low free-stream turbulence), a two-dimensional Tollmien-Schlichting instability wave initially grew exponentially in the streamwise direction. Furthermore, the initial exponential disturbance growth was in accordance with linear stability theory (e.g., Boiko et al., 2002). Later studies showed that, with further spatial amplification of the disturbance, non-linear interactions between disturbances occurred via two possible regimes: (i) K-regime (after Klebanoff) and (ii) the subharmonic N-regime[1] (after Novosibirsk group) (e.g., Boiko et al., 2002). Within the K-regime, a staggered pattern of Λ-vortices developed, producing spikes in the velocity signals at higher harmonics of the fundamental frequency. Conversely, the N-regime, typical for low external disturbance environments, gives rise to a non-staggered pattern of Λ-vortices and produces spikes in the velocity signals at a subharmonic of the fundamental frequency. Three-dimensional breakdown to turbulence is continued by the formation of point-like disturbances, referred to as turbulent spots, which grow and eventually merge forming a turbulent boundary layer (e.g., Emmons, 1951; Grek et al., 1987).

[1] *The N-regime is also referred to as the H-regime (after Herbert).*

Within a free shear layer, a two-dimensional disturbance also grows exponentially with streamwise distance (e.g., Miksad, 1972; Ho & Huerre, 1984; Huang & Ho, 1990) via an inviscid Kelvin-Helmholtz instability (Ho & Huerre, 1984). Non-linear interactions between amplified disturbances are manifested through subharmonic resonance, resulting in vortex-pairing and eventually leading to a three-dimensional breakdown to turbulence (Ho & Huerre, 1984).

1.3.2 Separation Bubble on a Flat Plate

In the late 1960's, Gaster (1967) devised an experiment in which a transitional separation bubble could be generated on a flat plate subjected to an adverse pressure gradient. Since then, various experimental and numerical studies have been conducted based on such a configuration, the results of which are discussed in this section.

In an experiment conducted by Watmuff (1999), a small-magnitude impulsive disturbance was injected into the attached laminar boundary layer and its evolution was examined through the separated flow region. After separation, the small-amplitude disturbance grew exponentially in agreement with linear stability theory. Contours of spanwise vorticity revealed a cat's eye pattern reminiscent of a Kelvin-Helmholtz instability. Following a region of exponential growth, the shear layer roll-up evolved into large vortex loops with non-uniform spanwise spacing. Within the reattached turbulent boundary layer, heart-shaped patterns resembling turbulent spots were observed in the wall-normal Reynolds stress. Another experimental study conducted by Häggmark (2000) revealed a region of two-dimensional exponential growth with amplitude profiles resembling those dominated by

Kelvin-Helmholtz instability. Following the exponential growth region, three-dimensional ordered structures emerged prior to reattachment.

A series of DNS and experimental studies performed by Rist & Maucher (1994), Lang et al. (2004), Marxen et al. (2004), and Marxen & Rist (2005) observed initial disturbance growth and shear layer roll-up similar to that reported by Watmuff (1999). Near reattachment, Alam & Sandham (2000) observed a staggered arrangement of Λ-vortices, also similar to the structures reported by Watmuff (1999), reminiscent of the K-type regime in a transitional flat plate boundary layer. McAuliffe & Yaras (2010) observed the emergence of hairpin structures following the breakdown of spanwise coherent vortices. Common to all the aforementioned studies, spatial growth of disturbances was convective in nature. Alam & Sandham (2000) showed that convective instabilities occurred in a separation bubble when the reverse flow velocity was less than about 15-20% of the free-stream speed. This criterion was also confirmed by Rist & Maucher (2002), Marquillie & Ehrenstein (2003), and McAulliffe & Yaras (2010).

Rist & Maucher (2002) examined the association between the disturbance amplitude profile shape and the instability mechanisms in the separated flow region using streamwise velocity eigenfunction profiles predicted from linear stability theory. The analysis predicted the formation of a double-maxima amplitude profile in a separated flow region. The authors found that the outer maximum was associated with an inviscid Kelvin-Helmholtz instability, while the inner maximum was associated with a viscous Tollmien-Schlichting instability. The relative magnitude of the two maxima indicates the dominant instability mechanism in the separated flow region. McAuliffe & Yaras (2010) observed disturbance amplitude profiles with a maximum associated with an inviscid instability mechanism in the laminar

portion of the separated shear layer, while a double-maxima profile was found in the turbulent portion of the bubble. Alam & Sandham (2000) also observed double-maxima disturbance amplitude profiles near reattachment. Collectively, the results of Alam & Sandham (2000), Rist & Maucher (2002), and McAuliffe & Yaras (2010) indicates that the development of the disturbance amplitude profiles in the separated flow region exhibit similar characteristics to profiles observed in an attached boundary layer and a detached shear layer.

In a DNS study conducted by Marxen & Rist (2010), the interrelation between laminar-to-turbulent transition and mean flow evolution was examined in a separation bubble generated on a flat plate. A small amplitude and periodic artificial disturbance was introduced into the laminar boundary layer upstream of the separation bubble. The authors found that the small-amplitude artificial disturbance amplified through the separation bubble in the streamwise direction, causing an earlier reattachment relative to simulations without the artificial disturbance. The change in the mean flow downstream of transition modulated the pressure distribution and the mean velocity profiles in the laminar portion of the separation bubble. As a consequence, the initial spatial growth rate associated with transition also changed, thus, creating a feedback loop process.

1.3.3 Separation Bubble on an Airfoil

The studies discussed in §1.3.2 pertain to a transitional separation bubble generated on a flat plate, which is relevant to the present investigation since flow separation with subsequent reattachment occurs over an airfoil surface at low Reynolds numbers. However, the flow development over an airfoil surface is more complex, resulting in distinct differences. Unlike

a separation bubble on a flat plate, where laminar boundary layer separation is induced at a controlled location, on an airfoil surface, the location of laminar boundary layer separation changes with the angle of attack and/or Reynolds number. In addition, the extent of the separated flow region changes with these flow parameters and the separated shear layer may not reattach to the airfoil surface. In this section, the effect of flow parameters on the separated flow region is discussed. In addition, separated shear layer development is examined for regimes of flow separation with and without reattachment.

O'Meara & Mueller (1987) showed that, as the angle of attack was increased, the location of laminar separation advanced toward the leading-edge and, on the average, the separation bubble thickness increased and length decreased. Conversely, as the Reynolds number was increased, the change in the location of laminar separation was marginal, but the separation bubble thickness and length decreased. From this discussion, it is apparent that a change in flow parameters, such as Reynolds number and/or angle of attack, affects separation bubble position and length, which is partially attributed to the strong influence of these flow parameters on the laminar-to-turbulent transition process in the separated shear layer.

The transition mechanism observed in the separated shear layer is similar for both regimes of flow separation with and without reattachment. Within the separated flow region, for a low-disturbance free-stream environment, it was shown that initially small-amplitude disturbances grow exponentially via a Kelvin-Helmholtz inviscid instability, resulting in roll-up vortices in the separated shear layer (e.g., Brendel & Mueller, 1988, 1990; Yarusevych et al., 2006, 2009; Burgmann et al., 2006, 2007; Burgmann & Schröder, 2008; Zhang et al., 2008). The initial disturbance growth and shear-layer roll-up process is similar to that

described by Watmuff (1999) for a separation bubble generated on a flat plate. Following shear layer roll-up, interactions between disturbances result in a region of non-linear growth. Within this region, perturbations at the subharmonic and higher harmonics of the fundamental frequency have been reported in the separation bubble (e.g., Brendel & Mueller, 1988, 1990; Boiko et al., 1989; Dovgal et al., 1994). In the investigations by Yarusevych et al. (2006, 2009), the authors found peaks in the spectra of fluctuating velocity at harmonics of the fundamental frequency within the separation bubble. When the separated shear layer failed to reattach to the airfoil surface, subharmonic and harmonics of the fundamental frequency were observed. Brendel & Mueller (1990) found that growth of the subharmonic disturbance exceeded that of the fundamental disturbance when the separation bubble thickness increased, similar to a free shear layer. Furthermore, growth of the subharmonic disturbance was checked below the fundamental disturbance when the separation bubble thickness decreased. Boiko et al. (1989), Yarusevych et al. (2006), and Burgmann et al. (2006) estimated convective velocities on the order of $0.4U_o$-$0.6U_o$, comparable to the mean velocity at the inflection point ($0.5U_o$) , which characterizes convective velocities of disturbances in free shear layers (Dovgal et al., 1994). The aforementioned discussion substantiates that, for both regimes, laminar-to-turbulent transition in the separated shear layer is influenced by both inviscid and viscous effects governed by separated shear layer proximity to the airfoil surface.

The existence of a global instability mechanism in the separation bubble was examined experimentally by Boiko et al. (2002). The authors determined that, within the reattachment region, instability waves may be excited by external disturbances, which induce perturbations in the reattaching flow. A backward effect occurs in which these perturbations propagate upstream through the separation bubble and modulate mean flow properties such

as length and depth of the separation bubble (Boiko et al., 2002). However, the authors concluded that the local properties responsible for initial disturbance amplification remain unaffected, which is contrary to the feedback effect reported by Marxen & Rist (2010) within a separation bubble generated on a flat plate (see §1.3.2). Thus, a feedback mechanism of this nature precludes the existence of a global instability mechanism. In a DNS study conducted by Jones et al. (2008), instability mechanisms were explored in a separation bubble generated on a full airfoil configuration. From linear stability analysis, these authors concluded that a convective instability occurred for all two-dimensional and three-dimensional simulations since the reverse flow criterion established by Alam & Sandham (2000) was not exceeded. However, further analysis within the reattachment region revealed an exponential temporal growth of disturbances. The authors concluded that this was due to a combination of instability mechanisms observed in bluff-body wakes that differ from classical definitions of absolute instability. More recently, Jones et al. (2010) revisited this test case to further explore the instability mechanisms. The global instability was explored by introducing a periodic artificial disturbance for a finite duration in the laminar boundary layer upstream of the separation bubble and examining the flow development over the upper surface of the airfoil. The response of the flow field to the disturbance was monitored using time-series signals of fluctuating pressure at the y/c location of maximum vorticity in the shear layer and isocontours of the disturbance dilation rate. The authors found that the artificial disturbance amplified as it convected downstream over the upper surface of the airfoil. Once the disturbance reached the trailing-edge, upstream travelling pressure waves were generated by acoustic scattering at the trailing-edge. Once the upstream pressure wave reached the leading-edge, downstream convecting disturbances re-emerged in the separated flow region and the process was repeated. In addition, temporal exponential growth of oscillations in the pressure

signal was observed at x/c = 0.95. Therefore, the authors concluded that there was no evidence of a global instability within the separated flow region; however, the flow field was unstable to the acoustic feedback loop process.

The structure and evolution of coherent structures forming in the separated shear layer of a separation bubble was reported by Burgmann et al. (2006, 2007) and Burgmann & Schröder (2008). Spanwise coherent structures formed due to shear layer roll-up undergo deformation in the aft portion of the bubble, resulting in the formation of c-shaped vortices. This occurred due to differences in convective velocities, namely, the outer portions of the roll-up vortices moved faster than the cores. The periodic ejection of coherent structures from the separation bubble caused vertical oscillations in the separated shear layer and fluctuations of the reattachment location, producing separation bubble 'flapping' motion characterized by a low-frequency band oscillation detected in some studies (e.g., Boiko et al., 1989; Zhang et al., 2008). Downstream of reattachment, entrainment of free-stream fluid into the centerplane of the shed vortex caused the vortex arms to realign in the streamwise direction due to a redistribution of fluid in the vortex. The authors referred to these structures as screwdriver vortex-pairs (Burgmann et al., 2007; Burgmann & Schröder, 2008). In the reattaching turbulent boundary layer, the streamwise-oriented structures interacted and produced arc-like structures reminiscent of Λ-vortices.

The development of coherent structures in the separated shear layer for flow separation without reattachment was examined by Yarusevych et al. (2006, 2009) using smoke-wire visualization. A region of reverse flow was revealed adjacent to the airfoil surface by the entrainment of smoke in the upstream direction, bounded between the airfoil surface and separated shear layer. A series of coherent vortices associated with shear layer

roll-up were identified in the separated shear layer. It was confirmed that the frequency of the shedding vortices was linked to the most amplified band of disturbances in the separated shear layer, centered at the fundamental frequency in the spectra of fluctuating velocity. It was revealed from a sequence of flow visualization images that vortices were also formed by the merging of two shed vortices. The frequency of the merged vortices was half the vortex shedding frequency, which coincides with the subharmonic of the fundamental frequency in the spectra of fluctuating velocity. The authors suggested that, within the regime of flow separation without reattachment, the non-linear stage of transition with subharmonic disturbance growth was associated with merging of vortices shed from the separated shear layer. Following merging, the vortices broke down into smaller scale structures, similar to the breakdown of coherent vortices in the separation bubble reported by Burgmann et al. (2006, 2007) and Burgmann & Schröder (2008).

Yarusevych et al. (2006, 2009) have also shown that the behaviour and characteristics of coherent structures in the separated shear layer are linked to the Reynolds number and flow regime. For a given angle of attack and flow regime, the fundamental frequency scales with the Reynolds number as $f_o \sim (Re_c)^n$ (Yarusevych et al., 2006, 2009).

1.4 Conventional Experimental Flow Diagnostics Techniques

Studies discussed in §1.3.2 and §1.3.3 employed a variety of experimental techniques to characterize separated shear layer development. These techniques include: flow visualization, static (mean) pressure, hot wire anemometry, laser Doppler anemometry (LDA), and particle image velocimetry (PIV).

Smoke-wire visualization (e.g., Mueller & Batill, 1982; Yarusevych et al., 2006, 2009) and liquid-crystal visualization (e.g., Nakano et al., 2007) techniques have been employed for both qualitative and quantitative purposes. For instance, separated shear layer roll-up was observed in smoke-wire visualizations reported by Yarusevych et al. (2009), whereas locations of separation and reattachment were estimated from liquid-crystal visualization by Nakano et al. (2007).

Static surface pressure data, typically in the form of a pressure coefficient distribution, can be utilized to estimate locations of flow separation, transition, and reattachment (e.g., Tani, 1964; O'Meara & Mueller, 1987; Yarusevych et al., 2006, 2009). Lift coefficients can also be obtained from the pressure coefficient distributions (e.g., Tani, 1964; Lee & Gerontakos, 2002).

Time-resolved velocity measurements via hot wire anemometry (e.g., Boiko et al., 1989; Brendel & Mueller, 1988, 1990; Watmuff, 1999; Häggmark, 2000; Yarusevych et al., 2006, 2009) and LDA (e.g., Brendel & Mueller, 1988, 1990; Lang et al., 2004) have been employed to obtain boundary layer profiles (e.g., Watmuff, 1999; Häggmark, 2000; Lang et al., 2004) as well as disturbance growth rates (e.g., Brendel & Mueller, 1988, 1990; Watmuff, 1999; Häggmark, 2000; Lang et al., 2004; Yarusevych et al., 2006, 2009) and frequency content (e.g., Boiko et al., 1989; Yarusevych et al., 2006, 2009). Boundary layer profiles can be used to estimate separation and reattachment locations and separated shear layer trajectory. Furthermore, the shape of wall-normal disturbance amplitude profiles can shed light on instability mechanisms governing separated shear layer transition (e.g., Häggmark, 2000). From the frequency content of time-resolved velocity measurements, Boiko et al. (1989) and Yarusevych et al. (2006, 2009) identified the frequency of the

fundamental and subharmonic disturbances. Since the hot wire probe must be immersed in the flow to acquire measurements, hot wire anemometry is an invasive technique and care must be taken not to perturb the sensitive separation bubble. Furthermore, for boundary layer measurements, it is limited to single-point measurements, where a single probe is positioned in the flow by an automated traversing mechanism (e.g., Watmuff, 1999). On the other hand, LDA is non-invasive, therefore mitigating the risk of perturbing the separation bubble, however, it must be operated in carefully controlled laboratory conditions since flow seeding is required and high-powered lasers are operated.

PIV and stereoscopic PIV (SPIV) are capable of time-resolved, multi-point, and three-dimensional flow field measurements, as reported in Burgmann et al. (2006, 2007) and Burgmann & Schröder (2008). Its ability to resolve velocity vectors within a finite flow region is of particular importance for the flow of interest. Similar to LDA, PIV and SPIV techniques are used in carefully controlled laboratory environments since flow seeding, lasers, and optical equipment are required.

1.5 Time-Resolved Surface Pressure Measurements

The earliest reports of time-resolved surface pressure measurements date back to the 1950s. One of the first studies to report measurements of fluctuating surface pressure within a turbulent boundary layer were that by Willmarth (1956) for wind tunnel measurements and Mull & Algranti (1956) on the surface of an aircraft. McLeod & Jordon (1958) showed that noise within the fuselage of an aircraft in flight at subsonic cruise conditions was attributed to fuselage boundary layer noise. For the in flight experiments, microphones were embedded in the aircraft surface to facilitate measurements of fluctuating surface pressure. In contrast to

the aforementioned studies, where only single-point measurements of fluctuating surface pressure were obtained, Willmarth (1958) pioneered multi-point measurements of fluctuating surface pressure and showed that large-scale disturbances propagate convectively through a turbulent boundary layer.

Relevant for airfoils operating at low Reynolds numbers is the utility of time-resolved surface pressure fluctuation measurements for characterizing the separated flow region. However, studies employing measurements of fluctuating surface pressure in the separated flow region on an airfoil surface at low Reynolds numbers are limited likely due to the complexity of separated shear layer development. Alternatively, a number of studies involving measurements of time-resolved fluctuating surface pressure in the separated flow region were performed on simpler geometries. These geometries shown in Fig. 1.5 are the blunt-face splitter plate (BFSP), the backward-facing step (BFS), the splitter plate with fence (SPF)[2], and the circular cylinder. Studies employing measurements of time-resolved fluctuating surface pressure on these simpler geometries are relevant since they examine regimes of flow separation with reattachment (i.e., BFSP, BFS, SPF, and circular cylinder) and flow separation without reattachment (i.e., circular cylinder). For an extensive description of the flow field for these geometries, the author recommends reviewing Kiya & Sasaki (1981, 1983), Eaton & Johnson (1981), Castro & Haque (1987), and Zdravkovich (1997) for the BFSP, BFS, SPF, and circular cylinder, respectively. For studies involving separation with reattachment (i.e., BFSP, BFS, and SPF), boundary layer separation was induced by a sharp edge, with a separating and reattaching shear layer enclosing a recirculating flow region. The boundary layer prior to flow separation was laminar for the

[2] *This is also referred to as a spoiler in some literature (e.g., see Mabey, 1972).*

BFSP and SPF studies and turbulent for the BFS studies. In the investigations on BFSP and SPF, transition to turbulence occurred within the initial 5% - 10% of the separation bubble length, thus, the majority of flow measurements were within the turbulent portion of the bubble. In addition, for flow parameters relevant to this investigation, flow over a circular cylinder involves both regimes of flow separation with and without reattachment. The laminar boundary layer separates from the surface of the cylinder as a consequence of an adverse pressure gradient, with laminar-to-turbulent transition occurring in the separated shear layer. When the separated shear layer fails to reattach to the cylinder surface, roll-up vortices form in the wake of the cylinder. Conversely, the separated shear layer may reattach to the cylinder surface and a turbulent boundary layer subsequently separates.

Mabey (1972) reviewed single-point measurements of time-resolved fluctuating surface pressure in the separated flow region on a forward-facing step (FFS), BFS, and SPF. For these geometries, it was found that surface pressure fluctuations within the separated flow region increased steadily, reaching a maximum just upstream of reattachment and decaying further downstream. More extensive studies employing single-point and multi-point measurements of time-resolved fluctuating surface pressure in the separated flow region were performed on a BFSP (e.g., Kiya & Sasaki, 1983; Cherry et al., 1984), BFS (e.g., Farabee & Casarella, 1986; Driver et al., 1987; Lee & Sung, 2001; Hudy et al., 2007), SPF (e.g., Hudy et al., 2003), and a circular cylinder (e.g, Norberg, 1986, 2003; Norberg & Sundén, 1987). In the studies on the BFSP, BFS, and SPF, some common observations were consistent with those reported by Mabey (1972), notably, that the surface pressure fluctuations increase steadily and reach a maximum just upstream of reattachment followed by decay further downstream (e.g., Cherry et al., 1984; Farabee & Casarella, 1986; Driver et al., 1987; Lee & Sung, 2001; Hudy et al., 2003). Furthermore, two dominant peaks in the spectra of

fluctuating surface pressure were observed: (i) a peak near separation attributed to separated shear layer flapping, and (ii) a higher frequency peak emerges and dominates downstream of separation, which is associated with vortex shedding in the separated shear layer (e.g., Kiya & Sasaki, 1983; Cherry et al., 1984; Driver et al., 1987; Lee & Sung, 2001; Hudy et al., 2003).

In §1.5.1 through §1.5.4, studies employing extensive single-point and multi-point measurements of time-resolved fluctuating surface pressure to examine separated shear layer development is discussed for a BFSP, BFS, SPF, and circular cylinder, respectively. The utility of time-resolved surface pressure fluctuation measurements on an airfoil surface is discussed in §1.5.5.

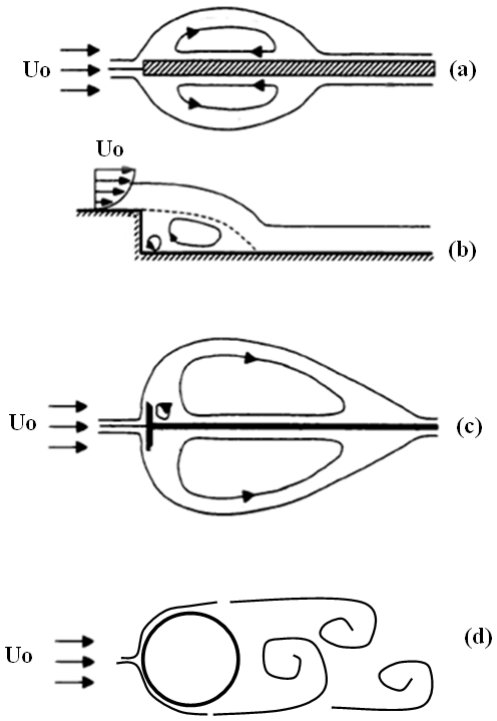

Figure 1.5: Schematic of two-dimensional flow topology for simpler flow geometries: (a) blunt-face splitter plate (BFSP), (b) backward-facing step (BFS), (c) splitter plate with fence (spoiler) (SPF), and (d) circular cylinder. Images (a) through (c) are reproduced from Hudy (2003) and image (d) is reproduced from Williamson (1996).

1.5.1 Flow over a Blunt Face Splitter Plate

Kiya & Sasaki (1983) employed two-point measurements of fluctuating surface pressure in a separating-reattaching flow over a blunt face splitter plate. Analysis of Spectra of fluctuating velocity and surface pressure revealed the following two distinct frequencies: (i) a flapping frequency associated with unsteady motion of the separation bubble in the streamwise direction and (ii) a frequency associated with vortex shedding from the separated shear layer. These results confirmed that velocity fluctuations in the separated shear layer lead to distinct pressure fluctuations on the underlying surface. From cross-correlation analysis of fluctuating surface pressure acquired from two neighbouring pressure sensors embedded in the surface near reattachment, it was found that surface pressure fluctuations convect at a velocity of $0.5U_o$. This estimate was in close agreement with a convective velocity estimated from two-point measurements of fluctuating velocity in the corresponding region. Two-point cross-spectral analysis was performed for measurements of fluctuating surface pressure obtained from a pressure sensor near separation and another near reattachment. A phase angle analysis of the cross-spectrum results revealed a 180-degree phase shift for frequencies less than the flapping frequency. Thus, surface pressure fluctuations near separation and reattachment occur out-of-phase. The authors indicated that positive surface pressure fluctuations at separation were associated with negative surface pressure fluctuations at reattachment and an upstream movement of the instantaneous reattachment line. Moreover, a downstream movement of the instantaneous reattachment line occurred when the surface pressure fluctuations at separation and reattachment changed sign. Hence, the authors speculated that out-of-phase pressure fluctuations near separation and reattachment were associated with an unsteady modulation of the separation bubble length.

Cherry et al. (1984) performed a similar study employing two-point measurements of fluctuating surface pressure. Similar to the findings of Kiya & Sasaki (1983), matching spectral characteristics were obtained from measurements of fluctuating velocity and surface pressure. The convective velocity was also estimated to be $0.5U_o$ based on measurements of fluctuating surface pressure, compared to $0.63U_o$ estimated from measurements of fluctuating velocity in the separated shear layer. The authors speculated that the latter convective velocity was higher since it was acquired in the separated shear layer and therefore biased towards larger-scale disturbances with higher propagation speeds. A cross-correlation analysis of two-point measurements of fluctuating surface pressure was performed near separation in the spanwise direction to examine the spanwise movement of the separation location. The results revealed that the correlation coefficient magnitude decreased and changed sign for increasing spanwise distance. The authors concluded that the negative correlation coefficients indicate a tendency for an out-of-phase shear layer flapping motion in the spanwise direction (Cherry et al., 1984). Downstream of separation, the spanwise correlation coefficient magnitude decayed more rapidly with increasing spanwise distance from the midspan plane and negative correlation coefficients were not observed. The authors concluded that the flow field becomes more three-dimensional with an increase in streamwise distances.

1.5.2 Flow over a Backward-Facing Step

Farabee & Casarella (1986) studied the streamwise convection of surface pressure fluctuations in the reattaching separated shear layer and developing turbulent boundary layer behind a backward-facing step. Single-point and two-point measurements of fluctuating

surface pressure were obtained from microphones mounted flush with the underlying surface in a single streamwise row. Simultaneous measurements were acquired for various pairs of microphones separated by the same streamwise distance. Mean and RMS velocity profiles were also acquired in the corresponding region. Spectra of fluctuating surface pressure revealed a dominant and broad spectral peak at lower frequencies near reattachment in the frequency range from 100 Hz to 1,000 Hz. The low frequency spectral peak decayed with streamwise distance and eventually resulted in a spectrum of fluctuating surface pressure reminiscent of a velocity fluctuation spectrum for a fully-developed turbulent boundary layer on a flat plate. The authors also found that a dominant peak in the RMS velocity profile occurred near the wall at reattachment, which broadened and diffused away from the wall with increasing streamwise distance in the developing turbulent boundary layer. The streamwise phase velocity through reattachment and the developing turbulent boundary layer was estimated from the phase angle of the cross-spectrum for various pairs of microphones. Near reattachment, the phase velocity at the low frequency spectral peak was on the order of $0.4U_o$ to $0.5U_o$. The decay in the spectral peak with increasing streamwise distance was associated with an increase in the phase velocity to a value in the range from $0.7U_o$ to $0.75U_o$ across the frequency bandwidth relevant for frequencies in the flow field. The authors concluded that the pressure fluctuations near reattachment were associated with the low frequency turbulent activity, which was located near the wall where the mean velocity was lower, and hence, corresponded to a lower convective velocity. As the pressure fluctuations convected downstream through the developing turbulent boundary layer, the turbulent activity diffused away from the wall, where the mean velocity was higher and therefore corresponded to a higher convective velocity.

Lee and Sung (2001) used an embedded 32-microphone grid with a single streamwise row and a single spanwise row to study the flow field in the streamwise and spanwise directions, respectively. For analysis purposes, simultaneous measurements of time-resolved fluctuating surface pressure were acquired for various pairs of microphones. The spatial location of the upstream microphone was fixed and the separation distance between the pair of microphones was varied. Phase velocities were computed in the streamwise direction and the coherence of structures in the separated shear layer was examined in the spanwise direction. In the streamwise direction, the phase velocity was computed based on the phase angle of the cross-spectrum for various pairs of microphones. The authors found a phase velocity of $0.6U_o$ associated with surface pressure fluctuations at the vortex shedding frequency. In the spanwise direction near separation, the coherence of fluctuating surface pressure was strong for a wide band of frequencies centered at the vortex shedding frequency. However, in the aft portion of the bubble, a broadband decay occurred in spanwise coherence, except at the shedding frequency. The authors concluded that the vortices shed in the separated shear layer are strongly two-dimensional in the spanwise direction through the bubble.

Hudy et al. (2007) also investigated the separating-reattaching flow field using 32 microphones embedded in the surface in a streamwise row. Simultaneous measurements were acquired for various pairs of microphones separated by the same streamwise distance. A downstream convective velocity of surface pressure fluctuations was detected, which varied non-linearly in the streamwise direction.

1.5.3 Flow over a Splitter Plate with Fence

An extensive study of the separated flow region over a splitter plate with fence was performed by Hudy et al. (2003) using an embedded 80-microphone array. Simultaneous measurements of various microphone pairs were acquired in the streamwise direction. Hudy et al. (2003) defined the convective velocity as the average propagation of disturbances for various timescales (i.e., biased towards the propagation of the dominant disturbance), while the phase velocity was defined as the propagation of disturbances associated with a specific timescale or frequency. Convective velocities of the roll-up vortex were estimated from cross-correlation results in a region near the fence to the middle of the bubble and in the aft portion of the bubble. At a distance of approximately 25% of the bubble length downstream of separation, there was a discrete change from a region of upstream convective velocity of $0.21U_o$ to a region of downstream convective velocity of $0.47U_o$. Conversely, only a downstream convective velocity of $0.57U_o$ was estimated in the aft portion of the bubble. From phase angle analysis, phase velocities were estimated through the entire separation bubble at the flapping frequency. A zone of upstream phase velocity of $0.31U_o$ was revealed from separation to the middle of the bubble, which was larger than the convective velocity computed in the same region. The authors did not provide an explanation for the difference in the magnitudes of the convective and phase velocities. Further downstream through the bubble, a phase angle jump of 180-degrees marked a switch to a zone of downstream phase velocity. The authors conjectured that the phase jump was reminiscent of a standing-wave-like disturbance, separating regions of upstream and downstream travelling disturbances. Furthermore, the authors speculated that the standing-wave is linked to an absolute instability responsible for shear layer flapping.

1.5.4 Flow over a Cylinder

In §1.5.1 and §1.5.3, studies employing measurements of time-resolved fluctuating surface pressure to characterize separated shear layer development in a separation bubble were discussed for simpler geometries. However, none of these studies explored separated shear layer development for flow separation without reattachment. In this section, studies utilizing measurements of time-resolved fluctuating surface pressure to characterize separated shear layer development over a circular cylinder are discussed for regimes of flow separation with and without reattachment.

A sketch of the flow topology around a circular cylinder with flow separation is shown in Fig. 1. It should be noted that the Reynolds number is defined based on the cylinder diameter ($Re_D = U_0 D/\nu$). In Fig. 1.6, the oncoming flow stagnates at the front of the cylinder and accelerates as it deflects around the cylinder, forming a laminar boundary layer on the surface. Within the subcritical and critical flow regimes, which are relevant for this investigation (i.e., $1000 < Re_D < 3x10^5$), the laminar boundary layer separates from the cylinder surface as a consequence of an adverse pressure gradient. For a comprehensive description of the flow development in these regimes, the author suggests reviewing work done by Zdravkovich (1997). Within the subcritical regime ($1000 < Re_D < 1\text{-}2x10^5$), laminar-to-turbulent transition occurs in the separated shear layer with subsequent formation of roll-up vortices in the cylinder wake. The laminar separation location advances upstream along the cylinder surface and the roll-up vortices form closer to the rear of the cylinder with an increase in the Reynolds number. Within the critical regime ($Re_D > 1\text{-}2x10^5$), following transition in the separated shear layer, the flow may reattach to the cylinder surface and the turbulent boundary layer may subsequently separate. As this regime is approached,

separation is typically delayed and the strength of vortices decreases, which is associated with a delay in vortex formation.

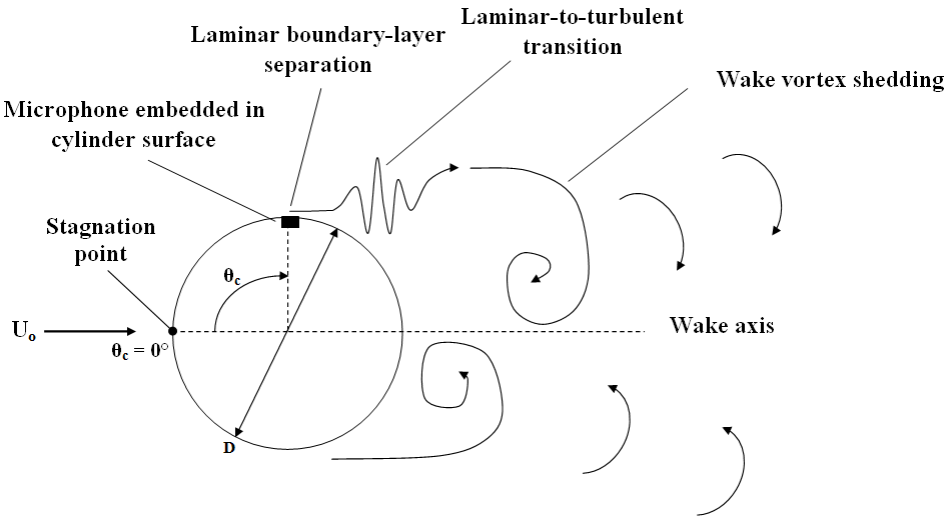

Figure 1.6: Flow topology around a circular cylinder within the subcritical flow regime. Note that the image is reproduced from Williamson (1996).

A few studies employing measurements of time-resolved fluctuating surface pressure around a circular cylinder in the subcritical and critical flow regimes have been reported by Norberg (1986, 2003) and Norberg & Sundén (1987). In these studies, a microphone was embedded in the cylinder surface and its position was changed by rotating the cylinder through an angle (θ_c) measured from the stagnation point ($\theta_c = 0°$) (Fig. 1.6).Within the subcritical regime, measurements revealed that fluctuating surface pressure increased steadily from the stagnation point, reaching a maximum at the location of laminar separation (primary maximum). With increasing Reynolds number, the primary maximum advanced upstream with the separation location. Depending on the Reynolds number, two distinct regions can be identified in the RMS fluctuating surface pressure distributions downstream of separation.

For Reynolds numbers from $1x10^3$ to $5x10^3$, pressure fluctuations decreased steadily downstream of separation (e.g., Norberg, 2003). For $5x10^3 \leq Re_D \leq 60x10^3$, a secondary maximum emerged in the RMS fluctuating surface pressure distributions centered at θ_c = 150° (e.g., Norberg, 1986, 2003; Norberg & Sundén, 1987). Norberg & Sundén (1987) concluded that the secondary maximum was related to the roll-up vortex moving closer to the base of the cylinder, therefore increasing the fluctuating surface pressure at this location. This was further substantiated since a peak in the spectra of time-resolved fluctuating surface pressure at the vortex shedding frequency emerged at θ_c = 150°, which coincides with the location of the secondary maximum. Spanwise correlation was also examined by Norberg & Sundén (1987) from the cross-correlation of two microphones separated in the spanwise direction, where the spanwise separation distance between the microphones was varied. The authors defined a spanwise correlation length as the separation distance for which the correlation coefficient decreased to a value of 0.5. With this definition, the correlation length decreased from 3.5D to 1.0D at θ_c = 45° and θ_c = 180°, respectively. Norberg & Sundén (1987) measured time-resolved fluctuating surface pressures in the separated flow region when the Reynolds number was increased from the subcritical regime to the critical regime. From spectral analysis of time-resolved fluctuating surface pressure, for Reynolds numbers upwards $1.3x10^5$, the shedding frequency and its harmonic were observed. For higher Reynolds numbers upwards of $3x10^5$, the harmonic disappeared and the peak associated with the shedding frequency broadened. The authors concluded that the aforementioned observations were consistent with a decrease in vortex strength and delay of vortex formation, which are characteristics of the critical regime. The change in flow development through these regimes was further explored with mean surface pressure and RMS fluctuating surface pressure distributions. For Reynolds numbers from $1x10^5$ to $3x10^5$, the pressure

fluctuation amplitude associated with the primary maximum decreased and shifted in the downstream direction, consistent with a delay in separation location. The secondary maximum also decreased and eventually vanished, which the authors concluded was consistent with weakening vortex strength and delay in vortex formation. At a location between these maxima, an intermediate maximum emerged and dominated. The location of the intermediate maximum coincided with the shear layer reattachment location as indicated from the mean surface pressure distribution. For a Reynolds number of $3x10^5$, the RMS fluctuating surface pressure increased steadily from the stagnation point to a maximum at reattachment, and decreased steadily around the backside of the cylinder. This observation further substantiates the universality of the RMS fluctuating surface pressure distribution through a separation bubble as reported by Mabey (1972).

1.5.5 Flow over an Airfoil

Measurements of time-resolved fluctuating surface pressure within the separated flow region over an airfoil surface are less common than those performed within separated flow region forming on simpler geometries (e.g., Fig. 1.5) due to the added complexity of separated shear layer development over an airfoil surface. For instance, the location and extent of the separated flow region changes with flow conditions. As a consequence, it is difficult to design and instrument an airfoil with an array of pressure transducers to adequately resolve and cover the separated flow region for various flow conditions.

Weibust et al. (1987) performed single-point measurements of time-resolved fluctuating surface pressure within a separation bubble on the surface of an airfoil using a novel experimental setup. The setup consisted of two pressure transducers separated in the

streamwise direction and mounted on a movable ribbon embedded in the airfoil surface. Measurements of fluctuating surface pressure were recorded while the transducers were positioned at fixed locations within the bubble and while the transducers were slowly moving through the bubble in the streamwise direction. In the time-series signals of fluctuating surface pressure, the results show negligible surface pressure fluctuations underneath the laminar portion of the separated shear layer. Flow transition was accompanied by growth of surface pressure fluctuations through the aft portion of the bubble, reaching a maximum just upstream of reattachment. These observations indicate that the streamwise evolution of the RMS fluctuating surface pressure distribution corresponds to the distributions described by Mabey (1972) on simpler geometries (see §1.5). Additionally, the region of amplified surface pressure fluctuations was contained within the separation bubble, which moved along the airfoil surface with changes in the Reynolds number and/or angle of attack. At a given location within the separation bubble, there was marginal variation in the magnitude of the surface pressure fluctuations with changes in the flow parameters.

Yarusevych et al. (2008) also performed single-point measurements of time-resolved fluctuating surface pressure within the separated flow region with and without subsequent reattachment. Spectra of fluctuating velocity and surface pressure were obtained at matching streamwise locations. Also, cross-correlation analysis was performed between measurements of fluctuating vertical velocity and surface pressure at the same streamwise locations. The results indicate that the dominant frequency of fluctuating surface pressure matches that of the fluctuating velocity in the separated shear layer. However, the authors indicated that, the ability to detect surface pressure fluctuations produced by disturbances in the shear layer is dependent on both the proximity of the shear layer to the underlying surface and the strength of velocity fluctuations at a given streamwise location.

Barrett (2000) measured surface pressure fluctuations in a transitional separation bubble on an inclined flat plate with an elliptical leading-edge. The streamwise RMS fluctuating surface pressure distributions were similar to those observed in all the aforementioned studies within separation bubbles on simpler geometries (see §1.5), notably, the peak fluctuation occurred just upstream of reattachment.

Swalwell et al. (2003) examined the frequency of vortex shedding from the separated shear layer on the upper surface of a NACA 0021 airfoil at post-stall angles of attack and a Reynolds number of 2.7×10^5. Measurements of fluctuating surface pressure were obtained from two streamwise rows of pressure taps, symmetrically distributed on the upper and lower surface of the airfoil. 1.7 m long pressure lines connected the pressure taps to a pressure scanner module. The pressure measurements were corrected for effect of the tubing on the amplitude and phase of the signal. Time-resolved lift and drag coefficients were computed from a spline fit to the corrected fluctuating surface pressure measurements for each sample (i.e., time step). The vortex shedding frequencies were estimated from the spectra of fluctuating lift and drag coefficients. The authors found that the vortex shedding frequency declined from 100 Hz to 45 Hz with an increase in the angle of attack for $30° \leq \alpha \leq 90°$, which was a similar trend to that observed by Chen & Feng (1996) for a stalled inclined flat plate.

Paterson et al. (1973) examined vortex shedding characteristics for a NACA 0012 airfoil from measurements of fluctuating surface pressure and far-field acoustic measurements. The airfoil was equipped with five flush-mounted microphones embedded in the upper surface in a streamwise row. In addition, a microphone was embedded on a slider ribbon which could be traversed in the spanwise direction on the airfoil surface similar to the

technique reported by Weibust et al. (1987). Far-field acoustic measurements were also acquired from an off-surface microphone. For the flow parameters investigated, measurements from the microphones embedded in the airfoil surface were obtained within a laminar and turbulent boundary layer developing on the airfoil surface. Measurements reported at $Re_c = 4.6x10^5$ and $\alpha = 6°$ revealed a discrete frequency in the far-field acoustic spectrum, which matched the frequency associated with the peak in the fluctuating velocity spectrum measured just downstream of the airfoil trailing-edge. A peak in the spectra of fluctuating surface pressure obtained from the microphones embedded in the airfoil surface also occurred at the same frequency. The authors attributed the tonal noise emission to the interaction between the turbulent boundary layer on the upper surface and the laminar boundary layer on the lower surface just downstream of the trailing-edge. The spanwise correlation of the fluctuating surface pressure was computed from a microphone in the streamwise row at x/c = 0.38 and the microphone in the slider ribbon at x/c = 0.30. The authors found that the spanwise correlation was almost unity for a spanwise separation between the microphones upwards of 40% of the airfoil span. The authors concluded that the surface pressure fluctuations associated with tonal noise emission were coherent over a considerable spanwise extent on the airfoil surface. A convective velocity of surface pressure fluctuations was estimated from streamwise correlation computed for pairs of microphones separated in the streamwise direction. For all pairs of microphones, the authors found an upstream convective velocity ranging from 317 to 378 m/s, which was close to the speed of sound. Thus, the authors suggested that the pressure waves generated over the airfoil surface at the tonal frequency were associated with an acoustic disturbance which emanated from just downstream of the trailing-edge and propagated upstream over the airfoil upper surface. Such findings are similar to the acoustic feedback loop reported in the DNS study by Jones et

al. (2010) (see §1.3.3). When the Reynolds number was increased to $2.2x10^6$, the tonal noise was not detected in the far-field spectra or in the spectra of fluctuating surface pressure. The streamwise convective velocity of surface pressure fluctuations was estimated to be $0.83U_o$ in the downstream direction, which was the same value estimated by Willmarth & Wooldridge (1962) in a turbulent boundary layer on a flat plate. The authors suggested that this evidence precludes the existence, or at least detection, of tonal noise emission from the airfoil at this Reynolds number.

A comprehensive study of noise generated within the turbulent boundary layer on an airfoil surface upstream of a sharp trailing-edge was reported by Brooks & Hodgson (1981). Although this study was not conducted in a separated flow region, similar to the study reported by Paterson et al. (1973), a microphone array was utilized to examine the flow field. The array consisted of 36 microphones embedded in an airfoil, which were distributed symmetrically on the upper and lower surfaces in the vicinity of the trailing-edge. Coherence analysis was performed for pressure signals captured by microphone pairs near the trailing-edge in the streamwise and spanwise directions for the same microphone spacing and flow conditions. The results revealed a broad peak centered at a frequency of 700 Hz in both the streamwise and spanwise coherence and the broadband coherence was stronger in the streamwise direction. The authors suggested that the peak in the streamwise coherence indicated that the eddy centered at a frequency of 700 Hz was the strongest coherent structure propagating in the streamwise direction between the pair of microphones relative to eddies at other frequencies. Additionally, the eddy associated with the peak spanwise coherence was the most two-dimensional structure in the flow relative to eddies at other frequencies. Thus, the authors concluded that spanwise coherence is an indication of an eddy's spanwise length scale, while streamwise coherence is an indication of the lifespan (or decay) of an eddy. The

authors further conjectured that the streamwise and spanwise coherence were interrelated. For instance, eddies with largest spanwise length scale have the longest lifespan.

Another study performed by Choudhari et al. (2002) examined the radiated acoustic field from a full high-lift wing configuration. Specifically, measurements focused on identifying noise emission from a leading-edge slat and part-span trailing-edge flap. Single-point measurements of fluctuating surface pressure were used to identify the frequencies of vortices shed from the leading-edge slat and trailing-edge flap sections believed to be associated with tonal noise generation. Also, off-surface measurements of acoustic emissions were obtained from large aperture microphone arrays, where each array consisted of approximately 60 microphones. Analysis of the on-surface and off-surface microphone measurements revealed that vortex shedding from the leading-edge slat and trailing-edge flap was responsible for noise emissions.

1.6 Motivation and Objective

1.6.1 Motivation

Throughout this chapter, it has been shown that the flow development over an airfoil surface is complex and highly unsteady at low Reynolds numbers. The laminar boundary layer may separate from the upper surface of an airfoil and subsequently undergo laminar-to-turbulent transition in the separated shear layer. Following transition, the separated shear layer will either reattach to the airfoil surface or remain separated, with the latter resulting in an airfoil stall. The time-dependent nature of separated shear layer development can be characterized using spatially resolved instantaneous flow field measurements. In fact, such measurements

could be performed in flight using a field-applicable measurement system configured for online flow diagnostics, which could serve as an integral subsystem for active flow control. Active flow control is aimed at manipulating the mean and fluctuating flow characteristics by controlled generation of disturbances, thereby reducing and/or eliminating the separated flow region (Boiko et al., 2002). As a result, performance degradation and noise emission associated with flow separation can be mitigated. A field-applicable measurement system serves to provide knowledge of the amplitude, oscillation, and location to apply controlled excitation.

Conventional experimental measurement techniques have been successfully employed in a number of studies to investigate the separated flow region over an airfoil surface at low Reynolds numbers. These studies have advanced understanding of the separated flow region topology, instability mechanisms responsible for laminar-to-turbulent transition, and the evolution of coherent structures. However, conventional measurement techniques are only suitable for laboratory conditions and are not field-applicable. Thus, there is a need for a field-applicable measurement system that has the capabilities of conventional laboratory measurement techniques. Of particular interest are time-resolved, single-point, and multi-point flow field measurements capabilities. In addition, the measurement system must be non-intrusive since the flow transition process is highly sensitive to disturbances (e.g., Boiko et al., 2002).

It is proposed that a novel time-resolved surface pressure measurement system can be used to characterize the separated flow region over an airfoil surface at low Reynolds numbers. Using an array of pressure sensors embedded in an airfoil surface, single-point and/or multi-point measurements of time-resolved fluctuating surface pressure can be

realized. Furthermore, the system is non-invasive and suitable for field-applicability since the pressure sensors would be embedded in the airfoil surface and therefore would not perturb the flow.

1.6.2 Objective

There are two main objectives for this thesis:

1) Develop a time-resolved fluctuating surface pressure measurement system for flow diagnostics over an airfoil at low Reynolds numbers

   i. Design an airfoil testbed consisting of:

      - An array of pressure taps for static surface pressure measurements
      - An array of microphones embedded in the airfoil surface for measurements of time-resolved fluctuating surface pressure

   ii. Perform an extensive aerodynamic characterization of the airfoil testbed using conventional flow diagnostics techniques

   iii. Verify the capabilities of time-resolved fluctuating surface pressure measurements with conventional diagnostics measurements in the separated flow region

2) Use the system to explore the analysis capabilities of time-resolved fluctuating surface pressure measurements for estimating salient flow characteristics in the separated flow region of an airfoil at low Reynolds numbers

To the knowledge of the author, this is the first study to utilize multi-point measurements of time-resolved fluctuating surface pressure to examine separated shear layer development on an airfoil operating in low Reynolds number flows.

2 Experimental Description

2.1 University of Waterloo Adaptive-Wall Wind Tunnel

Experiments reported in this thesis were conducted in a wind tunnel located at the University of Waterloo. The wind tunnel facility was originally built in 1963 and underwent extensive modifications in 1991 to extend the test section and implement two flexible walls to facilitate wall-adaptation (Kankainen et al., 1994). Recently, flow quality improvements were implemented to upgrade the wind tunnel to a modern research grade testing facility (Bishop, 2010).

The present configuration of this open-return, suction-type wind tunnel is depicted in Fig. 2.1. The rectangular test section of the wind tunnel, comprised of rigid side walls and flexible top and bottom walls, has a height 890 mm (35 inches), a width of 610 mm (24 inches), and a length of 6 m. On the viewing-side of the wind tunnel, the rigid side walls are constructed of 25.4 mm (1 inch) thick clear cast acrylic. On the solid-side of the wind tunnel, the rigid side walls are constructed of 25.4 mm (1 inch) thick laminated plywood with a matte-black painted surface. The flexible top and bottom walls are made of Lexan polycarbonate sheets.

Flow enters the test section through a honeycomb and four screens positioned upstream of a 9:1 contraction. Within the test section, the free-stream speed can be varied from 2 to 40 m/s with a background turbulence intensity of less than 0.3%. The free-stream speed within the test section was set by measuring the pressure drop across the 9:1 contraction. The pressure drop was calibrated against a pitot-static tube positioned in the midspan of the test section two chord lengths upstream of the airfoil leading-edge at zero

angle of attack. The contraction pressure drop was monitored by a Schaevitz Lucas 0-2 ''H_2O differential pressure transducer, while the pitot-static tube dynamic pressure was monitored by 0-0.25 ''H_2O and 0-1 ''H_2O inclined manometers. The free-stream speed was obtained from a calibration curve of the dynamic pressure versus contraction pressure drop. The uncertainty of the free-stream speed measurements was estimated to be less than 2.5%.

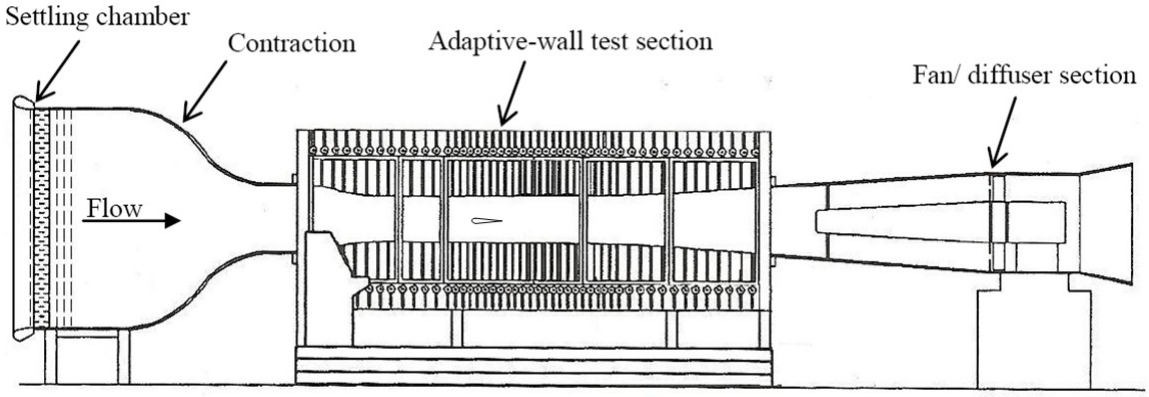

Figure 2.1: University of Waterloo adaptive-wall wind tunnel.

2.2 Airfoil Model

2.2.1 Selection of Airfoil Profile

The majority of previous studies on airfoils operating at low Reynolds numbers were performed for cambered airfoils (e.g., McCullough & Gault, 1951; Mueller, 1985; Brendel & Mueller, 1988, 1990; Burgmann et al., 2006, 2007; Burgmann & Schröder, 2008; Zhang et al., 2008) and symmetric airfoils with thicknesses up to 15% of the chord (e.g., McCroskey, 1989; McAlister & Takahashi, 1991; Huang & Lin, 1995; Lee & Basu, 1998; Lee & Gerontakos, 2004; Greenblatt, 2005; Gerontakos & Lee, 2006, 2007; Gerontakos, 2008;

Alam et al., 2009). Jacobs & Sherman (1939) and Sheldahl & Klimas (1981) examined airfoil thickness effects on performance characteristics for a thickness range from 9% to 18% and 9% to 25%, respectively. However, the experiments of Jacobs & Sherman (1939) were performed in a wind tunnel with a relatively high free-stream turbulence intensity of 2%; thus, the results are expected to differ from those obtained in a low free-stream turbulence facility (e.g., Laitone, 1997). Furthermore, Sheldahl & Klimas (1981) only obtained experimental data for airfoil thicknesses from 9% to 15% and extrapolated these data to obtain estimates for thicker profiles. Some experimental studies have been performed for thick symmetric airfoils, notably, boundary layer and wake characteristics of a NACA 0025 airfoil have been extensively examined by Yarusevych et al. (2006, 2008, 2009). A few studies have been performed for a NACA 0018 airfoil (e.g., Raghunathan & Ombaka, 1986; Nakano et al., 2007; Timmer, 2008). However, only a limited range of performance data and boundary layer characteristics were investigated.

Based on the preceding discussion, a symmetric NACA 0018 airfoil model was selected for this thesis since the results database for this profile is limited at low Reynolds numbers. Thick airfoil sections are required in applications such as vertical axis wind turbines and water turbines to improve blade stiffness (Tangler & Sommers, 1995). Since the blades oscillate through positive and negative angles of attack, relatively thick symmetric airfoils are used in these applications to maintain uniform blade loading (e.g., Raghunathan & Ombaka, 1986; Sheldahl & Klimas, 1981). In fact, Raghunathan & Ombaka (1986) reported that the peak efficiency of a water turbine can be achieved for a symmetric airfoil with a thickness around 18%. Therefore, current and futures studies performed on this airfoil model can provide valuable novel results for the aerospace community. Also, the geometry

of the selected profile is relatively simple (i.e., symmetric) and is thick enough to accommodate instrumentation within the model.

2.2.2 Airfoil Model Structure

A NACA 0018 aluminum airfoil model was fabricated with the following characteristics:

- Chord length, c = 0.2 m
- Span, b = 0.61 m
- Aspect ratio, AR = 3:1
- Chord-to-tunnel height, c/h = 0.23

The model was mounted horizontally in the test section 2 m downstream of the contraction, spanning the entire width of the test section. The coordinate system used for data presentation is shown in Fig. 2.2.

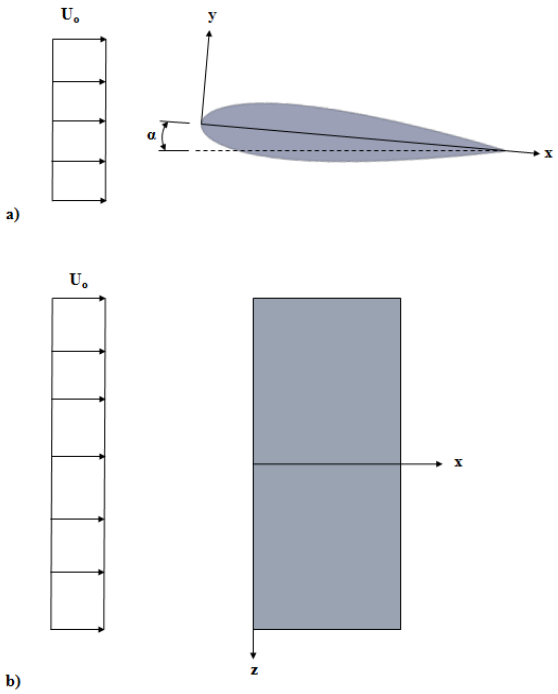

Figure 2.2: Coordinate system viewed from the a) side and b) top.

Cross-sectional and isometric views of the airfoil model are shown in Fig. 2.3. A hollow core segment of the airfoil facilitates the required installation of static pressure taps, fast-response pressure transducers, and transducer amplification circuitry. For structural integrity and manufacturability, solid aluminum nose and tail cap sections are required. A total of four ribs are installed within the airfoil core segment for structural purposes and to ensure the airfoil skin conforms to the NACA 0018 profile. Two leading-edge and two trailing-edge interface plates are installed within the hollow core segment of the model. The interface plates join the nose and tail caps to the four ribs. There are a total of 22 tapped holes in the top and bottom surfaces of each interface plate for attaching the skin to the model. Countersunk screws are inserted into countersunk holes drilled in the leading-edge and trailing-edge portions of the 18-gauge aluminum sheet metal skin in order to secure it to the interface plates. Two skin tensioning brackets are attached to the leading-edge interface plates near the model midspan (Fig. 2.4). Since the spacing between the countersunk screws is greatest at the midspan, the skin is fastened to the tensioning brackets to reduce the spacing, thereby increasing the holding force on the skin near the midspan. A radius is rolled into the skin near the leading-edge to maintain the high curvature of the profile. Two solid endcaps complete the spanwise extent of the model (Fig. 2.3b). On the upper and lower surface of each endcap, 12 tapped holes are drilled normal to the surface for fastening the skin at the farthest spanwise extent. The model is supported by two axles connected to two concentrically-aligned orifices in the solid-side and viewing-side endcaps. A 25.4 mm (1 inch) diameter stainless steel tubular axle on the solid-side is securely connected to the airfoil and model-support mechanism, which serves to adjust the angle of attack and has an angular resolution of ± 0.1°. A 12.7 mm (0.5 inch) diameter solid stainless steel axle on the viewing-side idles in a bearing located within a viewing-side panel of the test section. Experiments

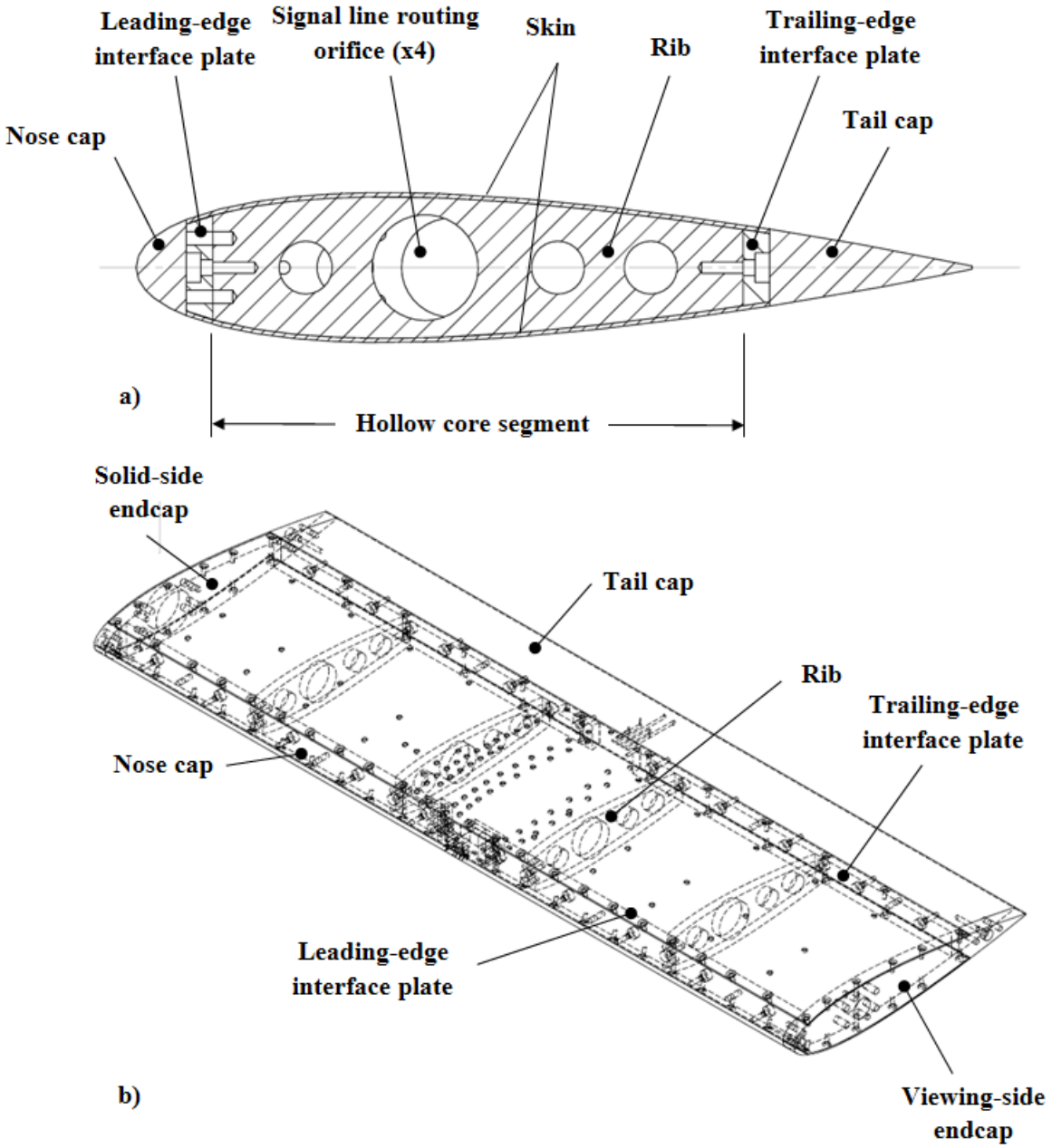

Figure 2.3: a) airfoil cross-section view sectioned through a rib, and b) isometric wireframe view.

involving investigations of shear layer transition were performed with endplates installed approximately 50.8 mm (2 inches) inboard of the test section vertical sidewalls (Fig. 2.5). The viewing-side endplate is fabricated from Lexan for visualization purposes, while the solid-side endplate is fabricated from aluminum and painted matte-black for contrast with

smoke visualizations and to minimize reflections. An isometric view drawing of the fully-instrumented airfoil with endplates is presented in Fig. 2.6. Identified in the figure are two streamwise rows and three spanwise rows of static pressure taps for measuring mean surface pressure. In addition, two streamwise rows and one spanwise row of pressure transducers used for measuring fluctuating surface pressure are also labelled. See Appendix A for a set of detailed drawings of the airfoil model.

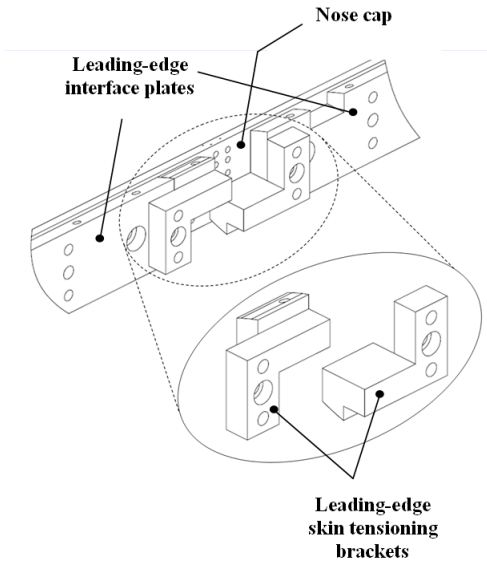

Figure 2.4: Leading-edge skin tensioning brackets attached to leading-edge interface plates.

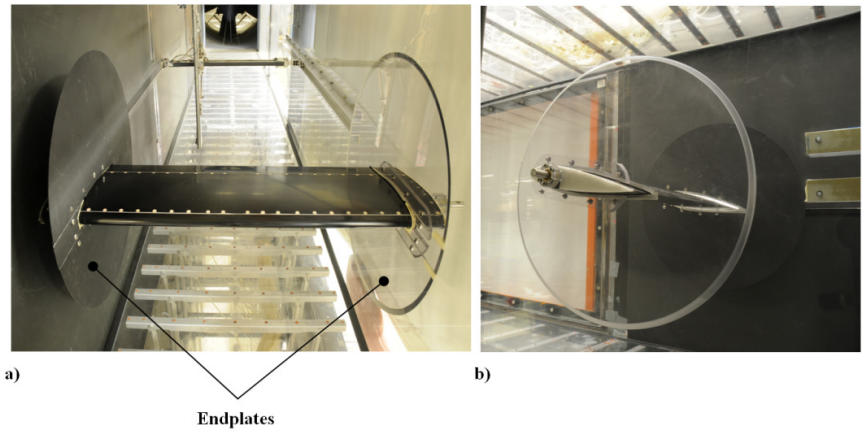

Figure 2.5: airfoil model installed in test section with endplates; a) streamwise and b) spanwise views.

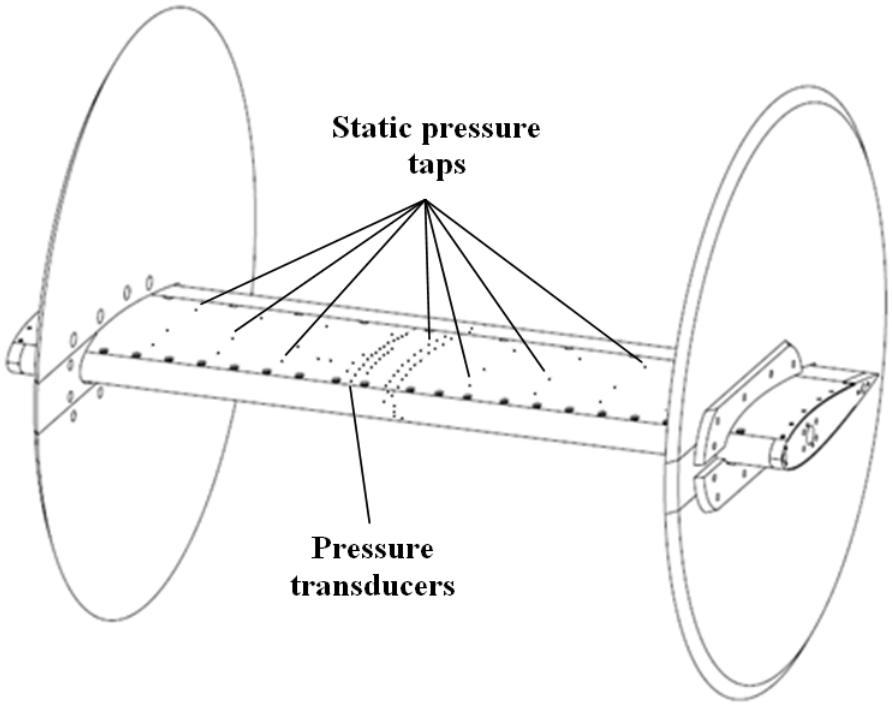

Figure 2.6: Isometric view of fully-instrumented airfoil with endplates.

Pressure Tap Allocation and Pressure Line Routing

Since the available literature for a NACA 0018 airfoil at low Reynolds numbers is limited, numerical simulations were performed using XFOIL to obtain detailed predictions of surface pressure distributions for the range of flow parameters of interest. It is important to maintain a relatively high concentration of pressure taps near the leading-edge to resolve steep pressure gradients in this region. Conversely, a lower concentration of pressure taps is acceptable near the trailing-edge since the pressure recovery is gradual in that region. To optimize the number of required pressure taps, a comparative analysis of several curve fits containing a feasible number of data points was performed. Based on this analysis, it was concluded that 65 pressure taps symmetrically distributed on the upper and lower surfaces along the model midspan provide an optimum degree of resolution within practical

constraints. The static pressure tap allocation is shown in Fig. 2.7. In addition to the centerline static pressure taps, three rows of lateral taps (10 taps/row) are installed at chordwise locations of x/c = 0.15, 0.3, and 0.6 along the upper surface of the airfoil. The lateral taps span the entire model and are used to assess spanwise flow uniformity. These chordwise locations are chosen since they are estimated to be upstream, within, and downstream of the separated flow region on the upper surface, respectively, for a range of Reynolds numbers and angles of attack relevant for this study. Centerline and lateral tap coordinates are detailed in Appendix A.

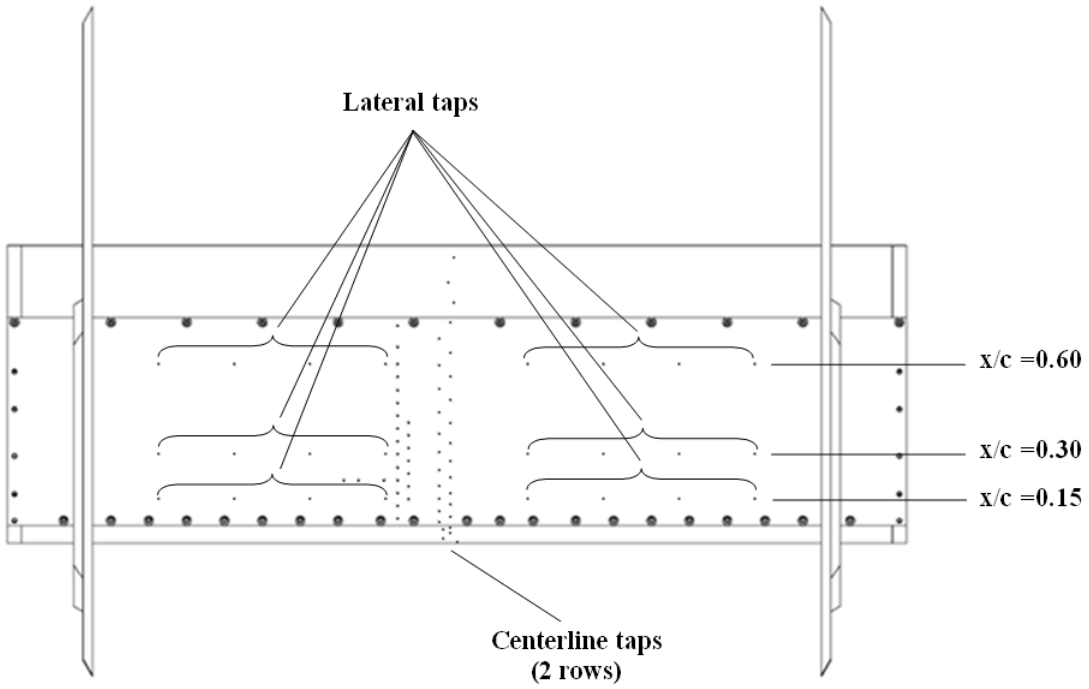

Figure 2.7: Static pressure taps allocation.

All static surface pressure taps are drilled 0.4 mm in diameter and normal to the airfoil surface. 1 mm (0.040 inch) urethane Scanivalve tubing (model URTH-040) is utilized

for all pressure lines in the model. Within the hollow core segment of the airfoil, each pressure line is epoxied and siliconed into a hollow stainless steel collar (tap connector), which is in turn epoxied and siliconed to the static tap on the inside surface of the skin (Fig. 2.8). Because of space limitations within the nose and tail cap regions, precise channels were machined in the nose and tail cap sections along the midspan to permit linking surface pressure taps and pressure lines via tap cross-holes (Fig. 2.9). The nose and tail cap pressure lines are epoxied and siliconed into the cross-holes, as shown in Fig. 2.9. Pressure lines are routed through machined orifices in the ribs (Fig. 2.3) and exit the airfoil through the solid-side tubular axle. This routing configuration ensures that the pressure lines do not obstruct the viewing-side for flow visualization purposes. An illustration of the pressure line routing is shown in Fig. 2.10. Upon exiting the solid-side tubular axle, the pressure lines are connected to a pressure manifold, which is connected to a pressure scanner module. The static pressure measurement system is discussed in §2.3.2.

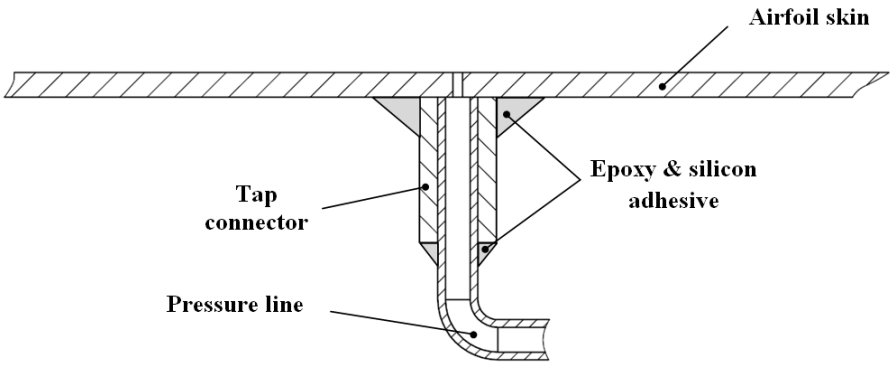

Figure 2.8: Core segment static tap and pressure line connection.

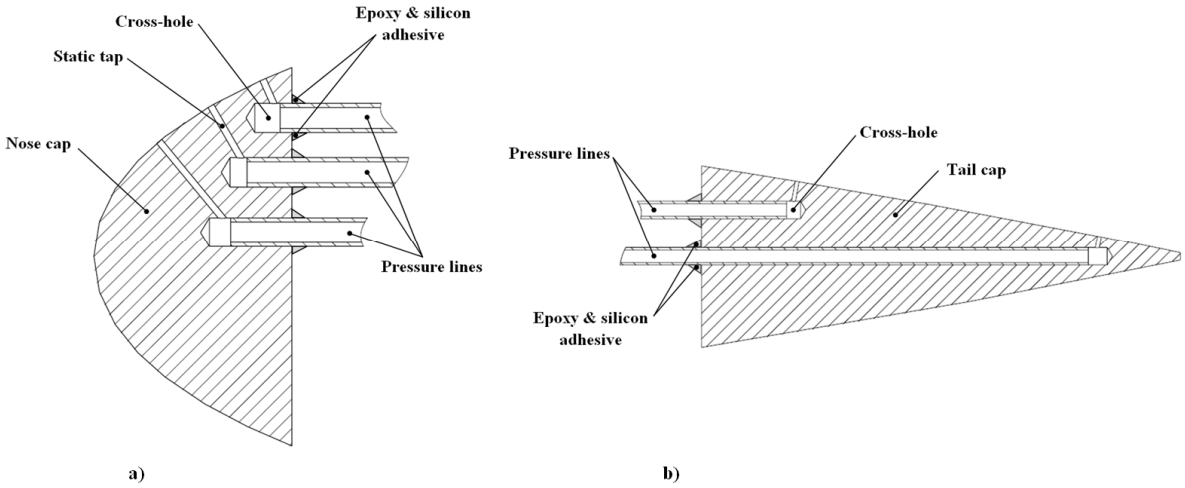

Figure 2.9: Static pressure tap configurations for a) nose cap and b) tail cap. (note: image scales are not the same)

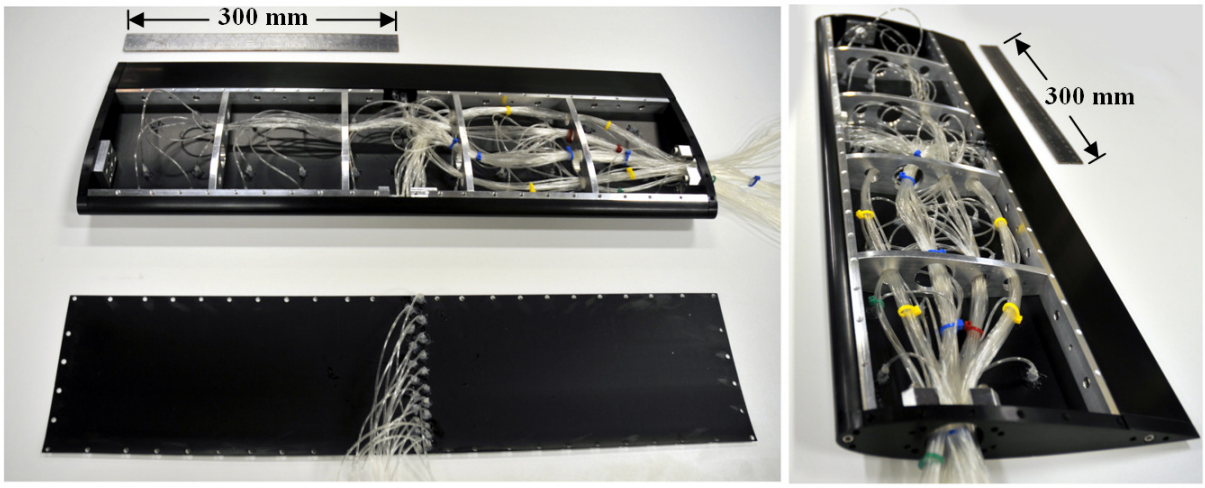

Figure 2.10: Lower surface is removed to expose pressure line routing from the airfoil model.

Pressure Transducer Allocation

In order to facilitate measurements of time-resolved fluctuating surface pressure, pressure transducers are embedded in the airfoil surface. The pressure transducers can be adequately

distributed in the airfoil model with knowledge of the separated flow region. Since experimental data for a NACA 0018 airfoil at low Reynolds numbers is limited, static surface pressure measurements were acquired prior to allocating the pressure transducers. Based on these tests, 25 pressure transducers were allocated in three rows, spanning the extent of the separated flow region for the flow conditions of interest. The pressure transducers were distributed in three rows to examine the pressure field in the streamwise and spanwise directions. As shown in Fig. 2.11, the three transducer rows are located approximately 38.1 mm (1.5 inches) away from the midspan plane on the solid-side. In the partial row and full row, transducers are distributed in the streamwise direction from approximately 15% to 40% of the chord and 10% to 70% of the chord, respectively. In the spanwise row, four transducers are distributed in the spanwise direction from approximately 25% to 40% of the chord relative to the midspan plane. See Appendix A for the coordinates of all 25 pressure transducers. A detailed discussion of the time-resolved surface pressure measurement system is presented in §2.3.3.

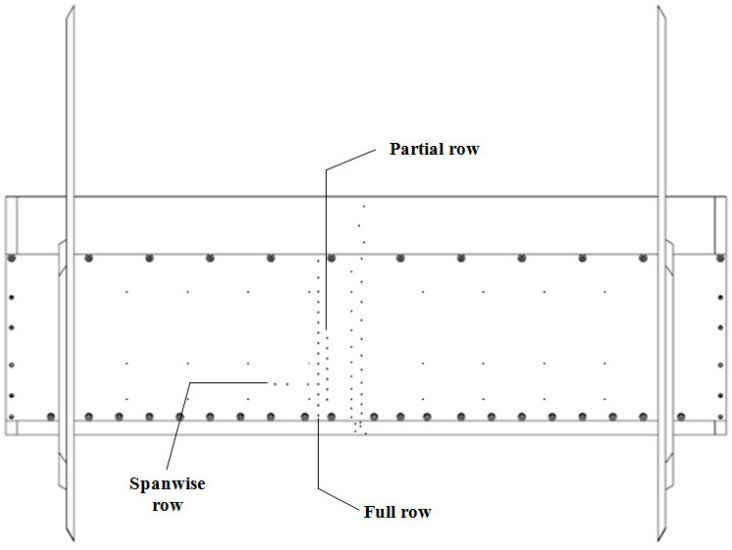

Figure 2.11: Pressure transducer allocation.

Surface Treatment

The exterior components of the model (i.e., the nose and tail caps, endcaps, and skin) were polished, since surface roughness is known to affect transition to turbulence (Schlichting & Gersten, 2000). A systematic sanding and polishing treatment of successively finer grit sandpaper (see Table 2.1) was performed to each component. A wet polishing compound, a mixture of cutting-oil and Varsol constituents, was used with higher grit-number sandpaper polishing stages. To achieve a fine surface finish with consistent surface roughness, the final polishing was performed using an alumina polishing compound, consisting of aluminum oxide powder mixed with the wet polishing compound, applied with a soft cloth. Following polishing, anodizing was performed to produce a matte-black surface for flow visualization purposes. The anodizing was selected over conventional painting since the resulting uniformity of the deposited anodizing film (to within approximately 0.001 inches) did not compromise the pre-anodized surface finish. Also, anodizing increases abrasion resistance of the model exterior. Once the anodizing treatment was applied to model components, the airfoil was assembled with the instrumentation installed in the model. An automotive body filler was then applied to the leading-edge interface between the nose cap and skin and the trailing-edge interface between the skin and tail cap. All countersunk screw holes drilled into the skin were also filled with body filler. The body filler was sanded and polished once again using the systematic polishing treatment in Table 2.1 to eliminate local surface discontinuities. Following application of the body filler, a spot-filler glaze was applied to further improve the surface finish by filling infinitesimal pores in the body filler. The interfaces were polished once again using the alumina polishing compound (Table 2.1).

Table 2.1: Systematic sanding and polishing treatment.

sandpaper grit designation	polishing conditions
120	dry
180	
240	
320	
400	wet
600	
1200	
aluminum oxide	

2.3 Instrumentation and Flow Measurements

2.3.1 Boundary layer Velocity Measurement system

Boundary layer velocity measurements were acquired using hot wire anemometry. A Dantec 55P15 boundary layer probe was used with a Dantec 56C16 bridge. Analog output signals from the bridge were digitized using a National Instruments PCI-4472 data acquisition card. The probe was attached to a probe holder and mounted on a traversing mechanism. The design of the traversing mechanism is discussed in Gerakopulos (2008), while the control software and electrical hardware is detailed in Bishop (2010). The mechanism has three axes of motion and each axis is independently controlled by high precision stepper motors. The range of motion of the vertical, spanwise, and streamwise axes is 0.65 m, 0.4 m, and 1.8 m, respectively. The positioning accuracy is ± 0.025 mm in the vertical and spanwise directions and ± 0.05 mm in the streamwise direction.

The boundary layer probe was calibrated against a pitot-static tube. The probe and pitot-static tube were mounted in a rake holder separated by 10 mm in the vertical direction. The calibration was performed in the midspan plane and the instruments were positioned upstream of the airfoil model with an angle of attack of zero degrees. A calibration curve of the free-stream velocity versus output voltage from the boundary layer probe was obtained from a 5^{th} order polynomial fit to the calibration data.

For boundary layer measurements, the probe was installed in a holder that can be adjusted manually to change the probe angle in the x-y plane. To minimize probe interference effects, the angle between the probe and the local tangent to the airfoil surface was kept between 0° and 10° at each measurement location, as recommended by Brendel & Mueller (1988). Boundary layer measurements were performed in the vertical plane in between the full and partial rows of pressure transducers. Error estimates of hot wire velocity measurements were obtained in accordance with the work of Kawall et al. (1983). The maximum uncertainty was estimated to be less than 5% within the separated shear layer. See Appendix D for the uncertainty analysis of the hot wire velocity measurements.

2.3.2 Static Surface Pressure Measurement System

An automated system was used to acquire static surface pressure measurements sequentially from 95 static pressure taps in the airfoil model. The automated measurement system and software were developed in Labview by Bishop (2010) to acquire wall pressure measurements within the test section for wall adaptation. The software was modified by the author for airfoil static surface pressure measurements.

Pressure measurements were performed using two electronic pressure scanner modules (Scanivalve ZOC33). Each module contains 64 piezoresistive differential pressure sensors with a pressure range of 0 to 5 ''H_2O. Since the sensors are duplexed (i.e., each sensor can be connected to one of two pneumatic inputs), each module can handle 128 pneumatic inputs. A control diagram for a single pressure scanner module is shown in Fig. 2.12. The pressure scanners can operate in one of two modes of operation: (i) calibrate mode and (ii) operate mode. In calibrate mode, each sensor is connected to a reference pressure (REF) and a calibration pressure (CAL), facilitating calibration of all sensors. Calibrate mode can also be used to obtain temperature-based zero-offset voltages by measuring the voltage difference when the REF and CAL pressures are equal. Zero-offset voltages can be obtained while the tunnel is running, which is desirable for operational purposes. To compensate for diurnal temperature variation within the testing facility, zero-offset voltages were measured and adjusted prior to acquiring every static surface pressure distribution. In operate mode, which is used to measure airfoil static surface pressures, each sensor is connected to an airfoil pressure input and a reference pressure common to all sensors. The reference pressure is obtained from a centerline wall pressure tap installed in the test section upstream of the airfoil model.

Control of the pressure scanner modules is facilitated by pneumatic and electrical auxiliary systems. The mode of operation is set by supplying pressure to specified pneumatic control lines configured in a binary logic state. The binary logic state is triggered by a solenoid bank, which charges the appropriate pneumatic control lines for a desired mode of operation. All digital signals sent to the pressure scanner modules and auxiliary systems (i.e., to specify the binary logic state) are controlled from a PC with a National Instruments PCI-

6259 data acquisition card (DAQ). The output of a sensor is accessed by specifying a unique digital address and then sampled by the same DAQ.

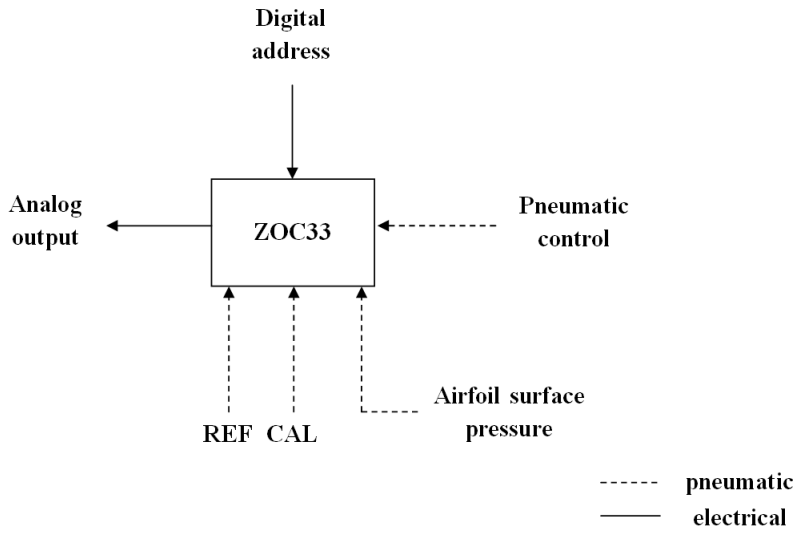

Figure 2.12: ZOC module control diagram for airfoil surface pressure measurements.

2.3.3 Time-Resolved Surface Pressure Measurement System

The transducer selected for measuring time-resolved fluctuating surface pressure is a Panasonic (WM-62C) omnidirectional back electret condenser microphone cartridge. The microphone cartridge is cylindrical with a diameter of 6 mm and a height of 2.2 mm. The cartridges have a nominal sensitivity of -45 ± 4 dB for a frequency bandwidth of 20 – 20,000 Hz.

Ideally, installing the microphones flush with the outer surface of the airfoil skin exposes the diaphragm directly to the pressure field over the airfoil surface. However, due to the curvature of the airfoil surface, the microphone cartridges in such an arrangement would create discontinuities in the airfoil surface and perturb the flow. To avoid this, each

microphone was attached to the inside surface of the airfoil skin beneath a sensor port drilled through the skin, linking the microphone sound port to the pressure field. Each microphone is installed in a polyvinyl chloride (PVC) collar, which is aligned concentrically with a sensor port and adhered to the surface with epoxy and silicon (Fig. 2.13). A bead of silicon was added to the backside of each microphone cartridge, sealing it within the PVC collar. To facilitate measurements of fluctuating surface pressure, the pressure is equalized on either side of the diaphragm through an internal barometric ventilation passage within the cartridge. Since barometric ventilation is achieved through the microphone sound port, for the chosen microphone mounting arrangement, the diaphragm will remain ventilated with variation in flow parameters.

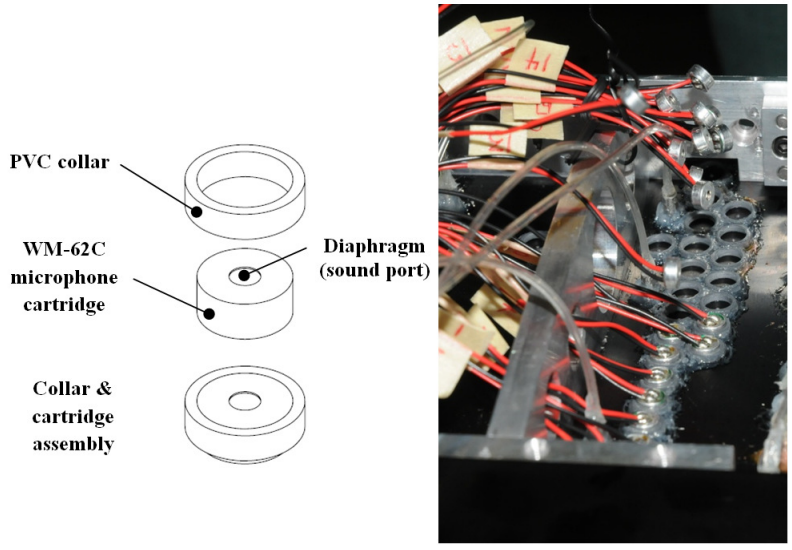

Figure 2.13: Microphone and collar a) assembly and b) installation in airfoil model.

It is well known that recessing a microphone in a surface may attenuate the surface pressure fluctuation signal and/or cause resonance (e.g., Mueller, 2002). When a microphone is displaced sufficiently far below the surface, the pressure field is usually linked to the microphone sound port through a sensing line (i.e., short pressure line). In this configuration, the pressure fluctuations decay exponentially in the wall normal direction and the measured signal may be severely attenuated (Mueller, 2002). In the present setup, signal attenuation is minimized by mounting the microphone directly beneath the airfoil skin, thereby reducing the sensing length to the airfoil skin thickness (i.e., the depth of the drilled sensor port). However, for small recesses on the order of the sensing port depth, two types of resonance may occur: (i) Helmholtz resonance and (ii) cavity resonance. The Helmholtz resonance may occur when air flows in and out of the sensor port, creating a self-sustained oscillation at the resonant frequency (e.g., Wheeler, 2004). In case of cavity resonance, strong periodic pressure fluctuations within the cavity (i.e., sensor port) are caused by flow instabilities developed in the shear layer over the sensor port (e.g., Kook, 1997). Based on a resonance analysis of the sensor port, a sensor port diameter of 0.8 mm was selected. For this sensor port geometry, it was concluded that cavity resonance would likely be avoided and the Helmholtz resonant frequency would be higher than the maximum measured frequency in the flow field for the range of flow parameters of interest. In addition, the measured pressure may be 5% greater than that of the actual pressure over the airfoil surface as a consequence of Helmholtz resonance in the sensor port (See Appendix C for details).

Microphone Amplification Bus and Signal Transmission

Since the output voltage from the microphones is relatively low (i.e., on the order of millivolts), the signal may be susceptible to electrical noise contamination while transmitting

from the signal source to the data acquisition system (e.g., Wheeler, 2004). Thus, an amplification bus is required to increase the low voltage signal output from the microphones prior to transmission. The amplification bus was solely designed by the author and an electronics technician, Neil Griffett. The amplification bus consists of 25 independent channels to amplify each microphone in the array. This is facilitated by 13 Linear Technology low-noise and high-speed precision dual op-amp chips (LT 1126), i.e., each chip contains two amplification circuits. The amplifier bus is powered by a 15V DC power supply. A schematic of the op-amp circuit for a single channel is shown in Fig. 2.14. The complete amplification bus is presented in Fig. 2.15. See Appendix C for a comprehensive list of the components used in the amplification bus circuit. The amplifier performance was optimized through several iterative stages. As a consequence, a $10x10^3$ Ω resistor was added to the positive input terminal of the op-amp to minimize the output signal DC offset and reduce the impulse response time. Furthermore, the magnitude of the input capacitor (3.3 μF) on the positive terminal of the op-amp was sufficient for filtering out the DC component of the signal and minimizing the low-frequency capacitance discharge to the output signal.

The cable used for signal transmission from each microphone to the data acquisition system is discretized into two segments: (i) the airfoil interface signal line (Belden RG-178 mini coax cable) and (ii) the transmission signal line (Belden RG-174 mini coax cable). The airfoil interface signal line extends from the amplification bus through the solid-side tubular axle. A maximum of 25 signal lines could feasibly fit inside the airfoil support axle, and therefore maximum 25 microphones could be allocated in the microphone array. The braided shield is satisfactory for low-to-moderate frequency shielding, which is appropriate for the range of frequencies within the flow field for the flow parameters of interest. The cable length was restricted to 914.4 mm (three feet) since the cable is relatively expensive and the

resistance is higher than conventional coax cables. The signal transmission line extends from the free-end of the airfoil interface signal line to the data acquisition system. The transmission line has a lower resistance and cost in comparison to the airfoil interface line, which is suitable for a greater transmission length. Braid and foil shielding ensures the signal is shielded over a broad frequency range. The total signal line length from the source to the DAQ is 20 feet. The mini coax cables are joined using snap-fit SMB connectors and the free-

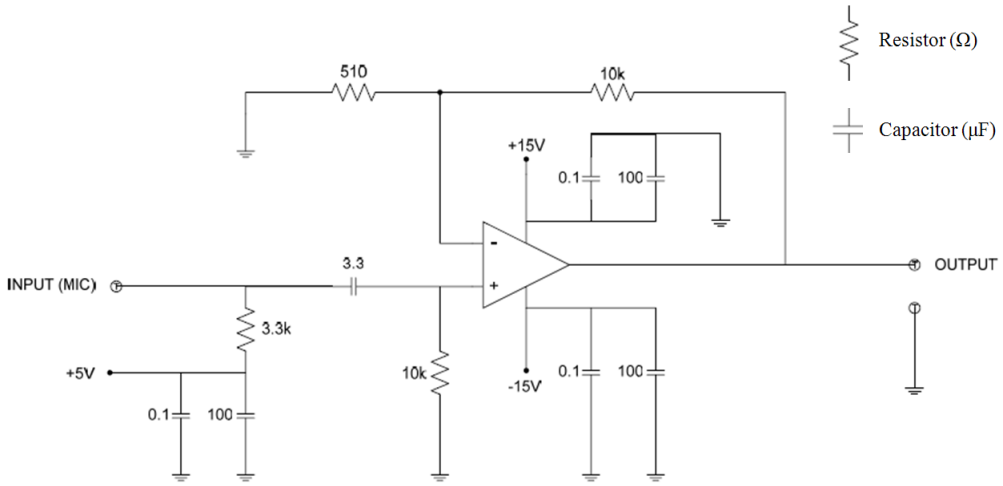

Figure 2.14: Schematic of the op-amp circuit for a single channel.

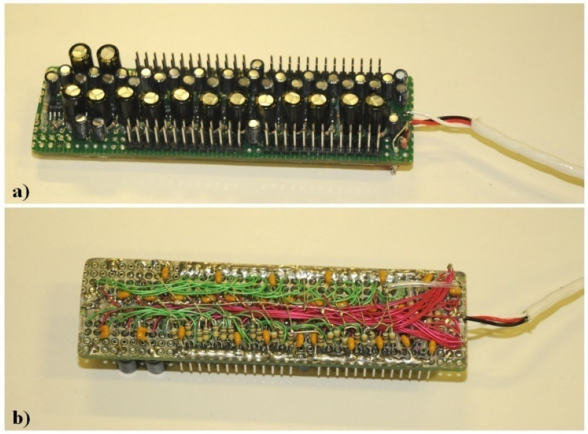

Figure 2.15: Microphone amplification bus: a) top view, b) bottom view.

end of the transmission line is connected to the data acquisition system using a male BNC connector (Fig. 2.16).

All analog output signals from the microphone array were digitized using a National Instruments PCI-4472 data acquisition card. This DAQ has a 24-bit resolution and a configurable input voltage range from ±1.25 - ±10 V. The board allows acquiring simultaneous measurements from up to eight microphones. Each analog input channel can be configured independently as AC-coupled or DC-coupled. Channels are configured as AC-coupled (i.e., signals with zero-mean offset) for microphone measurements and DC-coupled (i.e., signals with DC offset) for hot wire measurements. All measurement software was solely created by the author in Labview.

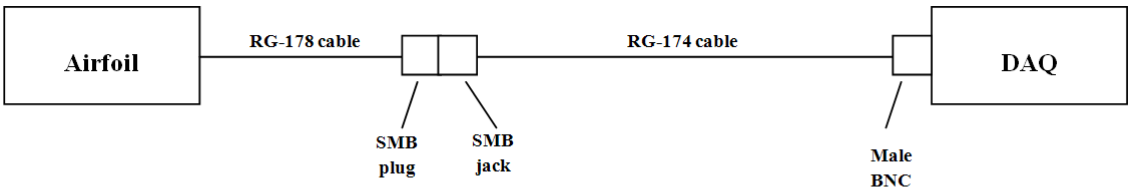

Connector Specifications

- Tyco Electronics SMB plug (female socket) (part no. 413985-6) (quantity = 25)
- Pomona Electronics SMB jack (male pins) (part no. 72984) (quantity = 8)
- Tyco Electronics BNC plug (male pins) (part no. 2-5221128-1) (quantity = 8)

Figure 2.16: Signal line and connector diagram.

Microphone Calibration

The calibration was performed in an anechoic chamber to minimize any effects of environmental disturbances. A detailed report of the chamber design and control software

can be found in McPhee (2009). A list of the equipment used to facilitate the calibration is provided below and a block diagram of the acoustic chamber setup is shown in Fig. 2.17.

- Calibration chamber with acoustically-insulating foam
- 25 mm diameter B&C DE10 speaker sound source
- 0.5 inch diameter B&K 4192 working-standard reference microphone
- 1 inch diameter and 4 inch long aluminum coupling tube with PVC insert
- National Instruments PCI-6143 simultaneous DAQ

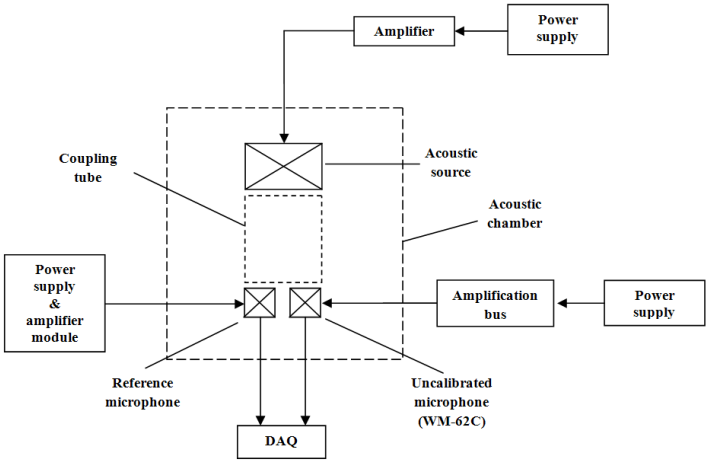

Figure 2.17: Acoustic chamber block diagram configured for microphone calibration.

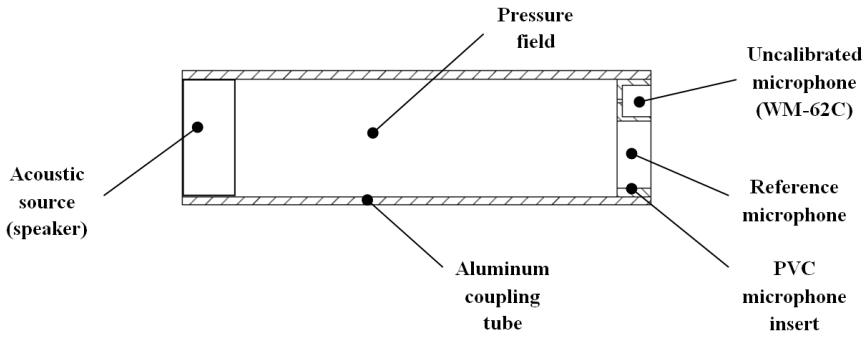

Figure 2.18: Comparative calibration using an acoustic coupler.

A comparative calibration was employed in this study (e.g., Brüel & Kjær, 1996; Frederiksen, 2009). Specifically, each microphone was calibrated by comparing its response to a previously calibrated reference microphone, with the two microphones exposed simultaneously to the same sound pressure through an acoustic coupler. Figure 2.18 shows the arrangement of microphones used during calibration. Within the cylindrical coupling tube, a pressure wave is generated by a speaker installed at one end and received by the uncalibrated and reference microphones at the other end. Both microphones are installed in a PVC insert, which is fitted to the coupling tube. The uncalibrated microphone is exposed to the pressure field through a sensor port with the same geometry as that designed for the airfoil and the reference microphone is flush-mounted with the insert surface exposed to the pressure field. Each microphone was calibrated for a range of frequencies from 100 Hz to 2,000 Hz, which is appropriate for the range of frequencies measured in the flow field for the flow parameters of interest. See Appendix C for a comprehensive description of the calibration methodology and results.

2.4 Fully-Instrumented Airfoil Testbed

The airfoil model instrumented with static pressure taps, microphone array, and amplification bus is shown in Fig. 2.19. A detailed view of the instrumentation in the midspan compartment of the airfoil is shown in Fig. 2.20. The amplification bus was installed in the compartment adjacent to the microphone array and tied down to prevent it from moving during installation and with a change in angle of attack. The bus is mounted on a sheet of electrostatic plastic for isolation from the underlying airfoil surface.

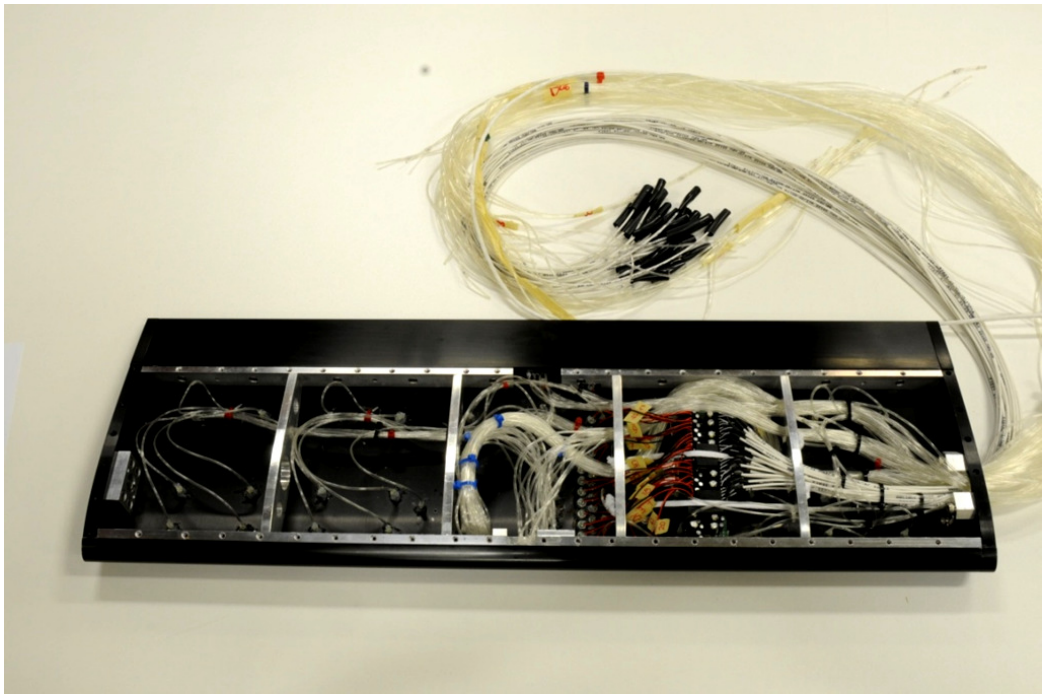

Figure 2.19: View of fully-instrumented airfoil with the lower surface skin removed.

Figure 2.20: Detailed view of midspan instrumentation, including a cluster of static pressure taps, microphone array, and amplification bus.

2.5 Data Analysis

The mean surface pressure coefficient distribution is represented by Eq. 2.1,

$$C_p = \frac{P - P_o}{\frac{1}{2}\rho U_o^{\,2}} \tag{2.1}$$

where P is the mean surface pressure measured from a static pressure tap on the airfoil surface, P_o is the free-stream static pressure measured at a centerline wall pressure tap located in the test section floor panel upstream of the airfoil model, , ρ is the density of air, and U_o is the free-stream velocity. Mean pressures were computed from a sample size of 50,000 data points sampled at a rate of 5,000 Hz. The uncertainty of mean surface pressure measurements was estimated to be $C_p \pm 0.022$ (see Appendix D for details).

The lift coefficient was computed by integrating the mean surface pressure coefficient distribution using Eq. 2.2,

$$C_l = \int_0^1 \left[\left(C_p\right)_{lower} - \left(C_p\right)_{upper} \right] d\left(\frac{x}{c}\right) \cos(\alpha) \tag{2.2}$$

where $\left(C_p\right)_{lower}$ and $\left(C_p\right)_{upper}$ are the mean surface pressure coefficients on the lower and upper surfaces, respectively.

Spectral analysis was used to identify the frequency associated with dominant disturbances in the separated flow region from fluctuating velocity and surface pressure. Signals acquired at a sampling rate of 5,000 Hz and with a sample size of 2,097,152 data points were discretized into 128 segments. The autospectral density was computed from the fast Fourier transform (FFT) of each signal segment. The FFTs were averaged over the number of segments and normalized by the variance of the signal so that the area under the

curve was unity. The resulting frequency resolution bandwidth was 0.3 Hz. The uncertainty in determining the central frequency associated with the dominant spectral peak was estimated to be less than ± 100 Hz for the range of flow parameters of interest (see Appendix D for details).

The cross-correlation function in equation Eq. 2.3 was employed to examine the interrelation between two flow parameters.

$$R_{12}(\tau) = \lim_{T\to\infty}\left\{\frac{1}{T}\left[\int_0^T s_1(t)s_2(t-\tau)dt\right]\right\} \tag{2.3}$$

In the preceding equation, τ is the time-lag, T is the duration of a signal segment, and s_1 and s_2 are the fluctuating components of two different time-resolved signals. Signals acquired at 10,000 Hz with a sample size of 2,097,152 data points were discretized into 128 segments and the cross-correlation function was computed for each segment. The cross-correlations were averaged by the total number of segments. The cross-correlation coefficient is defined by Eq. 2.4,

$$\rho_{12} = \frac{R_{12}}{s_1' s_2'} \tag{2.4}$$

where the cross-correlation function R_{12} is normalized by the RMS of each signal (i.e., s_1' & s_2').

Complimentary to cross-correlation analysis, coherence analysis was used to investigate the interrelation between two time-resolved surface pressure fluctuation signals aimed specifically at frequencies associated with dominant flow structures. The one-sided coherence was computed using Eq. 2.5,

$$\Gamma_{12}(f) = \frac{|\varphi_{12}(f)|}{\sqrt{E_{11}(f)E_{22}(f)}} \tag{2.5}$$

where f is a frequency index, $|\varphi_{12}|$ is the magnitude of the cross-spectrum between two signals, and E_{11} and E_{22} are the corresponding autospectra. Spectral averaging was performed for each constituent of the coherence function. Coherence analysis was performed for signals with a sample size of 2,097,152 data points obtained at a sampling rate of 10,000 Hz. The one-sided cross-spectrum (φ_{12}) was computed using Eq. 2.6,

$$\phi_{12}(\mathrm{f}) = 2\int_{-\infty}^{\infty} \mathrm{R}_{12}(\tau)\mathrm{e}^{-\mathrm{j}2\pi\mathrm{f}\tau}\mathrm{d}\tau \tag{2.6}$$

where j is an imaginary number, R_{12} is the cross-correlation function, τ is the time lag, and f is the frequency index.

3 Baseline Aerodynamic Characterization

Experimental results presented here pertain to a range of Reynolds numbers from $80x10^3$ to $200x10^3$ and a range of angles of attack from 0° to 18°. In this parameter range, both boundary layer flow regimes are observed: flow separation with subsequent reattachment and flow separation without subsequent reattachment.

3.1 Lift Coefficient Curves

Lift coefficient data, computed based on surface pressure distributions, are presented in Fig. 3.1. The results show that, on the average, the stall angle increases with increasing Reynolds number. An increase in the Reynolds number from $Re_c = 80x10^3$ to $Re_c = 200x10^3$ results in an increase in the stall angle from $\alpha = 10°$ to $\alpha = 14°$ (Fig. 3.1) and an increase in the maximum lift coefficient from 0.89 to 1.03 (Fig. 3.2). For a given angle of attack in the range $0° \leq \alpha \leq 6°$, the lift coefficient decreases as the Reynolds number increases. In contrast, at higher angles of attack up to the stall angle, the lift coefficient increases with increasing Reynolds number.

For a given Reynolds number, a conventional nearly linear growth of the lift coefficient with increasing angle of attack occurs from $\alpha = 0°$ to $\alpha \approx 6°$ (Fig. 3.1). This is followed by a more gradual lift coefficient growth up to the stall angle. At the stall angle, a sudden and significant reduction in the lift coefficient is observed. The lift coefficient subsequently recovers with increasing post-stall angle of attack.

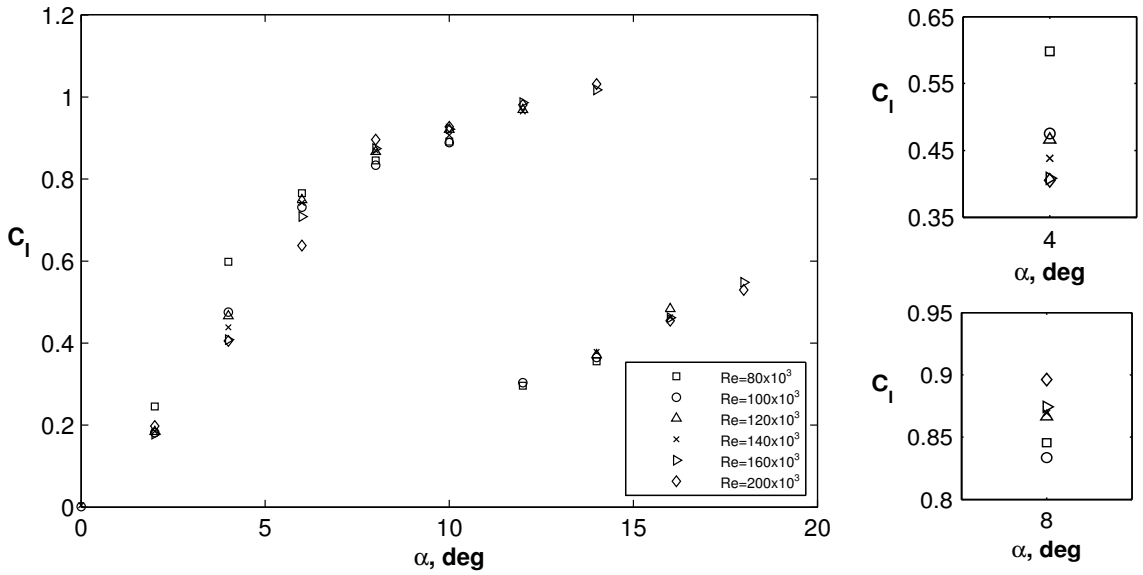

Figure 3.1: Experimental lift coefficient data. The associated uncertainty was estimated to be less than 4%.

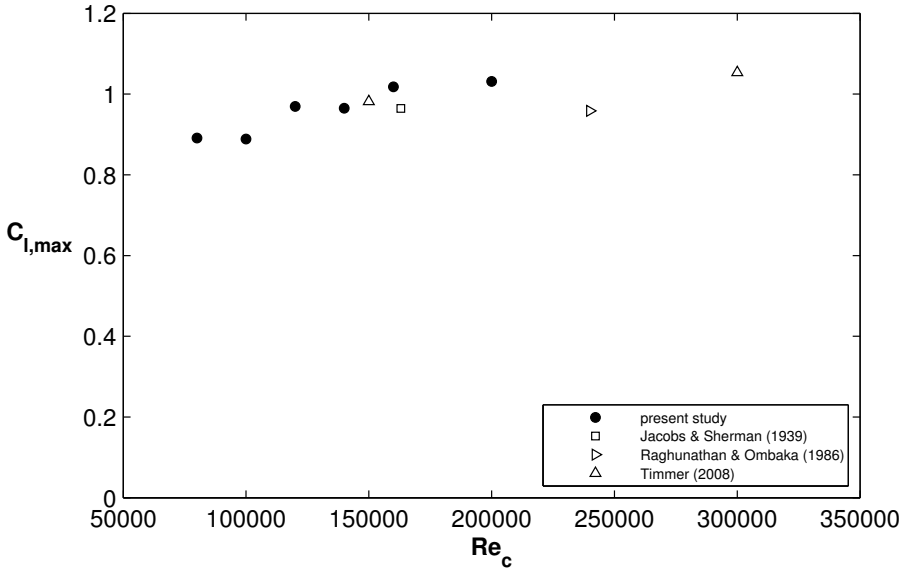

Figure 3.2: Maximum lift coefficient. Note that discontinuous increase in the maximum lift coefficient with the Reynolds number is attributed to a relatively coarse angle of attack increment of 2° used to acquire data near the stall angle in the present study.

The present results are compared with experimental lift coefficient data for a NACA 0018 from other studies in Fig. 3.3. The lift coefficient data of Timmer (2008) were acquired using a force balance for $Re_c = 150x10^3$ and $300x10^3$. Agreeing well with the present findings, the results of Timmer (2008) indicate that, for $0° \leq \alpha \leq 7°$, higher lift coefficients are obtained at lower Reynolds numbers for a given angle of attack. A reverse trend is observed between $\alpha = 7°$ and the stall angle. Conventional linear growth of the lift coefficient is observed for $0° \leq \alpha \leq 7°$, which is similar to the trend observed in the present study. The present results compare reasonably well with the data of Jacobs & Sherman (1939) and of Raghunathan & Ombaka (1986), for $\alpha < 6°$. The variation between these data sets at higher angles of attack is likely attributed to variation in the level of free-stream turbulence, which is known to have a significant effect on flow development over an airfoil at low Reynolds numbers (Marchman, 1987; Laitone, 1997; Ol et al., 2005). Specifically, the results of Timmer (2008) and those of the present investigation, which compare well, were obtained in wind tunnels with a free-stream turbulence intensity of less than 0.07% and 0.3%, respectively. Conversely, the results of Jacobs & Sherman (1939) were obtained in a facility with a higher free-stream turbulence intensity of approximately 2%. Since the free-stream turbulence intensities reported for the present investigation (0.3%) and Timmer (2008) (0.07%) are comparable to that reported by Raghunathan & Ombaka (1986) (0.2%), the discrepancy between the results in these studies is likely attributed to model geometry and/or measurement inaccuracies in the study by Raghunathan & Ombaka (1986). Selig & McGranahan (2004) also obtained experimental lift coefficient data using a force balance for various asymmetric airfoils in the Reynolds number range from $100x10^3$ to $200x10^3$. These authors found that, contrary to the present findings, for a given angle of attack, the lift coefficient increased with an increase in the Reynolds number at lower angles of attack

within the conventional lift coefficient growth region for an Eppler E387 airfoil. Furthermore, for the FX 63-137, S822, and S834 airfoils, similar observations were found. Conversely, at higher pre-stall angles of attack, the lift coefficient decreased with an increase in the Reynolds number for the Eppler E387 airfoil, which is also contrary to the present findings.

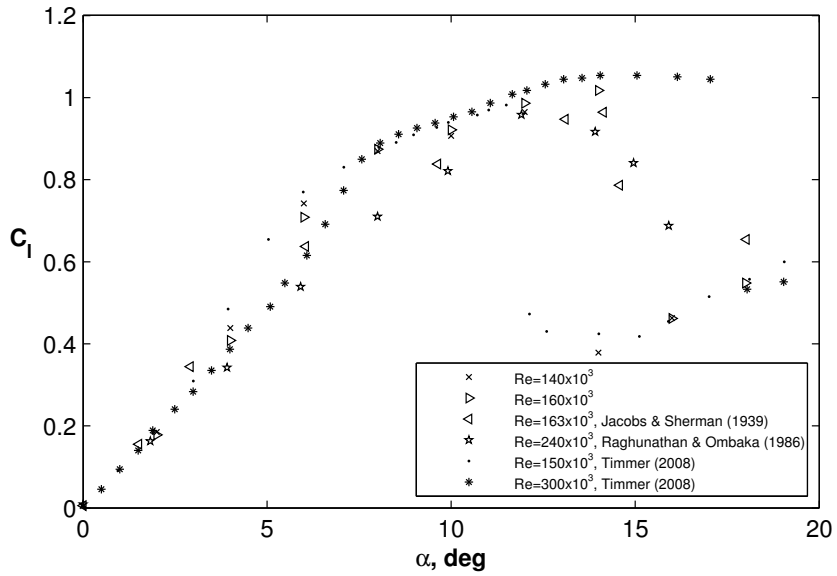

Figure 3.3: Comparison of present results with lift coefficient data from previous investigations.

The experimental lift coefficient data are compared with analytical and numerical results in Fig. 3.4. The analytical lift coefficient data were computed at lower pre-stall angles of attack based on the conventional lift curve slope of 2π predicted by thin-airfoil theory (e.g., Anderson, 2011). The numerical lift coefficient data were estimated using XFOIL, which is a commonly used computational design tool for predicting the flow field over airfoils at low Reynolds numbers. The author recommends reviewing Drela & Giles (1987) and Drela (1989) for a detailed description of the flow solver. Numerical predictions of the flow field are obtained from the flow solver, which solves Euler's equations using a panel

method coupled with boundary layer formulations. Using an e^n method, the transition location is predicted as the location where the most amplified unstable Tollmien-Schlichting wave, based on the spatial amplification rate predicted from the Orr-Sommerfeld equation, in the shear layer has grown to some threshold, specified by the value of e^n (Drela & Giles, 1987). For the numerical results in the present investigation, a value of n = 5 was specified as it is suitable for a free stream-turbulence intensity of approximately 0.3% (Drela, 1989). Similar to the experimental data, the numerical results from XFOIL show a region of conventional linear growth at lower pre-stall angles of attack, followed by more gradual growth at higher pre-stall angles of attack for the flow parameters investigated. Furthermore, the maximum lift coefficient and stall angle of attack increase with increasing Reynolds number. However, for a given Reynolds number, the predicted stall angle of attack and the magnitude of the maximum lift coefficient do not follow the experimental data closely. For a given angle of attack in the range $0° \leq \alpha \leq 7°$, the predicted lift coefficient decreases with an increase in the Reynolds number in agreement with the experimental findings. Furthermore, the reverse trend occurs for $\alpha \geq 9°$ up to the stall angle of attack, which is also consistent with the experimental results. Conventional linear growth of the lift coefficient is predicted at lower pre-stall angles of attack for $0° \leq \alpha \leq 6°$ at $Re_c = 80x10^3$ and the extent of this range increases to $0° \leq \alpha \leq 9°$ for $Re_c \geq 160x10^3$. For $Re_c \geq 160x10^3$, the slope of the experimental and numerical lift coefficient data approaches the analytical lift curve slope of 2π in the conventional linear growth region. Vorobiev et al. (2010) also compared experimental lift coefficient data obtained from a force balance to analytical lift coefficient predictions for a NACA 0009 airfoil at $Re_c = 131x10^3$. Similar to the present findings for $Re_c < 160x10^3$, the authors found that, the lift coefficient exceeded the analytical lift coefficient at a given angle of attack for lower pre-stall angles of attack in the conventional linear growth region. For the

present findings and those reported by Vorobiev et al. (2010), such deviation between the experimental and analytical lift coefficient data is associated with a separation bubble on the upper surface of the airfoil near the mid-chord location. Thus, it is speculated that such a mid-chord separation bubble acts to effectively change the airfoil geometry, resulting in an increase in the lift coefficient.

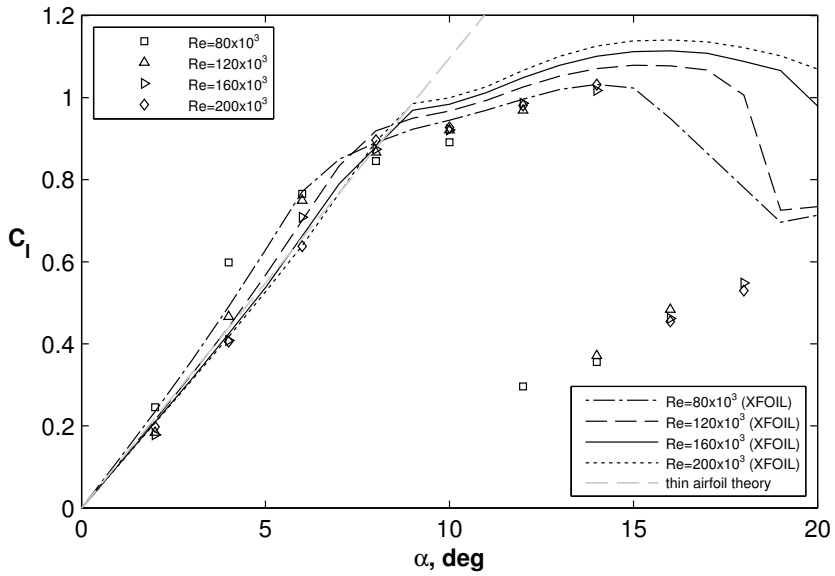

Figure 3.4: Comparison of experimental and numerical lift coefficient data. Note that the numerical lift coefficient data were obtained from XFOIL for flow conditions matching those of the experimental results.

3.2 Mean Surface Pressure Coefficient Distributions

To investigate the development of the separated flow region over the upper surface of an airfoil, surface pressure measurements were acquired and used to estimate locations of flow separation, transition, and reattachment. Recall, the laminar boundary layer separation point can be approximately identified as the start of the region over which the surface pressure is nearly constant (Tani, 1964; Carmichael, 1981). When the flow fails to reattach, this

constant-pressure region extends to the trailing-edge (Tani, 1964; Carmichael, 1981). Conversely, a sudden surface pressure recovery following the constant-pressure region is an indication of transition and subsequent flow reattachment. Thus, a constant-pressure region followed by sudden surface pressure recovery signifies the presence of a separation bubble on the airfoil surface.

Upper surface pressure coefficient distributions for the Reynolds numbers and angles of attack investigated are presented in Fig. 3.5. For a given Reynolds number, the separation bubble moves upstream toward the leading-edge and the length of the separation bubble decreases as the angle of attack increases. Increasing the angle of attack up to the stall angle causes the separation bubble to burst near the leading-edge, resulting in a sudden and significant decrease in the suction peak. For example, for $Re_c = 80x10^3$, the separation bubble is present for angles of attack from 0° to 10° (Fig. 3.5a). Increasing the angle of attack to $\alpha \approx 12°$ causes the bubble to burst, reducing the suction peak by approximately 80%.

The results in Fig. 3.5 show that, as the Reynolds number increases from $80x10^3$ to $200x10^3$, the stall angle increases from 10° to 14°, with a corresponding increase in the maximum suction peak from $C_p = -2.6$ to $C_p = -4.0$. Upper surface pressure coefficient distributions for Reynolds numbers from $80x10^3$ to $200x10^3$ at $\alpha = 8°$ are presented in Fig. 3.6. The results show that, for a given angle of attack, an increase of the Reynolds number causes a reduction in the length of the separation bubble, evidenced by a decrease in the length of the nearly-constant pressure region centered at about $x/c = 0.25$.

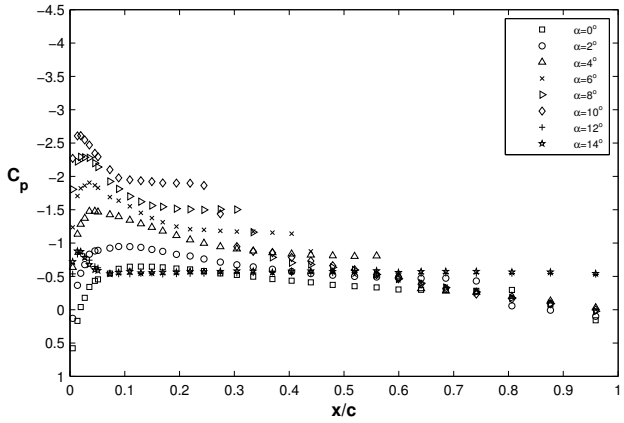

a) $Re_c = 80x10^3$

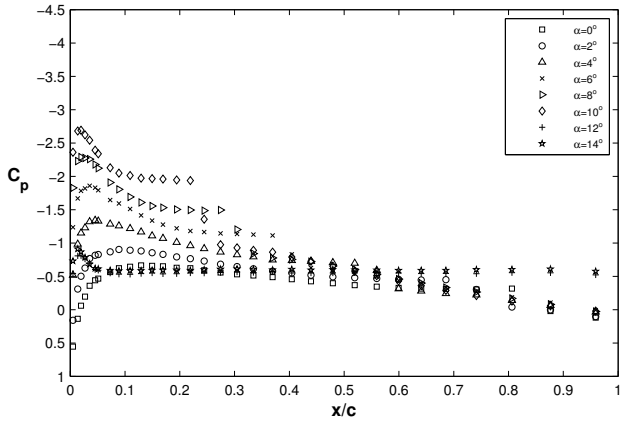

b) $Re_c = 100x10^3$

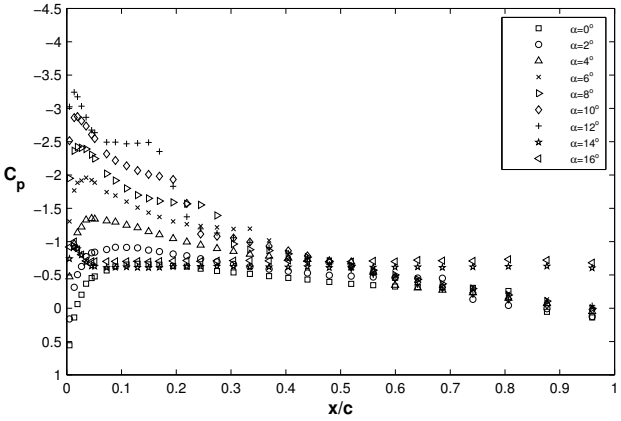

c) $Re_c = 120x10^3$

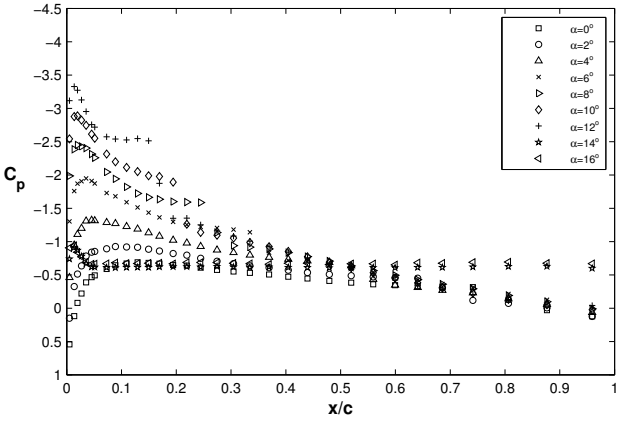

d) $Re_c = 140x10^3$

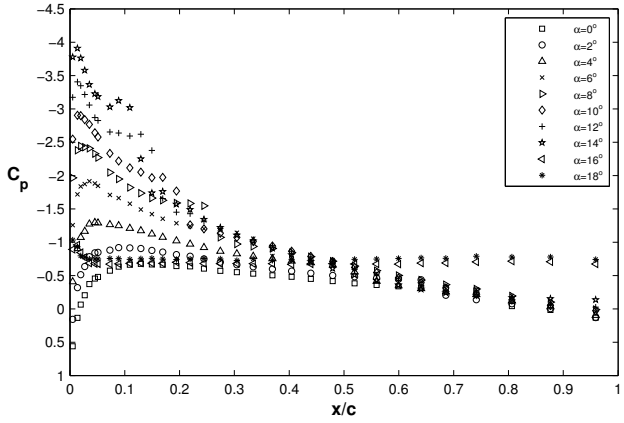

e) $Re_c = 160x10^3$

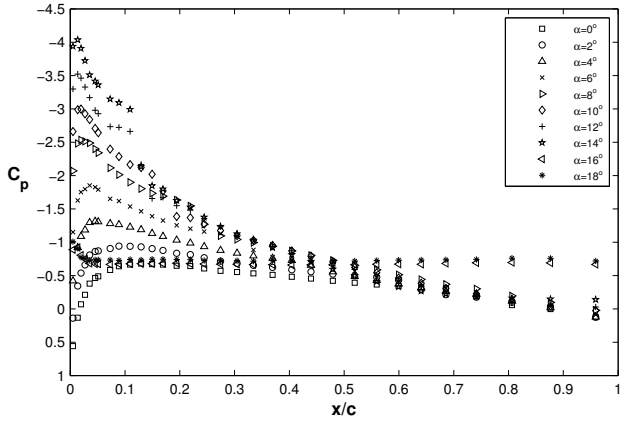

f) $Re_c = 200x10^3$

Figure 3.5: Upper surface pressure distributions. The associated uncertainty was estimated to be Cp ± 0.022.

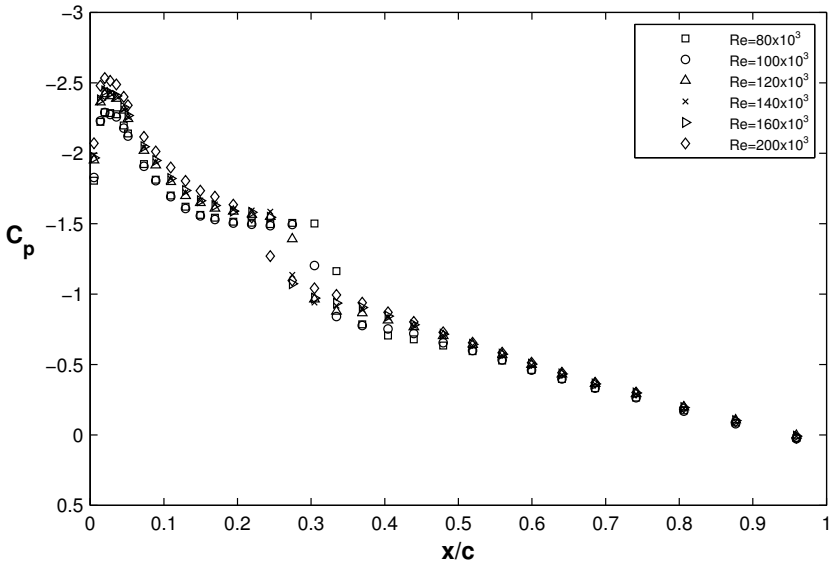

Figure 3.6: Upper surface pressure distributions at α = 8°. The associated uncertainty was estimated to be Cp ± 0.022.

3.3 Separation Bubble Characteristics

In the present study, the following methodology was employed to estimate the locations of boundary layer separation, transition, and reattachment, denoted by S, T, and R, respectively, based on surface pressure measurements. As illustrated in Fig. 3.7, the separation location was estimated as the intersection of (i) a linear fit to the nearly linear surface pressure recovery region following the suction peak and (ii) a linear fit to the nearly constant surface pressure region within the laminar portion of the separation bubble. To estimate transition and reattachment locations, a shape-preserving polynomial fit was applied to the discrete surface pressure distribution data in the regions of constant surface pressure and subsequent rapid surface pressure recovery (Fig. 3.7). The transition location, associated with a sudden increase in surface pressure in the aft portion of the separation bubble (Tani, 1964), was estimated as the local maximum in the second derivative of the polynomial fit. O'Meara & Mueller (1987) proposed that the reattachment location can be identified as the location

downstream of the transition point where a rapid decrease in the rate of surface pressure recovery is observed (O'Meara & Mueller, 1987). In accordance with this approach, the reattachment location was estimated as the location of the local minimum in the second derivative of the polynomial fit downstream of transition. This methodology was verified using published pressure distributions for which estimates of the S, T, and R locations determined based on velocity measurements were available. Moreover, the estimates of S, T, and R using the proposed methodology were also verified based on boundary layer velocity measurements from the present investigation. The uncertainty in the S, T, and R locations determined using the described methodology was estimated to be less than 0.04c in the present investigation.

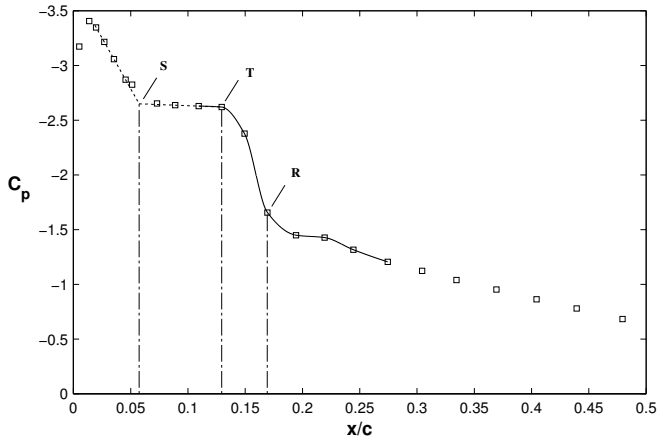

Figure 3.7: Estimates of separation, transition, and reattachment locations for $Re_c = 160x10^3$ at $\alpha = 10°$.

Figure 3.8 depicts the effect of the angle of attack on the S, T, and R locations. For all the Reynolds numbers investigated, increasing the angle of attack results in the separation bubble propagating upstream and reducing in length. For instance, for $Re_c = 100x10^3$, the separation bubble located between $0.54 \leq x/c \leq 0.88$ at $\alpha = 0°$ moves to a region $0.08 \leq x/c \leq 0.24$ at $\alpha = 10°$, corresponding to a 50% reduction in the separation bubble length (Fig. 3.8b).

A similar trend is observed in the results of Nakano et al. (2007) obtained based on liquid-crystal visualization for $Re_c = 160x10^3$ (Fig. 3.8e). For $\alpha < 6°$, separation and reattachment locations measured by Nakano et al. (2007) agree well with present results obtained for the matching Reynolds number. However, for $\alpha \geq 6°$, there is deviation between the corresponding data sets, which is likely attributed to differences in the model geometry near the leading-edge.

The effect of the Reynolds number on the S, T, and R locations is depicted in Fig. 3.9. The results suggest that at a given angle of attack, the separation location does not vary appreciably with the Reynolds number. Furthermore, on the average, both the transition and reattachment locations move upstream with increasing Reynolds number, resulting in a reduction of the separation bubble length. For example, as the Reynolds number is increased from $80x10^3$ to $200x10^3$ at $\alpha = 6°$, the separation location remains at approximately x/c = 0.19, the transition location advances from x/c = 0.40 to 0.30, and the reattachment location advances from x/c = 0.48 to 0.33. As a result, the separation bubble length is reduced by about 50%.

Similar to the present findings, a reduction in the separation bubble length with increasing angle of attack was also noted by Lee & Gerontakos (2004) using estimates from surface pressure coefficient distributions for a NACA 0012 airfoil. Burgmann et al. (2007) and Burgmann & Schröder (2008) observed a similar angle of attack effect on the separation bubble length and also a reduction in the separation bubble length with increasing Reynolds number using estimates from PIV images for a SD7003 airfoil. Burgmann & Schröder (2008) also found that the location of separation advanced with increasing angle of attack and was almost independent of the Reynolds number, which are consistent findings with those

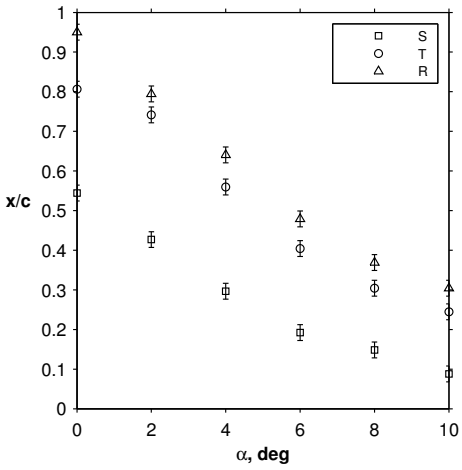

a) $Re_c = 80x10^3$

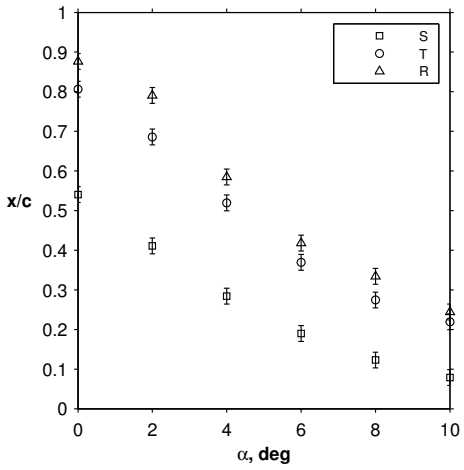

b) $Re_c = 100x10^3$

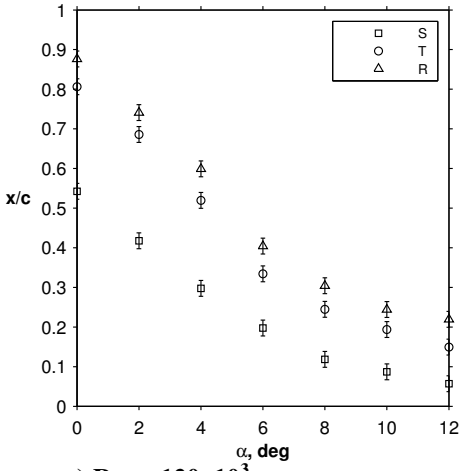

c) $Re_c = 120x10^3$

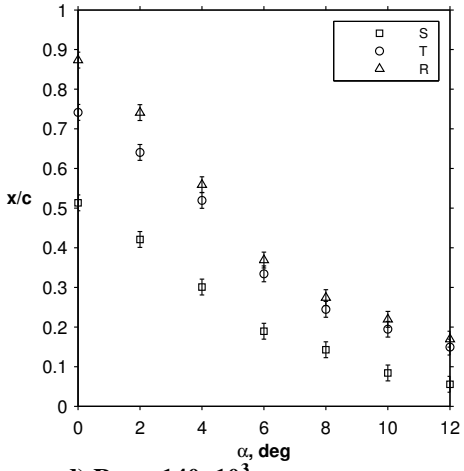

d) $Re_c = 140x10^3$

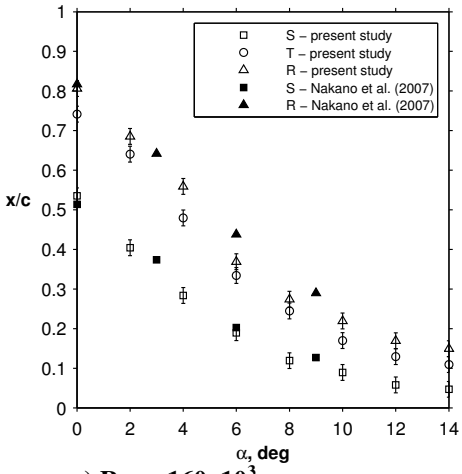

e) $Re_c = 160x10^3$

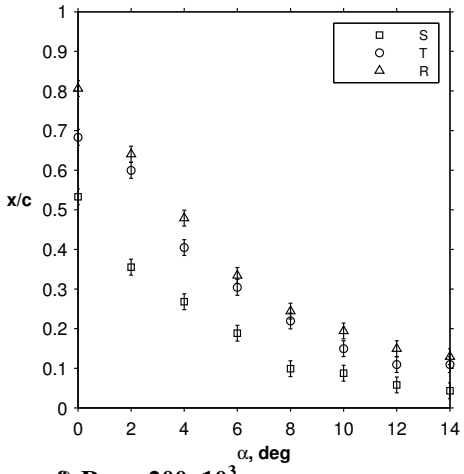

f) $Re_c = 200x10^3$

Figure 3.8: Variation of separation, transition, and reattachment locations with the angle of attack.

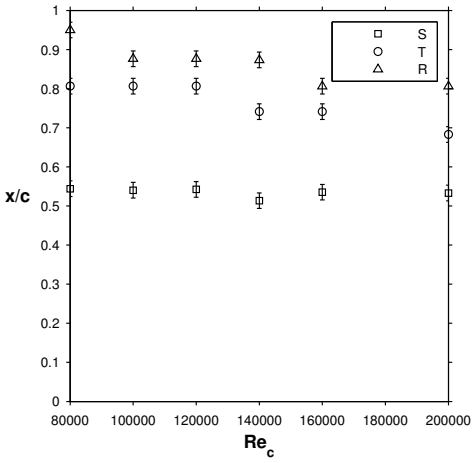

a) α = 0°

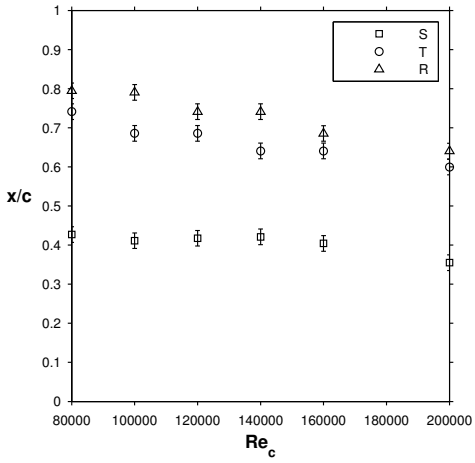

b) α = 2°

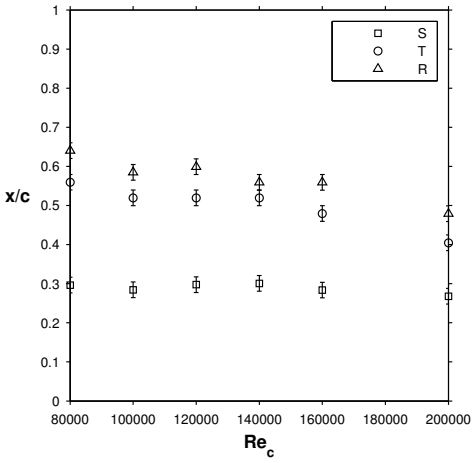

c) α = 4°

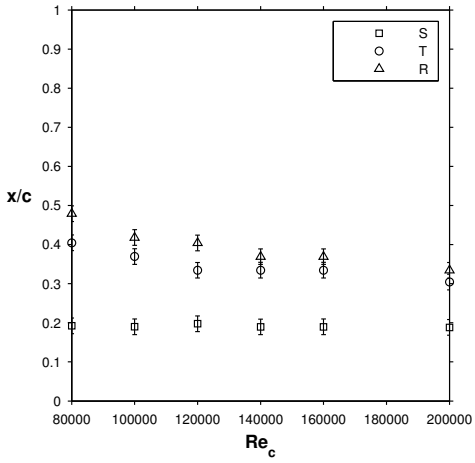

d) α = 6°

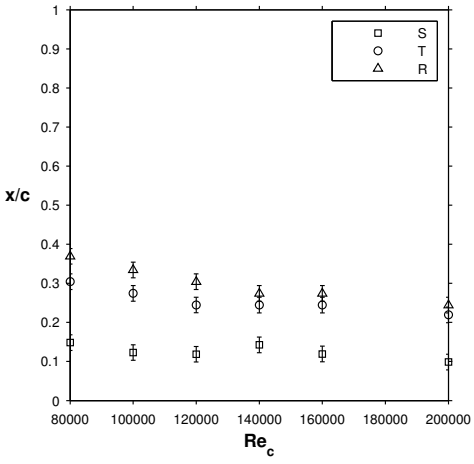

e) α = 8°

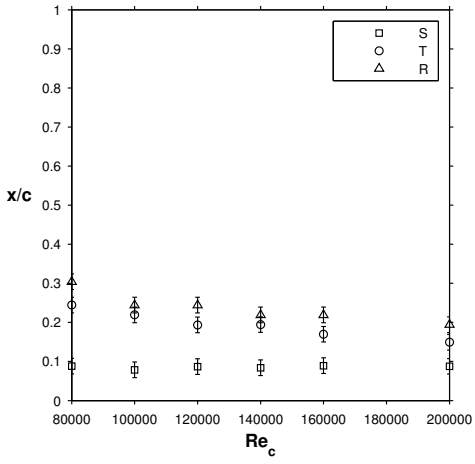

f) α = 10°

Figure 3.9: Variation of separation, transition, and reattachment locations with the Reynolds number.

reported in the present investigation. O'Meara & Mueller (1987) reported similar effects of the Reynolds number on the location of separation and the length of the separation bubble, however, these authors found that, on the average, the length of the separation bubble increased with increasing angle of attack, which is contrary to the present findings.

3.4 Effect of Separation Bubble Size and Position on Airfoil Lift

An analysis of the lift coefficient data (Fig. 3.1) has revealed a region of conventional linear growth in the lift coefficient at low angles of attack, which is depicted in Fig. 3.10 for the present results and those of Timmer (2008). It should be noted that a region of more gradual and nearly linear growth of the lift coefficient at higher pre-stall angles of attack is observed in the present results and a portion of the results of Timmer (2008). However, the results of Timmer (2008) indicate that, with greater resolution in the angle of attack, growth of the lift coefficient is nonlinear at higher pre-stall angles of attack. Figure 3.10a illustrates that, for $80x10^3 \leq Re_c \leq 200x10^3$, the conventional linear growth region extends to slightly higher angles of attack with increasing Reynolds number.

Slopes of the lift curves within the linear growth region are plotted in Fig. 3.11 for the range of Reynolds numbers investigated. The results show that, on the average, the slope of the lift curve decreases with increasing Reynolds number for the cases investigated (Fig. 3.11), and the same trend can be seen in Timmer's (2008) results (Fig. 3.10b).

The observed trends in the lift coefficient data must be related to boundary layer and separated shear layer development. A comparative evaluation of the lift coefficient results (Fig. 3.1) and the estimated separation bubble parameters (Fig. 3.8) suggests that, the lift

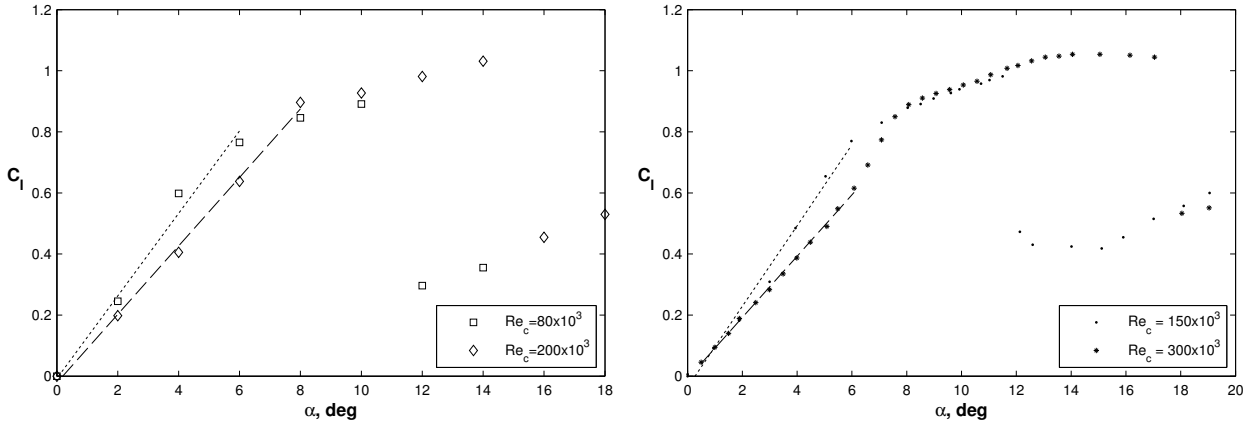

a) **b)**

Figure 3.10: Linear growth in lift coefficient curves a) present results and b) data from Timmer (2008). The associated uncertainty in the present results was estimated to be less than 4%.

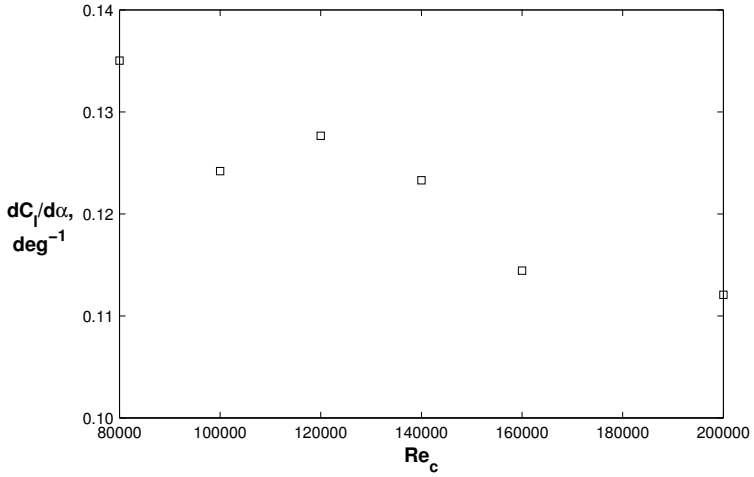

Figure 3.11: Lift curve slopes for the linear growth region.

curve slope is linked to the rate of advancement of the S, T, and R locations. This is depicted in Fig. 3.12 for $Re_c = 140x10^3$ and $0° \leq \alpha \leq 6°$. A lift curve slope of 0.12 corresponds to an advancement of S, T, and R locations towards the leading edge, with $dS/d\alpha = 0.06$, $dT/d\alpha = 0.07$, and $dR/d\alpha = 0.08$, respectively. Table 3.1 shows that the rate at which the S, T, or R locations advance towards the leading edge as the angle of attack increases is constant and proportional to the rate of change of the lift curve slope for the range of Reynolds numbers

investigated. It should be noted that variations in dS/dα, dT/dα, and dR/dα with the Reynolds number are within the experimental uncertainty associated with the estimation of the S, T, and R locations. Thus, the Reynolds number effect on these quantities and the corresponding variation in $dC_l/d\alpha$ cannot be assessed.

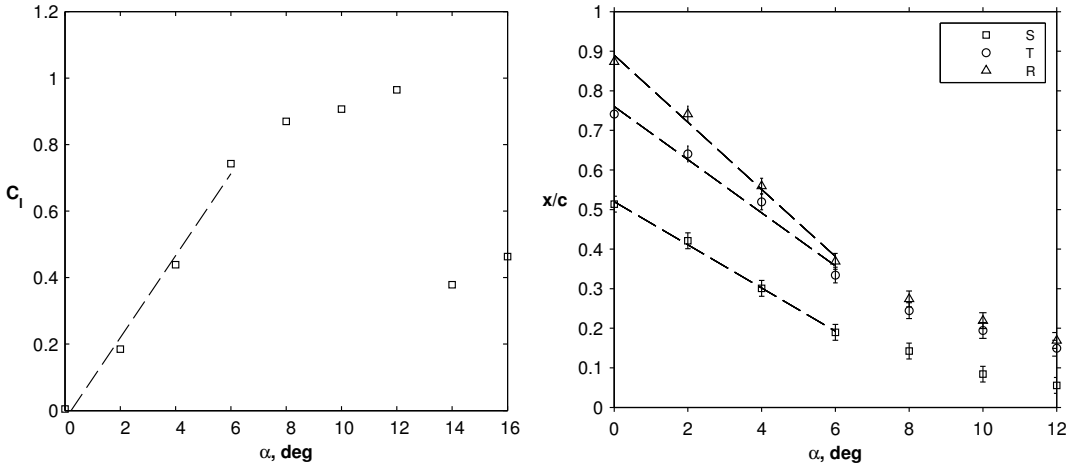

Figure 3.12: a) Lift curve slope and b) rate of upstream advancement of S, T, and R locations for Re_c = $140x10^3$. The associated uncertainty in the lift coefficient data is estimated to be less than 4%.

Table 3.1 : Magnitudes of lift curve slopes and rates of upstream advancement of the S, T, and R locations.

Re_c	Linear slope region [deg]	$dC_l/d\alpha$	$dS/d\alpha$	$dT/d\alpha$	$dR/d\alpha$
$80x10^3$	$0 \le \alpha \le 6$	0.14	0.06	0.07	0.08
$100x10^3$	$0 \le \alpha \le 6$	0.12	0.06	0.07	0.08
$120x10^3$	$0 \le \alpha \le 6$	0.13	0.06	0.08	0.08
$140x10^3$	$0 \le \alpha \le 6$	0.12	0.06	0.07	0.08
$160x10^3$	$0 \le \alpha \le 8$	0.11	0.05	0.07	0.07
$200x10^3$	$0 \le \alpha \le 8$	0.11	0.05	0.06	0.07

A similar relationship between the growth of the lift coefficient with angle of attack and the associated rate of advancement of the S and T locations have been noted by Lee &

Gerontakos (2004) for a NACA 0012 airfoil at low angles of attack. A comparison of their experimental results obtained for a single Reynolds number, $Re_c = 135x10^3$, and the present data for $Re_c = 140x10^3$ is shown in Fig. 3.13. Lee & Gerontakos (2004) note the presence of the linear growth in the lift curve at low angles of attack, agreeing with the present findings (Fig. 3.13). Comparing the results for the two airfoils, it can be seen that the lift curve slope and the rate of advancement of the S and T locations towards the leading edge are lower for the NACA 0012 airfoil. Also, decreasing the airfoil thickness extends the linear growth region to higher angles of attack. The lift curves in Fig. 3.13a show that the thinner NACA 0012 profile produces lower lift in the range of angles of attack from about 3° until stall, hence, producing lower maximum lift, but stalls at a higher angle of attack compared to the NACA 0018 airfoil.

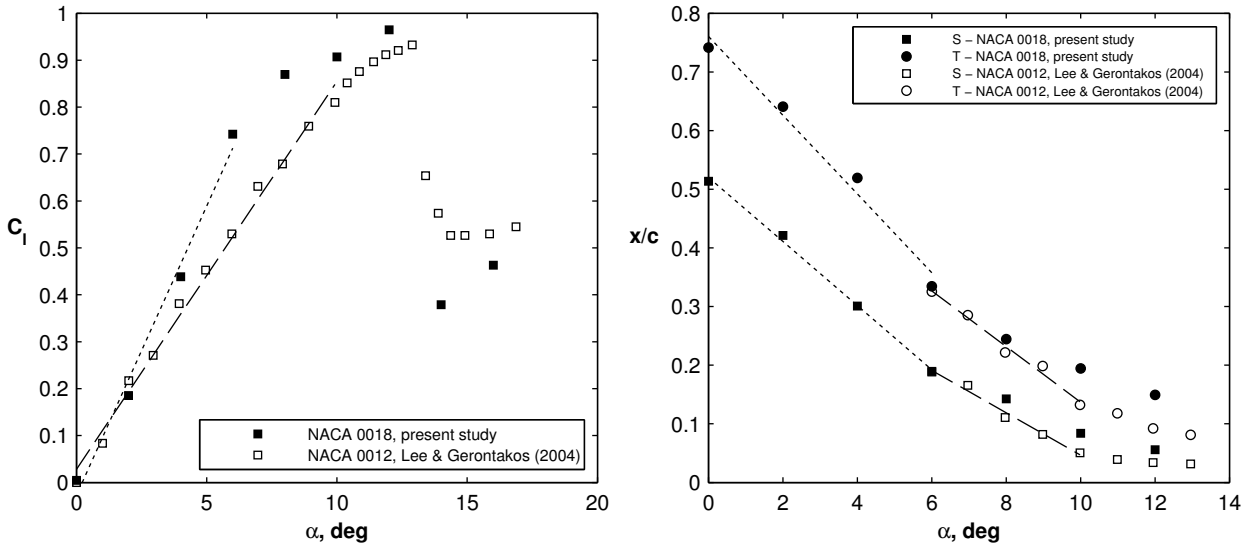

a) b)

Figure 3.13. Comparison of a) lift curves and b) S and T locations for a NACA 0018 airfoil at $Re_c = 140x10^3$ (present study) and a NACA 0012 airfoil at $Re_c = 135x10^3$ (Lee & Gerontakos, 2004). For the present results, the associated uncertainty in the lift coefficient is estimated to be less than 4% and the S, T, and R locations is estimated to be less than 0.04c.

3.5 Mean and RMS Velocity Profiles

Hotwire velocity measurements were acquired in the separated flow region to further examine separated shear layer development. It should be noted that a normal hot wire probe cannot detect the change in flow direction in the reverse flow region near the wall. However, such measurements can be used to identify the presence and the extent of the reverse flow region (e.g., Brendel & Mueller, 1988). At the same time, measurements in the separated shear layer can be investigated without limitations.

From the surface pressure coefficient distributions presented in Fig. 3.5, it is apparent that, for the range of flow parameters in the present investigation, regimes of flow separation with and without reattachment are observed. Accordingly, velocity measurements were acquired for $Re_c = 100x10^3$ at $\alpha = 8°$ and $\alpha = 12°$ to examine the flow development in more detail for regimes of flow separation with and without reattachment, respectively. Mean and RMS velocity profiles at $\alpha = 8°$ and $\alpha = 12°$ are shown in Fig. 3.14 and Fig. 3.15, respectively. Additionally, the streamwise growth of the maximum turbulence intensity (u'_{max}/U_o) is shown in Fig. 3.16. For these angles of attack, distinct differences in the evolution of velocity profiles are associated with reattachment of the separated shear layer. Thus, laminar-to-turbulent transition plays a key role in separated shear layer development and whether or not reattachment of the separated shear layer to the airfoil surface will follow. From surface pressure coefficient distributions, the separation location is estimated at x/c = 0.13 for $\alpha = 8°$ and at x/c = 0.06 for $\alpha = 12°$. For both flow regimes, boundary layer separation is characterized by nearly stagnant flow near the airfoil surface. The results illustrate that, downstream of separation, the evolution of the velocity profiles depends on the flow regime. At $\alpha = 8°$ (Fig. 3.14), the mean velocity decreases steadily towards the wall at

x/c = 0.15 and a region of stagnant flow associated with the reverse flow region emerges near the wall at x/c = 0.19. For x/c ≥ 0.32, the reverse flow region has vanished, indicating that the separated shear layer has undergone laminar-to-turbulent transition farther upstream and reattached to the airfoil surface near x/c = 0.32. The preceding findings are consistent with the transition location (x/c = 0.26) and reattachment location (x/c = 0.34) estimated from the mean surface pressure coefficient distribution. An inflection point past the separation location suggests that an amplified instability wave exists in the flow (e.g., Schlichting & Gersten, 2000). As shown in Fig. 3.16a, the maximum turbulence intensity increases steadily from x/c = 0.15 to x/c = 0.30, followed by a more gradually decrease with a further increase in the streamwise direction. A single maximum in the RMS profile is observed at x/c = 0.15 and three maxima emerge at x/c = 0.19 through x/c = 0.26. For $0.15 \leq x/c \leq 0.26$, the dominant maximum occurs in the separated shear layer. For x/c > 0.26, the shape of the RMS profile changes from three maxima to a single broad maximum within the near wall region. The shape of the RMS profiles for x/c > 0.26 differ from a viscous Tollmien-Schlichting-type eigenfunction observed in a flat plate boundary layer (e.g., Boiko et al., 2002; Rist & Maucher, 2002) since a weaker secondary maximum is not observed near the boundary layer edge in the present study. At α = 12° (Fig. 3.15), stagnant flow associated with the reverse flow region, marked by marginal variation in U/U_e with y/c, expands away from the wall with an increase in the streamwise distance, indicating that the separated shear layer does not reattach to the airfoil surface, resulting in an airfoil stall. As suggested at α = 8°, the existence of an inflection point in the mean velocity profiles past separation indicates that an amplified instability wave exists in the separated flow (e.g., Schlichting & Gersten, 2000). The maximum turbulence intensity increases from x/c = 0.13 to x/c = 0.26 and plateaus for x/c ≥ 0.26 (Fig. 3.16b). The dominant maximum in each RMS velocity profile is located in

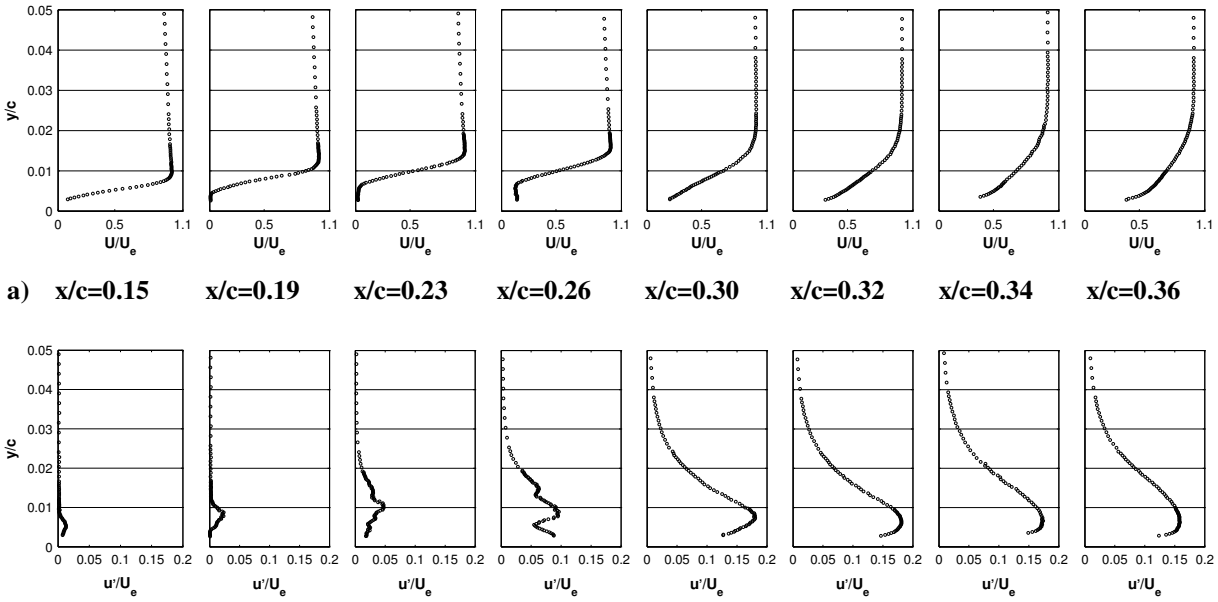

Figure 3.14: a) Mean and b) RMS boundary-layer velocity profiles for $Re_c = 100x10^3$ and $\alpha=8°$.

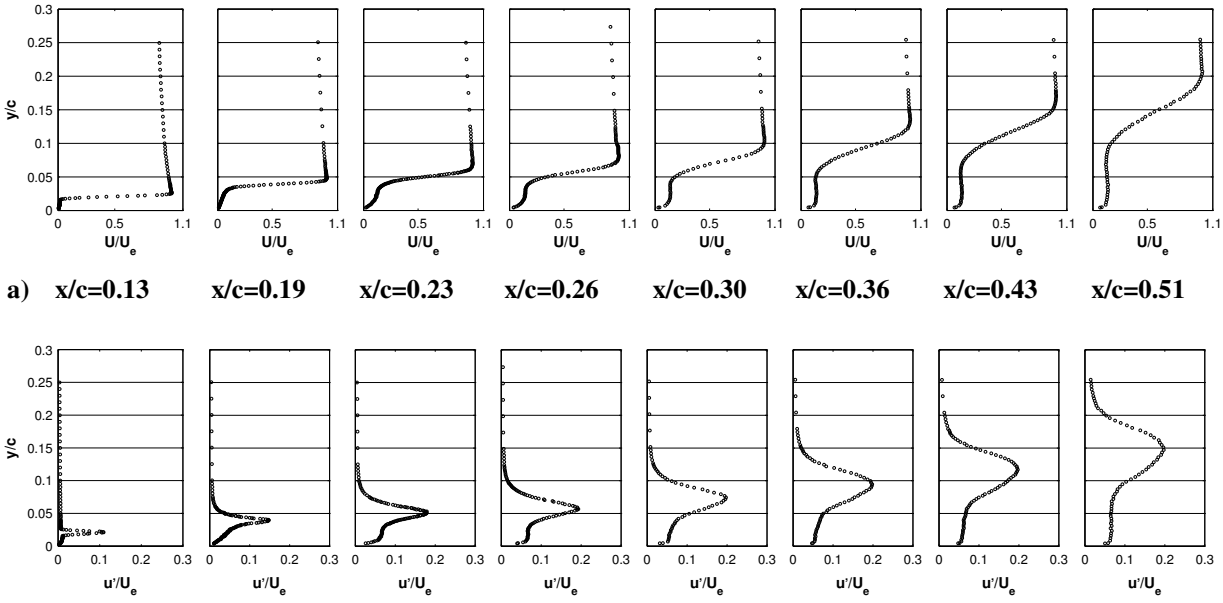

Figure 3.15: Mean and b) RMS boundary-layer velocity profiles for $Re_c = 100x10^3$ and $\alpha=12°$.

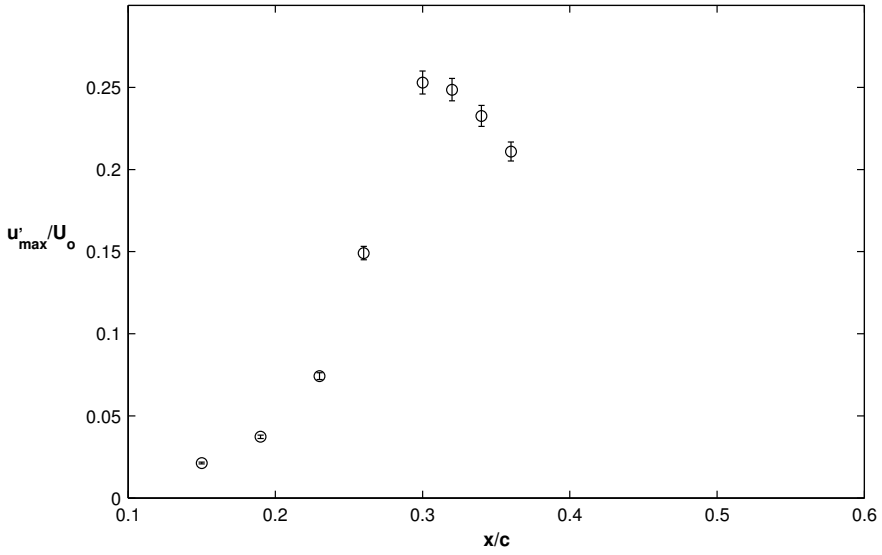

a)

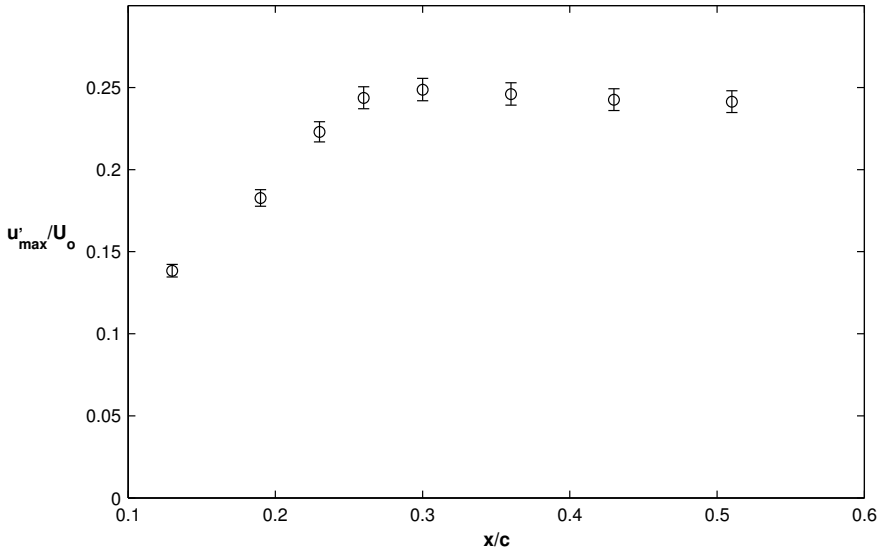

b)

Figure 3.16: Streamwise growth of maximum turbulence intensity for $Re_c = 100x10^3$ at a) $\alpha = 8°$ and b) $\alpha = 12°$.

the separated shear layer and is reminiscent of an eigenfunction of an inviscid Kelvin-Helmholtz instability commonly observed in free shear layers (e.g., Rist & Maucher, 2002).

3.6 Flow Transition

In order to gain additional insight into the transition process, streamwise velocity spectra are examined. Velocity signals for spectral analysis at each downstream location were acquired at y/c locations corresponding to the maximum turbulence intensity in the shear layer. Spectra of the streamwise fluctuating velocity component (E_{uu}) are shown in Fig. 3.17 at α = 8° and α = 12° for $Re_c = 100x10^3$, respectively. For clarity, the amplitude of each spectrum is stepped by three orders of magnitude with respect to the spectrum at the previous upstream location. Recall that, for this Reynolds number, α = 8° and α = 12° correspond to regimes of flow separation with and without reattachment, respectively. At α = 8° (Fig. 3.17a), downstream of the boundary layer separation location (x/c = 0.13), a band of disturbances from approximately 500 Hz to 1400 Hz with the spectral peak corresponding to the fundamental frequency of f_0 = 905 Hz emerges at x/c = 0.17 and amplifies further downstream, with the spectral peak remaining at the fundamental frequency. Additionally, harmonic and subharmonic spectral peaks are generated at x/c = 0.23, which is just upstream of the transition location (x/c = 0.26) estimated from the mean surface pressure coefficient distribution. Furthermore, the generation of harmonics and subharmonics is an indication of nonlinear interactions between the disturbances (Dovgal et al., 1994). The spectral peak associated with the fundamental frequency broadens at x/c = 0.26 and a turbulent spectrum is observed by x/c = 0.36, which is just downstream of the reattachment location (x/c = 0.34) estimated from the mean surface pressure coefficient distribution and observed in the mean velocity profiles (Fig. 3.14). Downstream of the boundary layer separation location (x/c = 0.06) at α = 12° (Fig. 3.17b), a similar transition process is observed, however, disturbances within a band of frequencies associated with a spectral peak at a lower fundamental frequency of f_0 = 560 Hz are amplified in the separated shear layer at and beyond x/c = 0.13.

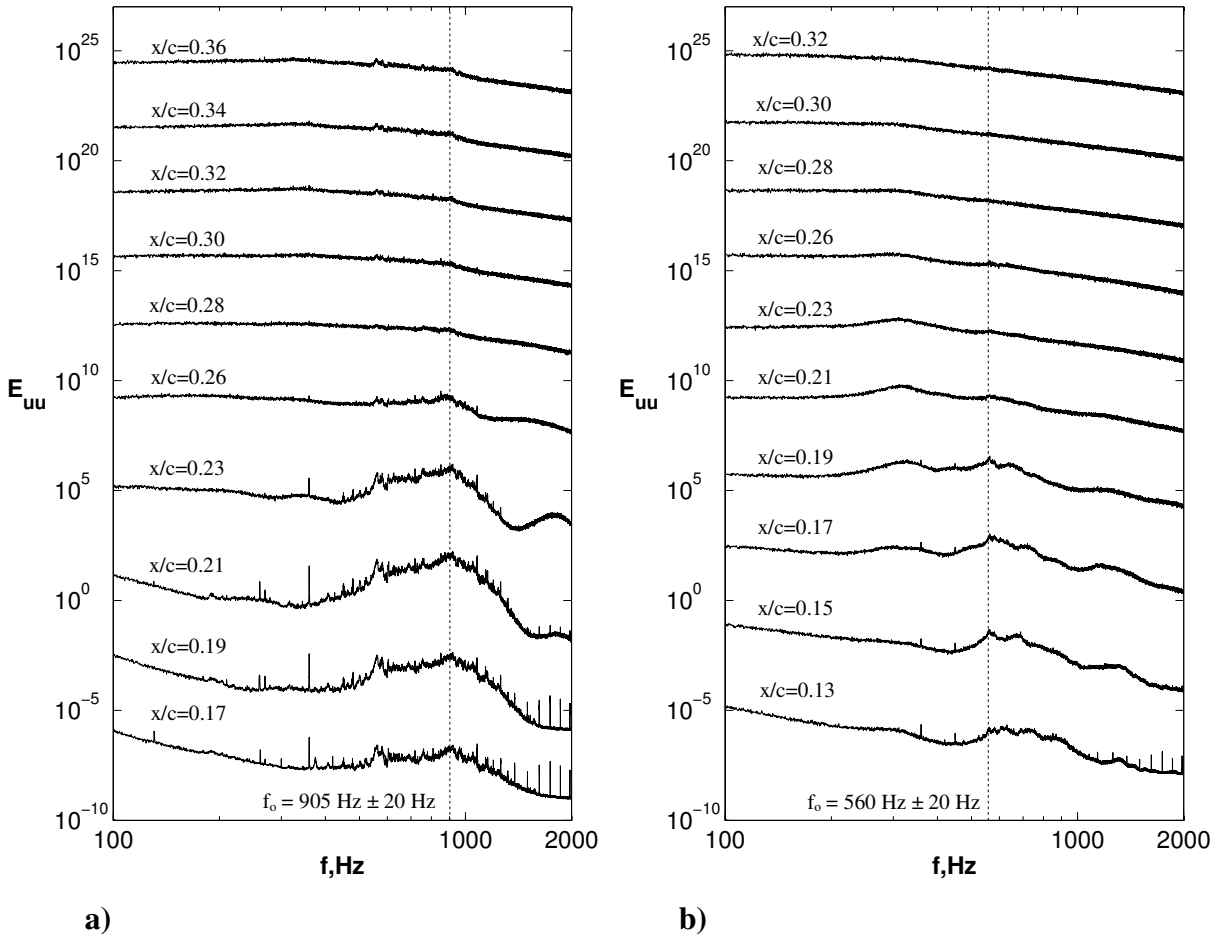

Figure 3.17: Spectra of the streamwise fluctuating velocity at $Re_c = 100x10^3$ for a) $\alpha = 8°$ and b) $\alpha = 2°$. The amplitude of each successive spectrum is increased by three orders of magnitude.

Laminar-to-turbulent transition in the separated shear layer leads to a fully-turbulent spectrum by x/c = 0.28.

Brendel & Mueller (1988, 1990), Boiko et al. (1989), Dovgal et al. (1994), and Yarusevych et al. (2006, 2009) also observed a similar streamwise evolution of the velocity spectra in the separated shear layer for a regime of separation bubble formation. Specifically, Brendel & Mueller (1988, 1990), Boiko et al. (1989), Dovgal et al. (1994) found that harmonics and subharmonics were generated, while Yarusevych et al. (2006, 2009) only

observed the generation of harmonics. For the regime of flow separation without reattachment, Yarusevych et al. (2006, 2009) observed the generation of harmonics and subharmonics, which is also contrary to the present findings.

The spatial growth of disturbances in the separated shear layer is shown in Fig. 3.17. Velocity signals were measured at y/c locations corresponding to the maximum turbulence intensity. The signals were filtered using a narrow bandpass filter centred at the fundamental frequency with a 5 Hz bandwidth. The amplitude of the most amplified disturbance is characterized using the RMS of the filtered signal (u_f'). For both flow regimes, the initial disturbance growth in the separated shear layer is almost exponential, with the slope of the corresponding dashed lines in Fig. 3.18 proportional to the spatial growth rate of the disturbances (e.g., Dovgal et al., 1994; Yarusevych et al., 2006). Accordingly, the initial exponential disturbance growth rate is greater at $\alpha = 12°$ than at $\alpha = 8°$. At $\alpha = 8°$, the region of initial exponential disturbance growth terminates at x/c = 0.23 and the disturbance growth

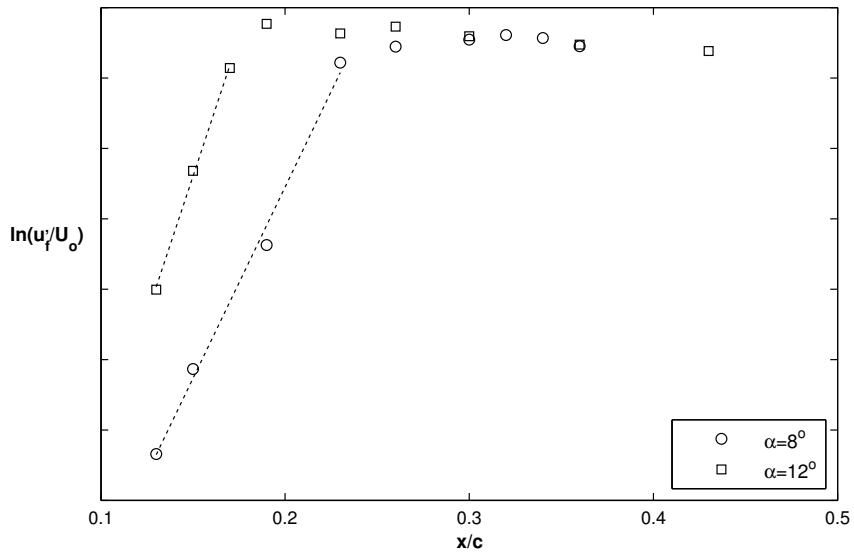

Figure 3.18: Streamwise growth of disturbances at the fundamental frequency in the separated shear layer for $Re_c = 100x10^3$.

saturates for $x/c \geq 0.26$, which coincides with the transition location estimated from the mean surface pressure coefficient distribution. In addition, the x/c location where the disturbance growth saturates corresponds to the x/c location where the spectral peak associated with the fundamental frequency broadens, which is followed by decay in the spectral peak with a further increase in the streamwise direction (Fig. 3.17a). At $\alpha = 12°$, the region of initial exponential disturbance growth terminates at $x/c = 0.17$ and the disturbance growth is checked for $x/c \geq 0.19$, which is further upstream than at $\alpha = 8°$. Similar to $\alpha = 8°$, the saturation of the disturbance growth corresponds to a decay in the spectral peak associated with the fundamental frequency (Fig. 3.17b).

4 Comparison of Time-Resolved Surface Pressure and Velocity Measurements for Flow Diagnostics

The results discussed in Chapter 3 indicate that laminar-to-turbulent transition in the separated shear layer is due to velocity fluctuations associated with a band of amplifying disturbances centred at the fundamental frequency. It is hypothesized that the attendant velocity fluctuations in the separated shear layer induce surface pressure fluctuations over the airfoil that can be detected by the embedded microphones. Thus, it is proposed that measurements of fluctuating surface pressure can be used to examine separated shear layer development over an airfoil surface. In order to validate this hypothesis, velocity signals in the separated shear layer and surface pressure signals at the same streamwise location are measured simultaneously and the results are discussed in this chapter.

4.1 General Comparison of Streamwise Velocity and Surface Pressure Fluctuations

The velocity and surface pressure fluctuation signals at several downstream locations through the separated flow region are compared in Fig. 4.1 and Fig. 4.2 for $Re_c = 100x10^3$ at $\alpha = 8°$ and at $\alpha = 12°$, corresponding to regimes of flow separation with and without reattachment, respectively. At $\alpha = 8°$ (Fig. 4.1), the presence and growth of fluctuations in the velocity signal are also captured in the surface pressure signals. Specifically, downstream of boundary layer separation location ($x/c = 0.13$), there is no discernible disturbance in the velocity and surface pressure signals until $x/c = 0.19$. For $0.21 \leq x/c \leq 0.26$, small-amplitude periodic fluctuations are observed with the period corresponding to the fundamental frequency. In

addition, the amplitude of the fluctuations increases with an increase in x/c. Beyond x/c = 0.26, which corresponds to the transition location estimated from the mean surface pressure coefficient distribution, the fluctuations become increasingly more disordered with an increase in x/c. The amplitude of the fluctuations also increases with an increase in x/c, reaching a maximum at x/c = 0.30, which is just upstream of the reattachment location (x/c = 0.34) estimated from the mean surface pressure coefficient distribution. At $\alpha = 12°$ (Fig. 4.2), oscillations are observed in the velocity and surface pressure signals, however, the amplitude of the oscillations in the surface pressure signal are lower than those observed at $\alpha = 8°$ (Fig. 4.1). Downstream of boundary layer separation (x/c = 0.06), periodic velocity fluctuations associated with growing disturbances in the separated shear layer emerge at x/c = 0.13, while fluctuations in the surface pressure signals are not detectable until x/c = 0.17. Specifically, oscillations in the velocity fluctuation signal with a period corresponding to the fundamental frequency are superimposed on oscillations with a period corresponding to a frequency of approximately 30 Hz. The 30 Hz oscillations do not correspond to the wake shedding frequency associated with coherent structures in the wake. It is speculated that these oscillations may be attributed to shear layer flapping, hot wire sensor vibration, or environmental noise in the wind tunnel test section, all of which are not related to the dominant shear layer disturbances associated with the transition process. Conversely, the period of the oscillations in the surface pressure signals is not quantifiable. For $x/c \geq 0.21$, fluctuations in the velocity signal become increasingly more disordered with an increase in x/c. In addition, on the average, the amplitude of the velocity fluctuations increases until x/c = 0.30, beyond which, growth of the disturbance amplitude is checked. For $x/c \geq 0.17$, on the average, the amplitude of fluctuations in the surface pressure signal increase with an increase

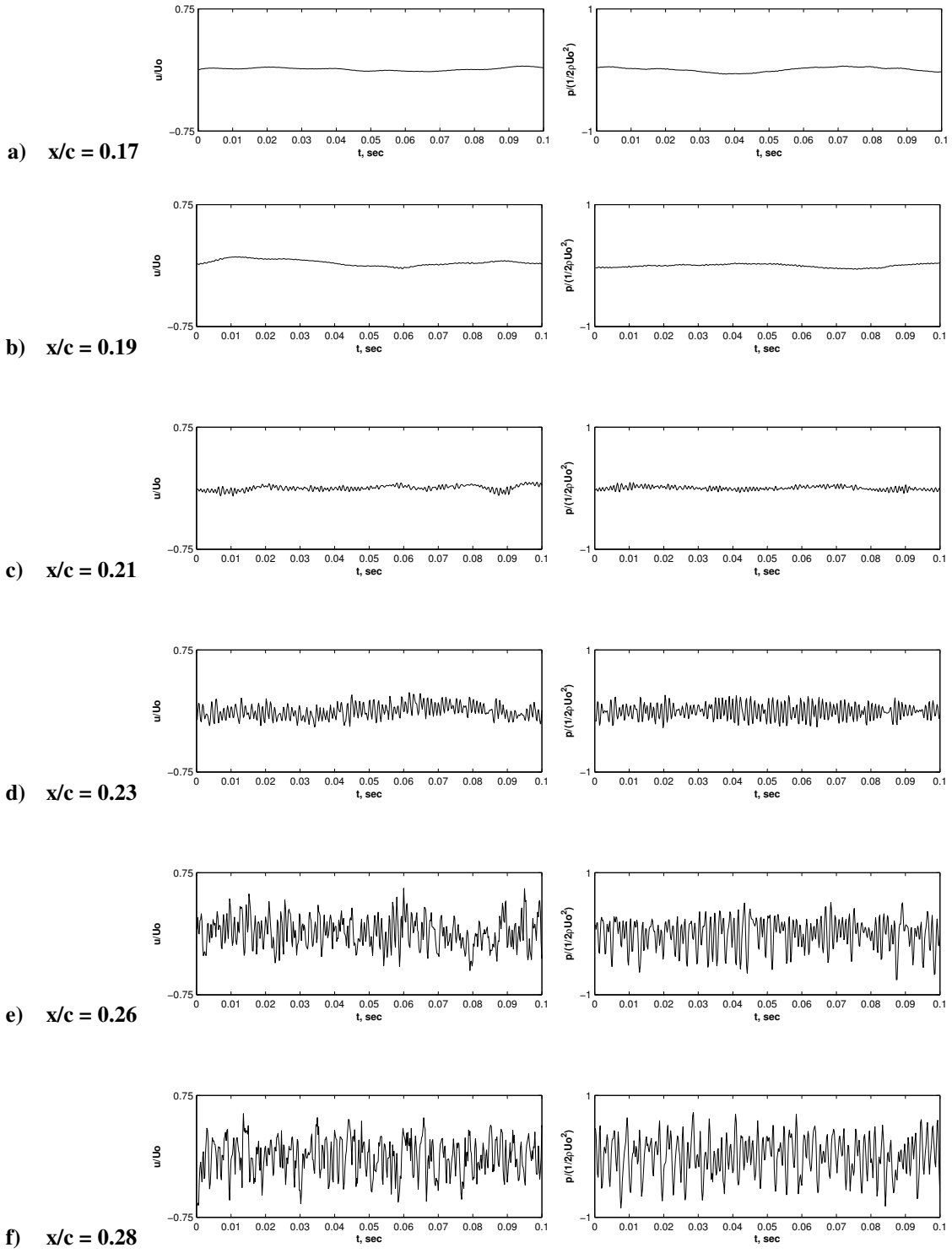

Figure 4.1: Streamwise fluctuating velocity component and surface pressure signals at $\alpha = 8^\circ$ for $Re_c = 100x10^3$.

g) x/c = 0.30

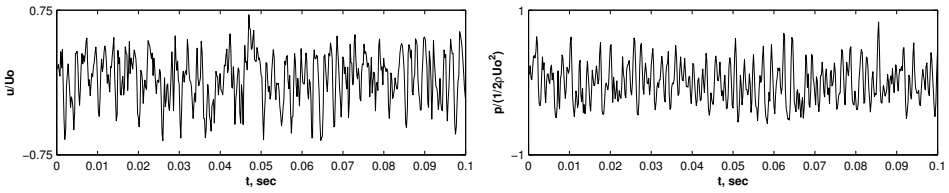

h) x/c = 0.32

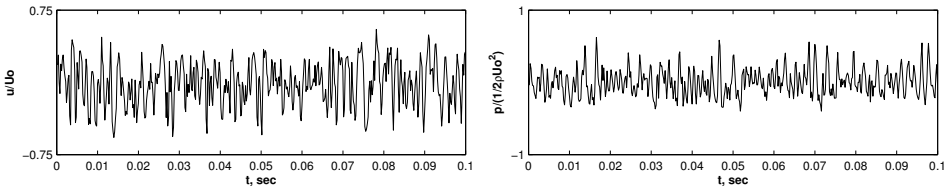

i) x/c = 0.36

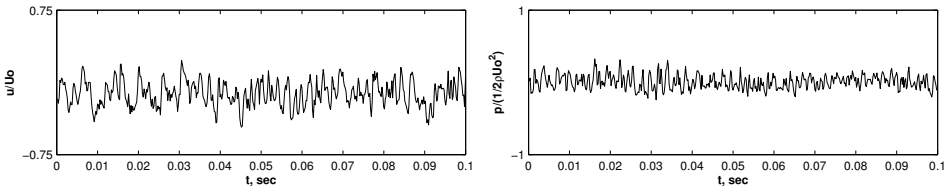

j) x/c = 0.39

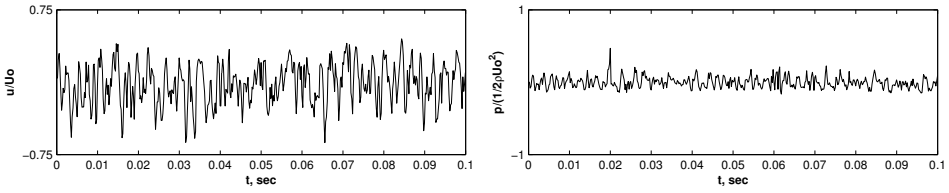

k) x/c = 0.43

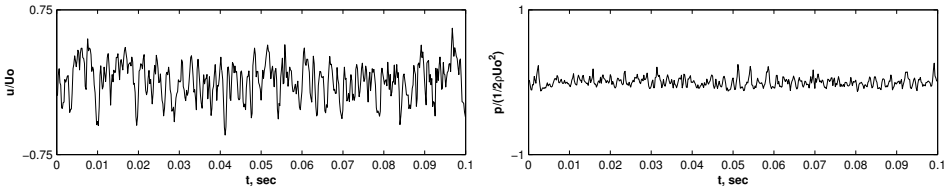

l) x/c = 0.56

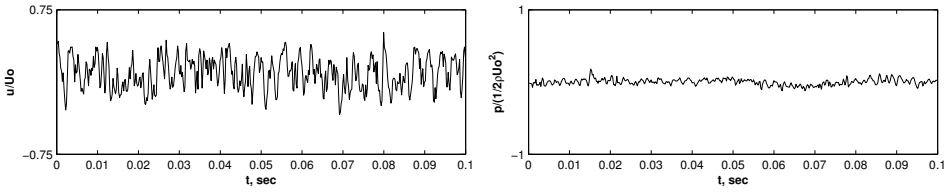

Figure 4.1 (g-l): See previous page.

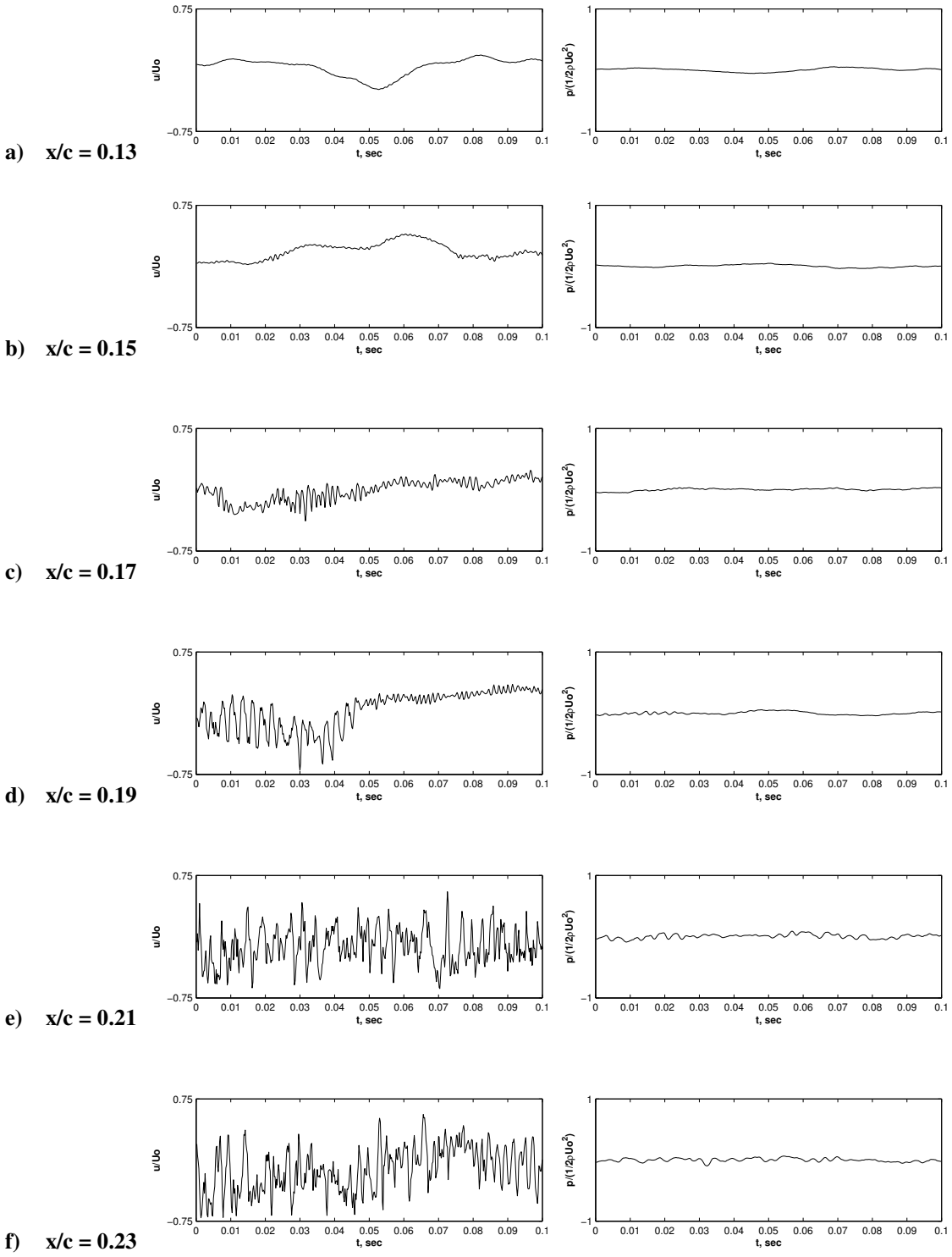

Figure 4.2: Streamwise fluctuating velocity component and surface pressure signals at α = 12° for $Re_c = 100x10^3$.

g) **x/c = 0.26**

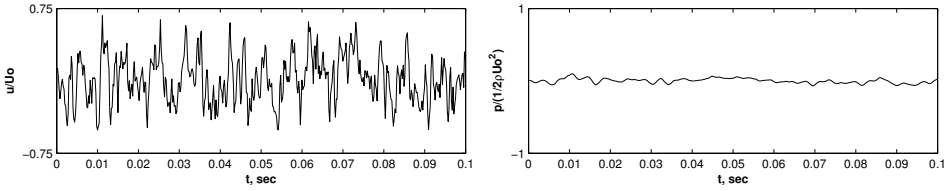

h) **x/c = 0.28**

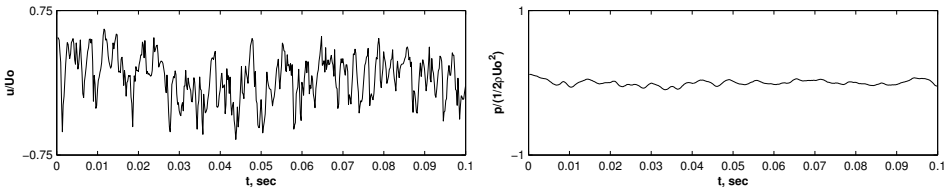

i) **x/c = 0.30**

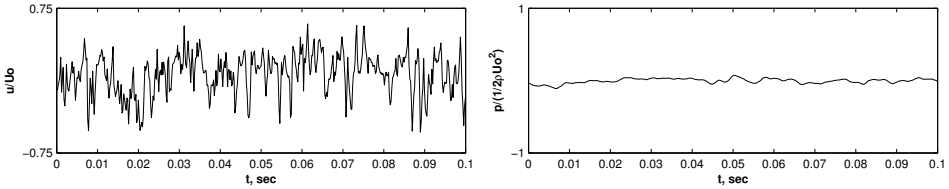

j) **x/c = 0.32**

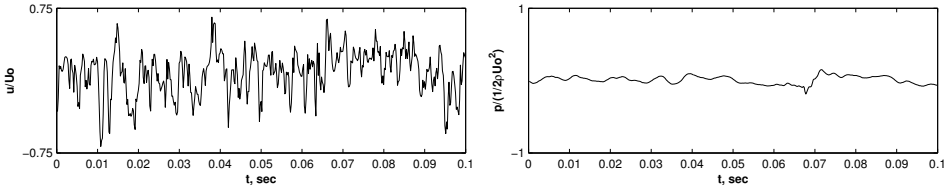

k) **x/c = 0.39**

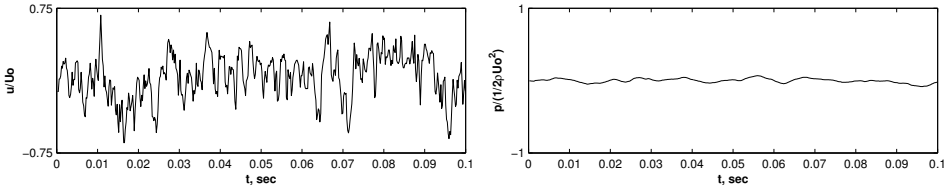

l) **x/c = 0.56**

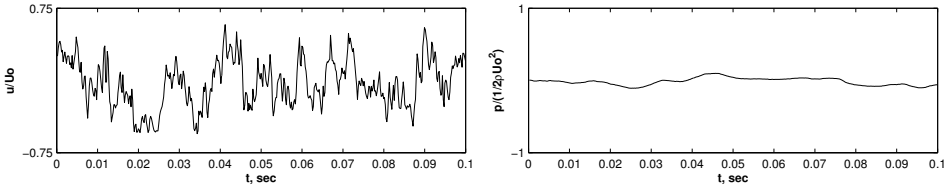

Figure 4.2 (g-1): See previous page.

in x/c. Comparison of velocity and surface pressure fluctuations in the separation bubble (Fig. 4.1) has revealed that the presence and growth of disturbances in the separation shear layer is reflected in velocity signals and is captured well in surface pressure signals. It can be concluded that as the angle of attack is increased from 8° to 12°, causing the separation bubble to burst, the distance between the separated shear layer and the airfoil surface increases and the corresponding amplitude of the surface pressure fluctuations decreases. Accordingly, when the airfoil is stalled (Fig. 4.2), the presence and growth of disturbances in the shear layer are reflected in the velocity signals; however, the period of the fluctuations in the surface pressure signals is not quantifiable. Thus, spectral analysis is explored to further examine the association between the amplifying disturbances in the velocity and surface pressure signals.

Spectra of streamwise fluctuating velocity and surface pressure for $Re_c = 100x10^3$ at $\alpha = 8°$ and at $\alpha = 12°$ are shown in Fig. 4.3 and Fig. 4.4, respectively. For the remainder of this thesis, spectra of fluctuating velocity and surface pressure will simply be referred to as velocity and surface pressure spectra, respectively. Analysis of the surface pressure spectra indicates that the frequency of the spectral peak of the amplified band of disturbances, corresponding to 903 Hz (Fig. 4.3b) and 558 Hz (Fig. 4.4b) at $\alpha = 8°$ and at $\alpha = 12°$, respectively, matches that of the fundamental frequency estimated from the velocity spectra. In addition, the frequency range of the amplified disturbance band in the surface pressure spectra matches that in the velocity spectra at a given x/c location. For both angles of attack, subharmonics and/or harmonics emerge at the same x/c locations in the velocity and surface pressure spectra. For separation bubble formation at $\alpha = 8°$, the spectral peak in the velocity and surface pressure spectra associated with the fundamental frequency dominates that of the subharmonic and harmonic frequencies at x/c locations where such spectral peaks are

detected. When the airfoil is stalled at α = 12°, the spectral peak in the velocity and surface pressure spectra associated with the subharmonic frequency exceeds that of the fundamental frequency for x/c ≥ 0.19. Velocity spectra for selective y/c locations at x/c = 0.23 and at x/c = 0.19 are presented in Fig. 4.5 for α = 8° and α = 12°, respectively. At α = 8° (Fig. 4.5a), the x/c location was chosen just upstream of the transition location (x/c = 0.26) estimated from the mean surface pressure coefficient distribution. Accordingly, the spectral peaks associated with the harmonic and fundamental frequency are strong, and the x/c location is just

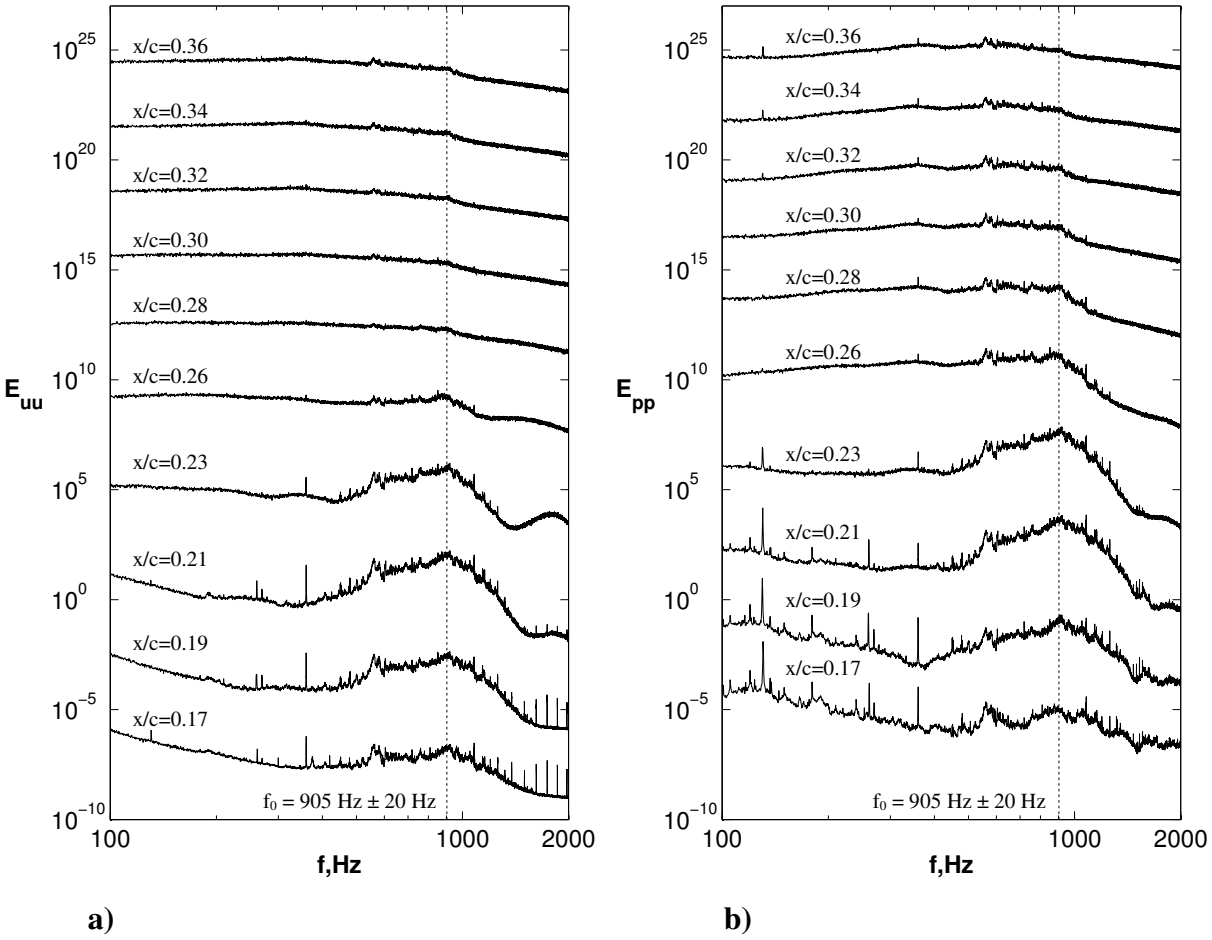

Figure 4.3: Spectra of the streamwise fluctuating a) velocity component, and b) surface pressure for Re_c = $100x10^3$ and α = 8°. The amplitude of each successive spectrum is increased by three orders of magnitude.

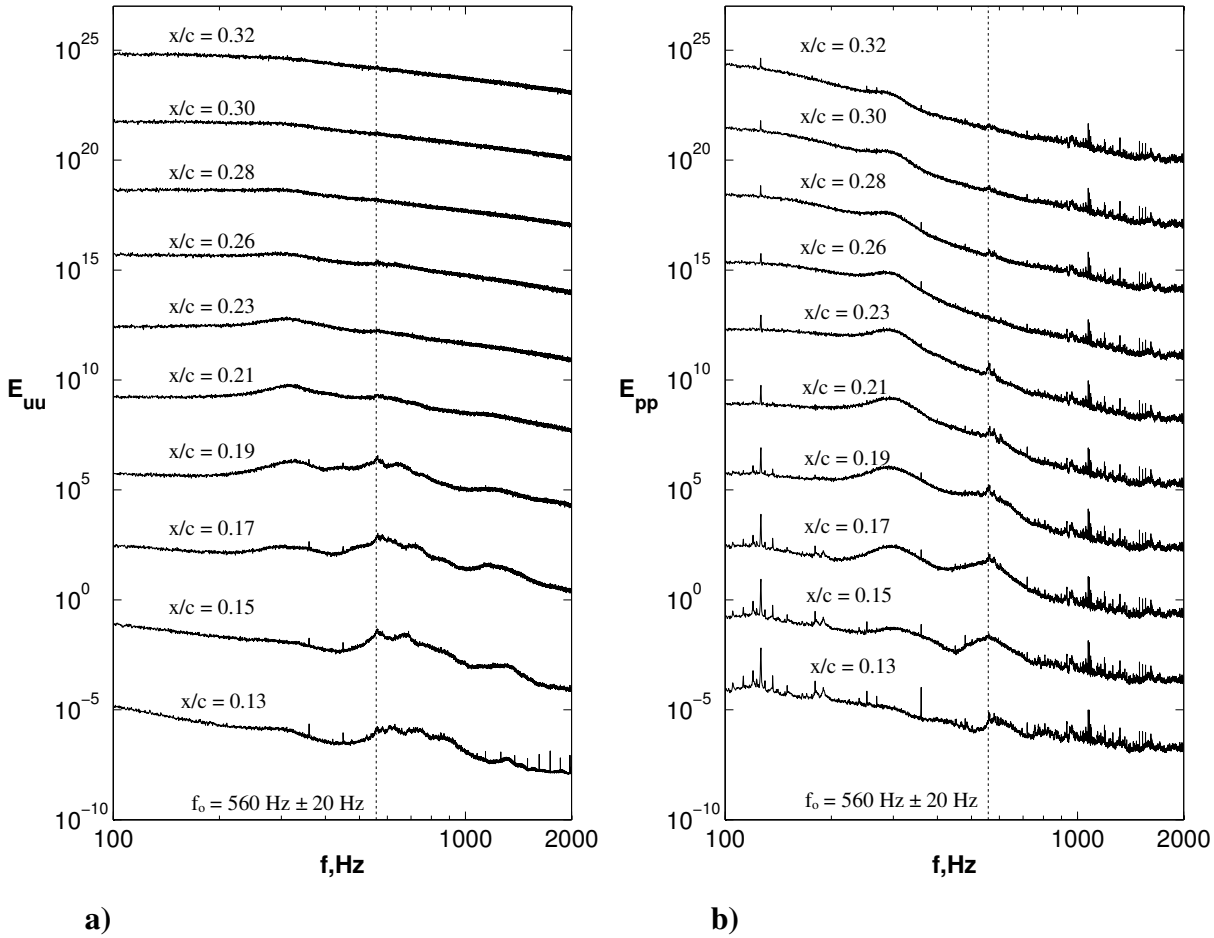

Figure 4.4: Spectra of the streamwise fluctuating a) velocity component, and b) surface pressure for Re_c = 100x10^3 and α = 12°. The amplitude of each successive spectrum is increased by three orders of magnitude.

upstream of the maximum separation distance between the shear layer and airfoil surface. Similarly, at α = 12° (Fig. 4.5b), the x/c location was selected to be near the latter stage of transition associated with nonlinear interactions between the disturbances, as evidenced by the presence of strong spectral peaks associated with the subharmonic and fundamental frequency. For both angles of attack, the amplitude of the spectral peak decreases with decreasing y/c. Specifically, for separation bubble formation at α = 8° (Fig. 4.5a), a strong spectral peak is still detectable closer to the airfoil surface (i.e. at lower y/c) than that observed when the shear layer is further from the airfoil surface when the airfoil is stalled at

α = 12° (Fig. 4.5b). This evidence further substantiates that the separation distance between the shear layer and the airfoil surface affects the velocity and corresponding surface pressure fluctuations near the airfoil surface associated with the disturbances in the shear layer.

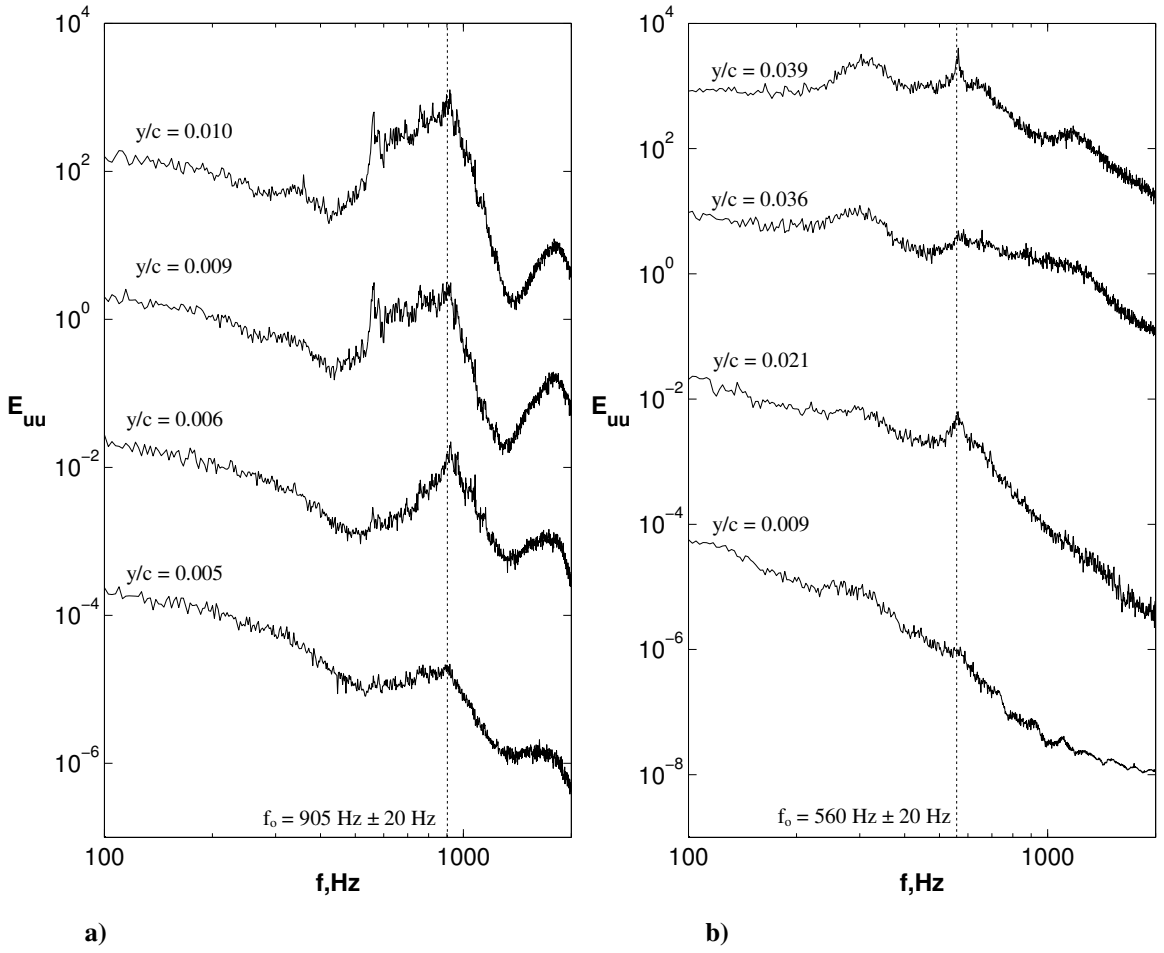

Figure 4.5: Spectra of the streamwise fluctuating velocity component at a) x/c = 0.23 and α = 8°, and at b) x/c = 0.19 and α = 12° for $Re_c = 100x10^3$. The amplitude of each successive spectrum is increased by two orders of magnitude. It should also be noted that δ/c = 0.0156 and δ/c = 0.0508 at α = 8° and α = 12°, respectively, where δ is the boundary layer thickness.

Distributions of streamwise RMS velocity and surface pressure fluctuations for $Re_c = 100x10^3$ at α = 8° and at α = 12°are shown in Fig. 4.6 and Fig. 4.7, respectively. Note that locations of separation, transition, and reattachment estimated from mean surface pressure distributions are marked in the figures by S, T, and R, respectively. Downstream of boundary

layer separation (x/c = 0.13) at α = 8° (Fig. 4.6), relatively low amplitude pressure fluctuations are observed with marginal variation for x/c < 0.21. For x/c ≥ 0.21, the amplitude of surface pressure and velocity fluctuations increase with x/c, reaching a maximum at x/c ≈ 0.30, which is just upstream of the reattachment location (x/c = 0.34) estimated from the mean surface pressure distributions. When the angle of attack is increased to α = 12° (Fig. 4.7) and the separated shear layer fails to reattach to the airfoil surface, the amplitude of the surface pressure fluctuations decreases by an order of magnitude relative to that at the matching streamwise locations for α = 8°. It should be noted, however, that the amplitude of the attendant surface pressure fluctuations is an order of magnitude greater than the background noise. Downstream of boundary layer separation (x/c = 0.06), on the average, the amplitude of the fluctuating surface pressure increases in the streamwise direction from x/c = 0.08 to x/c = 0.56. For x/c ≥ 0.56, the amplitude of the fluctuating surface pressure is checked. The amplitude of the velocity fluctuations increases with the streamwise distance within 0.13 ≤ x/c ≤ 0.30. Moreover, the amplitude of the velocity fluctuations is checked for x/c > 0.30, which coincides with the x/c location where a turbulent velocity spectrum emerges (Fig. 4.4). For both regimes, the streamwise evolution of the RMS surface pressure fluctuations follows the RMS velocity fluctuations in the separated shear layer reasonably well. Distinct estimates of the x/c locations corresponding to flow separation, transition, and reattachment cannot be quantified from the RMS surface pressure fluctuation distributions. Nevertheless, within the separation bubble, RMS surface pressure fluctuations are relatively low near separation and a maximum near reattachment, thus, the presence and extent of a separation bubble can readily be identified. The streamwise RMS surface pressure fluctuation distribution is distinctly different for a stalled flow regime relative to that for separation bubble formation; therefore, the presence of the former flow regime can also be identified.

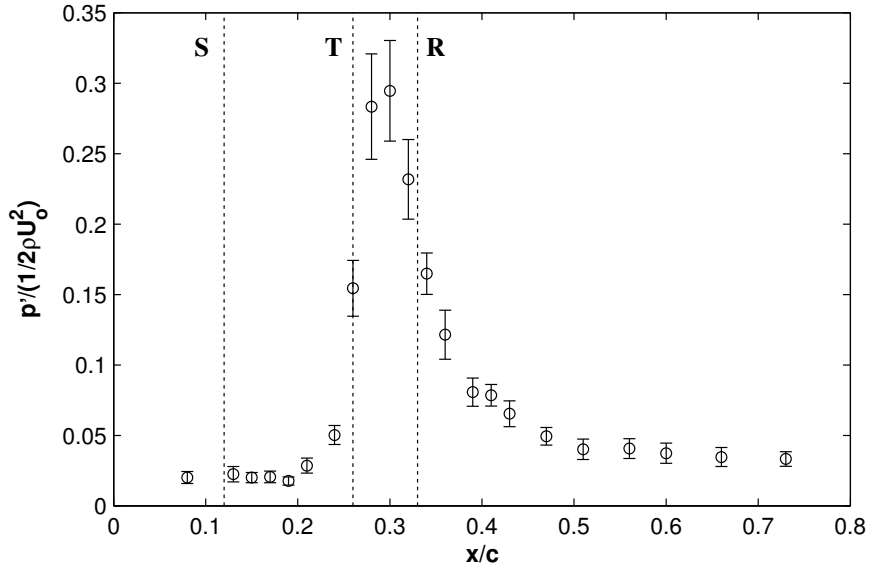

a)

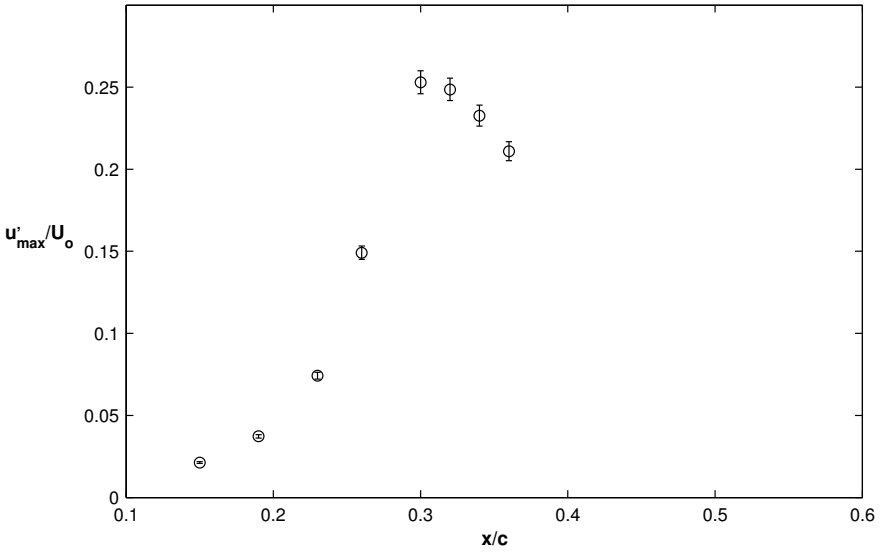

b)

Figure 4.6: Streamwise a) surface pressure fluctuation coefficient and b) maximum turbulence intensity at $\alpha = 8^\circ$ for $Re_c = 100x10^3$. The uncertainty in the rms

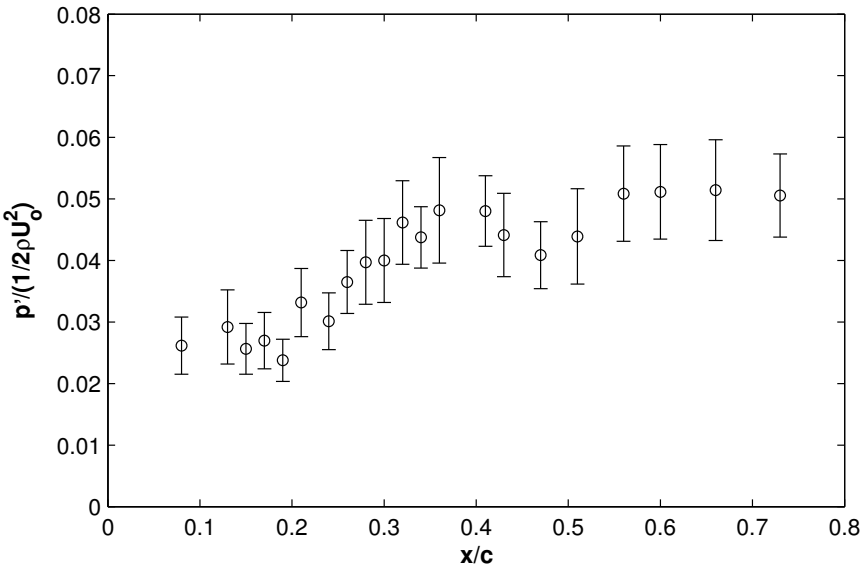

a)

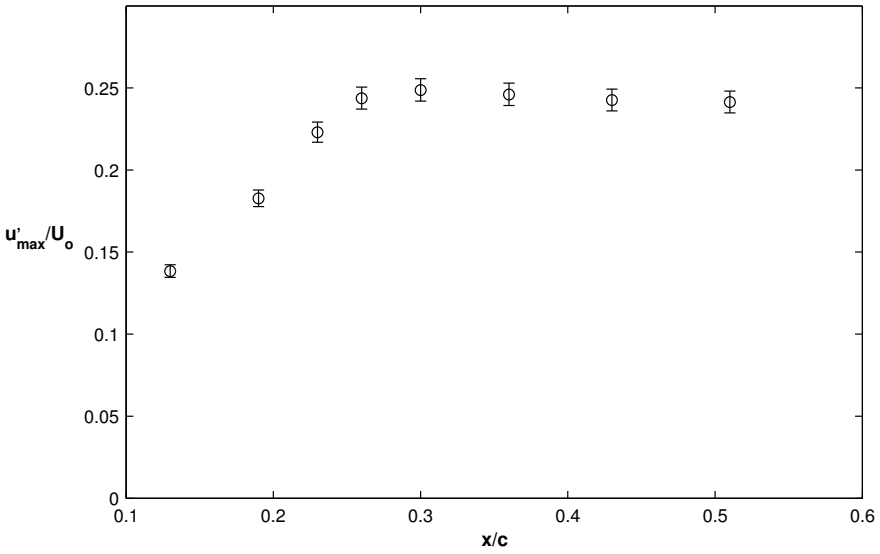

b)

Figure 4.7: Streamwise a) surface pressure fluctuation coefficient and b) maximum turbulence intensity at $\alpha = 12^{\circ}$ for $Re_c = 100x10^3$. Note that the location of separation estimated from mean surface pressure coefficient distribution occurs at x/c = 0.06, which is not identified in the figure.

4.2 Cross-Correlation of Fluctuating Velocity and Surface Pressure

In order to explore the association between velocity fluctuations in the separated shear layer and the corresponding surface pressure fluctuations in more detail, the cross-correlation between simultaneously acquired signals of streamwise velocity and surface pressure at the same x/c location was computed to quantify the degree of similarity between these signals. In order to examine how the cross-correlation between two signals can be interpreted, consider two sinusoidal signals, E_1 and E_2, described by Eq. 4.1 and Eq. 4.2, respectively.

$$E_1 = A\sin(2\pi ft) \tag{4.1}$$

$$E_2 = B\sin(2\pi ft + \theta) \tag{4.2}$$

In the preceding equations, A and B are the signal amplitudes such that amplitude A is greater than amplitude B by a factor of 2. In addition, f is the oscillation frequency, t is the time index, and θ is the phase shift. Signals E_1 and E_2 are shown in Figs. 4.8a and 4.8b for a phase shift of 0 degrees and 180 degrees, respectively. The cross-correlation coefficient function computed for E_1 and E_2 is shown in Figs. 4.9a and 4.9b for a phase shift of 0 degrees and 180 degrees, respectively. Recall from §2.5 that the magnitude of the cross-correlation coefficient function $\left|\rho_{E_1E_2}\right|$ ranges from 0 to 1. In Fig. 4.9, oscillations in the cross-correlation coefficient function are observed with a period corresponding to the oscillation frequency f. The greatest degree of similarity between signals E_1 and E_2 occurs when the cross-correlation coefficient function is maximum ($\rho_{E_1E_2}$*), which occurs at a time lag τ* of zero. In addition, the sign of $\rho_{E_1E_2}$* at τ* is linked to the phase between the signals. Specifically, $\rho_{E_1E_2}* = 1$

when there is no phase shift between the signals (Fig. 4.9a) and $\rho_{E_1E_2}* = -1$ when the signals are out of phase (Fig. 4.9b). It should be noted that, even though the amplitude of signals E_1 and E_2 differ, $\left|\rho_{E_1E_2}*\right| = 1$ irrespective of the phase shift between the signals, which is the maximum attainable value for the cross-correlation coefficient function.

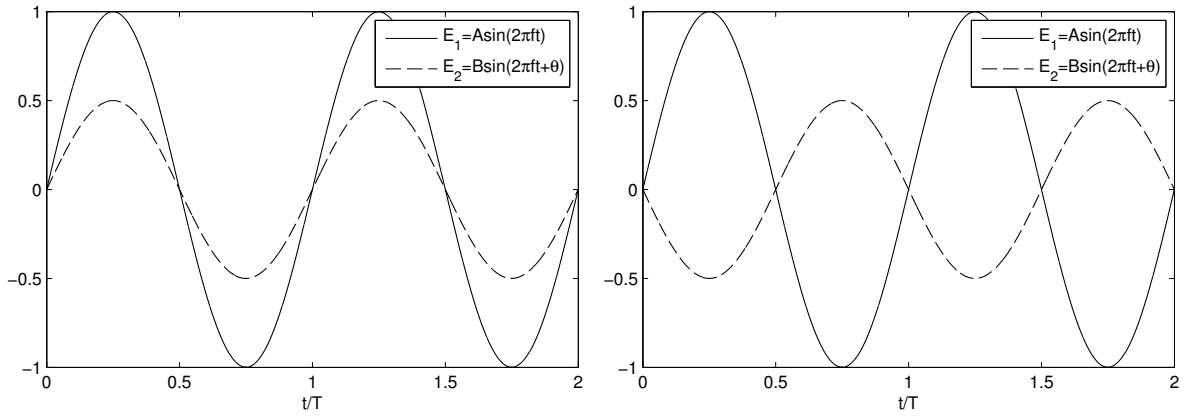

Figure 4.8: Sinusoidal signals with a) a 0 degree phase shift, and b) a 180 degree phase shift between the signals. Note that T is the period of the sinusoidal signal and amplitude A is greater than amplitude B by a factor of 2.

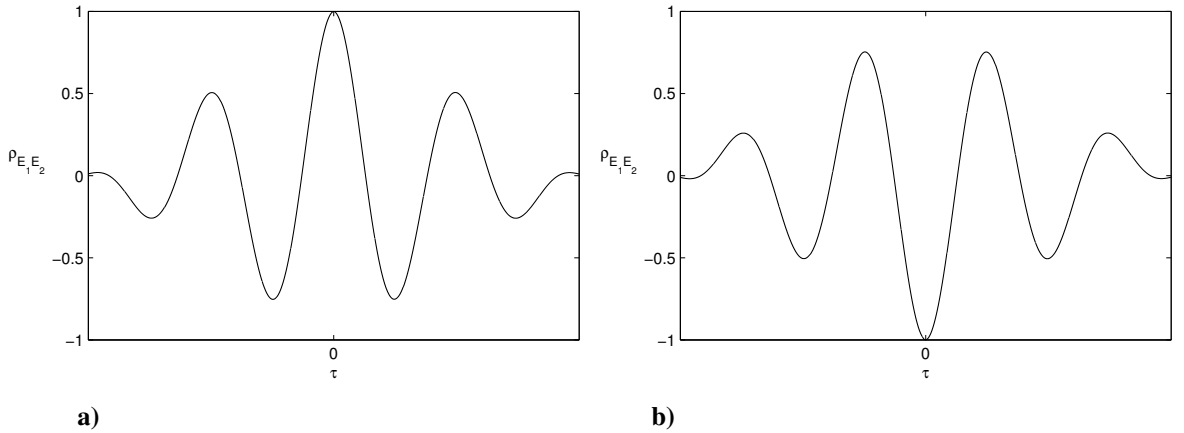

Figure 4.9: Cross-correlation coefficient function computed for sinusoidal signals E_1 and E_2 with a) a 0 degree phase-shift, and b) a 180 degree phase shift between the signals.

Interpretation of the cross-correlation coefficient (ρ_{up}) computed for velocity and surface pressure signals measured in the separated flow region over an airfoil surface can be inferred from the preceding discussion for the simulated signals. Specifically, for velocity and surface pressure signals acquired at the same streamwise location, it is speculated that $\tau^* = 0$ since it is expected that surface pressure fluctuations are linked to velocity fluctuations in the separated shear layer at the same streamwise location. In addition, based on the unsteady and irrotational Bernoulli's equation, it is expected that velocity and surface pressure fluctuations will be out of phase, thus, it is speculated that $\rho_{up}^* < 0$. Moreover, oscillations in the cross-correlation function are expected to occur with a period corresponding to the frequency of the dominant spectral peak in velocity and surface pressure spectra.

The streamwise evolution of the cross-correlation coefficient function is shown in Fig. 4.10 and Fig. 4.11 at $\alpha = 8°$ and at $\alpha = 12°$ for $Re_c = 100x10^3$, respectively. Within the separated flow region for both angles of attack, oscillations are observed in the cross-correlation coefficient function. Specifically, at $\alpha = 8°$, oscillations are observed for $0.21 \leq x/c \leq 0.36$ with the period corresponding to the fundamental frequency, which is the frequency of the dominant spectral peak for the associated x/c locations (Fig. 4.3). Similarly at $\alpha = 12°$, oscillations are observed for $0.19 \leq x/c \leq 0.23$ with the period corresponding to the subharmonic frequency, which is also the frequency of the dominant spectral peak for the associated x/c locations (Fig. 4.4). Accordingly, within the separated flow region for both angles of attack, the periodicity in the cross-correlation coefficient function indicates that the oscillations observed in the velocity and surface pressure signals originate from the same flow phenomenon, which is that of the disturbances in the separated shear layer. It should be noted that, on the average, the amplitude of the oscillations in the cross-correlation

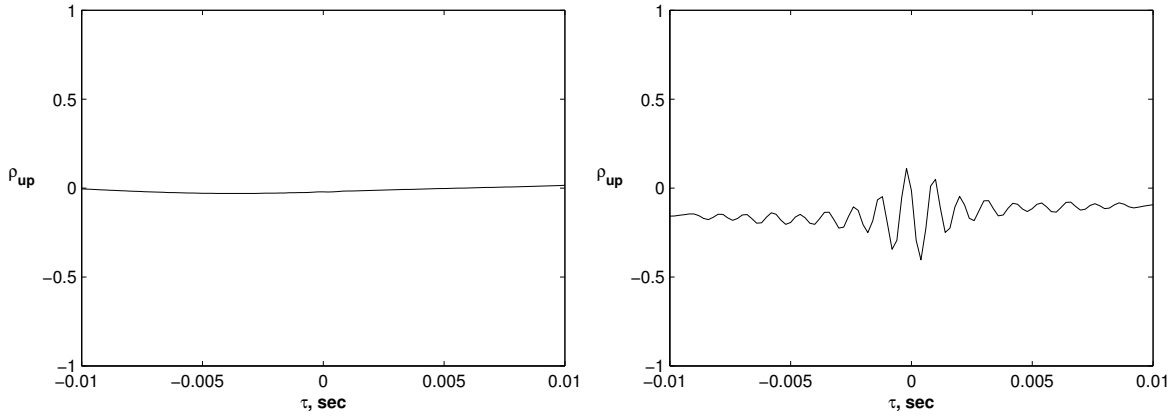

a) x/c = 0.17 **b) x/c = 0.21**

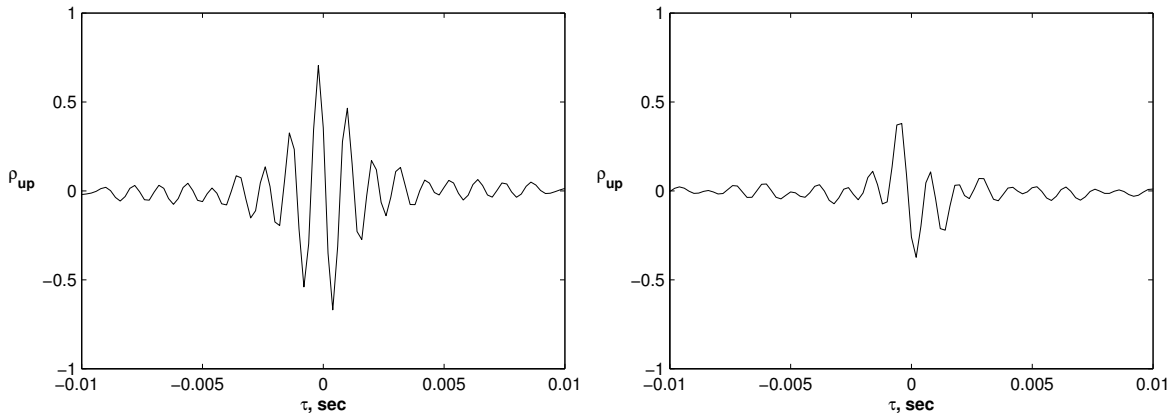

c) x/c = 0.23 **d) x/c = 0.26**

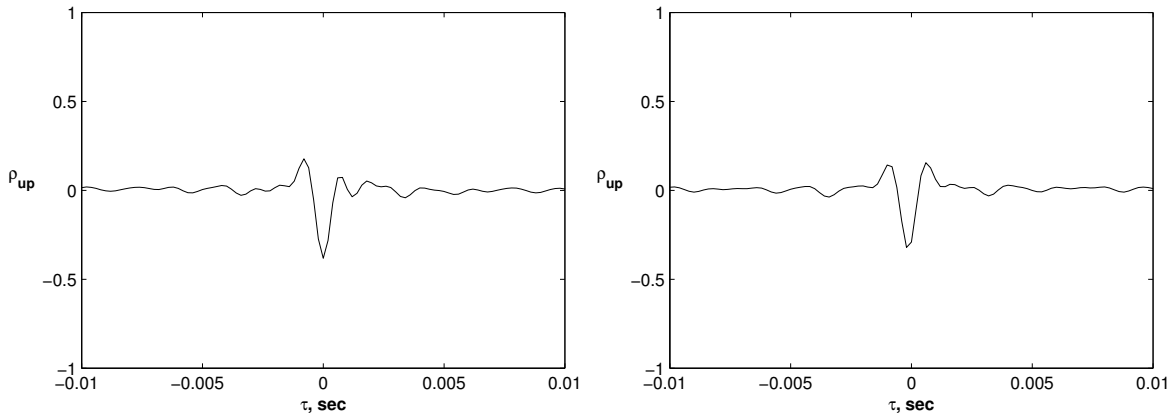

e) x/c = 0.30 **f) x/c = 0.36**

Figure 4.10: Cross-correlation coefficient functions based on streamwise fluctuating velocity and surface pressure for $Re_c = 100x10^3$ at $\alpha = 8°$.

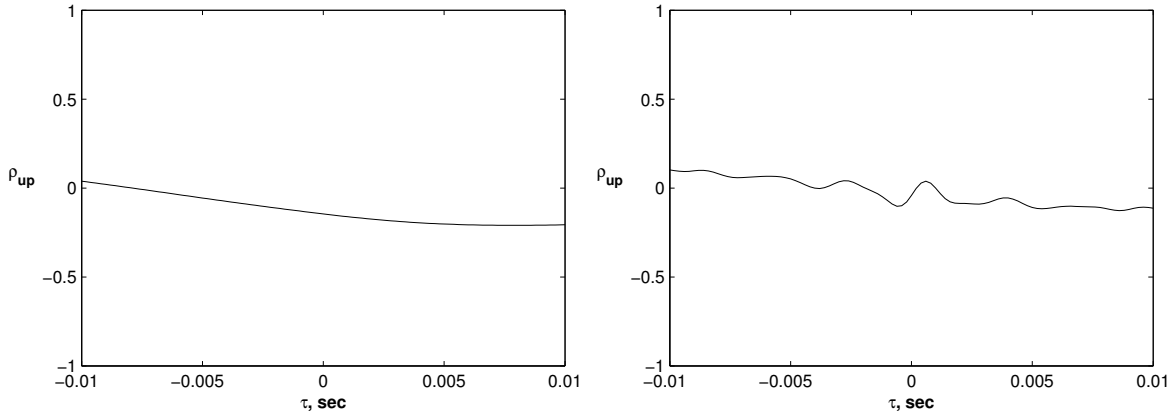

a) x/c = 0.13 **b) x/c = 0.19**

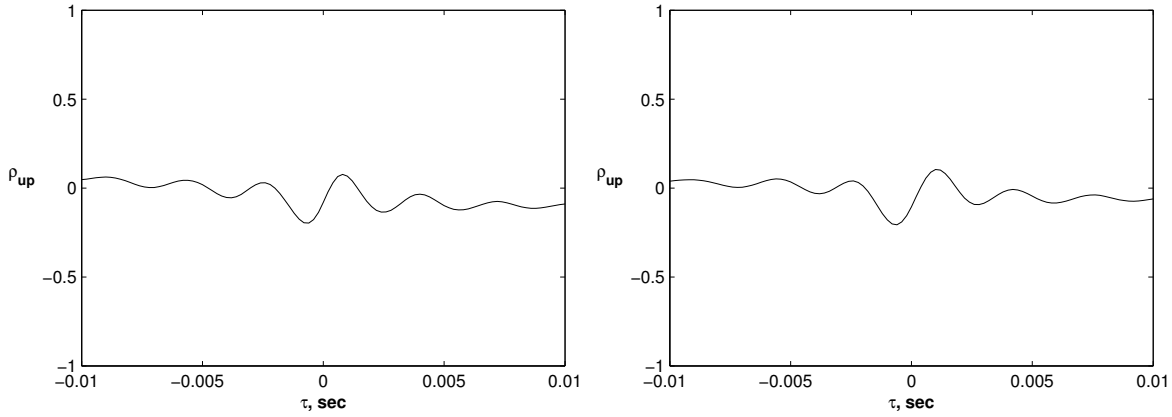

c) x/c = 0.21 **d) x/c = 0.23**

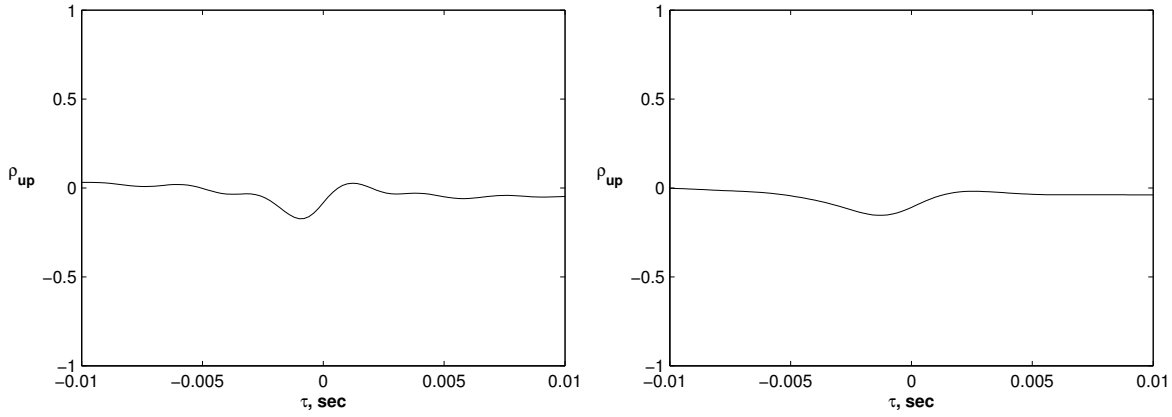

e) x/c = 0.26 **f) x/c = 0.32**

Figure 4.11: Cross-correlation coefficient functions based on streamwise fluctuating velocity and surface pressure for $Re_c = 100x10^3$ at $\alpha = 12°$.

coefficient function is greater at $\alpha = 8°$ than at $\alpha = 12°$. This observation substantiates that the proximity of the shear layer to the airfoil surface influences the degree of similarity between the surface pressure and velocity fluctuations associated with disturbances in the separated shear layer.

It is evident in Fig. 4.10 and Fig. 4.11 that τ^* is non-zero at some x/c locations for both angles of attack. In fact, the variability in τ^* is 0.0001 ± 0.0003 s for $0.21 \leq x/c \leq 0.36$ at $\alpha = 8°$ and -0.0006 s for $0.19 \leq x/c \leq 0.23$ at $\alpha = 12°$. τ^* estimates were only obtained at streamwise locations where the cross-correlation coefficient function exhibited oscillations with a distinct period corresponding to the fundamental and subharmonic frequencies for $\alpha = 8°$ and $\alpha = 12°$, respectively. The variability in the τ^* estimates and deviation from $\tau^* = 0$ ($\Delta\tau^*$) is attributed to two experimental factors: i) the uncertainty in positioning the hot wire sensor over the microphone at the same streamwise location, and ii) the resolution of the time lag due to the sampling frequency. As a result, the estimated uncertainty attributed to these experimental factors is $\Delta\tau^* = \pm 0.0003$ s and $\Delta\tau^* = \pm 0.0005$ s for $\alpha = 8°$ and $\alpha = 12°$, respectively. Since the range of τ^* estimates is comparable the experimental uncertainty ($\Delta\tau^*$) for both angles of attack, this analysis confirms that the fluctuating surface pressure detected by the microphones is linked to velocity fluctuations associated with disturbances amplifying in the separated shear layer at the same streamwise location.

5 Analysis of Time-Resolved Surface Pressure Measurements

In this chapter, a detailed analysis of time-resolved surface pressure measurements acquired with the embedded microphone array is presented. The results pertain to a range of Reynolds numbers from $60x10^3$ to $130x10^3$ and a range of angles of attack from 6° to 16°. These flow parameters encompass regimes of flow separation with and without reattachment.

5.1 Streamwise Distributions of RMS Surface Pressure Fluctuations

The effect of the Reynolds number and angle of attack on the streamwise distribution of RMS surface pressure fluctuations is shown in Fig. 5.1 for $6° \leq \alpha \leq 16°$ at $Re_c = 100x10^3$ and in Fig. 5.2 for $60x10^3 \leq Re_c \leq 130x10^3$ at $\alpha = 12°$. For $6° \leq \alpha \leq 10°$ at $Re_c = 100x10^3$ (Figs. 5.1a to 5.1c), a separation bubble is formed on the upper surface of the airfoil and the separated shear layer fails to reattach to the airfoil surface for $\alpha \geq 12°$ (Figs. 5.1d to 5.1f). At $\alpha = 12°$, the airfoil is stalled for $60x10^3 \leq Re_c \leq 80x10^3$ (Figs. 5.2a to 5.2c) and the separated shear layer reattaches to the airfoil surface for $Re_c \geq 110x10^3$ (Figs. 5.2d to 5.2f). Separation, transition, and reattachment locations estimated from mean surface pressure coefficient distributions are also shown in Figs. 5.1 and 5.2, denoted by S, T, and R, respectively, at flow parameters for which estimates of these locations were obtained.

The results in Figs. 5.1 and 5.2 show that the characteristics of the streamwise distribution of RMS surface pressure fluctuations depend significantly on the flow regime. Within the separation bubble (Figs. 5.1a to 5.1c and Figs. 5.2d to 5.2f), the surface pressure fluctuations increase with an increase in x/c, reaching a maximum just upstream of the reattachment location estimated from the mean surface pressure coefficient distribution.

Downstream of flow reattachment, the surface pressure fluctuations decrease with a further increase in x/c. Conversely, within the separated flow region when the airfoil is stalled (Figs. 5.1d to 5.1f and Figs. 5.2a to 5.2c), the surface pressure fluctuations decrease significantly compared to that observed in the separation bubble. It should be noted, however, that the amplitude of the attendant surface pressure fluctuations is an order of magnitude greater than the background noise.

Within the separation bubble, the increase of the surface pressure fluctuations in the streamwise direction with a maximum just upstream of flow reattachment was reported previously for separating-reattaching flows on such geometries as the forward-facing step (FFS) (e.g., Mabey, 1972), backward-facing step (BFS) (e.g., Mabey, 1972; Farabee & Casarella, 1986; Driver et al., 1987; Lee & Sung, 2001), and splitter plate with fence (SPF) (e.g., Mabey, 1972; Hudy et al., 2003). For the present study, it is also observed that the surface pressure fluctuations are greater within the turbulent boundary layer than in the laminar boundary layer prior to separation. For $Re_c = 100x10^3$ and $6° \leq \alpha \leq 10°$ (Figs. 5.1a to Fig. 5.1c), as the angle of attack is increased, the region of amplified surface pressure fluctuations advances upstream. This is accompanied by an upstream advancement and reduction in length of the separation bubble, which is evidenced by the separation, transition, and reattachment locations marked in Figs. 5.1a to 5.1c. Within the separation bubble for $6° \leq \alpha \leq 10°$ at $Re_c = 100x10^3$ (Figs. 5.1a to 5.1c) and for $110x10^3 \leq Re_c \leq 130x10^3$ at $\alpha = 12°$ (Figs. 5.2d to 5.2f), the surface pressure fluctuations are comparable within the laminar boundary layer and the laminar portion of the separation bubble just downstream of boundary layer separation. Within the experimental uncertainty, the maximum surface pressure fluctuations are also comparable within the separation bubble for the corresponding range of flow parameters.

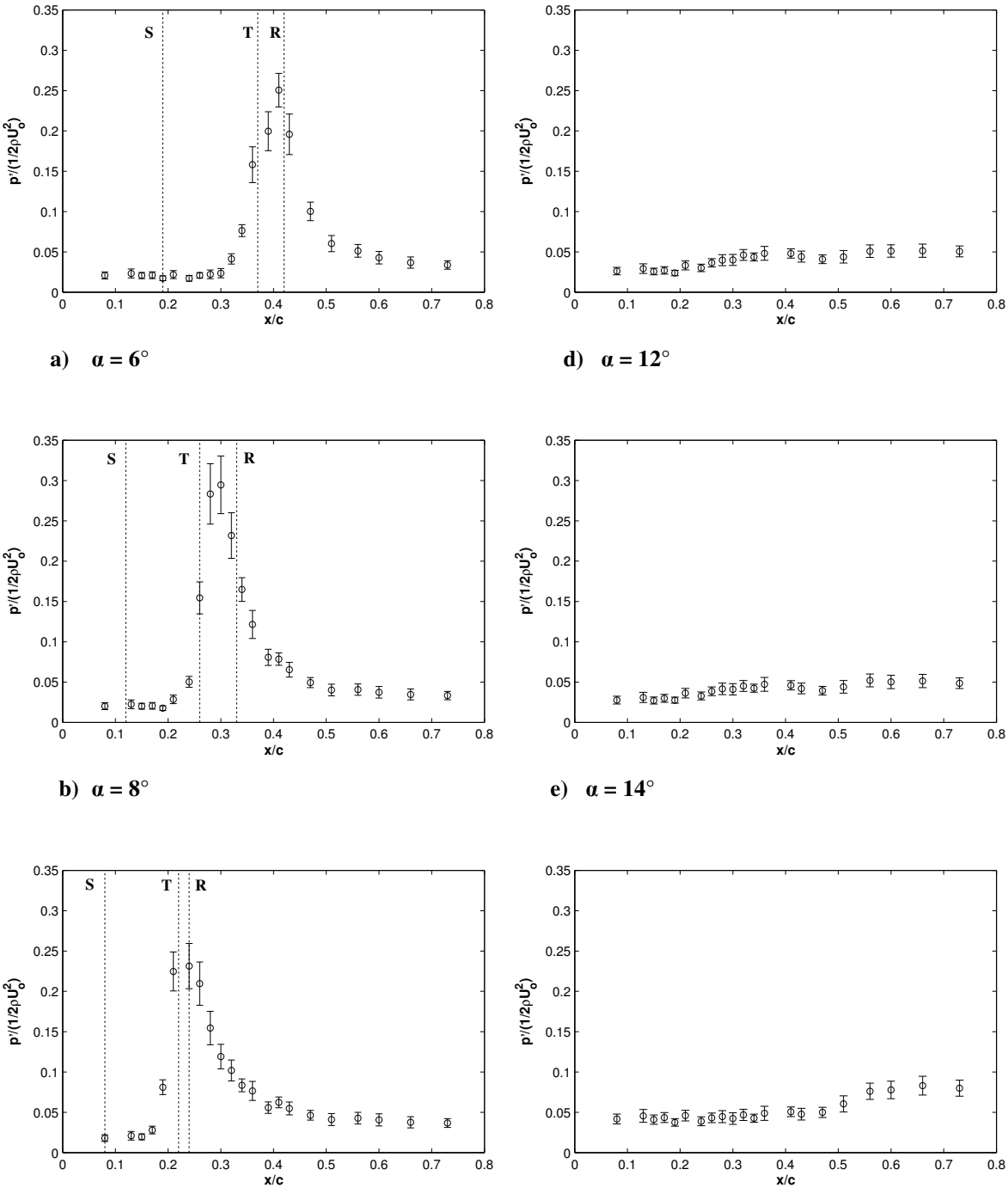

Figure 5.1: Streamwise distributions of RMS surface pressure fluctuations for $Re_c = 100x10^3$.

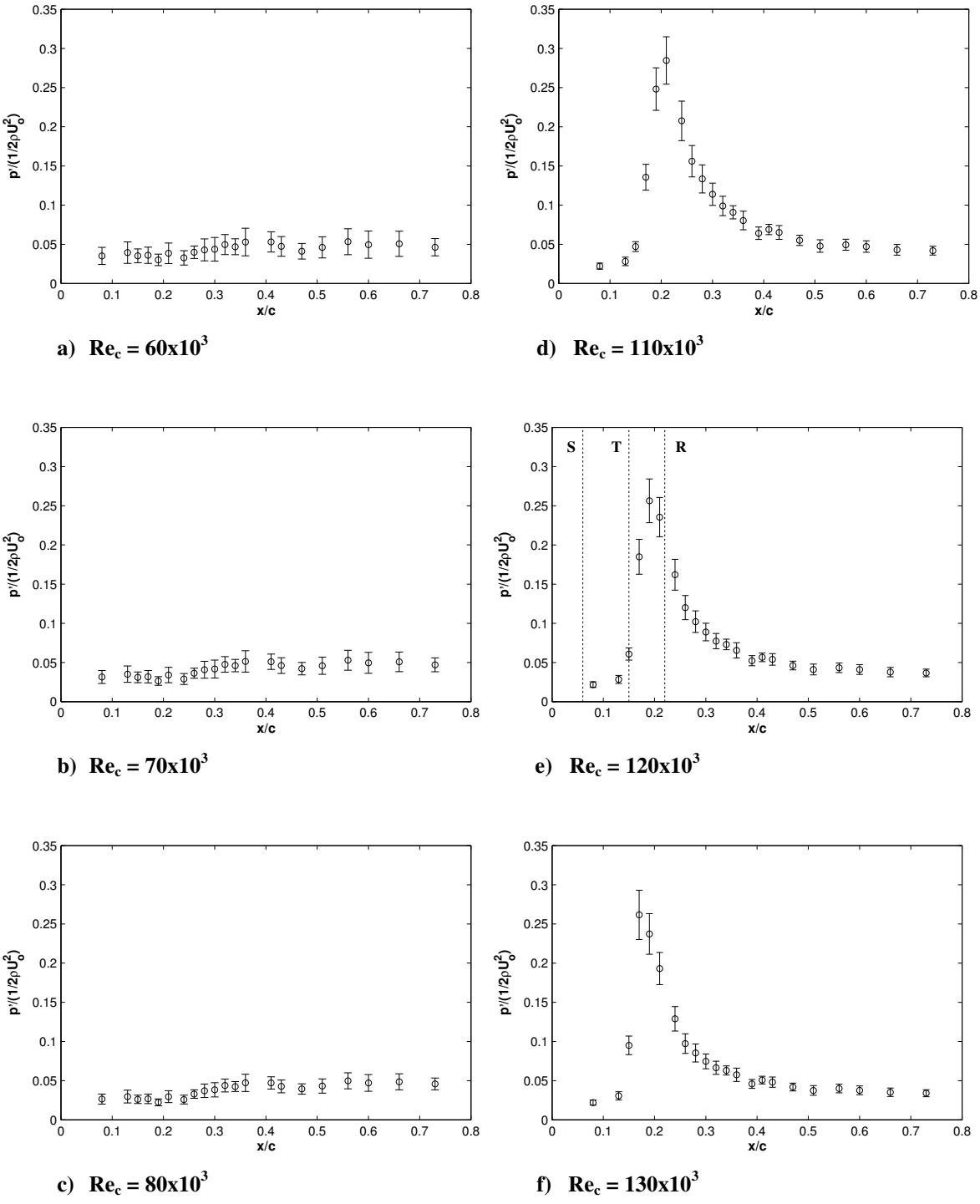

Figure 5.2: Streamwise distributions of RMS surface pressure fluctuations for α = 12°.

When the airfoil is stalled (Figs. 5.1d to 5.1f and Figs. 5.2a to 5.2c), for a given angle of attack and Reynolds number, on the average, the surface pressure fluctuations increase

with an increase in x/c until x/c = 0.56. Beyond this x/c location, variation in the surface pressure fluctuations is marginal. At a given x/c location, variation in the surface pressure fluctuations is marginal for the range of flow parameters investigated.

5.2 Spectra of Fluctuating Surface Pressure and Frequency Scaling

Spectral analysis of pressure measurements acquired from the embedded microphone array was performed in order to gain additional insight into the formation and evolution of coherence structures in the separated shear layer. The results are presented in Fig. 5.3 for $6° \leq \alpha \leq 16°$ at $Re_c = 100x10^3$ and in Fig. 5.4 for $60x10^3 \leq Re_c \leq 130x10^3$ at $\alpha = 12°$. Recall that the analysis of velocity spectra in §0 showed that a similar transition mechanism is attendant in the two flow regimes, i.e., flow separation with and without reattachment. In particular, a band of disturbances with a spectral peak at the fundamental frequency are amplified in the separated shear layer leading to transition.

The pressure spectra associated with flow separation without reattachment pertain to $12° \leq \alpha \leq 16°$ at $Re_c = 100x10^3$ (Figs. 5.3d to 5.3f) and $60x10^3 \leq Re_c \leq 80x10^3$ at $\alpha = 12°$ (Figs. 5.4a to 5.4c). In this flow regime, the initial band of disturbances with a spectral peak at the fundamental frequency amplifies in the streamwise direction followed by the emergence and growth of a band of disturbances with a spectral peak at the subharmonic frequency. The disturbance at the subharmonic frequency eventually dominates as the disturbance at the fundamental frequency decays in the streamwise direction. With further increase in x/c, the subharmonic peak decays and eventually vanishes, leaving a broadband spectrum reminiscent of a velocity spectrum in a turbulent flow. As the angle of attack is increased from 12° to 16° at $Re_c = 100x10^3$, there is a marginal increase in the fundamental

frequency from 560 Hz to 570 Hz. In contrast, as the Reynolds number is increased from $60x10^3$ to $100x10^3$ at $\alpha = 12°$, a more significant increase in the fundamental frequency is observed from 195 Hz to 560 Hz.

The pressure spectra associated with flow separation with reattachment are shown in Figs. 5.3a to 5.3c for $6° \leq \alpha \leq 10°$ at $Re_c = 100x10^3$ and in Figs. 5.4d to 5.4f at $\alpha = 12°$ for $110x10^3 \leq Re_c \leq 130x10^3$. Within this regime, a broader band of disturbances is amplified with a spectral peak at a higher fundamental frequency than that for cases of separation without reattachment. For instance, when $Re_c = 100x10^3$, the fundamental frequency of 1245 Hz at $\alpha = 10°$ (Fig. 5.3c) decreases to 558 Hz when the angle of attack is increased to 12° (Fig. 5.3d), stalling the airfoil.

The results reveal that there are significant changes in the characteristics of coherent structures (i.e., frequency) in the separated shear layer with variation in the Reynolds number and/or angle of attack. The effect of the angle of attack and Reynolds number on the fundamental frequency and the corresponding Strouhal number ($St_0 = f_0 d/U_o$, where d is the projected height of the airfoil on the vertical plane) was examined, and the results are presented in Figs. 5.5 and 5.6. The results suggest that the fundamental frequency and Strouhal number have a power-law dependency on the Reynolds number of the form $f_0 \sim (Re_c)^n$ and $St_0 \sim (Re_c)^{n-1}$ within each flow regime. In both flow regimes, f_0 and St_0 increase with an increase in the Reynolds number or angle of attack. The formation of a separation bubble on the upper surface of the airfoil is associated with a sudden increase in f_0 and St_0. For each plot in Figs. 5.5 and 5.6, a curve fit was applied to the distinct set of data within each flow regime, which is identified by the dashed lines. The equations associated with the

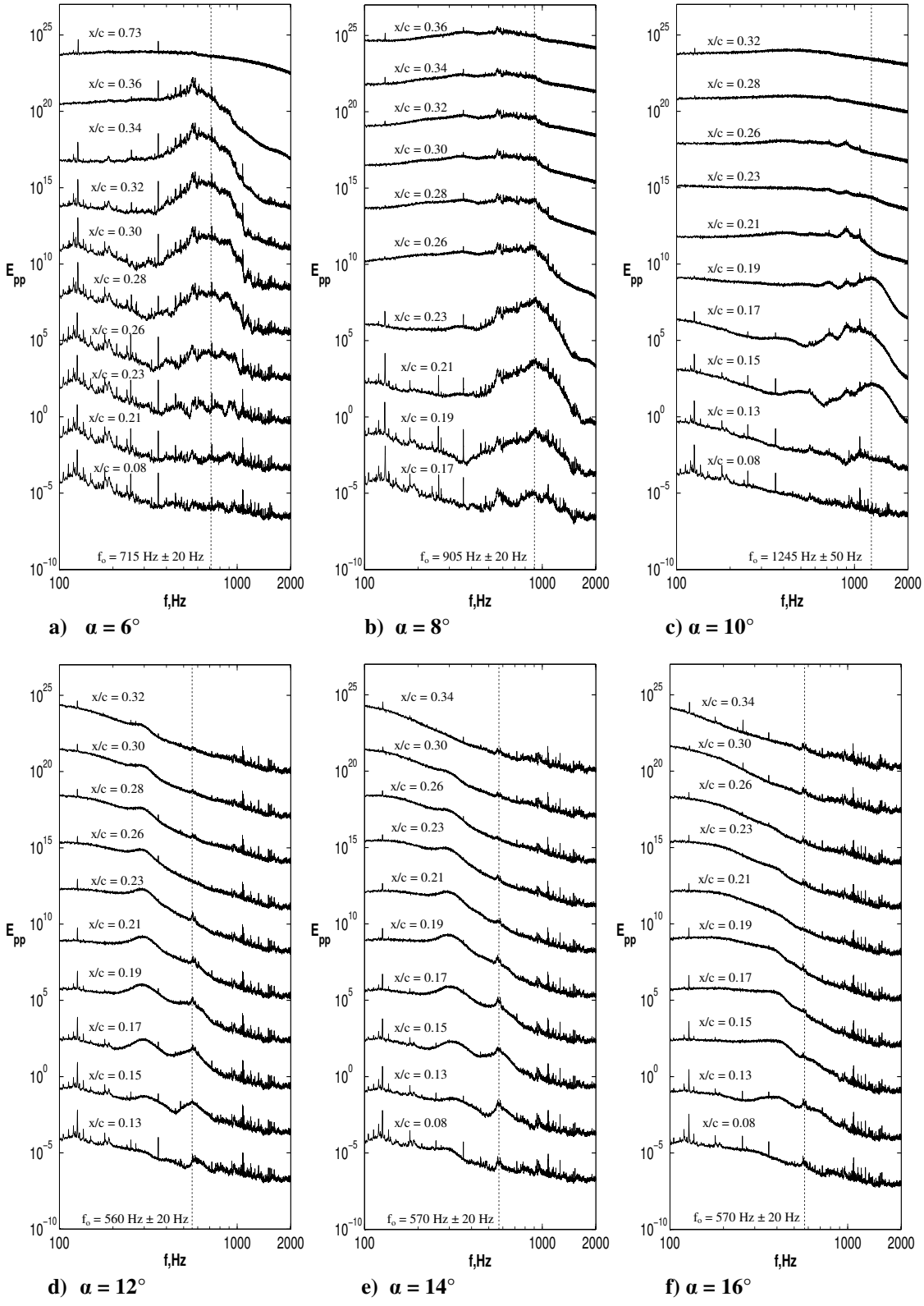

Figure 5.3: Streamwise surface pressure spectra at Re_c = 100x10^3. The amplitude of each successive spectrum is increased by three orders of magnitude.

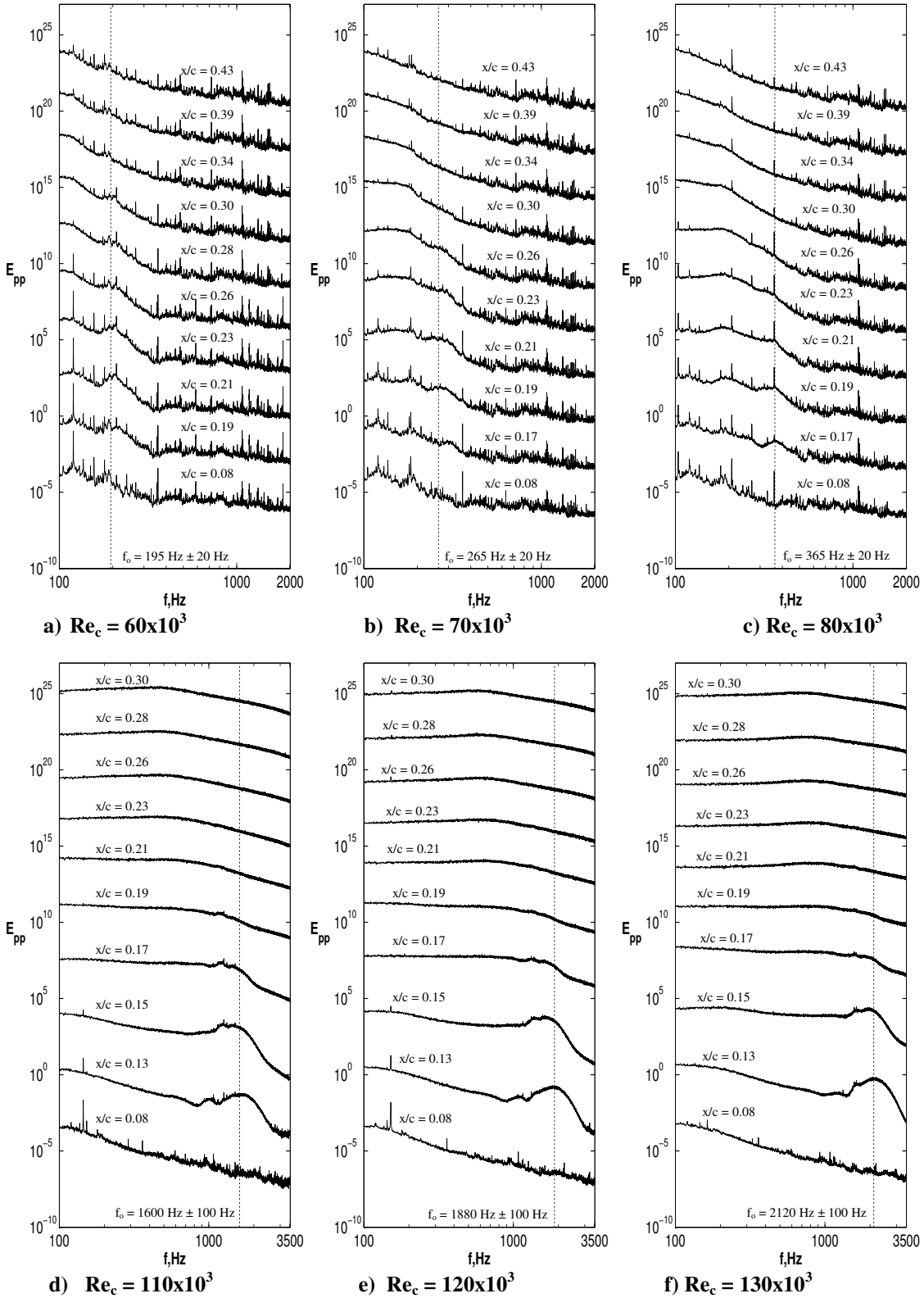

a) $Re_c = 60x10^3$ **b) $Re_c = 70x10^3$** **c) $Re_c = 80x10^3$**

d) $Re_c = 110x10^3$ **e) $Re_c = 120x10^3$** **f) $Re_c = 130x10^3$**

Figure 5.4: Streamwise surface pressure spectra at α = 12°. The amplitude of each successive spectrum is increased by three orders of magnitude.

power-law dependency of f_0 and St_0 on the Reynolds number for both flow regimes are presented in Eqns. 5.1 and 5.2.

$$f_0 = 10^{-7.651}(\mathrm{Re}_c)^{2.08} \qquad \alpha = 12^o,\ 60x10^3 \le \mathrm{Re}_c \le 100x10^3 \qquad (5.1a)$$

$$f_0 = 10^{-5.191}(\mathrm{Re}_c)^{1.67} \qquad \alpha = 12^o,\ 110x10^3 \le \mathrm{Re}_c \le 130x10^3 \qquad (5.1b)$$

$$St_0 = 10^{-4.725}(\mathrm{Re}_c)^{1.06} \qquad \alpha = 12^o,\ 60x10^3 \le \mathrm{Re}_c \le 100x10^3 \qquad (5.2a)$$

$$St_0 = 10^{-2.652}(\mathrm{Re}_c)^{0.72} \qquad \alpha = 12^o,\ 110x10^3 \le \mathrm{Re}_c \le 130x10^3 \qquad (5.2b)$$

Yarusevych et al. (2009) also found a distinct power-law dependency of the fundamental frequency and Strouhal number on the Reynolds number within each flow regime for a NACA 0025 airfoil, their data for $\alpha = 10°$ is shown in Fig. 5.5 for comparison. Yarusevych et al. (2009) also compiled a power-law relationship of the fundamental frequency and Strouhal number dependency on the Reynolds number for the results of LeBlanc et al. (1989), Huang & Lin (1995), and Burgmann & Schröder (2008). The collective results from these studies, including those of Yarusevych et al. (2009), indicates that $0.9 \le n \le 1.9$, which agrees well with the present results of $1.7 \le n \le 2$. It is also observed in Fig. 5.6 that there is a distinct dependency of the fundamental frequency and Strouhal number on the angle of attack within each flow regime. Specifically, within the regime of separation with reattachment, the fundamental frequency increases with an increase in the angle of attack. The fundamental frequency suddenly decreases when the separation bubble bursts at $\alpha = 12°$. Within the stalled regime, there is marginal variation in the fundamental frequency with the angle of attack. In addition, it is apparent that a power-law dependency of

the fundamental frequency and Strouhal number on the angle of attack exists. However, such a dependency is not significant since the angle of attack is not a parameter that directly affects the fundamental frequency.

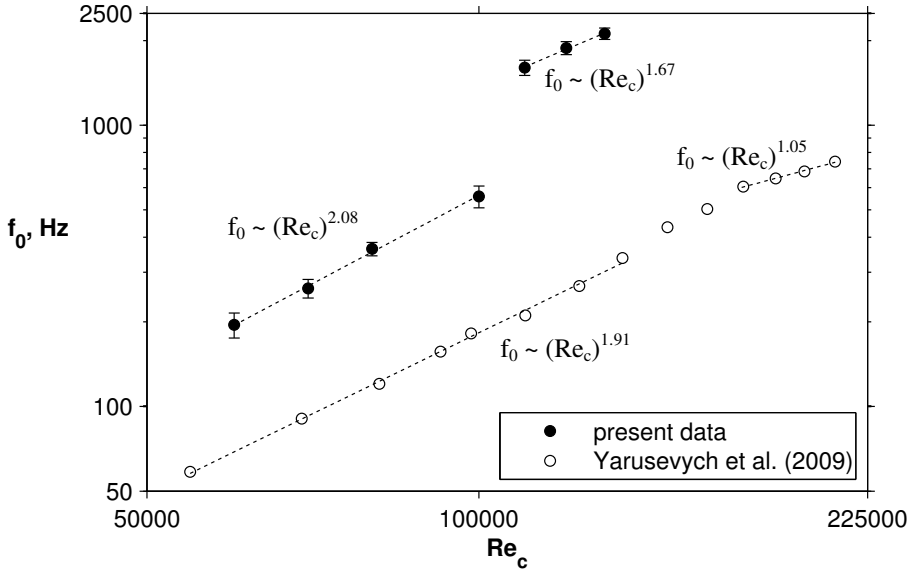

a)

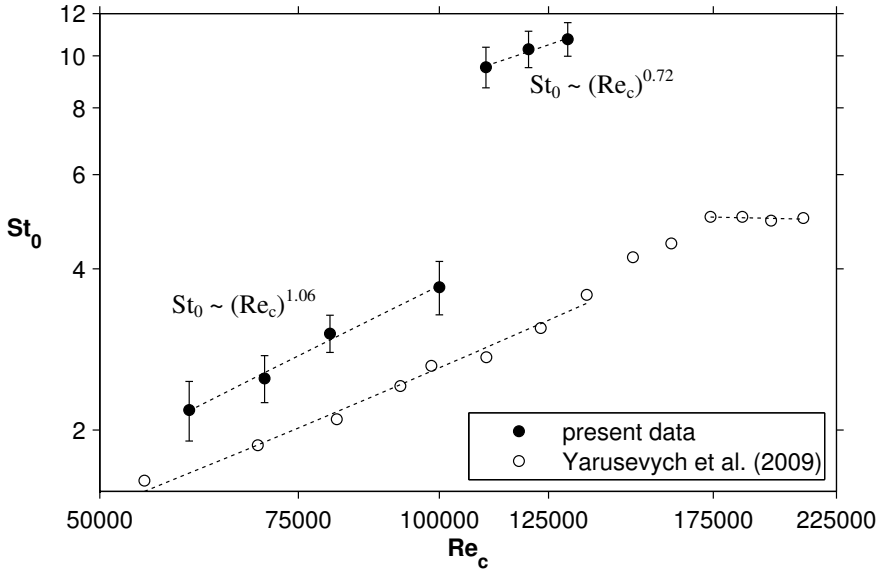

b)

Figure 5.5: Variation of a) the fundamental frequency of the amplified band of disturbances in the separated shear layer and b) the corresponding Strouhal number with the Reynolds number for α = 12°. Note that the data of Yarusevych et al. (2009) pertains to a NACA 0025 at α = 10°.

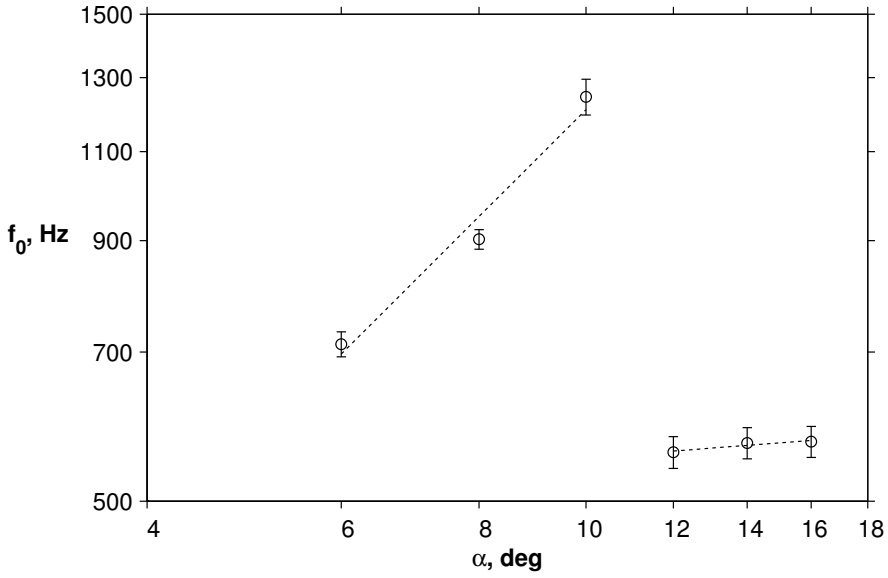

a)

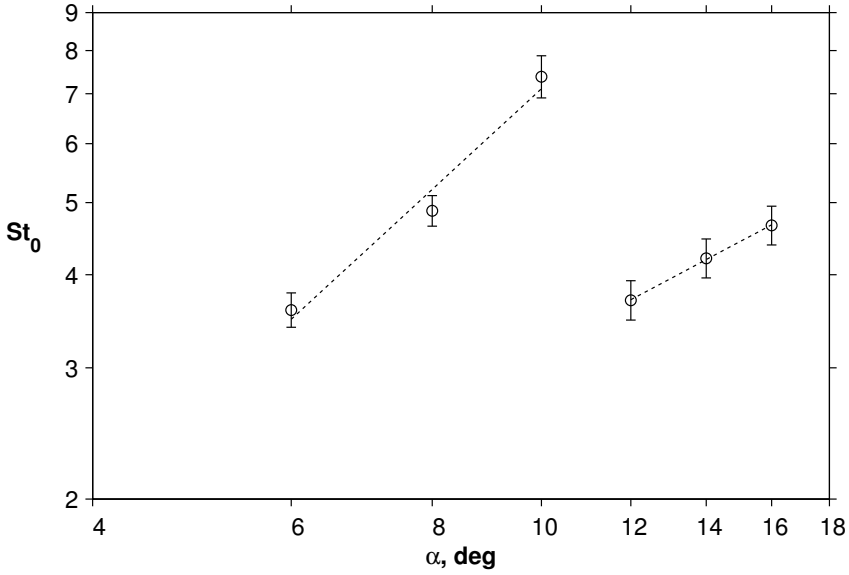

b)

Figure 5.6: Variation of a) the fundamental frequency of the amplified band of disturbances in the separated shear layer and b) the corresponding Strouhal number with the angle of attack for Re_c = $100x10^3$.

5.3 Streamwise Cross-Correlation and Convective Velocity Analysis

Simultaneous pressure measurements were performed using eight microphones from two streamwise rows to characterize the average convective velocity of disturbances in the separated shear layer for $6° \leq \alpha \leq 14°$ and $60x10^3 \leq Re_c \leq 120x10^3$. Cross-correlation analysis was performed on the pressure signals acquired from neighbouring pairs of microphones separated by the same streamwise distance. The streamwise evolution of the cross-correlation coefficient function through the separated flow region is depicted in Fig. 5.7 for $\alpha = 8°$ and $Re_c = 100x10^3$. Downstream of separation (x/c = 0.13), there is no visible oscillations in the cross-correlation coefficient function of the signals measured at x/c = 0.15 and x/c = 0.17 (Fig. 5.7a). Distinct oscillations emerge in the cross-correlation coefficient function further downstream for signals measured at x/c = 0.19 and x/c = 0.21 (Fig. 5.7c) with a period of oscillations corresponding to the fundamental frequency. The oscillations persist further downstream through the separated flow region from x/c = 0.23 to x/c = 0.34, where the latter x/c location coincides with the reattachment location estimated from the mean surface pressure coefficient distribution (Figs. 5.7d to 5.7i). Over the range of x/c locations where distinct oscillations are observed in the cross-correlation coefficient function, propagation of disturbances in the separated shear layer can be characterized by a time-lag τ_i^* associated with pressure signals acquired from neighbouring pairs of microphones. For two neighbouring microphones, microphone 1 and microphone 2, τ_i^* quantifies the time it takes for disturbances to propagate from the x/c location associated with microphone 1 to the x/c location associated with microphone 2. Indeed, $\tau_i^* < 0$ means that disturbances propagate downstream as expected. Accumulating the time-lags between pairs of microphones with increasing x/c, the streamwise distribution of the accumulated time-lag (τ^*) can be obtained, which is shown in Fig. 5.8 for $Re_c = 100x10^3$ at $\alpha = 8°$. For $x/c \geq 0.19$ in Fig. 5.8, τ^*

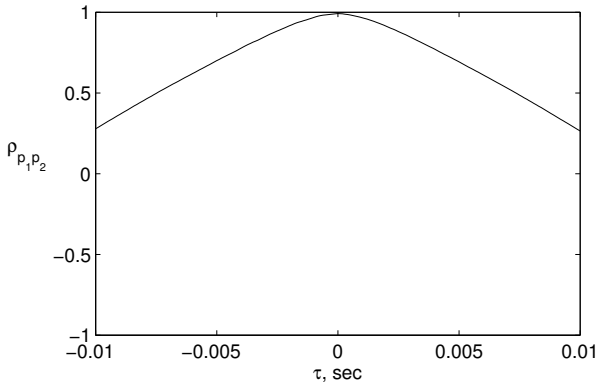

a) x/c = 0.15 & x/c = 0.17

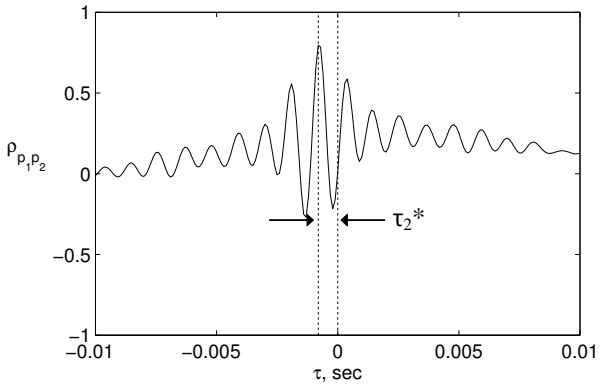

d) x/c = 0.21 & x/c = 0.23

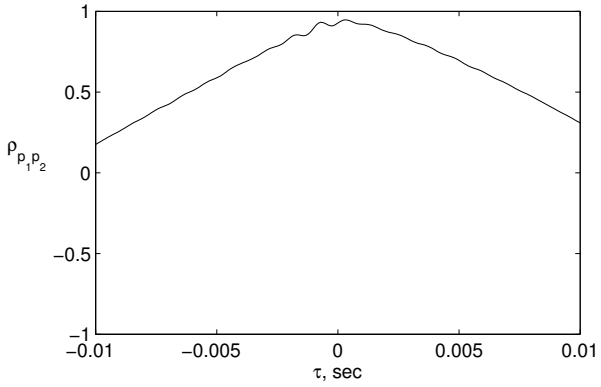

b) x/c = 0.17 & x/c = 0.19

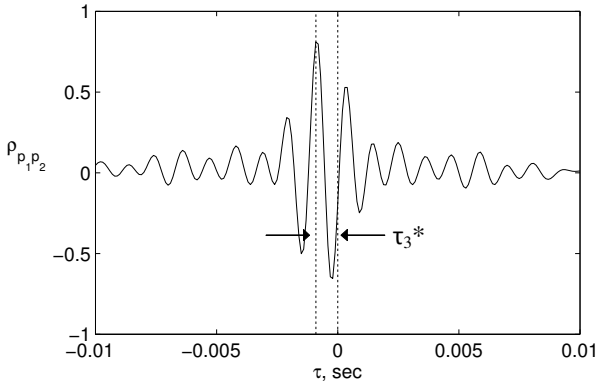

e) x/c = 0.23 & x/c = 0.26

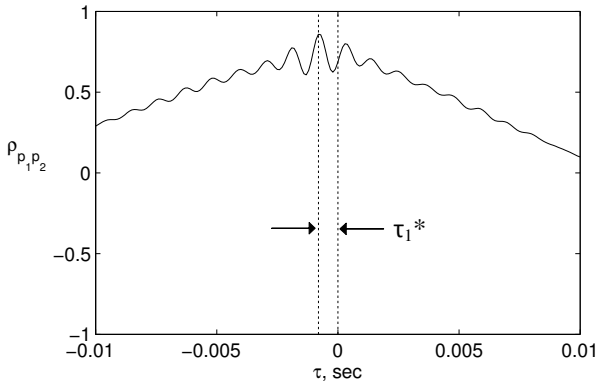

c) x/c = 0.19 & x/c = 0.21

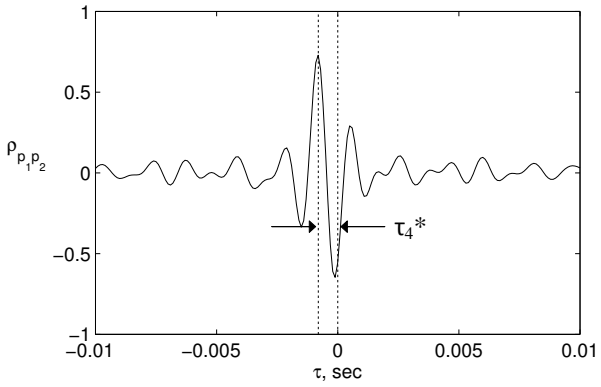

f) x/c = 0.26 & x/c = 0.28

Figure 5.7: Streamwise evolution of the cross-correlation coefficient function between neighbouring pairs of microphones for $Re_c = 100x10^3$ and $\alpha = 8°$.

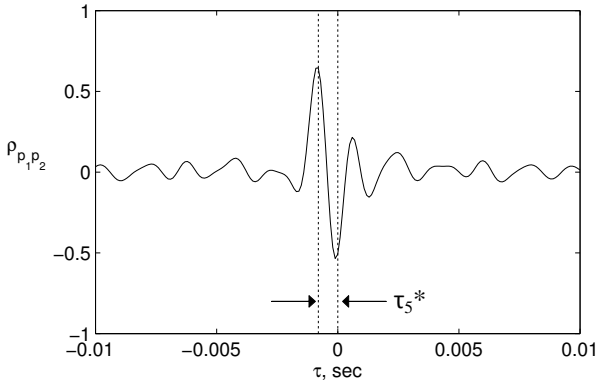

g) x/c = 0.28 & x/c = 0.30

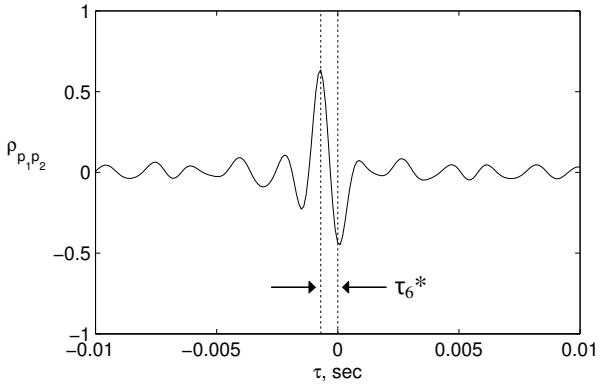

h) x/c = 0.30 & x/c = 0.32

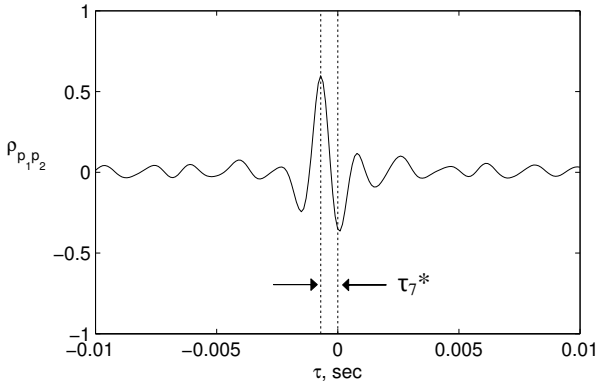

i) x/c = 0.32 & x/c = 0.34

Figure 5.7 (cont'd): see previous page for captions.

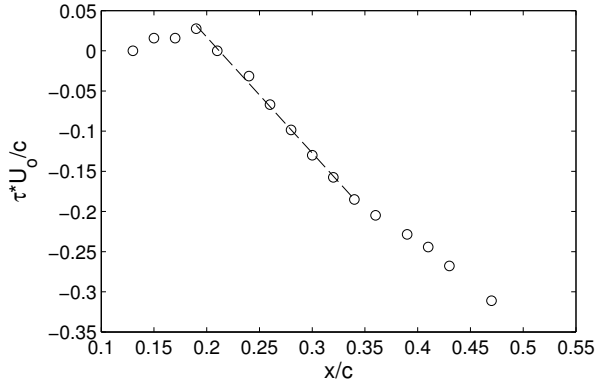

Figure 5.8: Streamwise distribution of the accumulated time-lag τ* at α = 12° for Re_c = 100x10^3. Note that the upstream reference location is x/c = 0.13. Also, the size of the error bars is on the order of the size of the data points, and therefore, the error bars are not included for clarity. The associated uncertainty in the time-lag was estimated to be less than 8%.

decreases linearly with an increase in x/c through the separation bubble until reattachment of the separated shear layer at x/c = 0.34. By applying a least-squares linear fit to the accumulated time-lag data for $0.19 \leq x/c \leq 0.34$ in Fig. 5.8, the convective velocity, U_c, through the separated flow region can be computed using Eqn. 5.3 with knowledge of the slope of the linear least-squares fit of the data ($\Delta\tau^*/\Delta x$).

$$U_c = \frac{1}{\left(\frac{\Delta\tau^*}{\Delta x}\right)} \tag{5.3}$$

The convective velocity represents the average speed of disturbances in the separated shear layer propagating downstream through the separated flow region.

To estimate the convective velocity for all flow parameters, the following approached was used. A maximum of eight microphones were selected with the range of x/c locations where growth of the disturbance is observed in the surface pressure spectra (Figs. 5.3 and 5.4). Within the regime of flow separation with reattachment, the first x/c location ($x/c_{,min}$) for the batch of eight microphones is defined as the location where the magnitude of the spectral peak at the fundamental frequency in the pressure spectrum exceeds the magnitude

of the background noise by a factor greater than approximately 30. Within the flow regime of separation without reattachment, the $x/c_{,min}$ location is defined as the most upstream location where the amplitude of the spectral peak at the subharmonic frequency exceeds that of the amplitude of the spectral peak at the fundamental frequency. For both flow regimes, in cases when the streamwise extent of the region associated with the disturbance growth is less than that covered by the eight microphones, the last x/c location ($x/c_{,max}$) is defined as the location where the dominant spectral peak vanishes. The dominant spectral peak is associated with the fundamental and subharmonic frequencies for the flow regimes of separation with and without reattachment, respectively. It should be noted that the amplitude of a spectral peak was defined as the magnitude of the spectral peak divided by the magnitude of the background noise.

Employing the discussed systematic methodology, the streamwise evolution of τ^* was evaluated for $6° \leq \alpha \leq 14°$ at $Re_c = 100x10^3$ and for $60x10^3 \leq Re_c \leq 120x10^3$ at $\alpha = 12°$, and the results are shown in Figs. 5.9 and 5.10. The results show that τ^* decreases linearly with an increase in x/c within the separated flow region, indicating that, on the average, disturbances within the separated shear layer propagate downstream at a distinct convective velocity U_c. It should be noted that, within the stalled regime for $Re_c < 100x10^3$ at $\alpha = 12°$ (Fig. 5.10), surface pressure fluctuations and the corresponding spectral peaks at the subharmonic and fundamental frequency were weaker relative to the background noise than at higher Reynolds numbers within the corresponding regime (see Figs. 5.3 and 5.4), resulting in fewer τ^* estimates. Once the separated shear layer reattached to the airfoil surface for $Re_c \geq 110x10^3$ (Figs. 5.10e and 5.10f), a short separation bubble formed near the leading-edge, and therefore only a few x/c locations were included in the τ^* versus x/c plots in the range of $0.15 \leq x/c \leq 0.20$.

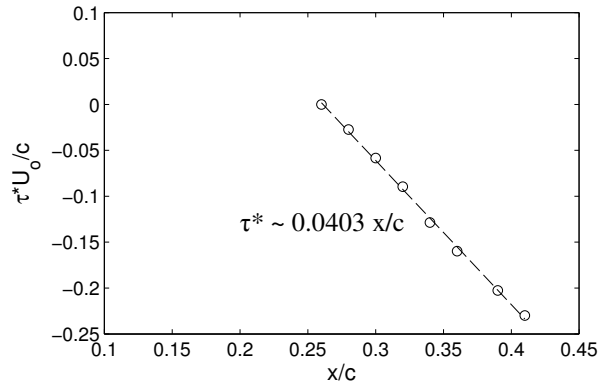

a) α = 6°

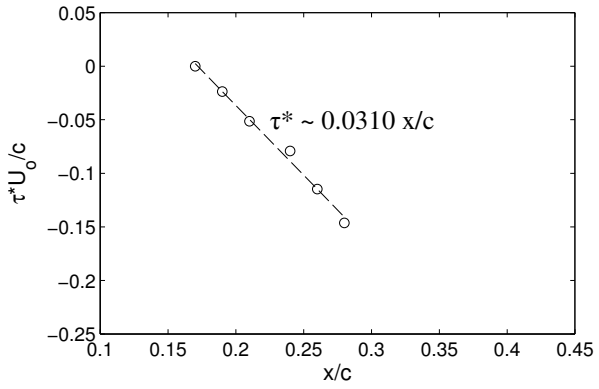

d) α = 12°

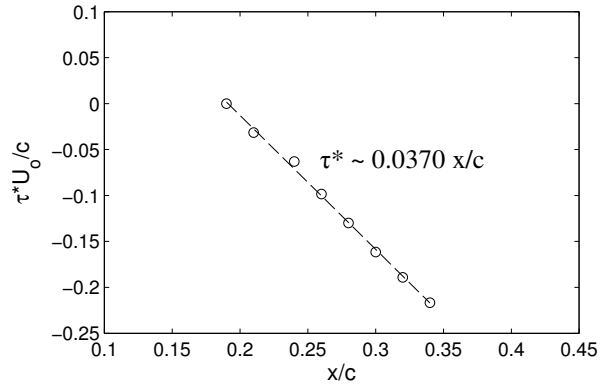

b) α = 8°

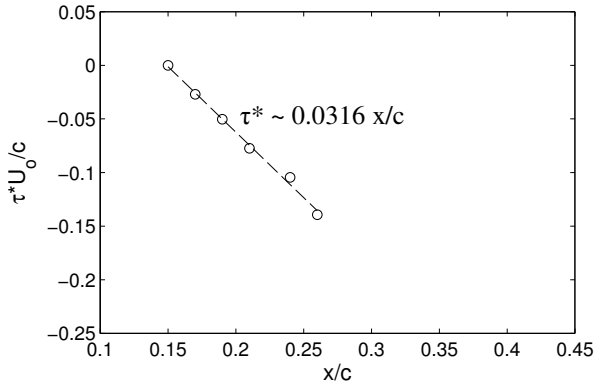

e) α = 14°

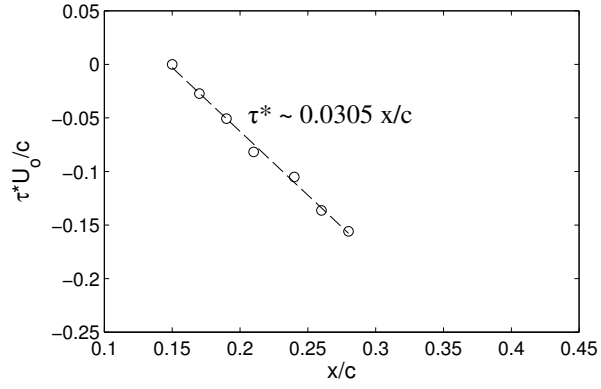

c) α = 10°

Figure 5.9: Streamwise convection velocity plot for $Re_c = 100x10^3$. Note that the size of the error bars is on the order of the size of the data points, and therefore, the error bars are not included for clarity. The associated uncertainty in the time-lag was estimated to be less than 8%.

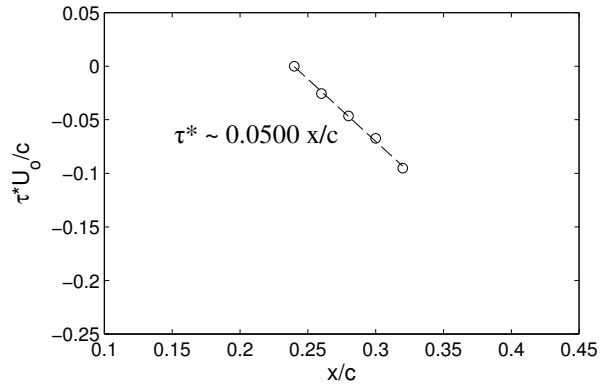

a) $Re_c = 60x10^3$

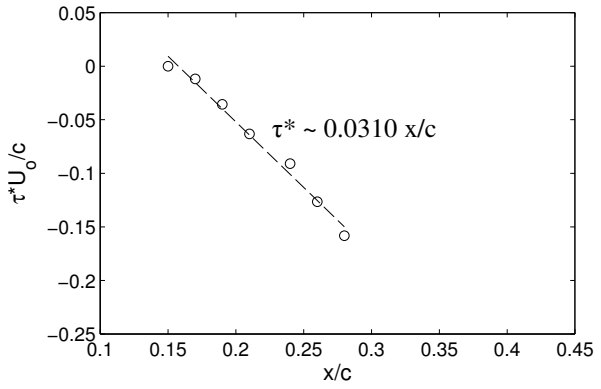

d) $Re_c = 100x10^3$

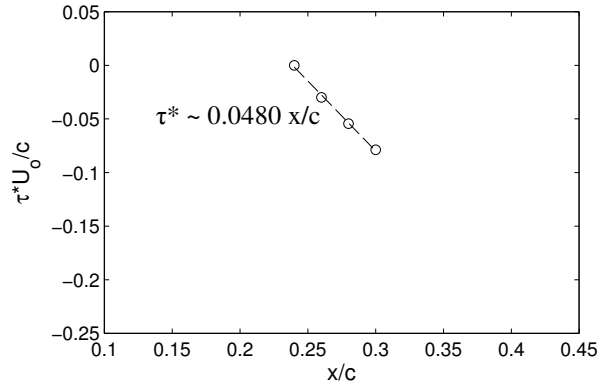

b) $Re_c = 70x10^3$

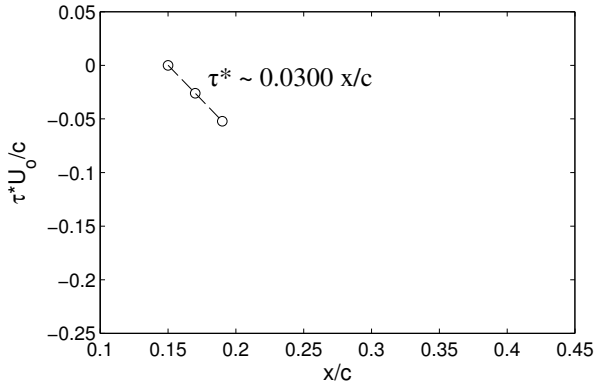

e) $Re_c = 110x10^3$

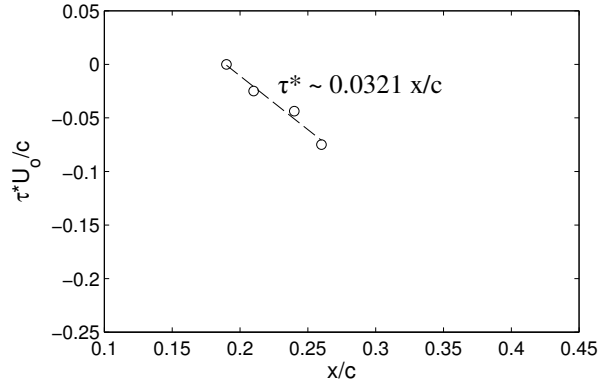

c) $Re_c = 80x10^3$

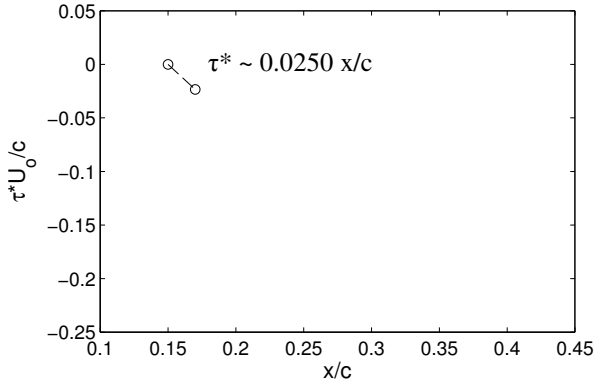

f) $Re_c = 120x10^3$

Figure 5.10: Streamwise convection velocity plot for $\alpha = 12°$. Note that the size of the error bars is on the order of the size of the data points, and therefore, the error bars are not included for clarity. The associated uncertainty in the time-lag was estimated to be less than 8%.

Using data in Figs. 5.9 and 5.10, the convective velocity of disturbances was computed. The variation of the convective velocity with the angle of attack and Reynolds number is shown in Figs. 5.11a and 5.11b, respectively. The convective velocity ranges from $0.64U_o$ to $1.0U_o$ with no apparent dependency on the Reynolds number or angle of attack within each flow regime for the flow parameters investigated. Burgmann & Schröder (2008) estimated a convective velocity of $0.60U_o$ associated with roll-up vortices in the separated shear layer for a separation bubble on the upper surface of an airfoil, which is comparable to the present results. Similarly, from a numerical study, Lin & Pauley (1990) estimated a convective velocity of $0.65U_o$ associated with roll-up vortices shed from a separation bubble generated on a flat plate.

It is expected that the convective velocity of vortices in a free shear layer will be approximately $0.5U_e$, where U_e is the edge velocity (e.g., Dovgal et al., 1994). Since the edge velocity can change substantially with the Reynolds number and/or angle of attack, it is more appropriate to scale the convective velocity by the local edge velocity rather than the free-stream velocity. For $\alpha = 8°$ and $\alpha = 12°$ at $Re_c = 100x10^3$, convective velocities of $0.49U_e$ and $0.69U_e$ were computed based on the average edge velocity from the mean velocity profiles in Figs. 3.13 and 3.14. Upon inspection of the mean and RMS velocity profiles in Figs. 3.13 and 3.14, it is apparent that the U_c/U_e estimates match the mean velocity at the y/c location corresponding to the maximum turbulent intensity (u'_{max}/U_o). Furthermore, $U_c/U_e = 0.49$ matches the expected value for free shear layers ($U_c/U_e = 0.50$) (e.g., Dovgal et al., 1994). Since velocity profiles were not acquired within the separated flow region for all flow parameters investigated, the edge velocity cannot be readily extracted. Since the mean surface pressure is nearly constant in the laminar portion of the separation bubble (see Fig. 3.4), the associated edge velocity would not vary appreciably from that estimated at

separation, U_{es}. The edge velocity at separation can be estimated from the pressure distribution as $U_{es} = U_o\sqrt{1-C_{p,s}}$, where $C_{p,s}$ is the upper-surface mean pressure coefficient at separation. The dependency of the convective velocity scaled by the edge velocity at separation on the angle of attack and Reynolds number is presented in Fig. 5.12. It is apparent from Fig. 5.12a that U_c ranges from $0.42U_{es}$ to $0.64U_{es}$ for $6° \leq \alpha \leq 14°$ at $Re_c = 100x10^3$. For these results, it is apparent that there is a distinct change in the convective velocity depending on the flow regime. Specifically, the convective velocity ranges from approximately $0.40U_{es}$ to $0.45U_{es}$ for $6° \leq \alpha \leq 8°$, corresponding to separation with reattachment, and increases to a range from $0.6U_{es}$ to $0.65U_{es}$ for $\alpha \geq 12°$ when the airfoil is stalled. The most significant change in the convective velocity occurs when there is a change in the flow regime between $10° < \alpha < 12°$. For the range of Reynolds numbers from $80x10^3$ to $120x10^3$ at $\alpha = 12°$ (Fig. 5.12b), the convective velocity is greater for a regime of flow separation without reattachment rather than for a regime of separation with reattachment. These findings are consistent with those found for the range of angles of attack at $Re_c = 100x10^3$ presented in Fig. 5.12a. When the airfoil is stalled for Reynolds numbers of $80x10^3$ and $100x10^3$, the convective velocity decreases from $0.80U_{es}$ to $0.61U_{es}$. Once the separated shear layer reattaches to the airfoil surface for $Re_c = 120x10^3$, the convective velocity further decreases to $0.45U_{es}$. A distinct change in the convective velocity depending on the flow regime was not observed for the range of Reynolds numbers presented in Fig. 5.12b due to insufficient data. Estimates of the convective velocity from experimental results acquired within the separated flow region on other airfoils are also presented in Fig. 5.12b, which range from approximately $0.40U_{es}$ to $0.50U_{es}$. The results obtained from these authors are

comparable to the results in the present study at $Re_c = 100x10^3$ for $6° \leq \alpha \leq 14°$ (Fig. 5.12a) and at $\alpha = 12°$ for $Re_c = 120x10^3$ (Fig. 5.12b).

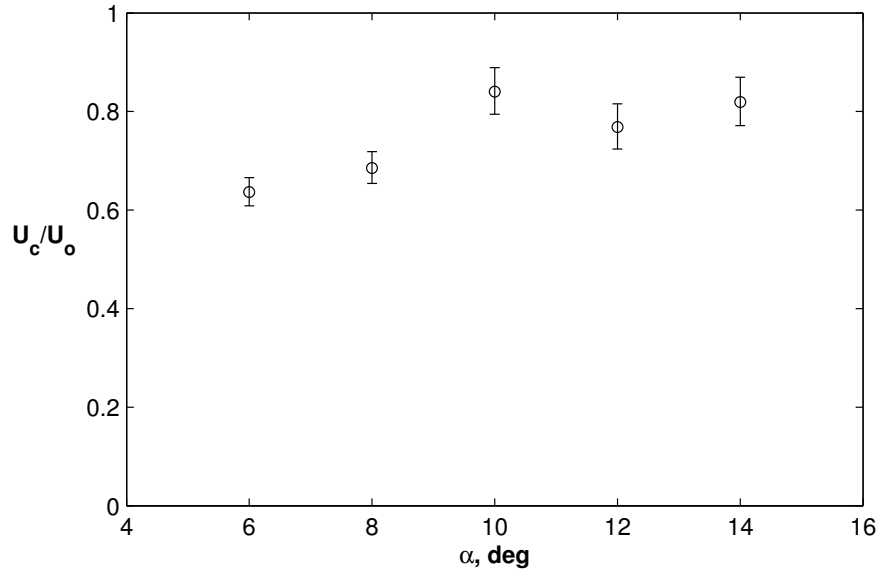

a)

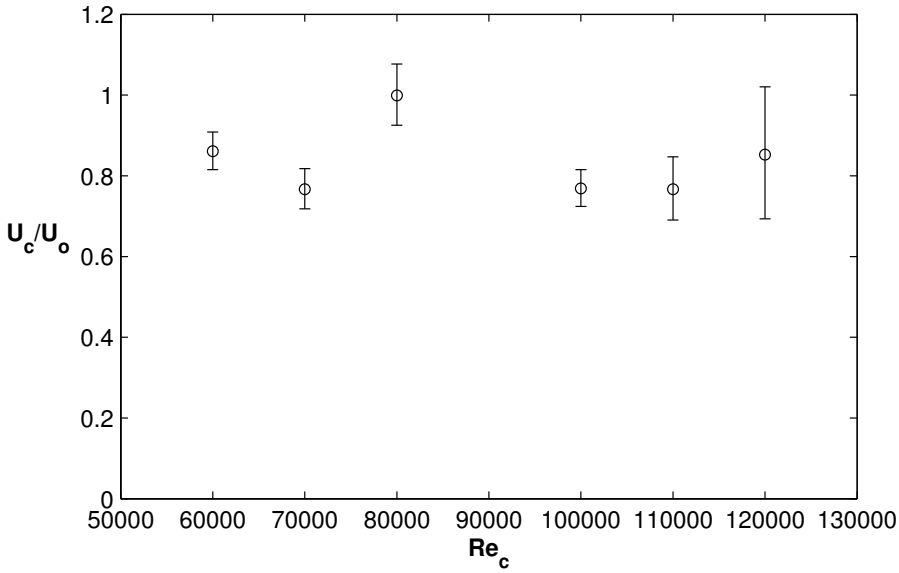

b)

Figure 5.11: Convective velocity plot for a) $Re_c = 100x10^3$ and b) $\alpha = 12°$.

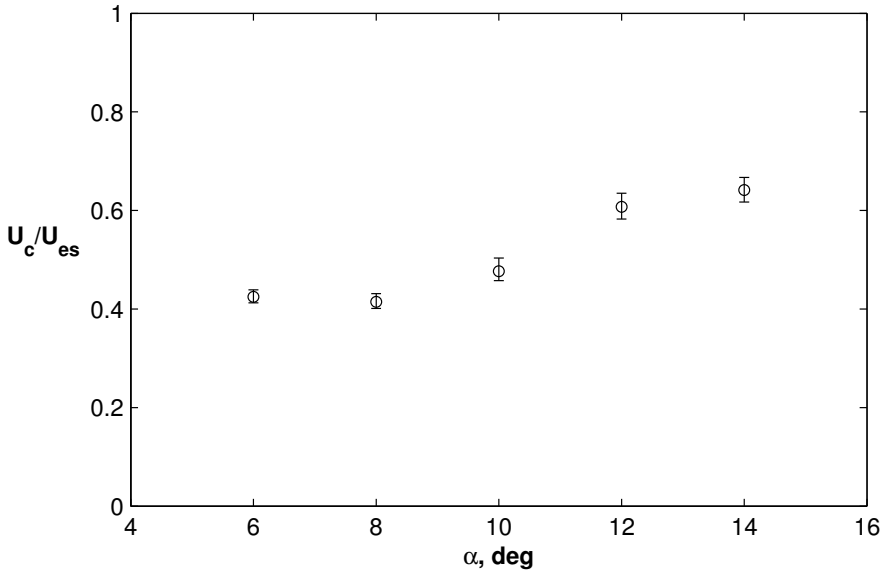

a)

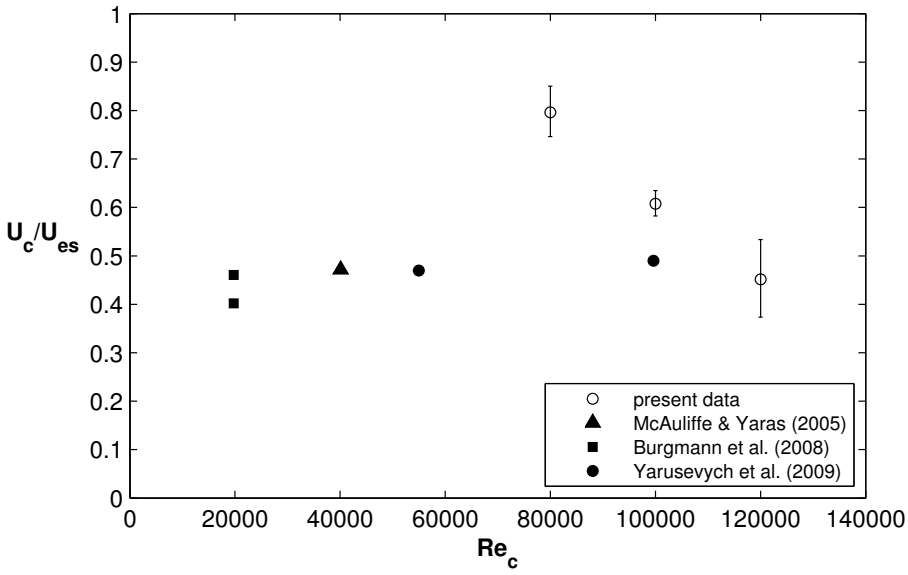

b)

Figure 5.12: Convection velocity plot for a) $Re_c = 100x10^3$ and b) $\alpha = 12°$. Note that the convection velocity is scaled by the edge velocity at separation, U_{es}.

5.4 Spanwise Cross-Correlation and Coherence Analysis

Simultaneous pressure measurements were performed using four microphones from a single spanwise row to characterize the spanwise uniformity of the roll-up and merged roll-up vortices in the separated flow region for $60x10^3 \leq Re_c \leq 130x10^3$ and $6° \leq \alpha \leq 16°$. This range of flow parameters encompasses regimes of flow separation with and without reattachment. Cross-correlation and coherence analysis was performed on the pressure signals from pairs of microphones in the spanwise direction. The arrangement of the microphones in the spanwise direction is shown in Fig. 5.13. Microphones 1 through 4 are located at a streamwise position of x/c = 0.21 and spanwise positions of z/c = 0.20, 0.24, 0.33, and 0.38, respectively, relative to the midspan plane. It should be noted that microphone 1 is also located within the streamwise row of microphones (i.e., full sensor row). By pairing microphone 1 with the remaining three microphones in the spanwise row (i.e., microphones 2 through 4), the cross-correlation and coherence of pressure signals can be explored for increasing spanwise separation distances between the microphones. For the cross-correlation analysis in the spanwise direction, the maximum of the cross-correlation coefficient function was computed for each pair of microphones. The coherence was computed at the frequency associated with the dominant spectral peak in the pressure spectra at the x/c location corresponding to the spanwise row of microphones. For the range of flow parameters investigated, the dominant spectral peak is associated with the fundamental and subharmonic frequencies for regimes of flow separation with and without reattachment, respectively.

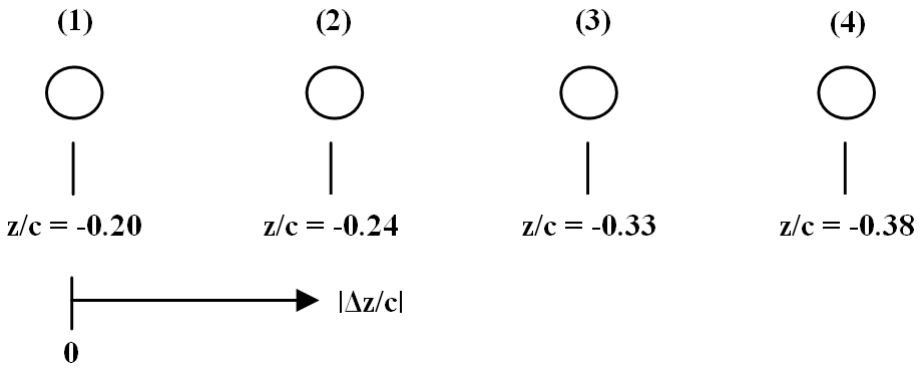

Figure 5.13: Arrangement of microphones in the spanwise direction with associated z/c coordinates.

From spectral analysis of pressure signals performed in the present investigation (See §5.2) and spectral analysis of velocity signals performed by Yarusevych et al. (2009), the streamwise evolution of the roll-up vortices was examined for regimes of flow separation with and without reattachment. For both regimes, it was found that the roll-up vortices breakdown in the streamwise direction through the latter stage of transition, which was evidenced by a decay and eventual vanishing of the spectral peak at the fundamental frequency. In this section of the present investigation, the spanwise cross-correlation and coherence analysis aims to compliment such findings by examining the spanwise evolution of the roll-up and merged roll-up vortices in the streamwise direction. In order to explore the spanwise evolution of the vortices in the streamwise direction, the Reynolds number and/or angle of attack is varied such that the streamwise location of transition in the separated shear layer is changed relative to the x/c location of the spanwise row of microphones. The spanwise cross-correlation and coherence is presented in Fig. 5.14 and Fig. 5.15 for regimes of flow separation with and without reattachment, respectively. In both figures, the streamwise location of the spanwise row of microphones (x) relative to the separation location (x_S) is expressed as $(x-x_S)/c$ for each set of flow parameters. In addition, for each set

of flow parameters corresponding to the regime of flow separation with reattachment, the streamwise location of the spanwise row of microphones is specified as a fraction of the total separation bubble length (L_B).

In the laminar portion of the separation bubble for $Re_c = 100x10^3$ and $6° \leq \alpha \leq 8°$ (Fig. 5.14), the cross-correlation and coherence of pressure signals at the fundamental frequency is uniform across the span at $\alpha = 6°$ with a marginal decrease in spanwise uniformity occurring as the spanwise row of microphones approaches the transition location (i.e., increasing the angle of attack from 6° to 8°). This indicates that the roll-up vortices associated with the fundamental frequency are strongly two-dimensional in the laminar portion of the separation bubble across the airfoil span for $0.2 \leq z/c \leq 0.38$. When the location of transition estimated from the mean surface pressure coefficient distribution coincides with the spanwise row of microphones at $\alpha = 10°$, there is a sudden decrease in the magnitude of the cross-correlation and coherence in the spanwise direction. Downstream of the transition location for $\alpha = 12°$ and $Re_c \geq 110x10^3$, the magnitude of the correlation and coherence decay further relative to that obtained at the transition location. This evidence implies that the two-dimensional roll-up vortices forming in the separated shear layer breakdown to smaller scale structures downstream of transition. These findings are consistent with previous findings from the surface pressure spectra (See §5.2) in the present investigation and the findings of Yarusevych et al. (2009) from velocity spectra, notably, that the roll-up vortices breakdown through the transition process. From analysis of PIV images, Burgmann et al. (2006, 2007) and Burgmann & Schröder (2008) also found that roll-up vortices were initially two-dimensional in the laminar portion of the separation bubble, which broke down to smaller scale structures downstream of the transition process.

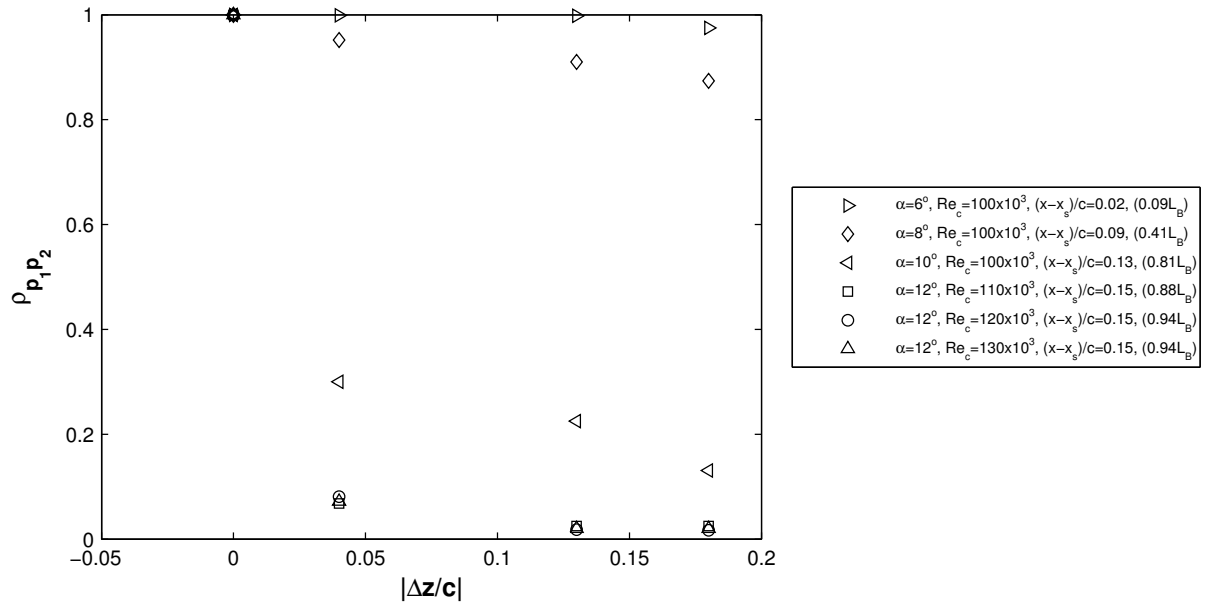

a)

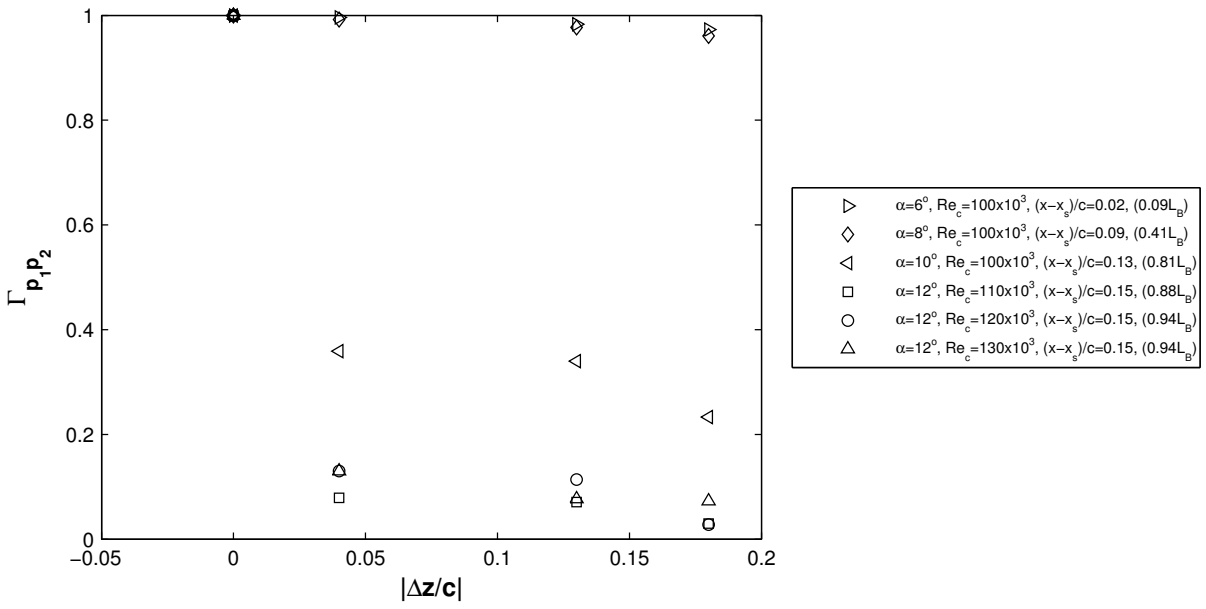

b)

Figure 5.14: Spanwise distribution of a) the maximum of the cross-correlation coefficient function, and b) the coherence function for flow separation with reattachment.

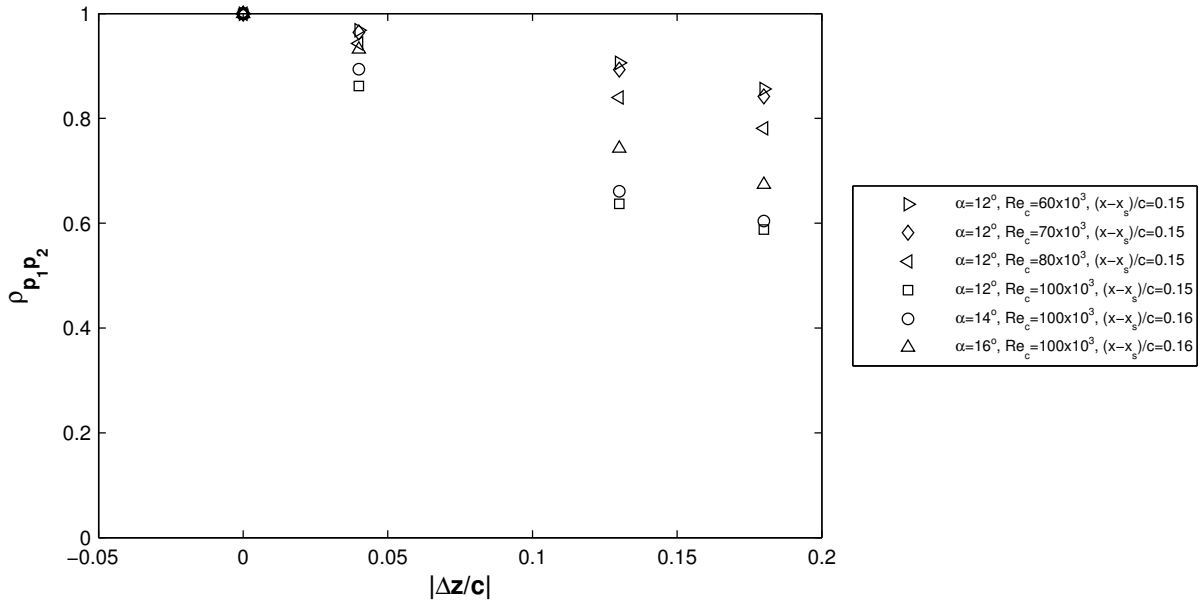

a)

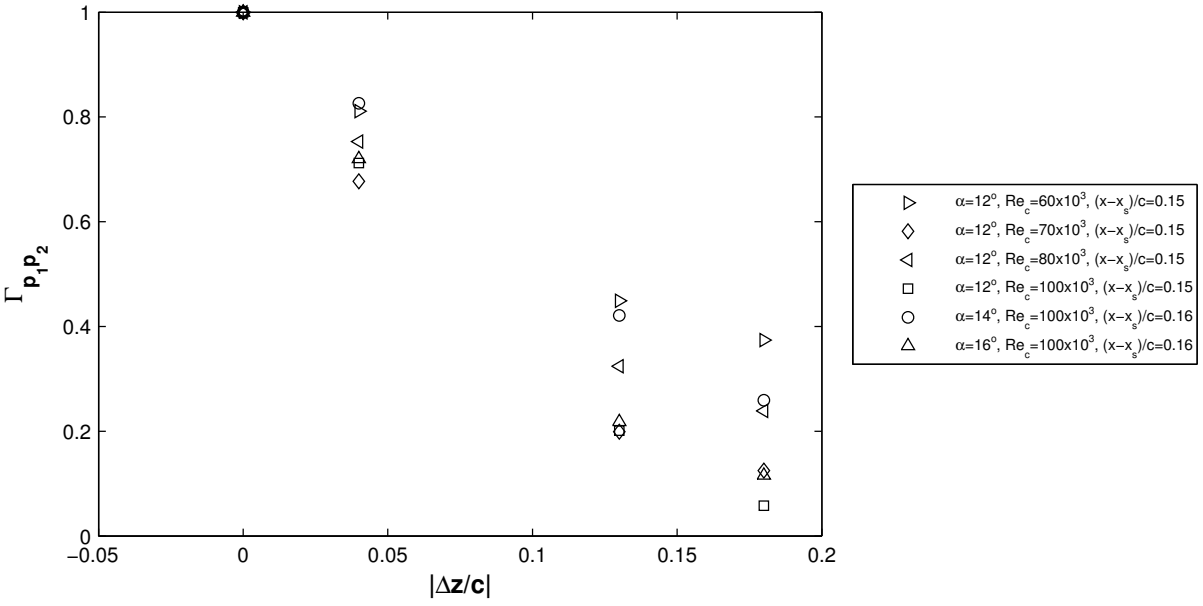

b)

Figure 5.15: Spanwise distribution of a) the maximum of the cross-correlation coefficient function, and b) the coherence function for flow separation without reattachment.

For the regime of flow separation without reattachment, the spanwise evolution of the cross-correlation and coherence through the laminar portion of the separated shear layer is presented in Fig. 5.15 for $\alpha = 12°$ and $60x10^3 \leq Re_c \leq 80x10^3$. The cross-correlation and coherence at the subharmonic frequency are uniform across the span within the laminar portion of the separated shear layer at $Re_c = 60x10^3$ and, on the average, the magnitude of the cross-correlation and coherence decrease in the spanwise direction as the spanwise row of microphones progresses through the transition process (i.e., increasing the Reynolds number from $60x10^3$ to $80x10^3$). For $\alpha = 12°$ and $Re_c = 100x10^3$, there is a greater reduction in the magnitude of the cross-correlation and coherence in the spanwise direction relative to that observed at lower Reynolds numbers. For $Re_c = 100x10^3$ and $\alpha > 12°$, at the x/c location of the spanwise row of microphones, the spectral peak at the subharmonic frequency is decreasing relative to that found at x/c locations further upstream (Fig. 5.3), indicating that the disturbances are in the latter stage of transition. For this range of flow parameters, the magnitude of the spanwise cross-correlation and coherence is comparable to that observed for $\alpha = 12°$ and $Re_c = 100x10^3$. These results indicate that the merged vortices associated with the subharmonic frequency are initially two-dimensional and breakdown to smaller scale turbulent structures through the transition process, which is similar to the streamwise evolution of the roll-up vortices described for the regime of flow separation with reattachment.

6 Concluding Remarks

A symmetric aluminum NACA 0018 airfoil model was constructed with a chord length of 0.2 m and a span of 0.61 m. The model was instrumented with 95 static pressure taps and 25 embedded microphones to enable novel time-resolved surface pressure measurements. The main objective of this investigation is to utilize time-resolved surface pressure measurements to estimate salient flow characteristics in the separated flow region over the upper surface of an airfoil. In order to examine the flow development over the surface of the airfoil in detail, tests were conducted in a wind tunnel using conventional experimental techniques such as hot wire anemometry and mean surface pressure for a range of Reynolds numbers from $80x10^3$ to $200x10^3$ and a range of angles of attack from 0° to 18°. Surface pressure measurements were used to identify the presence and extent of the separated flow region and to compute the lift coefficient. For the range of flow parameters, analysis of mean surface pressure coefficient distributions and velocity profiles revealed that laminar boundary layer separation occurs on the upper surface of the airfoil. In addition, two distinct flow regimes are observed: (i) separation with reattachment, resulting in the formation of a separation bubble, and (ii) separation without reattachment, resulting in an airfoil stall. Within the regime of flow separation with reattachment, for a given Reynolds number, the separation bubble advances toward the leading-edge and the length of the separation bubble decreases with an increase in the angle of attack. As the stall angle of attack is approached, the separation bubble bursts, which causes the suction peak and the lift coefficient to decrease. On the average, with an increase in the Reynolds number for a given angle of attack, the length of the separation bubble decreases and the separation bubble persists at higher angles of attacks so that the stall angle of attack and maximum lift coefficient increases. The results

from the present investigation and those from Timmer (2008) show that a region of conventional linear growth in the lift coefficient with the angle of attack occurs at low angles of attack. The extent of the region of linear growth in the lift coefficient increases with an increase in the Reynolds number. Furthermore, the slope of the lift curve decreases with an increase in the Reynolds number, such that the lift coefficient increases with a decrease in the Reynolds number for $0° \leq \alpha \leq 6°$. Comparing mean surface pressure coefficient distributions and the lift coefficients reveal that the region of conventional linear growth in the lift curve is linked to distinct trends in the rate of advancement of the separation bubble towards the leading-edge with an increase in the angle of attack. Specifically, the linear portion of the lift curve corresponds to a constant rate of advancement in the separation, transition, and reattachment locations towards the leading-edge with increasing angle of attack. Analogous trends were also observed by Lee & Gerontakos (2004) for a NACA 0012 airfoil.

Spectra of streamwise velocity signals acquired in the separated shear layer show that disturbances within a band of frequencies are amplified leading to transition. This band of amplified disturbances is centred at the fundamental frequency. When the separated shear layer fails to reattach to the airfoil surface, the initial growth of disturbances at the fundamental frequency is followed by subharmonic growth. In contrast, when the separated shear layer reattaches to the airfoil surface, subharmonic growth is not clearly identifiable. In both regimes, the energy of amplified disturbances gets distributed over a wide range of frequencies and the disturbance eventually vanishes during the last stages of transition.

In order to validate time-resolved surface pressure measurements, tests were conducted for $Re_c = 100x10^3$ at $\alpha = 8°$ and $\alpha = 12°$, corresponding to regimes of flow separation with and without reattachment, respectively. A comparative analysis of

simultaneous velocity and time-resolved surface pressure measurements showed that the characteristics and evolution of disturbances in the separated shear layer can be obtained from time-resolved surface pressure measurements. Specifically, within the separated flow region, the amplitude of periodic surface pressure fluctuations grows in the streamwise direction and the surface pressure fluctuations become increasingly more disordered through the transition process. From the cross-correlation of velocity and surface pressure signals at the same x/c locations within the separated flow region, it was found that oscillations developed in the cross-correlation coefficient function at a period corresponding to the frequency of the dominant spectral peak. Collectively, these findings substantiate that velocity and surface pressure fluctuations originate from disturbances in the separated shear layer. From spectral analysis, the frequency at the spectral peak associated with amplifying disturbances in the separated shear layer can be identified.

Following the validation tests, time-resolved surface pressure measurement analysis techniques were applied for a Reynolds number range from $60x10^3$ to $130x10^3$ and angles of attack from 6° to 16°. Within the separation bubble, surface pressure fluctuations increase with an increase in x/c and reach a maximum just upstream of the reattachment location estimated from mean surface pressure measurements. The observed trend is in agreement with previous results obtained for separating-reattaching flows on various geometries, such as the forward-facing step (e.g., Mabey, 1972), backward-facing step (e.g., Mabey, 1972; Farabee & Casarella, 1986; Driver et al., 1987; Lee & Sung, 2001), and splitter plate with fence (e.g., Mabey, 1972; Hudy et al., 2003). When the airfoil is stalled, surface pressure fluctuations increase with an increase in x/c, however, in contrast to the case of the separation bubble, no maximum is observed and the amplitude is significantly lower.

Surface pressure spectra were used to estimate the frequency of dominant disturbances in the separated shear layer. The results show that, within each flow regime, the fundamental frequency and Strouhal number exhibit a power-law dependency on the Reynolds number of the form $f_0 \sim (Re_c)^n$ and $St_0 \sim (Re_c)^{n-1}$. For the cases examined, the power-law exponent (n) ranges from 1.7 to 2, which is in agreement with the range reported by Yarusevych et al. (2009) ($0.9 \leq n \leq 1.9$).

Cross-correlation analysis of surface pressure signals was performed in order to determine the average convective velocity of disturbances in the separated shear layer for $6° \leq \alpha \leq 14°$ and $60x10^3 \leq Re_c \leq 120x10^3$. For $Re_c = 100x10^3$ at $\alpha = 8°$ and at $\alpha = 12°$, convective velocities were estimated to be $0.49U_e$ and $0.69U_e$ (where U_e is the edge velocity), respectively. These values approximately match the mean shear layer velocity at the location of maximum turbulence intensity. To investigate a possible variation of the convective velocity with flow regime, tests were conducted for $6° \leq \alpha \leq 14°$ at $Re_c = 100x10^3$. It was found that the convective velocity changed depending on the flow regime. For the separation bubble ($6° \leq \alpha \leq 8°$), the convective velocity ranged from $0.4U_{es}$ to $0.45U_{es}$ and increased to a range from $0.60U_{es}$ to $0.65U_{es}$ when the airfoil was stalled for $\alpha \geq 12°$. The most significant change in the convective velocity occurred when there was a change in the flow regime.

Cross-correlation and coherence analysis of surface pressure signals was performed in the spanwise direction in order to characterize the spanwise evolution of the roll-up and merged roll-up vortices in the streamwise direction. Within the separation bubble, the roll-up vortices associated with the fundamental frequency are two-dimensional across the span (i.e., over the spanwise extent covered by the spanwise row of microphones) in the laminar portion of the separation bubble and become three-dimensional through the transition process. The

evolution of the roll-up vortices through the separation bubble is consistent with that reported by Burgmann & Schröder (2008) based on PIV images. Within the separated flow region when the airfoil was stalled, similar observations were found, notably, that the merged roll-up vortices at the subharmonic frequency are uniform across the span in the laminar portion of the separated shear layer and become three-dimensional through the transition process.

7 Recommendations

Based on the present work, recommendations made in this chapter are aimed at: (i) improving capabilities of the wind tunnel, and (ii) expanding the present results. Since the flow stability degraded at relatively low Reynolds numbers, the lower-limit of the Reynolds number range was restricted for the present investigation. In order to improve the flow stability at relatively low Reynolds numbers, an additional fan can be installed in the diffuser upstream of the existing fan. A fan should be selected that has an operational range suitable for much lower rotational speeds than the existing fan. As a result, high quality measurements could be acquired over a greater range of flow parameters. For experiments conducted at higher speeds, the small fan could be removed without compromising the integrity of the diffuser and/or the existing fan.

Flow visualization experiments would be complementary to the presented results. Smoke wire visualizations could provide insight into the evolution of coherent structures in the separated shear layer. Accordingly, the frequency or convective velocity of these structures could be estimated and compared with the matching parameters from the present study. In addition, visualization of the separated flow region for both regimes could be enhanced by injecting smoke through a smoke port drilled in the airfoil upper surface. Such a technique may provide insight into the velocity of disturbances propagating through the separated shear layer and the proximity of the disturbances to the airfoil surface, which would further compliment the convective velocity analysis.

References

Alam, M., and Sandham, N. D., 2000, "Direct Numerical Simulation of Laminar Separation Bubbles with Turbulent Reattachment," Journal of Fluid Mechanics, Vol. 410, pp. 1-28.

Alam, M. M., Zhou, Y., Yang, H. X., Guo, H., and Mi, J., 2009, "The ultra-low Reynolds number airfoil wake," Experiments in Fluids, Vol. 48, No. 1, pp. 81-103.

Anderson, J. D., 2011, Fundamentals of Aerodynamics, McGraw-Hill, Dubuque.

Barrett, R. V., 2000, "Transition detection for laminar flow aircraft using microphones beneath the surface of laser drilled suction panels," Proceedings of the Institution of Mechanical Engineers, Part G: Journal of Aerospace Engineering, Vol. 214, No. 3, pp. 143-155.

Bishop, M. J., 2010, "Experimental Investigation of the Effect of Wall Adaptation on Flow over a Cylinder in a Modernized Adaptive-Wall Wind Tunnel," University of Waterloo, MASc thesis.

Boiko, A. V., Dovgal, A. V., and Kozlov, V. V., 1989, "Nonlinear interactions between perturbations in transition to turbulence in the zone of laminar boundary-layer separation," Soviet Journal of Applied Physics, Vol. 3, No. 2, pp. 46–52.

Boiko, A., Grek, G., Dovgal, A., and Kozlov, V., 2002, Origin of Turbulence in Near Wall Flows, Springer-Verlag, Berlin.

Brendel, M., and Mueller, T. J., 1988, "Boundary-layer measurements on an airfoil at low Reynolds numbers," Journal of aircraft, Vol. 25, No. 7, pp. 612–617.

Brendel, M., and Mueller, T. J., 1989, "Transition phenomena on airfoils operating at low chord Reynolds numbers in steady and unsteady flow," in Numerical and Physical Aspects of Aerodynamic Flows IV, Springer-Verlag, Berlin, pp. 333-344.

Brooks, T., and Hodgson T., 1981, "Trailing edge noise prediction from measured surface pressures," Journal of Sound and Vibration, Vol. 78, No. 1, pp. 69-117.

Brüel & Kjær, 1996, "Microphone Handbook, Vol. 1: Theory," Brüel & Kjær technical documentation.

Burgmann, S., and Schröder, W., 2008, "Investigation of the vortex induced unsteadiness of a separation bubble via time-resolved and scanning PIV measurements," Experiments in Fluids, Vol. 45, No. 4, pp. 675-691.

Burgmann, S., Brücker, C., and Schröder, W., 2006, "Scanning PIV measurements of a laminar separation bubble," Experiments in Fluids, Vol. 4, No. 2, pp. 319-326.

Burgmann, S., Dannemann, J., and Schröder, W., 2007, "Time-resolved and volumetric PIV measurements of a transitional separation bubble on an SD7003 airfoil," Experiments in Fluids, Vol. 44, No. 4, pp. 609-622.

Carmichael, B. H., 1981, "Low Reynolds number airfoil survey," NASA CR 165803, Vol. I, pp. 1-105.

Castro, I. P., and Haque, A., 1987, "The Structure of a Turbulent Shear Layer Bounding a Separation Region," Journal of Fluid Mechanics, Vol. 179, pp. 439-468.

Chen, J. M., and Fang, Y., 1996, "Strouhal numbers of inclined flat plates," Journal of Wind Engineering and Industrial Aerodynamics, Vol. 61, No. 2-3, pp. 99-112.

Cherry, N. J., Hillier, R., and Latour, M. E. M. P., 1984, "Unsteady Measurements in a Separated and Reattaching Flow," Journal of Fluid Mechanics, Vol. 144, pp. 13-46.

Choudhari, M. M., Lockard, D. P., Macaraeg, M. G., Singer, B. A., Streett, C. L., Neubert, G. R., Stoker, R. W., Underbrink, J. R., Berkman, M. E., Khorrami, M. R., and Sadowski, S., 2002, "Aeroacoustic experiments in the Langley low-turbulence pressure tunnel," NASA TM 2002-211432, pp. 1-46.

Crabtree, L. F., 1959, "The formation of regions of separated flow on wing surfaces," ARC R&M No. 3122, pp. 1-28.

Dovgal, A., Kozlov, V., and Michalke, A., 1994, "Laminar boundary layer separation: Instability and associated phenomena," Progress in Aerospace Sciences, Vol. 30, pp. 61-94.

Drela, M., 1989, “XFOIL- An analysis and design system for low Reynolds number airfoils,” Conference on Low Reynolds Number Aerodynamics, University of Notre Dame, pp. 1–12.

Drela, M., and Giles, M. B., 1987, “Viscous-inviscid analysis of transonic and low Reynolds number airfoils,” AIAA Journal, **Vol. 25**(No. 10), pp. 1347-1355.

Driver, D. M., Seegmiller, H. L., and Marvin, J. G., 1987, “Time-dependent behavior of a reattaching shear layer,” AIAA Journal, Vol. 25, No. 7, pp. 914-919.

Eaton, J. K., and Johnston, J. P., 1981, “A Review of Research on Subsonic Turbulent Flow Reattachment,” AIAA Journal, Vol. 19, No. 9, pp. 1093-1100.

Emmons, H. W., 1951, “The laminar-turbulent transition in a boundary layer-Part I,” Journal of Aeronautical Sciences, Vol. 18, No. 7, pp. 490-498.

Farabee, T. M., and Casarella, M. J., 1986, “Measurements of fluctuating wall pressure for separated/reattached boundary layer flows,” Journal of vibration, acoustics, stress, and reliability in design, Vol. 108, No. 3, pp. 301–307.

Frederiksen, E., 2009, “Microphone Calibration,” Handbook of Signal Processing in Acoustics, pp. 1293–1312.

Gaster, M., 1967, “The structure and behaviour of laminar separation bubbles,” ARC R&M No. 3595, pp. 1-32.

Gerakopulos, R., 2008, “Wind Tunnel Traversing Mechanism Integration and Flow Quality Assessment Report,” University of Waterloo, ME 482 report.

Gerontakos, P., 2008, “Unsteady airfoil flow control via a dynamically deflected trailing-edge flap,” McGill University, PhD thesis.

Gerontakos, P., and Lee, T., 2006, “Dynamic stall flow control via a trailing-edge flap,” AIAA journal, Vol. 44(No. 3), pp. 469–480.

Gerontakos, P., and Lee, T., 2007, “Trailing-Edge Flap Control of Dynamic Pitching Moment,” AIAA Journal, Vol. 45, No. 7, pp. 1688-1694.

Gleyzes, C., Cousteix, J., and Bonnet, J. L., 1985, "Theoretical and Experimental Study of Low Reynolds number Transitional Separation Bubbles," Proc. Conference on Low Reynolds Number Airfoil Aerodynamics, pp. 137-152.

Greenblatt, D., 2005, "Management of Vortices Trailing Flapped Wings via Separation Control," Conf. Proc. of the 43rd AIAA Aerospace Sciences Meeting and Exhibit, pp. 1-22.

Grek, G., Kozlov, V., and Ramazanov, M., 1987, "Laminar-turbulent transition at high free stream turbulence," Novosibirsk: RAS. Sib. Branch Inst. Theoret. Appl. Mech., pp. 8-87.

Häggmark, C. P., Bakchinov, A. A., and Alfredsson, P. H., 2000, "Experiments on a Two-Dimensional Laminar Separation Bubble," Philosophical Transactions: Mathematical, Physical and Engineering Sciences, Vol. 358, No. 1777, pp. 3193-3205.

Ho, C. M., and Huerre, P., 1984, "Perturbed free shear layers," Annual Review of Fluid Mechanics, Vol. 16, No. 1, pp. 365–422.

Hoffmann, J. A., 1991, "Effects of freestream turbulence on the performance characteristics of an airfoil," AIAA Journal, Vol. 29, No. 9, pp. 1353-1354.

Horton, H. P., 1967, "A semi-empirical theory for the growth and bursting of laminar separation bubbles. ARC Conf," ARC CP No. 1073, pp. 1-37.

Horton, H., 1968, "Laminar separation bubbles in two and three dimensional incompressible flow," Queen Mary College, PhD thesis.

Hsiao, F., Liu, C., and Tang, Z., 1989, "Aerodynamic performance and flow structure studies of a low Reynolds number airfoil," AIAA Journal, Vol. 27, No. 2, pp. 129-137.

Huang, L., and Ho, C., 1990, "Small-Scale Transition in a Plane Mixing Layer," Journal of Fluid Mechanics, Vol. 210, pp. 475-500.

Huang, R. F., and Lin, C. L., 1995, "Vortex shedding and shear-layer instability of wing at low-Reynolds numbers," AIAA Journal, Vol. 33, No. 8, pp. 1398-1403.

Hudy, L. M., 2001, "Simultaneous wall-pressure array and PIV measurements in a separating/reattaching flow region," Michigan State University, MASc thesis.

Hudy, L. M., Naguib, A. M., and Humphreys, W. M., 2003, "Wall-pressure-array measurements beneath a separating/reattaching flow region," Physics of Fluids, Vol. 15, No. 3, pp. 706-717.

Hudy, L. M., Naguib, A., and Humphreys, W. M., 2007, "Stochastic estimation of a separated-flow field using wall-pressure-array measurements," Physics of Fluids, Vol. 19, No. 2, pp. 1-18.

Jacobs, E., and Sherman, A., 1939, "Airfoil Section Characteristics as Affected by Variations of the Reynolds Number," NASA TR 586, pp. 1-48.

Jones, B. M., 1933, "An experimental study of the stalling of wings," ARC R&M No. 1588.

Jones, B. M., 1934, "Stalling," Journal of Royal Aeronautical Society, Vol. 38, pp. 753–770.

Jones, L. E., Sandberg, R. D., and Sandham, N. D., 2008, "Direct Numerical Simulations of Forced and Unforced Separation Bubbles on an Airfoil at Incidence," Journal of Fluid Mechanics, Vol. 602, pp. 175-207.

Jones, L. E., Sandberg, R. D., and Sandham, N. D., 2010, "Stability and receptivity characteristics of a laminar separation bubble on an aerofoil," Journal of Fluid Mechanics, Vol. 648, pp. 257.

Kankainen, P., Brundrett, E., and Kaiser, J., "A small wind tunnel significantly improved by a multi-purpose, two-flexible-wall test section," Journal of Fluids Engineering, Vol. 116, No. 3, pp. 419-423.

Kawall, J. G., Shokr, M., and Keffer, J. F., 1983, "A Digital Technique for the Simultaneous Measurement of Streamwise and Lateral Velocities in Turbulent Flows," Journal of Fluid Mechanics, Vol. 133, pp. 83-112.

Kiya, M., and Sasaki, K., 1983, "Structure of a Turbulent Separation Bubble," Journal of Fluid Mechanics, Vol. 137, pp. 83-113.

Kiya, M., Sasaki, K., and Arie, M., 1982, "Discrete-Vortex Simulation of a Turbulent Separation Bubble," Journal of Fluid Mechanics, Vol. 120, pp. 219-244.

Kook, H., 1997, "Prediction and control of the interior pressure fluctuations in a flow-excited Helmholtz resonator," Purdue University, PhD thesis.

Laitone, E. V., 1997, "Wind tunnel tests of wings at Reynolds numbers below 70 000," Experiments in Fluids, Vol. 23, No. 5, pp. 405–409.

Lang, M., Rist, U., and Wagner, S., 2004, "Investigations on controlled transition development in a laminar separation bubble by means of LDA and PIV," Experiments in Fluids, Vol. 36, No. 1, pp. 43-52.

LeBlanc, P., Blackwelder, R., and Liebeck, R., 1989, "A comparison between boundary layer measurements in a laminar separation bubble flow and linear stability theory calculations," Proc. of Low Reynolds Number Aerodynamics Conference, pp. 189–205.

Lee, T., and Basu, S., 1998, "Measurement of unsteady boundary layer developed on an oscillating airfoil using multiple hot-film sensors," Experiments in Fluids, Vol. 25, No. 2, pp. 108–117.

Lee, T., and Gerontakos, P., 2004, "Investigation of Flow Over an Oscillating Airfoil," Journal of Fluid Mechanics, Vol. 512, pp. 313-341.

Lee, I., and Sung, H. J., 2001, "Characteristics of wall pressure fluctuations in separated and reattaching flows over a backward-facing step:," Experiments in Fluids, Vol. 30, No. 3, pp. 262-272.

Lin, J. C. M., and Pauley, L. L., 1996, "Low-Reynolds-number separation on an airfoil," AIAA Journal, Vol. 34, No. 8, pp. 1570-1577.

Mabey, D. G., 1972, "Analysis and correlation of data on pressure fluctuations in separated flow," Journal of Aircraft, Vol. 9, No. 9, pp. 642–645.

Malkiel, E., and Mayle, R. E., 1996, "Transition in a Separation Bubble," Journal of Turbomachinery, Vol. 118, No. 4, pp. 752-759.

Marchman, J. F., 1987, "Aerodynamic testing at low Reynolds numbers," Journal of Aircraft, Vol. 24, No. 2, pp. 107-114.

Marquillie, M., and Ehrenstein, U., 2003, "On the Onset of Nonlinear Oscillations in a Separating Boundary-Layer Flow," Journal of Fluid Mechanics, Vol. 490, pp. 169-188.

Marxen, O., and Rist, U., 2006, "Direct numerical simulation of non-linear transitional stages in an experimentally investigated laminar separation bubble," High Performance Computing in Science and Engineering'05, pp. 103–117.

Marxen, O., and Rist, U., 2010, "Mean flow deformation in a laminar separation bubble: separation and stability characteristics," Journal of Fluid Mechanics, Vol. 660, pp. 37-54.

Marxen, O., Rist, U., and Wagner, S., 2004, "Effect of Spanwise-Modulated Disturbances on Transition in a Separated Boundary Layer," AIAA Journal, Vol. 42, No. 5, pp. 937-944.

McAlister, K. W., and Takahashi, R. K., 1991, "NACA 0015 wing pressure and trailing vortex measurements," NASA TP 3151, pp. 1-142.

McAuliffe, B. R., and Yaras, M. I., 2005, "Separation-bubble-transition measurements on a low-Re airfoil using particle image velocimetry," Proceedings of the ASME Turbo Expo 2005, Reno, NV, GT2005-68663.

McAuliffe, B. R., and Yaras, M. I., 2010, "Transition Mechanisms in Separation Bubbles under Low- and Elevated-Freestream Turbulence," Journal of Turbomachinery, Vol. 132, No. 1, pp. 1-10.

McCroskey, W. J., 1987, "A Critical Assessment of Wind Tunnel Results for the NACA 0012 Airfoil," NASA TM 100019, pp. 1-23.

McCullough, G. B., and Gault, D. E., 1951, "Examples of Three representative types of airfoil section stall at low speeds," NACA TN 2502.

McLeod, N., and Jordan, G., 1958, "Preliminary Flight Survey of Fuselage and Boundary-Layer Sound-Pressure Levels," NACA RM H58B11, pp. 1-25.

McPhee, A., 2009, “The development of a research technique for low speed aeroacoustics,” University of Waterloo, MASc thesis.

Miksad, R. W., 1972, “Experiments on the Nonlinear Stages of Free-Shear-Layer Transition,” Journal of Fluid Mechanics, Vol. 56, No. 4, pp. 695-719.

Mueller, T. J., 1985, “The influence of laminar separation and transition on low Reynolds number airfoil hysteresis,” Journal of Aircraft, Vol. 22, No. 9, pp. 763–770.

Mueller, T. J., 2002, Aeroacoustic measurements, Springer-Verlag, Berlin.

Mueller, T. J., and Batill, S. M., 1982, “Experimental Studies of Separation on a Two-Dimensional Airfoil at Low Reynolds Numbers,” AIAA Journal, Vol. 20, No. 4, pp. 457-463.

Mueller, T. J., and DeLaurier, J. D., 2003, “Aerodynamics of Small Vehicles,” Annual Review of Fluid Mechanics, Vol. 35, pp. 89-111.

Mull, H. R., and Algranti, J. S., 1956, “Preliminary Flight Survey of Aerodynamic Noise on an Airplane Wing,” NACA RM E55K07, pp. 1-8.

Nakano, T., Fujisawa, N., Oguma, Y., Takagi, Y., and Lee, S., 2007, “Experimental study on flow and noise characteristics of NACA0018 airfoil,” Journal of Wind Engineering and Industrial Aerodynamics, Vol. 95, No. 7, pp. 511-531.

Norberg, C., 1986, “Interaction between freestream turbulence and vortex shedding for a single tube in cross-flow,” Journal of Wind Engineering and Industrial Aerodynamics, Vol. 23, pp. 501-514.

Norberg, C., 2003, “Fluctuating lift on a circular cylinder: review and new measurements,” Journal of Fluids and Structures, Vol. 17, No. 1, pp. 57-96.

Norberg, C., and Sundén, B., 1987, “Turbulence and reynolds number effects on the flow and fluid forces on a single cylinder in cross flow,” Journal of Fluids and Structures, Vol. 1, No. 3, pp. 337-357.

Ol, M. V., McAuliffe, B. R., Hanff, E. S., Scholz, U., and Kähler, C., 2005, "Comparison of Laminar Separation Bubble Measurements on a Low Reynolds Number Airfoil in Three Facilities," 35th AIAA Fluid Dynamics Conference and Exhibit, AIAA 2005-5149, Toronto, Ontario, pp. 1-11.

O'Meara, M. M., and Mueller, T. J., 1987, "Laminar separation bubble characteristics on an airfoil at low Reynolds numbers," AIAA Journal, Vol. 25, No. 8, pp. 1033-1041.

Paterson, R. W., Vogt, P. G., Fink, M. R., and Munch, C. L., 1973, "Vortex noise of isolated airfoils," Journal of Aircraft, Vol. 10, No. 5, pp. 296–302.

Pauley, L. L., Moin, P., and Reynolds, W. C., 1990, "The Structure of Two-Dimensional Separation," Journal of Fluid Mechanics, Vol. 220, pp. 397-411.

Raghunathan, S., and Ombaka, O., 1986, "A thick symmetrical aerofoil oscillating about zero incidence angle," International Journal of Heat and Fluid Flow, Vol. 7, No. 2, pp. 155-159.

Rist, U., and Maucher, U., 1994, "Direct numerical simulation of 2-D and 3-D instability waves in a laminar separation bubble," Proc. Conf. Application of Direct and Large Eddy Simulation to Transition and turbulence, AGARD Cp-551,, pp. 34.1-34.7.

Rist, U., and Maucher, U., 2002, "Investigations of time-growing instabilities in laminar separation bubbles," European Journal of Mechanics - B/Fluids, Vol. 21, Vol. 5, pp. 495-509.

Roberts, W. B., 1980, "Calculation of Laminar Separation Bubbles and Their Effect on Airfoil Performance," AIAA Journal, Vol. 18, No. 1, pp. 25-31.

Sarohia, V., 1975, "Experimental and analytical investigation of oscillations in flows over cavities," California Institute of Technology, PhD thesis.

Schlichting, H., and Gersten, K., 2000, Boundary-layer theory, Springer-Verlag, Berlin.

Schubauer, G. B., and Skramstad, H. K., 1948, "Laminar-Boundary-Layer Oscillations and Transition on a Flat Plate," NASA TN 909, pp. 1-36.

Selig, M. S., and McGranahan, B. D., 2004, "Wind Tunnel Aerodynamic Tests of Six Airfoils for Use on Small Wind Turbines," Journal of Solar Energy Engineering, Vol. 126, No. 4, pp. 986-1001.

Sheldahl, R. E., and Klimas, P. C., 1981, "Aerodynamic characteristics of seven symmetrical airfoil sections through 180-degree angle of attack for use in aerodynamic analysis of vertical axis wind turbines," Sandia National Laboratories SAND80-2114, pp. 1-118.

Spalart, P. R., and Strelets, M. K., 2000, "Mechanisms of Transition and Heat Transfer in a Separation Bubble," Journal of Fluid Mechanics, Vol. 403, pp. 329-349.

Swalwell, K. E., Sheridan, J., and Melbourne, W. H., 2003, "Frequency analysis of surface pressures on an airfoil after stall," 21st AIAA Applied Aerodynamics Conference, AIAA-2003-3416, Washington, DC.

Tangler, J. L., and Somers, D. M., 1995, "NREL airfoil families for HAWTs," American Wind Energy Association WindPower '95 Conference, Washington, DC, pp. 1-12.

Tani, I., 1964, "Low-speed flows involving bubble separations," Progress in Aerospace Sciences, Vol. 5, pp. 70–103.

Timmer, W. A., 2008, "Two-dimensional low-Reynolds number wind tunnel results for airfoil NACA 0018," Wind engineering, Vol. 32, No. 6, pp. 525–537.

van Ingen, J. L., 1965, "Theoretical and experimental investigations of incompressible laminar boundary layers with and without suction," Delft University of Technology Rept. VTH-124.

Vorobiev, A., Rennie, R., and Jumper, E., 2010, "Lift Enhancement by Plasma Actuators at Low Reynolds Numbers," AIAA 5th Flow Control Conference, AIAA 2010-4836, Chicago, Illinois, pp. 1-12.

Watmuff, J. H., 1999, "Evolution of a Wave Packet into Vortex Loops in a Laminar Separation Bubble," Journal of Fluid Mechanics, Vol. 397, pp. 119-169.

Weibust, E., Bertelrud, A., and Ridder, S. O., 1987, "Experimental investigation of laminar separation bubbles and comparison with theory," Journal of Aircraft, Vol. 24, No. 5, pp. 291-297.

Wheeler, A. J., and Ganji, A. R., 2004, Introduction to Engineering Experimentation, Pearson Higher Education, New Jersey.

Williamson, C. H. K., 1996, "Vortex Dynamics in the Cylinder Wake," Annual Review of Fluid Mechanics, Vol. 28, pp. 477-539.

Willmarth, W. W., 1956, "Wall Pressure Fluctuations in a Turbulent Boundary Layer," The Journal of the Acoustical Society of America, Vol. 28, No. 6, pp. 1048-1053.

Willmarth, W., 1958 "Space-time corerlations of the fluctuating wall pressure in a turbulent boundary layer," Journal of Aerospace Science, Vol. 25, No. 5, pp. 335-337.

Willmarth, W. W., and Wooldridge, C. E., 1962, "Measurements of the Fluctuating Pressure at the Wall Beneath a Thick Turbulent Boundary Layer," Journal of Fluid Mechanics, Vol. 14, No. 2, pp. 187-210.

Wilson, P. G., and Pauley, L. L., 1998, "Two- and three-dimensional large-eddy simulations of a transitional separation bubble," Physics of Fluids, Vol. 10, No. 11, pp. 2932-2940.

Yarusevych, S., Sullivan, P. E., and Kawall, J. G., 2006, "Coherent structures in an airfoil boundary layer and wake at low Reynolds numbers," Physics of Fluids, Vol. 18, No. 4 (044101), pp. 1-11.

Yarusevych, S., Kawall, J. G., and Sullivan, P. E., 2008, "Unsteady Separated Flow Characterization on Airfoils Using Time-Resolved Surface Pressure Measurements," AIAA Journal, Vol. 46, No. 2, pp. 508-516.

Yarusevych, S., Sullivan, P. E., and Kawall, J. G., 2009, "On Vortex Shedding from an Airfoil in Low-Reynolds-Number Flows," Journal of Fluid Mechanics, Vol. 632, pp. 245-271.

Zdravkovich, M. M., 1997, Flow around Circular Cylinders Volume 1: Fundamentals, Oxford University Press, New York.

Zhang, W., Hain, R., and Kähler, C. J., 2008, "Scanning PIV investigation of the laminar separation bubble on a SD7003 airfoil," Experiments in Fluids, Vol. 45, No. 4, pp. 725-743.

Appendix A: Airfoil Model

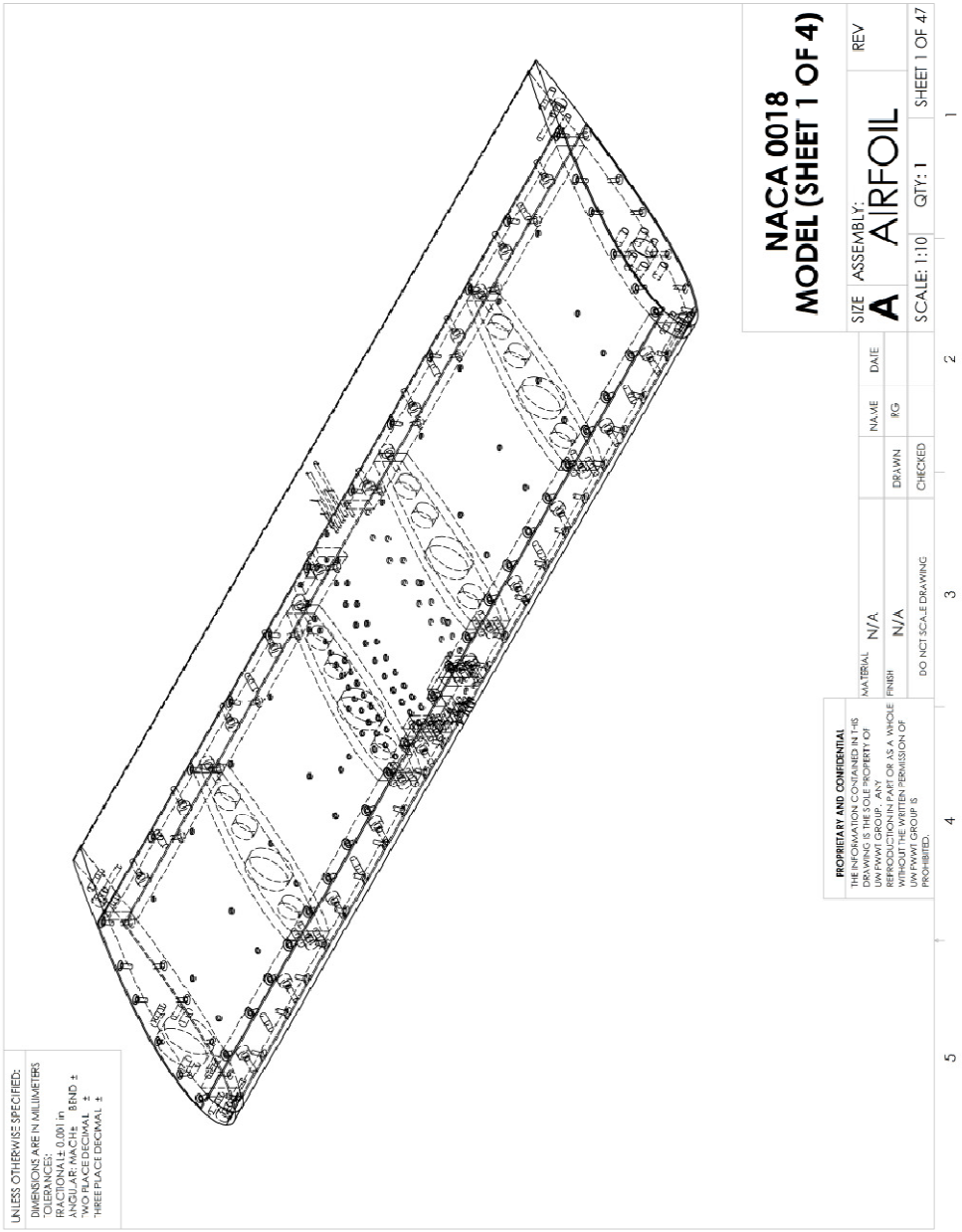

Figure A.1: Isometric view of airfoil model.

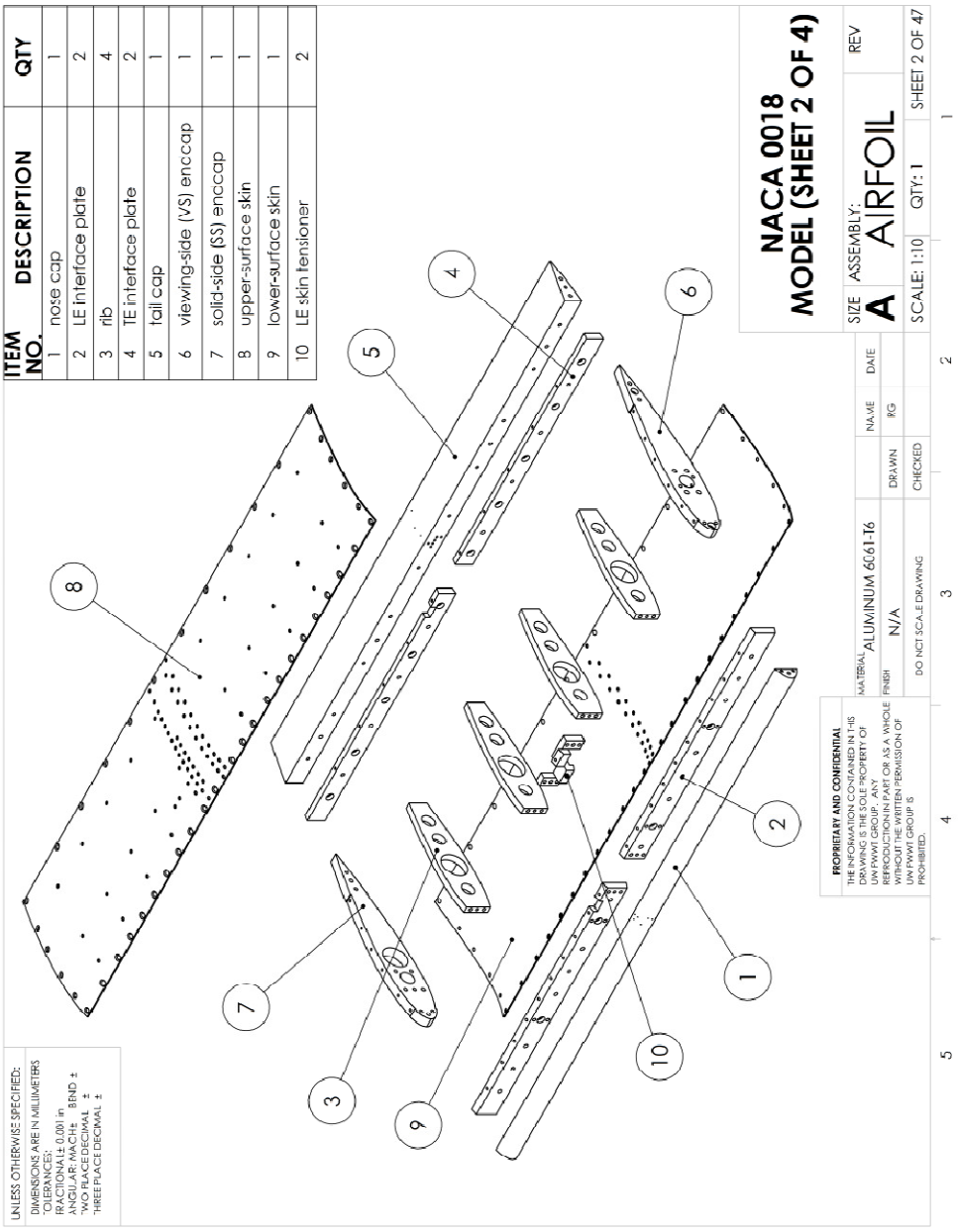

Figure A.2: Exploded view of airfoil model.

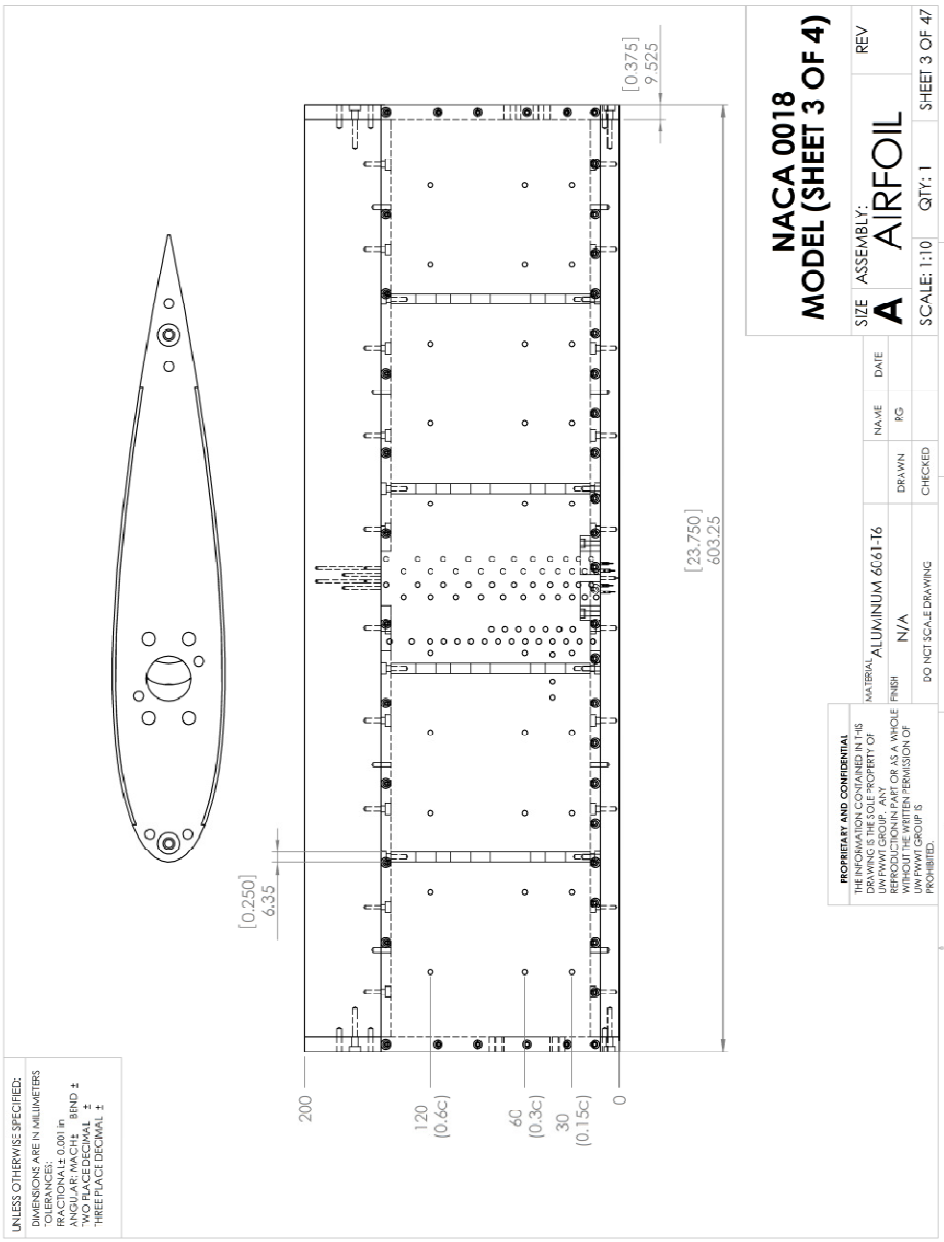

Figure A.3: Top view of airfoil model.

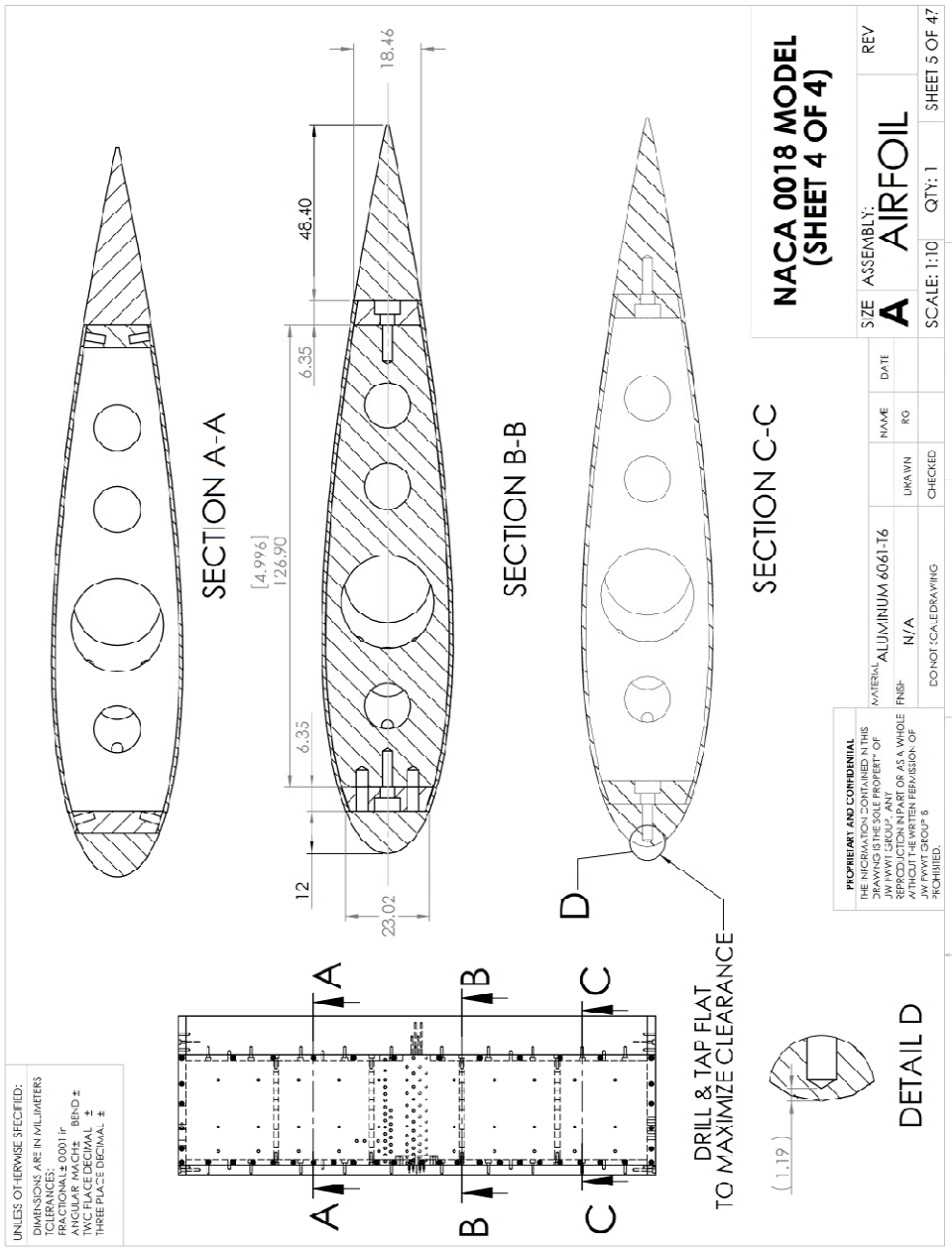

Figure A.4: sectional views of airfoil model.

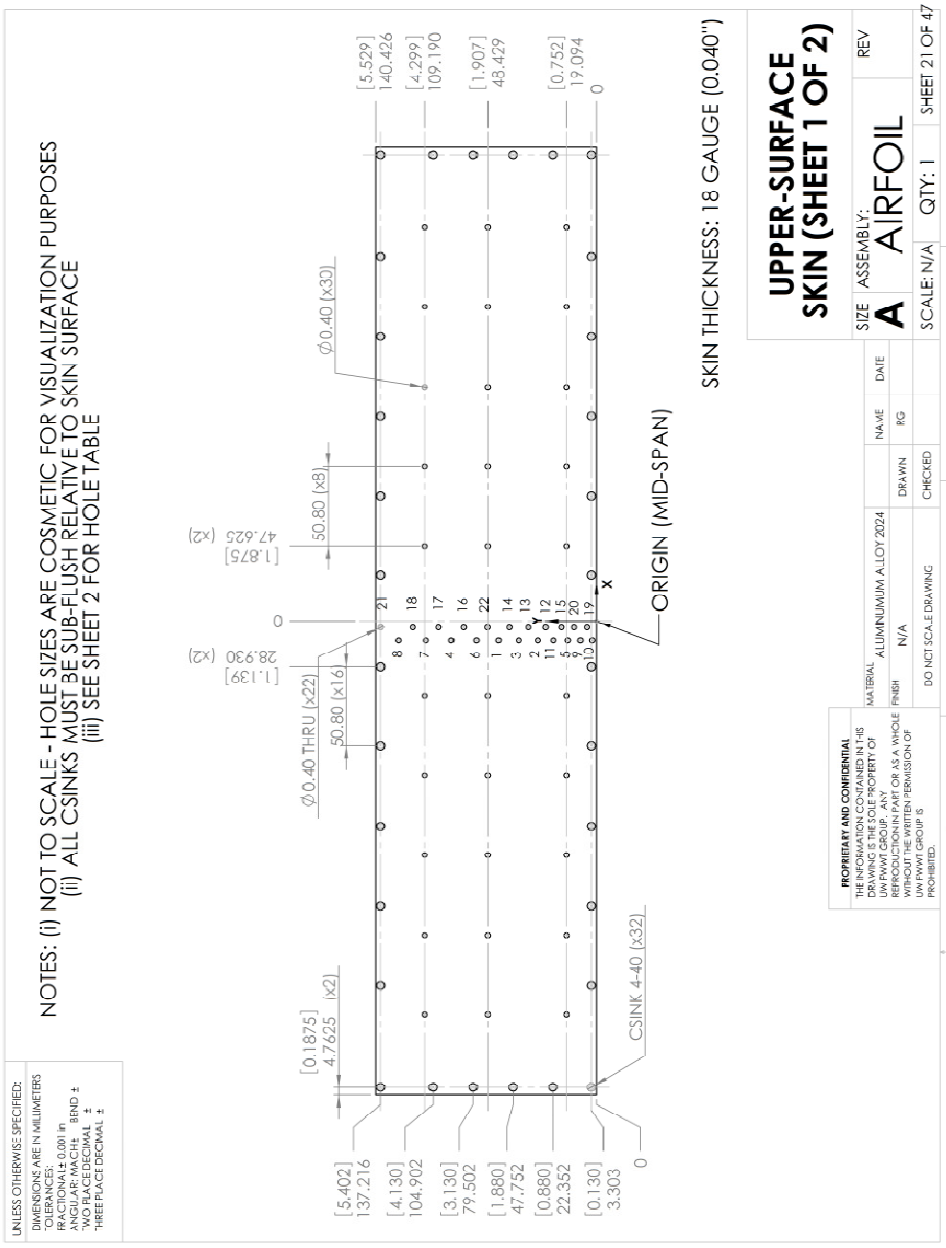

Figure A.5: Static pressure tap layout on top skin of airfoil.

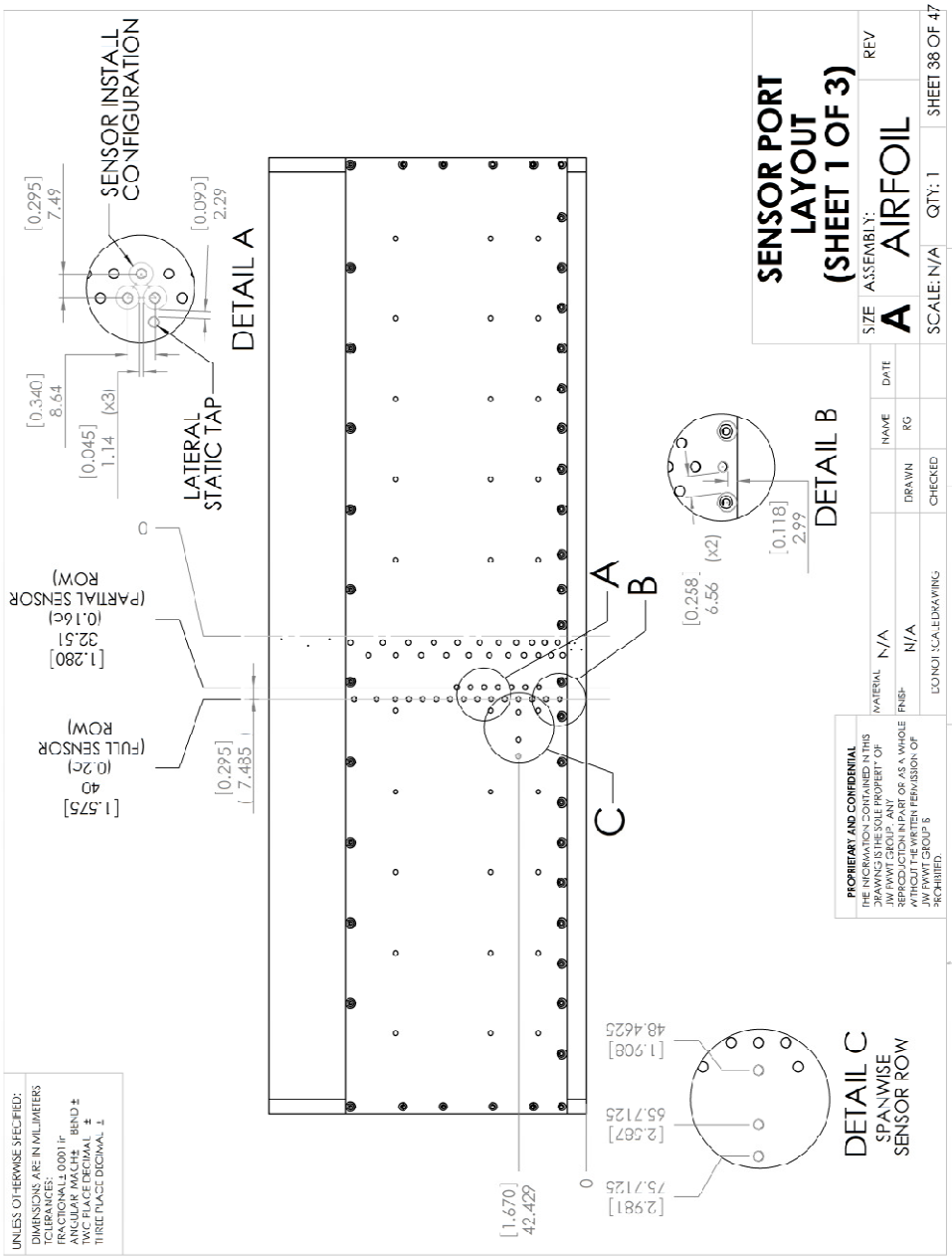

Figure A.6: Microphone sensor port layout on top skin of airfoil model.

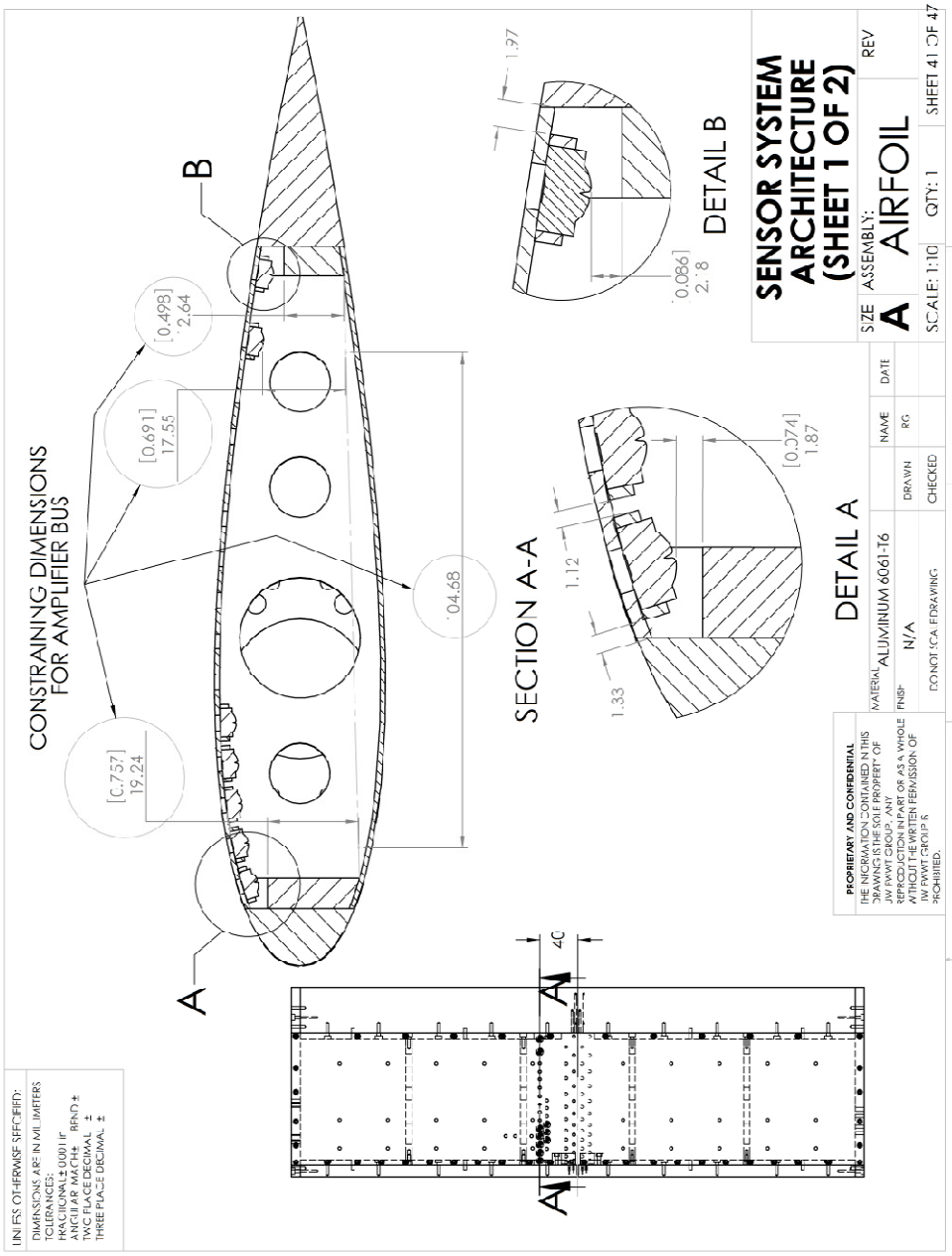

Figure A.7: Section view of airfoil showing microphone installation.

Table A.1: Centerline streamwise static pressure tap coordinates. Note that the origin is located at the leading-edge of the airfoil at the midspan plane.

x [mm]	y [mm]	x/c	y/c
0.000	0.000	0.0000	0.0000
1.020	3.700	0.0051	0.0185
2.754	5.947	0.0138	0.0297
3.950	7.038	0.0198	0.0352
5.384	8.113	0.0269	0.0406
7.085	9.178	0.0354	0.0459
9.099	10.241	0.0455	0.0512
10.242	10.773	0.0512	0.0539
14.590	12.459	0.0730	0.0623
17.763	13.448	0.0888	0.0672
21.877	14.501	0.1094	0.0725
25.876	15.327	0.1294	0.0766
29.876	16.013	0.1494	0.0801
33.876	16.562	0.1694	0.0828
38.876	17.109	0.1944	0.0855
43.876	17.501	0.2194	0.0875
48.876	17.770	0.2444	0.0889
54.876	17.957	0.2744	0.0898
60.876	17.996	0.3044	0.0900
66.876	17.926	0.3344	0.0896
73.876	17.700	0.3694	0.0885
80.876	17.358	0.4044	0.0868
87.876	16.896	0.4394	0.0845
95.876	16.254	0.4794	0.0813
103.876	15.502	0.5194	0.0775
111.876	14.645	0.5594	0.0732
119.876	13.702	0.5994	0.0685
128.126	12.647	0.6406	0.0632
137.126	11.407	0.6856	0.0570
148.260	9.749	0.7413	0.0487
161.275	7.657	0.8064	0.0383
175.323	5.205	0.8766	0.0260
191.824	2.056	0.9591	0.0103

Table A.2: Lateral static pressure tap coordinates. Note that the origin is located at the leading-edge of the airfoil at the midspan plane.

x [mm]	z [mm]	x/c	z/c
29.876	-250.825	0.1494	-1.2541
29.876	-200.025	0.1494	-1.0001
29.876	-149.225	0.1494	-0.7461
29.876	-98.425	0.1494	-0.4921
29.876	-47.625	0.1494	-0.2381
29.876	47.625	0.1494	0.2381
29.876	98.425	0.1494	0.4921
29.876	149.225	0.1494	0.7461
29.876	200.025	0.1494	1.0001
29.876	250.825	0.1494	1.2541
60.876	-250.825	0.3044	-1.2541
60.876	-200.025	0.3044	-1.0001
60.876	-149.225	0.3044	-0.7461
60.876	-98.425	0.3044	-0.4921
60.876	-47.625	0.3044	-0.2381
60.876	47.625	0.3044	0.2381
60.876	98.425	0.3044	0.4921
60.876	149.225	0.3044	0.7461
60.876	200.025	0.3044	1.0001
60.876	250.825	0.3044	1.2541
119.876	-250.825	0.5994	-1.2541
119.876	-200.025	0.5994	-1.0001
119.876	-149.225	0.5994	-0.7461
119.876	-98.425	0.5994	-0.4921
119.876	-47.625	0.5994	-0.2381
119.876	47.625	0.5994	0.2381
119.876	98.425	0.5994	0.4921
119.876	149.225	0.5994	0.7461
119.876	200.025	0.5994	1.0001
119.876	250.825	0.5994	1.2541

Appendix B: Effect of Traverse and Hot Wire Probe on Separated Shear Layer Development

Mean and RMS velocity measurements acquired within the separated flow region on the upper surface of the airfoil were used to characterize separated shear layer development. However, hot wire velocity measurements are intrusive since the hot wire sensor and traversing mechanism are immersed in the flow field. As a consequence, the proximity of the hot wire sensor and traversing mechanism to the airfoil may influence the flow development over the upper surface of the airfoil, which in turn may affect the mean and RMS velocity measured by the hot wire sensor.

The effect of the hot wire sensor and traversing mechanism on the mean surface pressure coefficient distribution are presented in Fig. B1 for $Re_c = 100x10^3$ and $\alpha = 8°$ and in Fig. B2 for $Re_c = 100x10^3$ and $\alpha = 12°$, respectively. Note that $\alpha = 8°$ and $\alpha = 12°$ pertains to flow regimes of separation with and without reattachment, respectively. For flow separation with reattachment, mean surface pressure coefficient distributions presented in Fig. B1 were acquired for the following test conditions when the hot wire sensor was positioned in the midspan plane:

- No traverse – the traversing mechanism was positioned at the most downstream x/c location in the test section
- Traverse – the traversing mechanism was positioned at the most upstream x/c location for mean and RMS velocity measurements in the separated flow region for the corresponding flow parameters
- S proximity – the hot wire sensor was positioned in the separated shear layer near the x/c location of flow separation

- T proximity – the hot wire sensor was positioned in the reverse flow region near the x/c location of transition
- R proximity – the hot wire sensor was positioned in the attached turbulent boundary layer near the x/c location of reattachment

The results in Fig. B1 indicate that there is variation in the magnitude of the mean surface pressure coefficient for each respective test. However, the locations of separation, transition, and reattachment remain unaffected and the variation of the magnitude of the mean surface pressure is within the experimental uncertainty. Therefore, the traversing mechanism and hot wire sensor have a marginal effect on the mean flow development in the separated flow region. A similar set of tests was performed for the regime of flow separation without reattachment (Fig. B.2):

- No traverse – same conditions as previously described
- Traverse proximity – the hot wire sensor was positioned in the reverse flow region near the x/c location of transition

Similar to the conclusions stated for the regime of flow separation with reattachment, the variability in the magnitude of the mean surface pressure coefficient is within the experimental uncertainty and the extent of the mean separated flow region is unaffected by the hot wire sensor and proximity of the traversing mechanism to the airfoil surface.

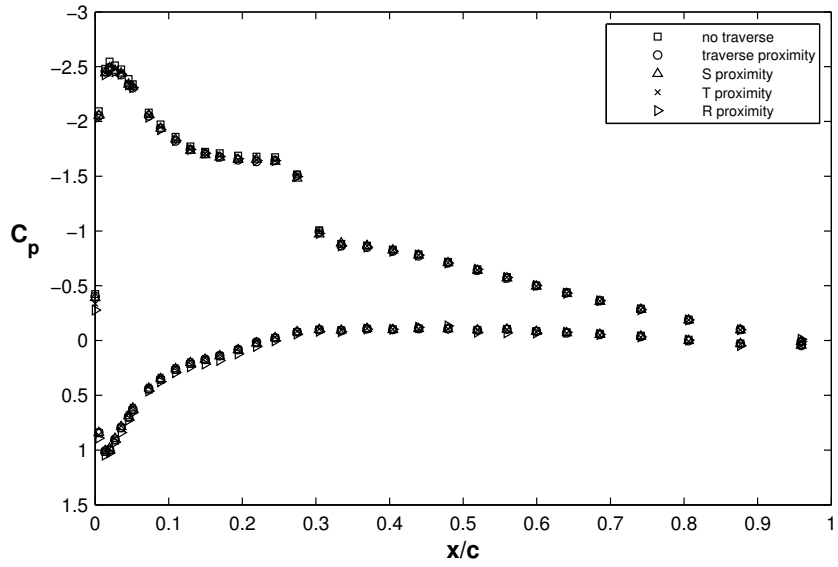

Figure B.1: Effect of the hot wire probe and traversing mechanism proximity to the airfoil surface on the upper and lower surface mean pressure coefficient distributions for $\alpha = 8^\circ$ and $Re_c = 100x10^3$.

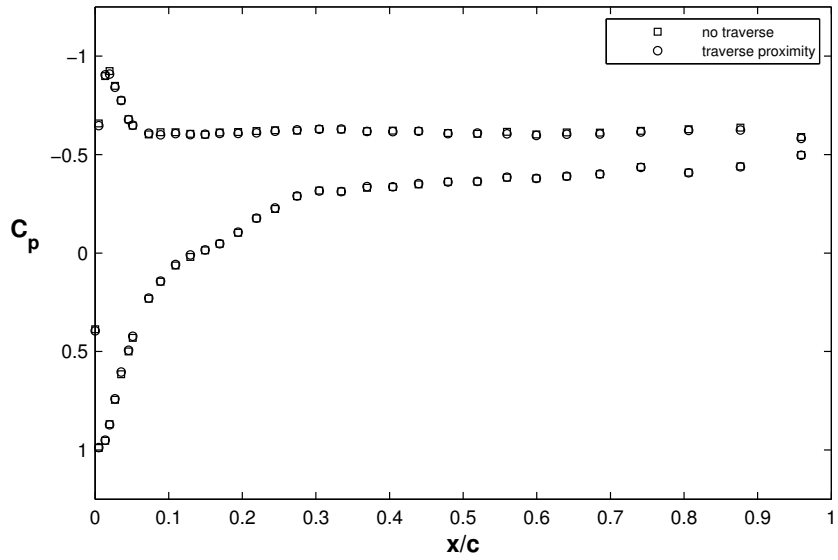

Figure B.2: Effect of the traversing mechanism proximity to the airfoil surface on the upper and lower surface mean pressure coefficient distributions for $\alpha = 12^\circ$ and $Re_c = 100x10^3$.

Appendix C: Embedded Microphone Array

Microphone Sensor Port Locations

Table C.1: Full sensor row microphone coordinates.

Sensor No.	x [mm]	x/c
S25	16.50	0.08
S24	25.14	0.13
S22	33.79	0.17
S17	42.43	0.21
S15	51.07	0.26
S13	59.72	0.30
S11	68.36	0.34
S09	77.00	0.39
S07	85.64	0.43
S06	94.29	0.47
S05	102.93	0.51
S04	111.57	0.56
S03	120.22	0.60
S02	132.00	0.66
S01	146.10	0.73

Table C.2: Partial sensor row microphone coordinates.

Sensor No	x [mm]	x/c
S23	29.465	0.15
S21	38.108	0.19
S16	46.751	0.23
S14	55.394	0.28
S12	64.037	0.32
S10	72.680	0.36
S08	81.323	0.41

Table C.3: Spanwise sensor row microphone coordinates.

Sensor No	x [mm]	x/c	z [mm]	z/c
S18	42.4290	0.21	48.6625	0.24
S19	42.4290	0.21	65.9125	0.33
S20	42.4290	0.21	75.9125	0.38

Amplification Bus Components List

Table C.4: Microphone amplification bus components list.

Component	Description	Digi Key Part No.	Tolerance	Quantity
Resistor	RES METAL FILM 3.30K OHM 1/4W 1% (10 RESISTORS/PACKAGE)	P3.30KCACT-ND	±1%	25
	RES METAL FILM 510 OHM 1/4W 1% (10 RESISTORS/PACKAGE)	P510CACT-ND	±1%	25
	RES METAL FILM 10.0K OHM 1/4W 1% (10 RESISTORS/PACKAGE)	P10.0KCACT-ND	±1%	50
Capacitor	CAP ELECT 100UF 25V FM RADIAL (10 CAPACTITORS/PACKAGE)	P12924-ND	±20%	50
	CAP 220UF 25V ELECT FM RADIAL (10 CAPACTITORS/PACKAGE)	P12383-ND	±20%	25
	KG RAD ALUM ELEC CAP 10UF 25V (10 CAPACTITORS/PACKAGE)	P916-ND	±20%	25
	KG RAD ALUM ELEC CAP 3.3UF 50V (10 CAPACITORS/PACKAGE)	P934-ND	±20%	25
Diode	DIODE ZENER 10V 1W DO-41	1N4740AFSCT-ND	±5%	1
Connectors	CONN HDR BRKWAY .100 80POS VERT (80 POSITIONS/PACKAGE)	A2 6536-40-ND	-	2
	CONN HOUSING 26POS .100 DUAL (26 POSITIONS/2 ROWS)	A3041-ND	-	4
	CONN SOCKET 20-24AWG TIN CRIMP (CRIMP SNAP-IN RECEPTACLE) (10 PINS/PACKAGE)	A25993-ND	-	3
Op-amp IC	IC OP-AMP DECOMPENSAT DUAL 8SOIC	LT1126CS8#PBF-ND	-	15
Breakout Board	ADAPTER BOARD SMT SOIC MED/WIDE	438-1014-ND	-	1

Sensor Port Cavity Resonance Analysis

Recall from §2.3.3 that each microphone was attached to the inner surface of the airfoil skin and linked to the pressure field by a sensor port drilled through the airfoil skin. A model of the sensor port is shown in Fig. C.1. In this figure, δ and U_e are the boundary layer thickness and edge velocity just upstream of the sensor port, respectively, while b and d are the diameter and depth of the cylindrical sensor port, respectively. For the selected microphone mounting arrangement, the sensor port depth is the airfoil skin thickness (d = 1.016 mm).

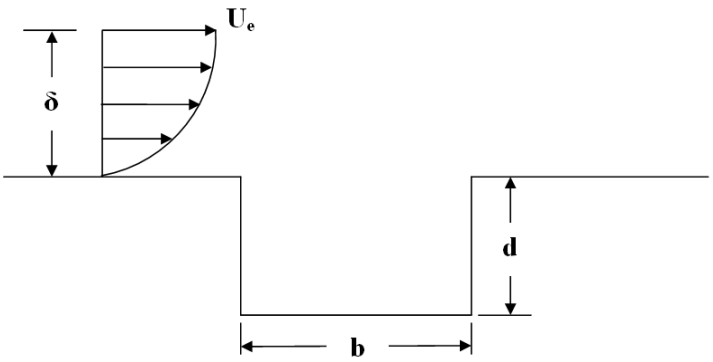

Figure C.1: Model of sensor port cavity and associated nomenclature.

The selection of an appropriate sensor port diameter is important since the geometry of the sensor port influences how the flow behaves within the cavity (e.g., Wheeler & Ganji, 2004; Sarohia, 1975), which may contaminate the fluctuating surface pressure signal measured by the microphone. Accordingly, the minimum sensor port diameter (b_1) of 0.4 mm was selected based on the smallest diameter which could feasibly be drilled in the airfoil surface. Conversely, the maximum diameter (b_2) was confined to 1.0 mm in order to

minimize the risk of the sensor port perturbing or tripping the sensitive laminar boundary layer. According to Sarohia (1975), the sensor port configuration is considered an open cavity for b/d < 7-8, which is applicable for the proposed range of sensor port diameters (b/d < 1). For such a configuration, the flow separates from the upstream corner of the sensor port and reattaches at the downstream corner. Furthermore, the open cavity is also considered deep for b/d < 1, where a deep and open cavity behaves like a resonator with the shear layer over the cavity acting as a forcing mechanism (Sarohia, 1975). Accordingly, the Helmholtz resonant frequency will be examined. Conversely, if b/d > 1, the open cavity would be considered shallow and the disturbances amplifying through the separated shear layer over the sensor port may produce flow oscillations in the cavity (Sarohia, 1975). Since the proposed sensor port geometry does not conform to an open and shallow cavity, it is speculated that the corresponding cavity resonance will not occur. However, the resonant frequency associated with cavity resonance was still explored during the design of the sensor port to be precautious.

The Helmholtz resonant frequency and damping ratio were computed using a method outlined by Wheeler & Ganji (2004), where the resonant frequency is computed using Eq. C1,

$$f_n = \frac{C}{2\pi d\sqrt{0.5 + \frac{\forall_t}{\forall_s}}} \tag{C.1}$$

where f_n is the resonant frequency, d is the sensor port depth, C is the speed of sound in air, $\forall_s$ is the sensor port volume, and $\forall_t$ is the volume contained between the inner surface of the airfoil skin and the microphone diaphragm. The damping ratio was computed using Eq. C.2,

$$\xi = \frac{R_l d}{2\rho C}\sqrt{0.5 + \frac{\forall t}{\forall s}} \tag{C.2}$$

where ζ is the damping ratio, ρ is the density of air, and R_l is the fluid resistance. The fluid resistance was calculated using Eq. C.3,

$$R_l = \frac{32\mu}{b^2} \tag{C.3}$$

where μ is the dynamic viscosity of air and b is the sensor port diameter. The frequency response of the error in the measured pressure amplitude (i.e., the ratio of the measured pressure amplitude to the actual pressure amplitude) was computed using Eq. C.4 (Mueller, 2002).

$$\frac{p_{measured}}{p_{actual}} = \left[\left(1 - \frac{f^2}{f_n{}^2}\right)^2 + \left(\frac{2\xi f}{f_n}\right)^2\right]^{-1/2} \tag{C.4}$$

A plot of the error in the pressure amplitude is presented in Fig. C.2 for sensor port diameters of 0.4 mm, 0.8 mm, and 1.0 mm. For a given sensor port diameter, error between the measured and actual pressure increases steadily with an increase in the frequency until the resonant frequency is approached, which is followed by a steady decrease in the error with a further increase in the frequency. As the sensor port diameter is increases from 0.4 mm to 1.0 mm, the resonant frequency also increases from 4838 Hz to 11971 mm. From this analysis, it is desirable to select $b \geq 0.8$ mm since there is marginal error in the measured pressure amplitude up to approximately 5000 Hz, which is greater than the maximum expected frequency for the flow parameters of interest. For the range of frequencies of interest from 70 Hz to 2000 Hz, the results suggest that, for the selected sensor port configuration (b = 0.8 mm), the measured pressure may be 5% greater than the actual pressure field due to flow resonance.

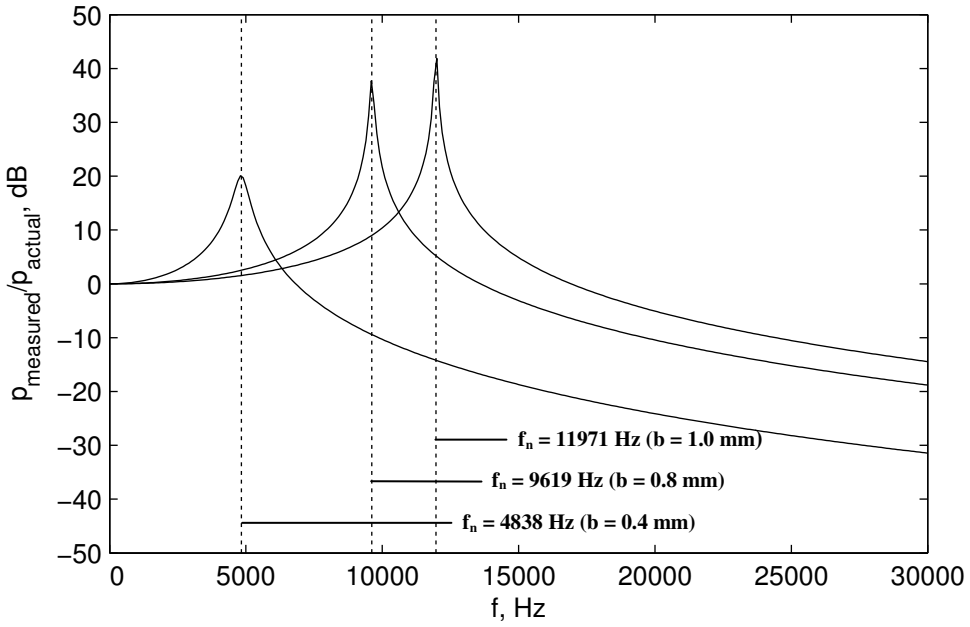

Figure C.2: Microphone sensor port Helmholtz resonance frequency response.

Estimates of the cavity resonance associated with an open and shallow cavity were computed for the minimum and maximum sensor port diameters, denoted by b_1 and b_2, respectively. Preliminary mean and RMS hot wire velocity measurements were acquired on the upper surface of the airfoil at $\alpha = 15°$ for $Re_c = 40x10^3$, $Re_c = 80x10^3$, and two distinct x/c locations. From these measurements, the corresponding boundary layer thickness and edge velocity was obtained. In addition, matching parameters were also extracted from the results of Nakano et al. (2007) on a NACA 0018 airfoil at $Re_c = 160x10^3$ and $\alpha = 6°$ at two x/c locations. From these results, the Reynolds number based on the boundary layer thickness and edge velocity ($Re_\delta = \delta U_e/\nu$) was computed for all sets of flow conditions. A summary of the collective parameters for all sets of flow conditions is shown in Table C.5. For all sets of flow conditions, Re_δ ranges from 1175 to 7900 and d/δ from 0.09 to 3. Sarohia (1975) derived a non-dimensional experimental relationship between the cavity resonant frequency ($f_{cav}b/U_e$, where f_{cav} is the cavity resonant frequency) and the cavity diameter (b/d) for Re_δ = 2860 and $d/\delta = 10$. Although the estimates of Re_δ and d/δ differ from the conditions in Sarohia (1975), it still provides a reasonable approximation of the cavity resonant frequency. From Table C.5, it is apparent that the cavity resonant frequency increases with a decrease in the sensor port diameter, which is contrary to the effect of observed for the Helmholtz resonant frequency. For $Re_c \geq 80x10^3$ and $6° \leq \alpha \leq 15°$, the estimated cavity resonant frequency is significantly greater than the maximum frequency expected in the flow for the flow parameters of interest.

From this cavity resonance analysis, it is desirable to minimize the sensor port diameter to maximize the cavity resonant frequency, however, it is unlikely to occur for the

flow parameters of interest and the selected sensor port geometry (i.e., since the cavity is considered open and deep rather than open and shallow). Conversely, the Helmholtz resonant frequency, which is more likely to occur for the sensor port geometry, decreases as the sensor port diameter increases. In order to minimize the effects of cavity and Helmholtz resonance, a sensor port diameter (b) of 0.8 mm was selected. From the resonance analysis in this section, for the selected sensor port diameter, it is speculated that the Helmholtz and cavity (which will likely be avoided based on the selected geometry) resonant frequencies will be significantly greater than the maximum frequency expected for the flow parameters of interest.

Table C.5: Estimates of the cavity resonance frequency. Results at $Re_c = 160x10^3$ and $\alpha = 6°$ were obtained from Nakano et al. (2007)

α[deg]	Re_c	x/c	δ [mm]	U_e [m/s]	b_1/δ	b_2/δ	d/δ	Re_δ	St	f_1 [Hz]	f_2 [Hz]
15	$40x10^3$	0.16	5.34	3.3	0.187	0.075	0.295	1175	0.9	2970	7425
		0.24	17.52	3.3	0.057	0.023	0.090	3854	0.9	2970	7425
	$80x10^3$	0.16	7.34	7.2	0.136	0.054	0.215	3523	1.9	13680	34200
		0.24	16.54	7.2	0.060	0.024	0.095	7939	2.9	20880	52200
6	$160x10^3$	0.18	0.56	42	1.786	0.714	2.812	1568	0.9	37800	94500
		0.33	0.8	42	1.250	0.500	1.969	2240	0.9	37800	94500

Microphone Calibration Methodology

Recall from §2.3.3 that the calibration was performed in an anechoic chamber to minimize the effects of environmental disturbances. The calibration was performed using a

comparative method in which the uncalibrated and pre-calibrated reference microphones were exposed to the same sound pressure field within a coupling tube generated by a speaker. A sinusoidal pressure wave was generated within the coupling tube by the speaker at a pure tone (i.e., discrete frequency) and constant amplitude of 114 dB. The voltage amplitudes of the reference and uncalibrated microphones were measured simultaneously and digitized by the DAQ. By measuring the voltage amplitudes from the two microphones simultaneously, the sensitivity of the uncalibrated microphone was determined as illustrated in the block diagram in Fig. C.3. Accordingly, the measured voltage amplitude and pre-calibrated sensitivity of the reference microphone were used to determine the sound pressure on the surface of the PVC insert, which is defined as the measurement plane. The sensitivity of the uncalibrated microphone can be determined with knowledge of the sound pressure and measured voltage amplitude. Therefore, the objective of the calibration was to determine the sensitivity of the uncalibrated microphone so that the amplitude of pressure fluctuations over the airfoil surface can be estimated.

A frequency response curve was generated for each uncalibrated microphone by repeatedly acquiring the uncalibrated microphone sensitivity at pure tone frequencies in the range from 70 to 12,000 Hz using $1/8^{th}$ octave increments. By rotating the PVC insert in the coupling tube, a frequency response curve was acquired at four circumferential positions on the measurement plane, with each position separated by 90 degrees. The four frequency response curves measured at each circumferential position were averaged at each frequency to generate a final response curve from which a unique calibration sensitivity was obtained

for each microphone. All sensitivities were normalized by the sensitivity at a common reference frequency of 250 Hz as recommended by Brüel & Kjær (1996) and the normalized

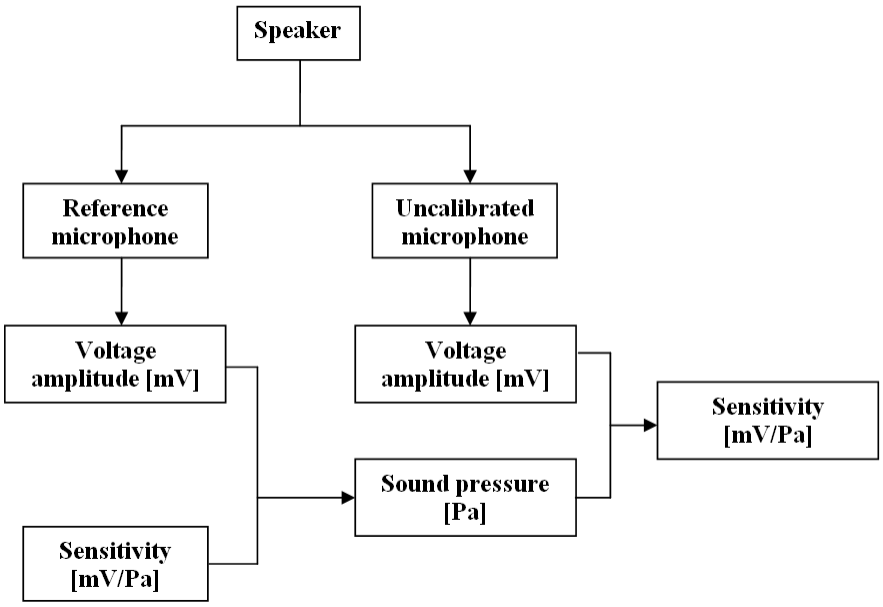

Figure C.3: microphone sensitivity estimate using comparison method (block diagram).

results were expressed in decibels. The frequency response curves for each microphone are presented in Fig. C.4. It is evident from this figure that the response is relatively flat from approximately 70 to 2,000 Hz. For higher frequencies, the response increases steadily, reaching a maximum around 7,000 Hz, and decaying with a further increase in the frequency. The frequency centered around 7,000 Hz is in close agreement with that predicted for the Helmholtz resonant frequency generated in the sensor port. The frequency response in the

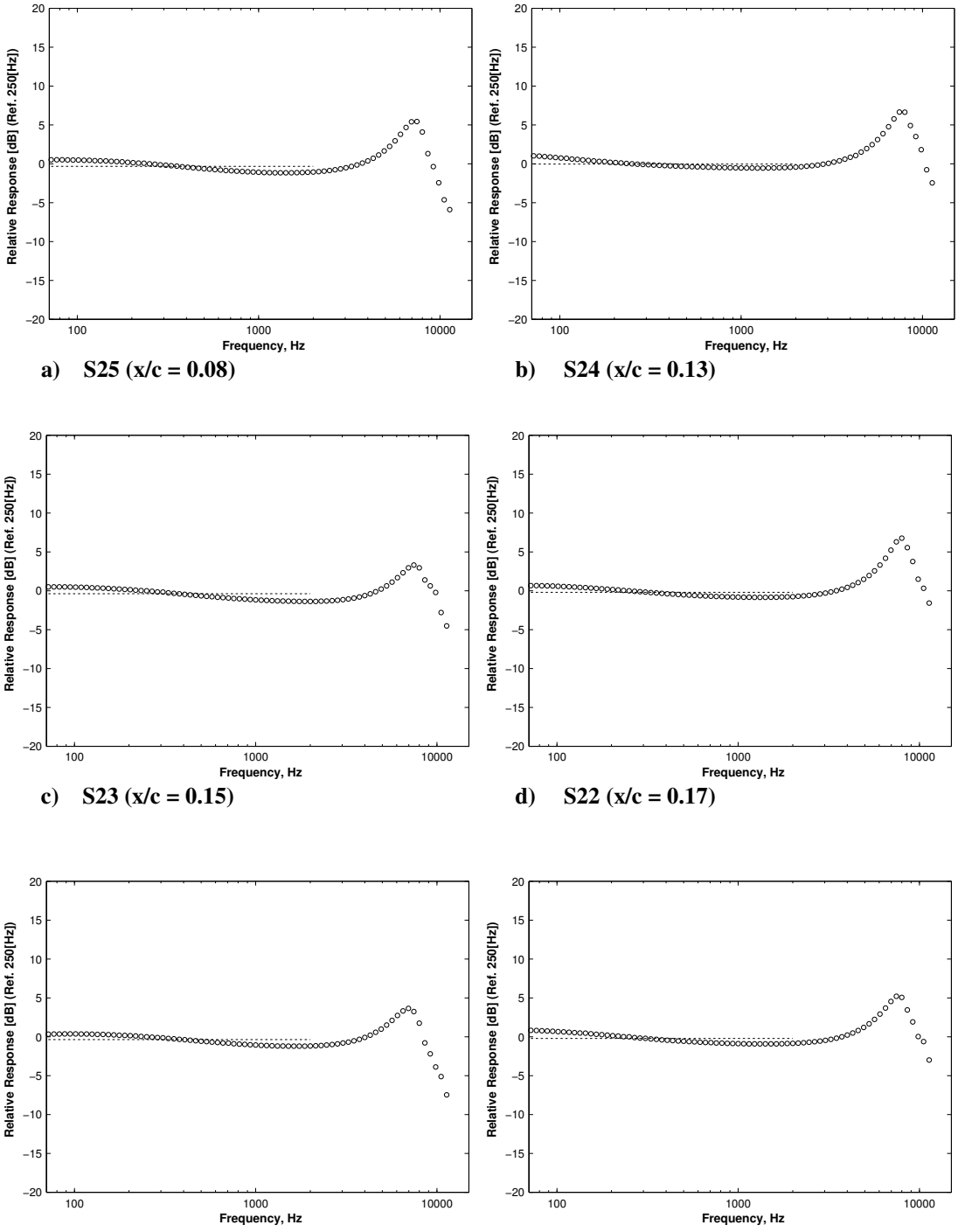

a) S25 (x/c = 0.08) **b) S24 (x/c = 0.13)**

c) S23 (x/c = 0.15) **d) S22 (x/c = 0.17)**

e) S21 (x/c = 0.19) **f) S20 (x/c = 0.21)**

Figure C.4: Microphone frequency response curves.

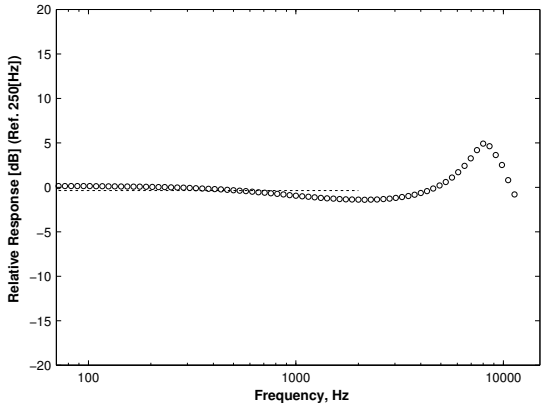

g) S19 (x/c = 0.21)

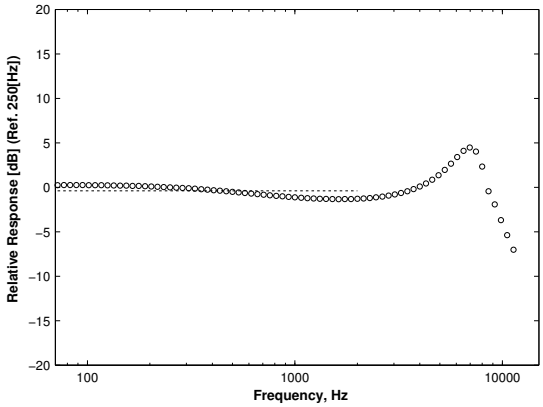

h) S18 (x/c = 0.21)

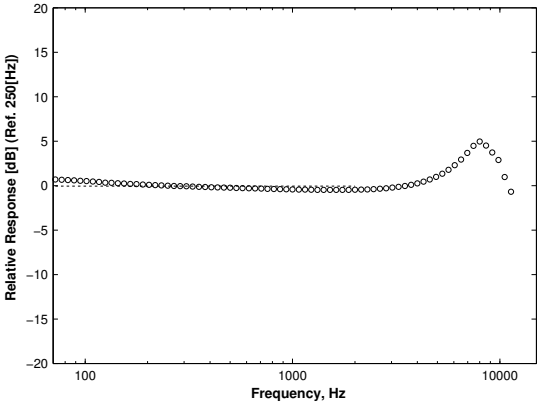

i) S17 (x/c = 0.21)

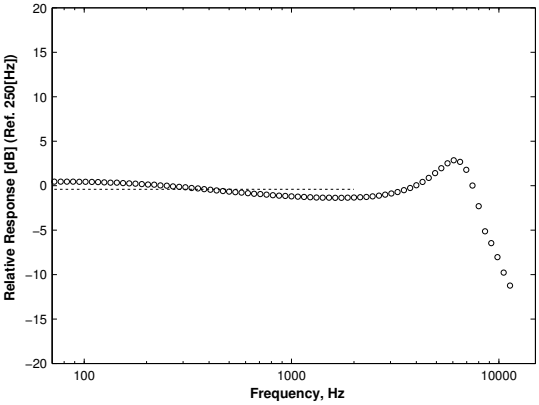

j) S16 (x/c = 0.17)

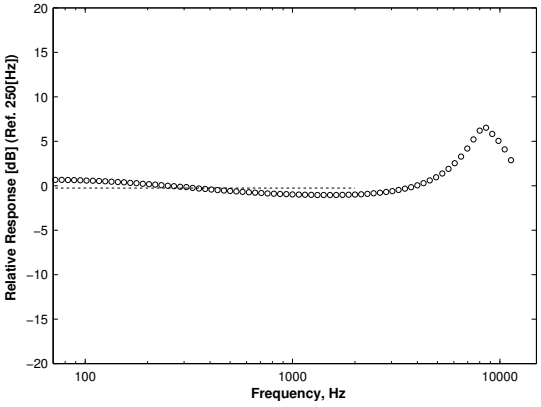

k) S15 (x/c = 0.19)

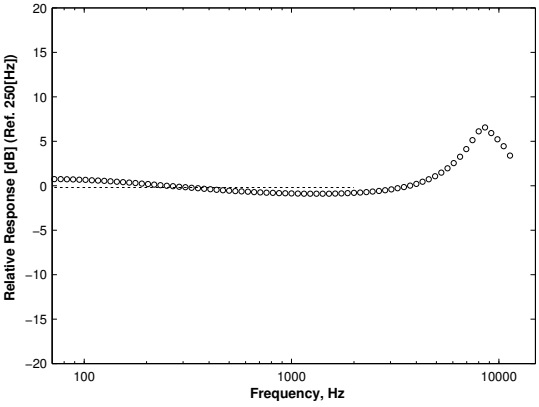

l) S14 (x/c = 0.21)

Figure C.4 (cont'd): see previous page.

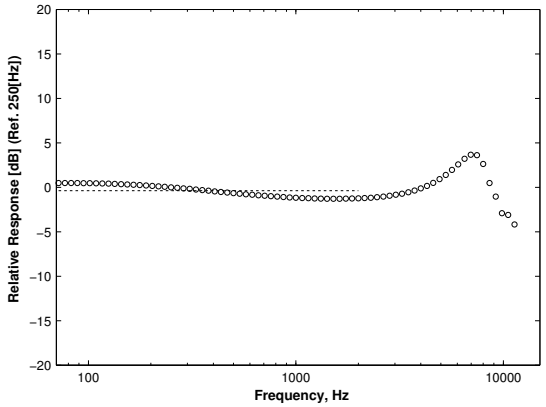

g) S13 (x/c = 0.30)

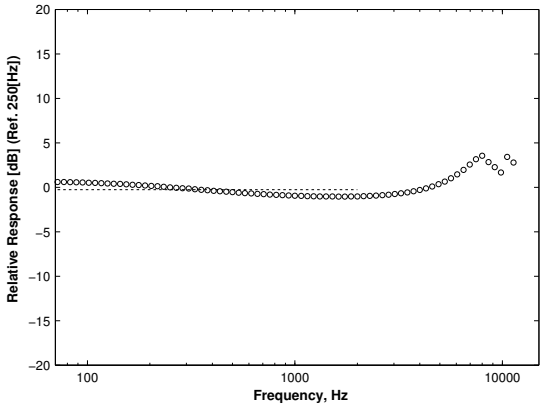

h) S12 (x/c = 0.32)

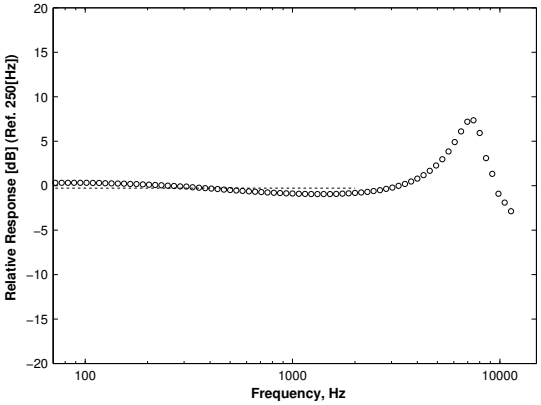

i) S11 (x/c = 0.34)

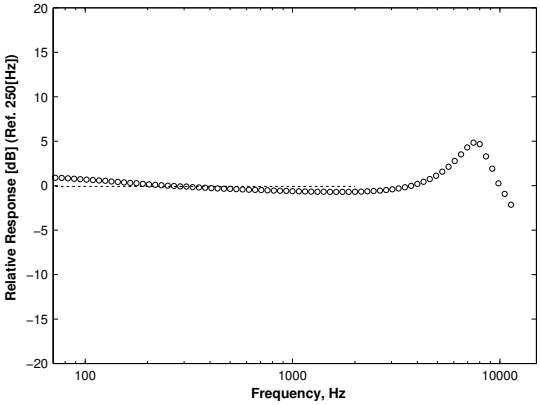

j) S10 (x/c = 0.36)

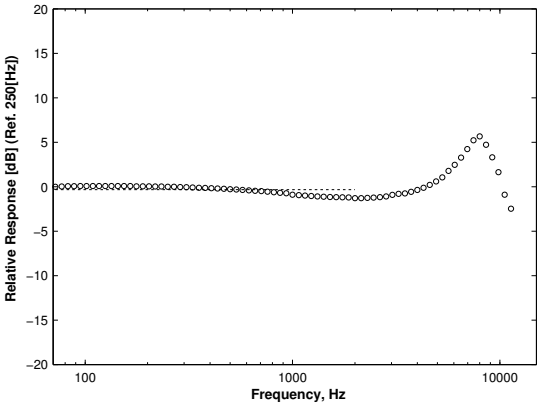

k) S09 (x/c = 0.39)

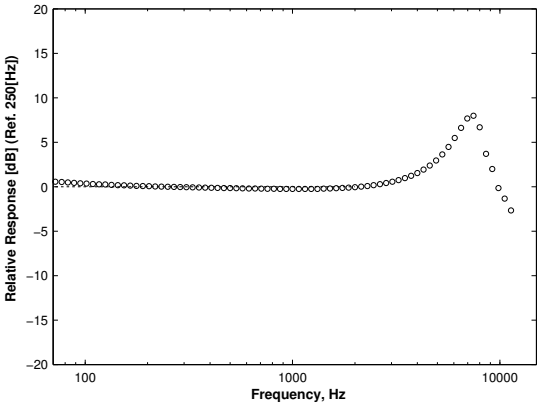

l) S08 (x/c = 0.41)

Figure C.4 (cont'd): see previous page.

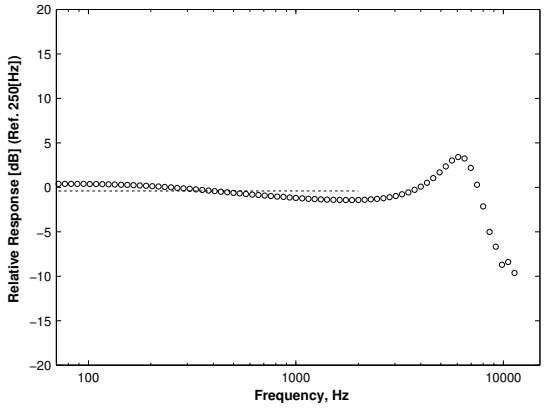

m) S07 (x/c = 0.43)

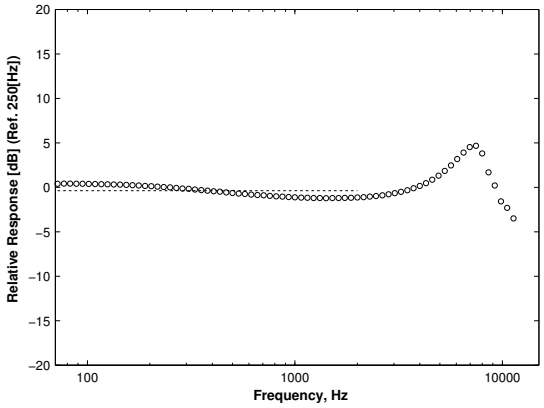

n) S06 (x/c = 0.47)

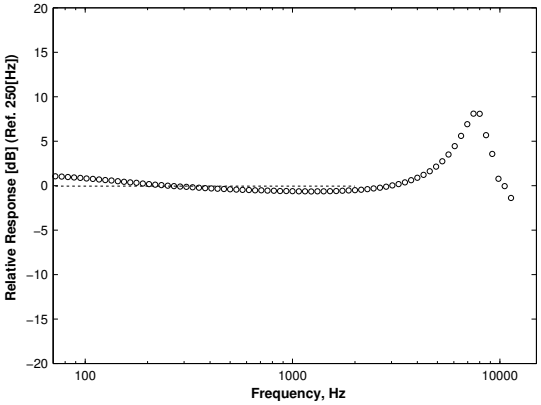

o) S05 (x/c = 0.51)

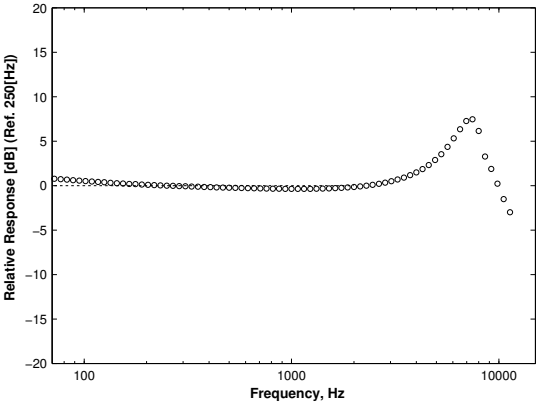

p) S04 (x/c = 0.56)

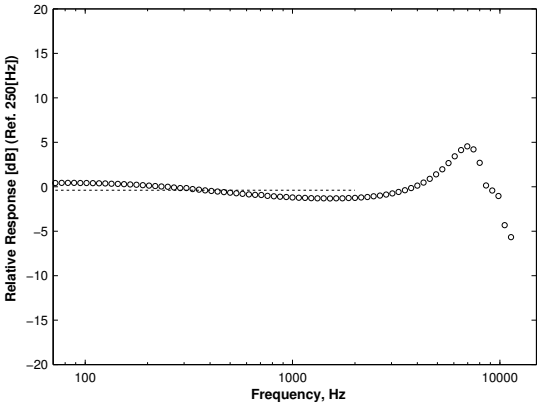

q) S03 (x/c = 0.60)

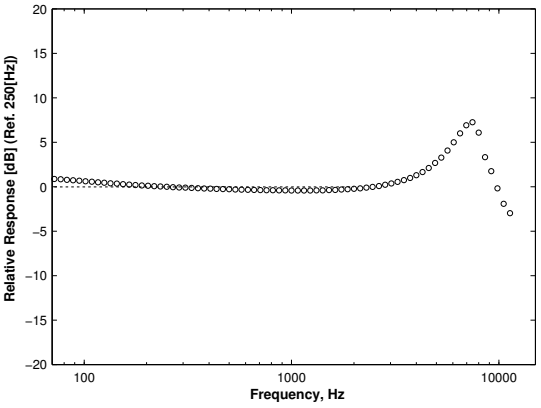

r) S02 (x/c = 0.66)

Figure C.4 (cont'd): see previous page.

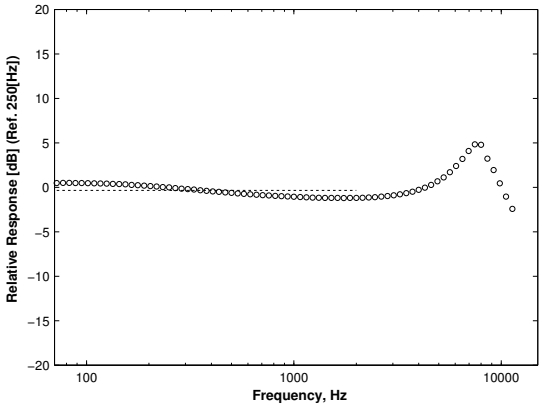

s) S01 (x/c = 0.73)

Figure C.4 (cont'd): see previous page.

range from 70 Hz to 2000 Hz is of interest since it includes the range of frequencies expected in the present investigation. The relative flatness of the response implies that the output voltage from the microphone is relatively constant at all frequencies for sound pressures of equal magnitude (Brüel & Kjær, 1996). As a consequence, it is reasonable to use a constant calibration sensitivity within the relatively flat frequency range. A constant calibration sensitivity was estimated by averaging the sensitivities at each frequency in the range from 70 to 2,000 Hz, which is depicted as a dashed line in the response curves in Fig. C.4. The calibration sensitivity for each microphone is summarized in Table. C.6.

Table C.6: Microphone calibration sensitivities.

Sensor	S [mV/Pa]
S25	184.18
S24	189.59
S23	156.7
S22	173.84
S21	181.57
S20	158.31
S19	209.87
S18	192.34
S17	193.75
S16	166.23
S15	150.00
S14	199.93
S13	197.48
S12	179.34
S11	159.45
S10	173.39
S09	193.55
S08	167.30
S07	167.91
S06	197.68
S05	189.61
S04	193.85
S03	205.47
S02	187.05
S01	191.32

Microphone Background Noise and Pure Tone Testing

Once the microphones were embedded in the airfoil and the airfoil was installed in the wind tunnel test section, the background noise of each microphone was measured while the wind tunnel was off. The corresponding RMS fluctuating surface pressure computed while the tunnel was off is summarized in Table C.7 for each microphone. Additionally, a speaker was mounted on the top flexible wall within the wind tunnel test section centered above the

embedded microphone array. A pure tone of 900 Hz was continuously generated by the speaker and the corresponding RMS fluctuating surface pressure and pressure spectra were acquired, the results of which are shown in Fig. C.5 and Table C.8, respectively. These results indicate that each microphone embedded in the airfoil surface is capable of resolving the 900 Hz pure tone and the computed RMS fluctuating surface pressure is comparable for each microphone.

Table C.7: microphone background noise acquired in no flow conditions.

Sensor	x/c	p'[Pa]
S25	0.08	0.119
S24	0.13	0.147
S23	0.15	0.091
S22	0.17	0.111
S21	0.19	0.077
S17	0.21	0.148
S16	0.24	0.098
S15	0.26	0.072
S14	0.28	0.151
S13	0.3	0.167
S12	0.32	0.133
S11	0.34	0.111
S10	0.36	0.190
S09	0.39	0.079
S08	0.41	0.144
S07	0.43	0.144
S06	0.47	0.105
S05	0.51	0.136
S04	0.56	0.183
S03	0.6	0.194
S02	0.66	0.175
S01	0.73	0.113

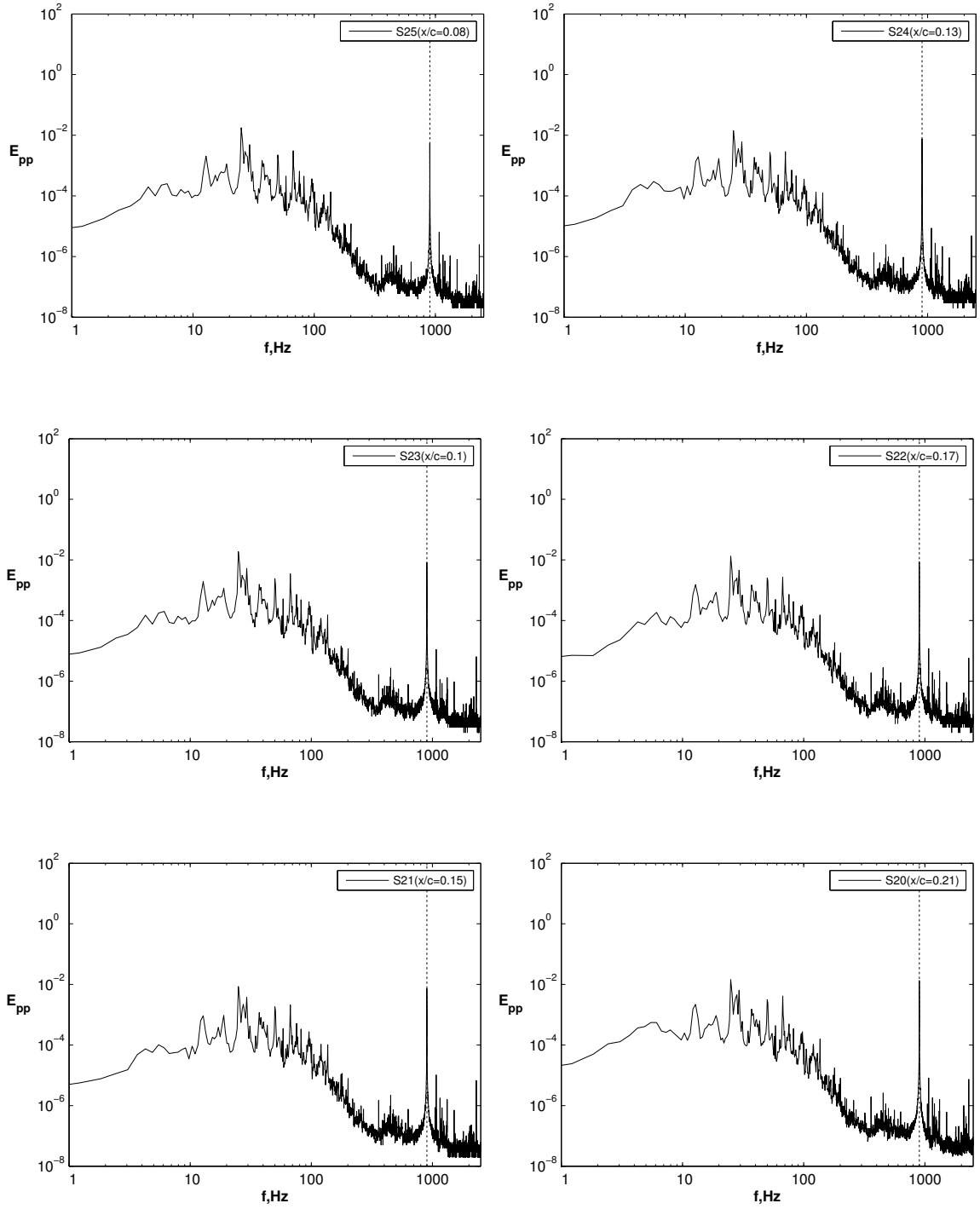

Figure C.5: Fluctuating surface pressure spectra when microphone array is exposed to a pure tone of 900 Hz.

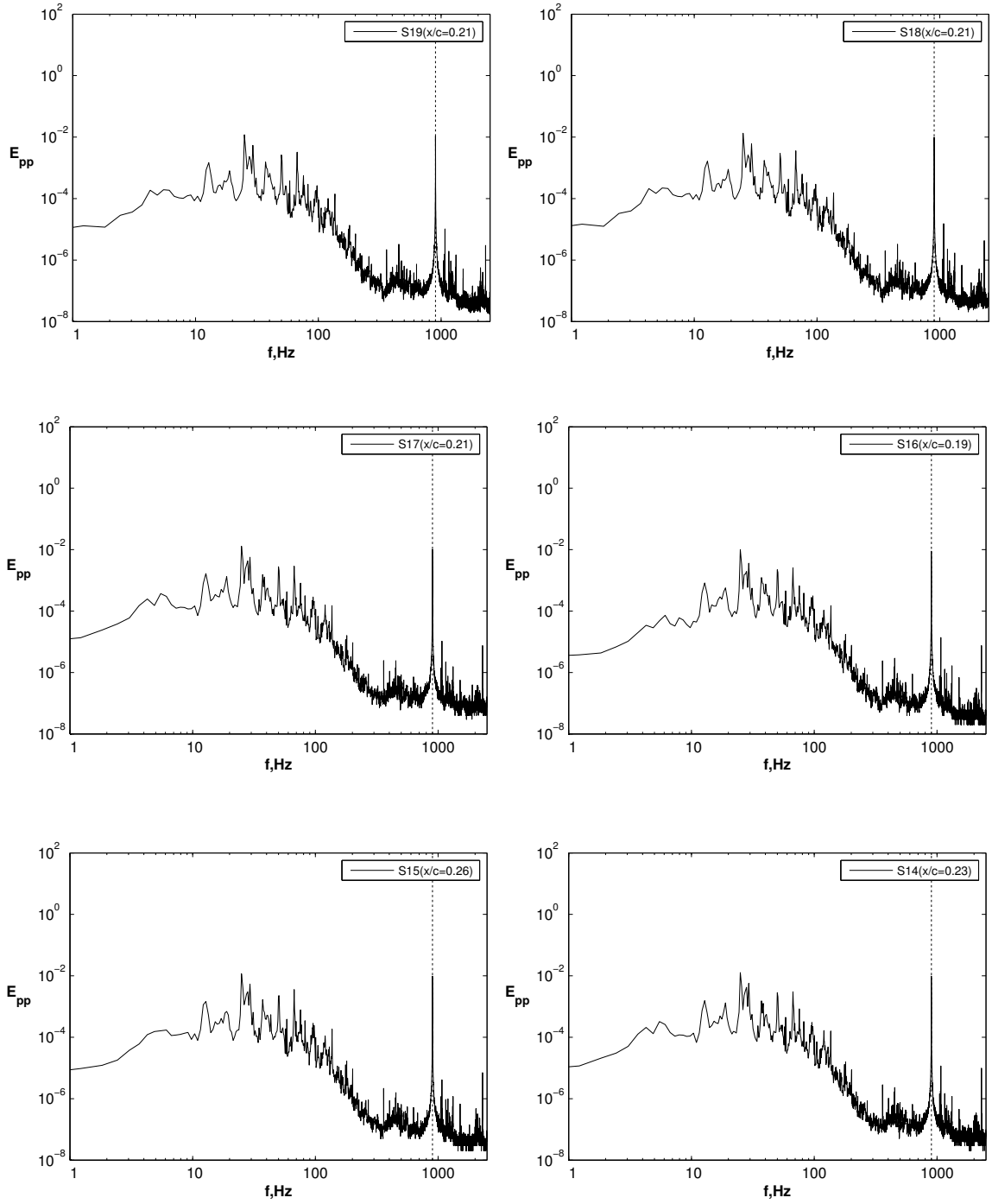

Figure C.5 (cont'd): See previous page.

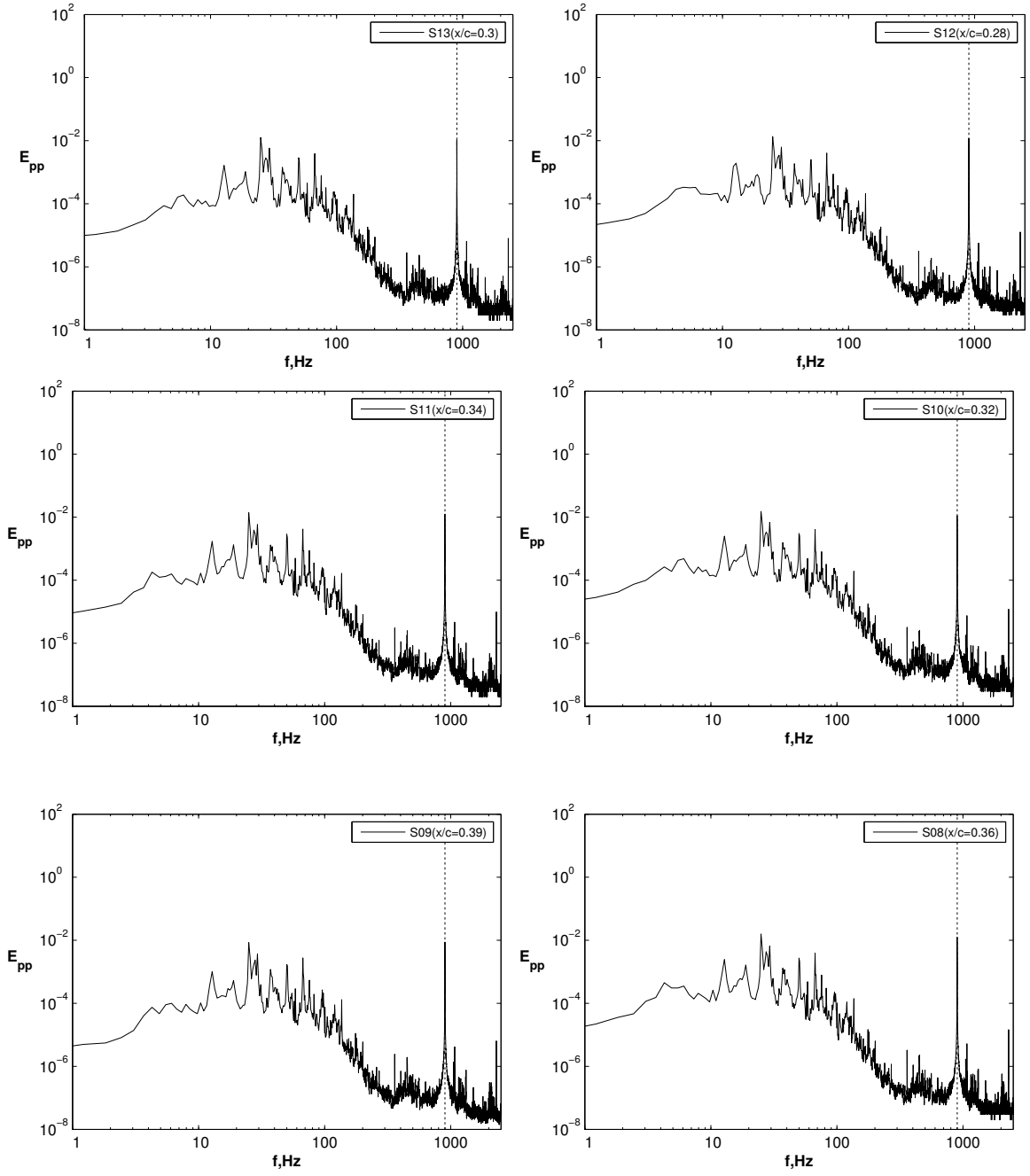

Figure C.5 (cont'd): See previous page.

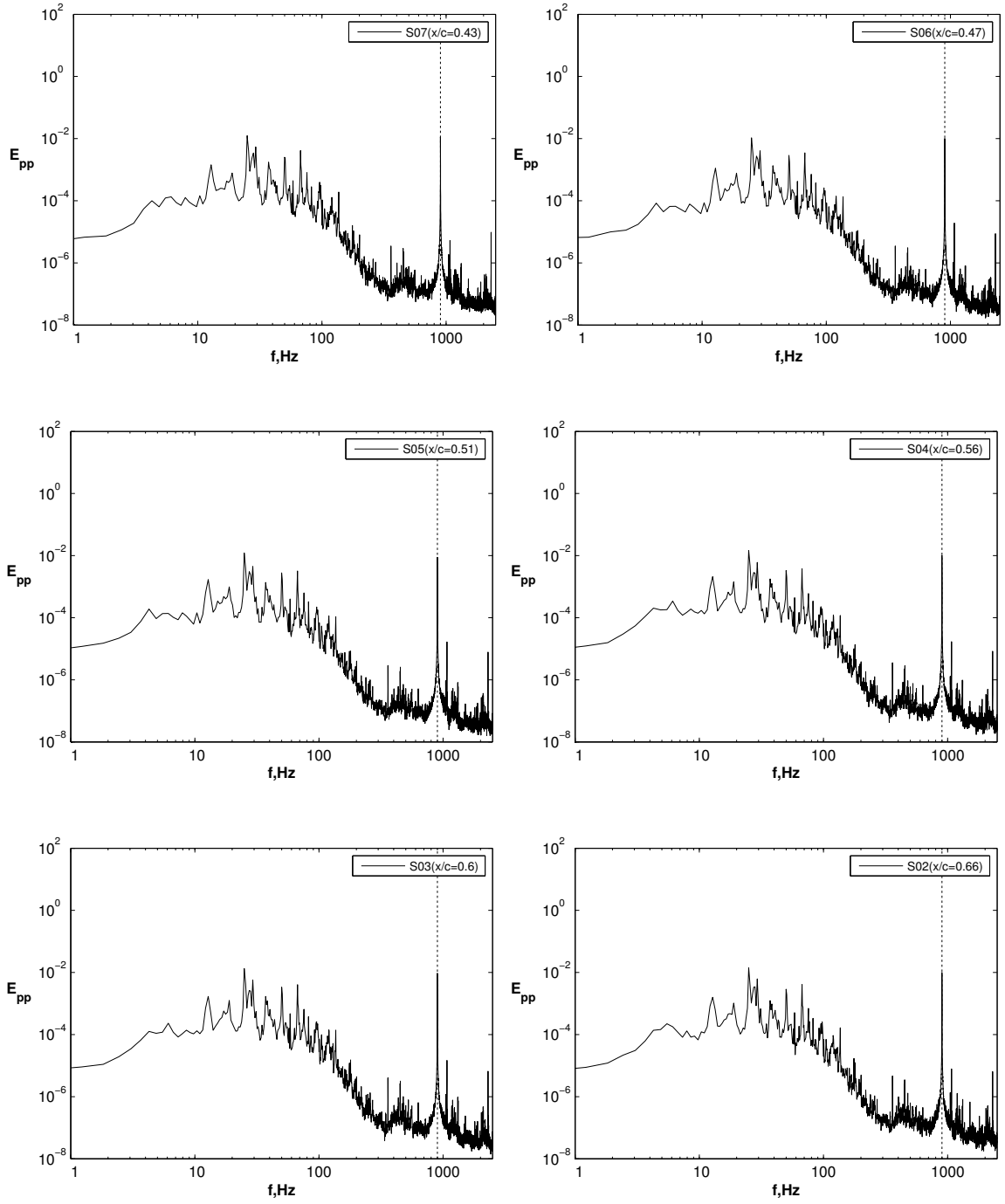

Figure C.5 (cont'd): See previous page.

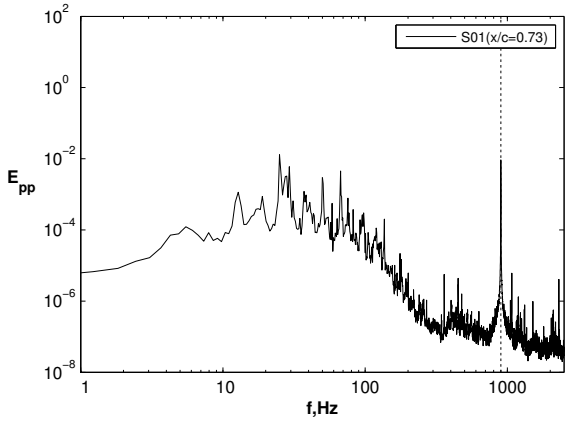

Figure C.5 (cont'd): See previous page.

Table C.8: Summary of RMS fluctuating pressure for pure tone test.

Sensor	p' [Pa]
S25	0.239
S24	0.250
S23	0.253
S22	0.240
S21	0.207
S20	0.269
S19	0.241
S18	0.249
S17	0.253
S16	0.221
S15	0.240
S14	0.252
S13	0.252
S12	0.261
S11	0.256
S10	0.270
S09	0.211
S08	0.264
S07	0.251
S06	0.231
S05	0.234
S04	0.255
S03	0.248
S02	0.246
S01	0.241

Appendix D: Uncertainty Analysis

In this appendix, the uncertainty associated with the experimental measurements and corresponding correlation and spectral analysis are presented. Specifically, the uncertainty analysis is partitioned into six distinct segments:

(i) Mean and fluctuating pressure and free-stream velocity measurements
(ii) Hot wire measurements
(iii) Hot wire probe positioning
(iv) Spectral peak frequency estimation
(v) Time-lag associated with velocity-pressure cross-correlation analysis
(vi) Time-lag and convection velocity analysis

(i) Mean and Fluctuating Pressure and Free-Stream Velocity Measurements

The uncertainty associated with experimental measurements was estimated using a method proposed by Moffat (1988) and employed by Bishop (2010) for mean pressure measurements using a similar experimental setup in the wind tunnel used for the present investigation. Accordingly, the error is comprised of the bias (Bi) and precision (S) error, which collectively, leads to the total root-mean-square uncertainty ($U_{0.95}$) presented in Eq. D.1.

$$U_{0.95} = \sqrt{Bi^2 + (2S)^2} \tag{D.1}$$

$U_{0.95}$ represents the 95% confidence level associated with an experimental measurement, which implies that the measured value is within $\pm U_{0.95}$ of the true value 95 times out of 100. The precision error, S, is statistical and computed using Eq. D.2,

$$S = \frac{\sigma}{N} \tag{D.2}$$

where σ is the standard deviation and N is the total number of samples. The total bias error, Bi, is computed using Eq. D.3.

$$Bi = \sqrt{Bi_{CAL}{}^2 + Bi_{PROBE}{}^2} \tag{D.3}$$

The main contributions to the bias error are associated with calibration (Bi_{CAL}) and the positioning and geometry of the probe (Bi_{PROBE}).

Two different pressure transducers were employed for measuring the dynamic pressure of the free-stream velocity and the mean surface pressure, which are shown in Table D.1. Signals were acquired from both pressure transducers at a sampling rate of 5,000 Hz with a sample size of 100,000 data points and calibrated against an inclined manometer. Thus, the bias error associated with calibration is based on the precision of the smallest division of the inclined manometer scale. The uncertainty associated with the positioning and the geometry of the pitot-static tube used for measuring the dynamic pressure was estimated to be 0.3% (Pope, 1966). Furthermore, the uncertainty in the pressure measurements associated with the pressure tap geometry was estimated to be 0.2% (Chue, 1977). The resulting precision error, bias error, and total uncertainty in the estimates of the free-stream velocity and mean surface pressure coefficient are summarized in Table D.2.

Table D.1: Pressure transducers and pressure ranges.

Measurement	Pressure Transducer	Model No.	Pressure Range [Pa]
Free-stream dynamic pressure	Lucas Schaevitz	P3061-2WD	0-498
Airfoil pressure	Scanivalve	ZOC33 S-SENSOR	0-1245

Table D 2: Summary of uncertainty estimates for the mean free-stream velocity and the mean surface pressure coefficient.

Measurement	S	Bi	$U_{0.95}$
U_o [m/s]	0.000	0.213	0.213
C_p	0.000	0.022	0.022

A similar methodology was employed for estimating the uncertainty associated with measurements of surface pressure fluctuations. The bias error was predominately associated with calibration and the noise floor. Since signals were acquired with a sample size of 2,097,152 data points and the RMS fluctuating surface pressure was less than approximately 10 Pa for the flow parameters of interest, the precision error was negligible in comparison to the bias error. Thus, the total root-mean-square uncertainty ($U_{0.95}$) associated with the RMS surface pressure fluctuations was computed using Eq. D.4,

$$U_{0.95} = \sqrt{Bi_{UNCAL}^{\ 2} + Bi_{REF}^{\ 2} + Bi_{LINEARITY}^{\ 2} + Bi_{NOISE}^{\ 2}} \qquad \text{(D.4)}$$

where the bias error Bi_{UNCAL} is associated with the accuracy of the uncalibrated microphone (i.e., the microphones in the sensor array), Bi_{REF} is associated with the accuracy of the reference microphone used for calibration, $Bi_{LINEARITY}$ is associated with the non-linearity of the uncalibrated microphone and amplification circuitry, and Bi_{NOISE} is associated with the noise floor. For each microphone, a unique $U_{0.95}$ was computed since the accuracy, non-linearity, and noise floor are distinct for each microphone. The bias error associated with the accuracy of the uncalibrated microphone was estimated as the deviation in the RMS surface pressure fluctuations computed at the maximum sensitivity relative to that computed at the mean calibration sensitivity within the range of frequencies from 70 Hz to 2,000 Hz. Since the reference microphone is precisely calibrated by the microphone manufacturer, the corresponding accuracy is provided (i.e., the sensitivity is -38 ± 1.5 dB). Accordingly, the bias error associated with the accuracy of the reference microphone was estimated as the deviation in the RMS surface pressure fluctuations computed at the maximum and nominal sensitivities. The resulting bias error associated with the reference microphone is approximately 15% that of the uncalibrated microphone, which is expected since it is a precision pressure sensor. The non-linearity of the uncalibrated microphone and amplification circuitry was estimated by measuring the amplitude response in the anechoic chamber. The amplitude response was obtained by measuring the sensitivity of the uncalibrated microphone subjected to a sound pressure level (SPL) that increased from 95 dB to 140 dB at a constant frequency of 1000 Hz. The amplitude response for an uncalibrated microphone is illustrated in Fig. D.1. The results indicate that the response is relatively flat for sound pressure levels from 95 dB to 125 dB, which corresponds to a pressure range from

1 Pa to 36 Pa, which is greater than the range of the surface pressure fluctuations observed in the present investigation for the range of flow parameters of interest. For this pressure range, the nonlinearity was estimated as the deviation between the maximum and mean sensitivities, resulting in a non-linearity of 7%. Accordingly, the bias error associated with non-linearity was estimated as the deviation in the RMS surface pressure fluctuations computed at the maximum sensitivity relative to that computed at the mean calibration sensitivity for a range of sound pressure levels from 95 dB to 125 dB. For comparison, the non-linearity bias error is approximately 2/3 that of the bias error due to the accuracy of the uncalibrated microphone.

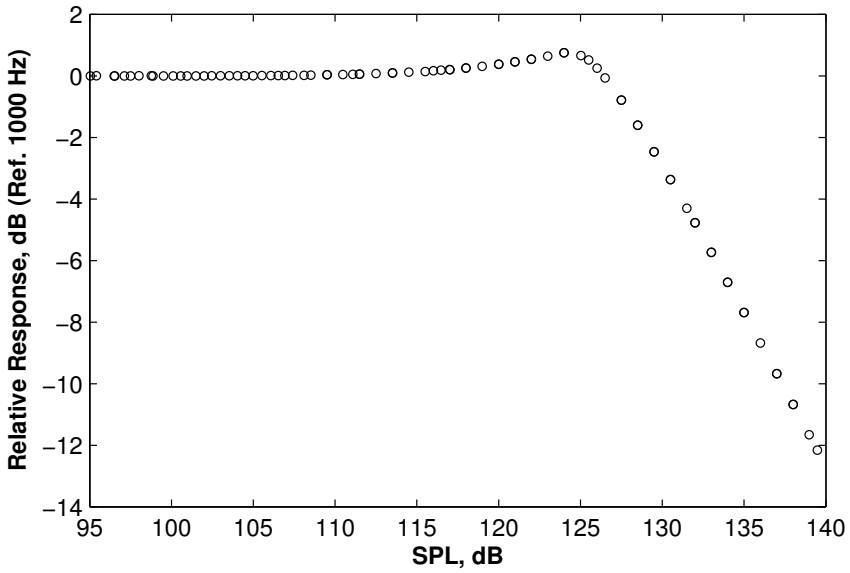

Figure D. 1: Microphone amplitude response curve.

The bias error due to the noise floor was estimated as the RMS fluctuating surface pressure computed when the wind tunnel was off (see Appendix C). Because of the distinctiveness of

the uncertainty for each microphone and set of flow parameters, the corresponding uncertainty is depicted as error bars on the streamwise RMS fluctuating surface pressure distributions in Fig. 5.1 and Fig. 5.2.

(ii) Hot Wire Measurement Uncertainty

An extensive investigation of the experimental uncertainty associated with time-resolved and mean hot wire velocity measurements was conducted by Kawall et al. (1983). For this investigation, the total estimated uncertainty was associated with the level of the turbulence intensity, calibration, and statistics. Employing this methodology, Kawall et al. (1983) compiled an extensive summary of the errors associated with various levels of turbulence intensity, and found that the accuracy of the hot wire velocity measurements decreases as the level of turbulence intensity increases. For the present investigation, the relevant errors in the hot wire velocity measurements are summarized in Table D.3. These results indicate that the accuracy of the velocity measurements is greatest outside of the separated flow region where the turbulent intensity is lower. Quantitatively, the error is less than 5% for all mean and RMS hot wire velocity profile measurements.

Table D.3: Error estimates for mean and RMS hot wire velocity measurements.

Type of Measurement	Relevant Figures	Error [%]
Mean streamwise velocity (inside the separated flow region)	3.13, 3.14	4.7
Mean streamwise velocity (outside the separated flow region)		0.1
RMS streamwise velocity (inside the separated flow region)		2.7
RMS streamwise velocity (outside the separated flow region)		1.1

(iii) Hot Wire Probe Positioning Uncertainty

The hot wire probe was positioned by a traversing mechanism in the streamwise (x), vertical (y), and spanwise (z) directions, where the motion of each axis was independently driven by stepper motors. The stepper motor control is reported in Bishop (2010). The vertical and spanwise stepper motors were connected to ¼''-20 lead screw while the streamwise stepper motor was connected to a ¾''-6 acme lead screw. Since the stepper motors were configured for a ½-step mode of operation, a single motor pulse corresponds to 0.9° of angular rotation of the motor shaft, a linear displacement of 0.003175 mm in the vertical and spanwise directions, and 0.01058 mm in the streamwise direction for a single motor pulse. The actual positioning accuracy of the probe was measured using an imaging system. The imaging system consists of a Nikon D300 digital SLR camera mounted on a tripod outside of the test section on the viewing-side. The camera was calibrated for positioning measurements on a designated measurement plane by taking an image of a grid installed on the airfoil at the z/c location in between the full and partial sensor rows of the microphone array. A calibration was performed by relating the known distance between grid cells to the corresponding number of pixels between the grid cells in the image (pixels/mm). This parameter will be referred to as to as the grid-pixel calibration density. By taking two images of the hot wire probe at two distinct positions on the measurement plane, the relative number pixels between the probe positions were measured from the image and the relative distance was computed with knowledge of the grid-pixel calibration density ({mm} = {pixels}/{pixels/mm}). Therefore, by employing this imaging system measurement methodology, the smallest probe

displacement that can be realized (i.e., the positioning accuracy) is ± 0.025 mm in the vertical and spanwise directions and ± 0.05 mm in the streamwise direction.

(iv) Spectral Peak Frequency Estimation Uncertainty

A systematic methodology was also developed in order to estimate the frequency of the spectral peak associated with the amplified band of disturbances at the fundamental and subharmonic frequencies. For a given spectral peak, a linear least-squares fit was applied to the set of spectral data in the region of increasing magnitude of the spectrum with increasing frequency. Similarly, a linear least-squares fit was also applied to the set of spectral data in the region of decreasing magnitude of the spectrum with increasing frequency. Note that each linear fit contained approximately 50 to 100 data points. The frequency associated with the spectral peak was estimated as the frequency at the intersection of the linear fits. For each set of flow parameters, the frequency associated with the spectral peak was estimated at three x/c locations where the amplitude of the spectral peak was greatest and the resulting frequency estimates were averaged. Based on the variability in the frequency estimated for these three x/c locations, it was found that the uncertainty in estimating the frequency was approximately ± 20 Hz. For flow parameters approaching transition between the flow regimes (i.e., for $Re_c = 100x10^3$ at $\alpha = 10°$ and for $Re_c = 110x10^3$ to $Re_c = 130x10^3$ at $\alpha = 12°$), it was observed that there was greater variability in the frequency associated with the spectral peak with increasing x/c location through the separated flow region. For these flow parameters, estimates of the frequency associated with the spectral peak were performed at the first x/c location where a distinct spectral peak emerged. In addition, the spectral peak was broader at

the flow parameters approaching transition between the flow regimes than observed at other flow parameters. Accordingly, the uncertainty in estimating the spectral peak was estimated to be less than ± 100 Hz.

(v) Time-lag Uncertainty Associated with Velocity-Pressure Cross-Correlation Analysis

Recall from §4.2 that the time-lag associated with the maximum of the cross-correlation coefficient function (τ^*) was computed for velocity and surface pressure fluctuation signals within the separated flow region. These computations were made for $Re_c = 100x10^3$ at $\alpha = 8°$ and $\alpha = 12°$, corresponding to regimes of flow separation with and without reattachment, respectively. It was found that the variability in the computed time-lag was 0.0001 ± 0.0003 s at $\alpha = 8°$ and -0.0006 s at $\alpha = 12°$. The uncertainty associated with the time-lag is based on three factors:

- the time-lag resolution ($\Delta\tau_R$)
- positioning the hot wire sensor over the sensor port ($\Delta\tau'$)
- positioning the hot wire sensor at the same x/c location as the sensor port as opposed to positioning the instruments at the same streamwise location ($\Delta\tau''$).

The resulting total root-mean-square uncertainty ($U_{0.95}$) is presented in Eq. D.5.

$$U_{0.95} = \sqrt{(\Delta\tau_R)^2 + (\Delta\tau')^2 + (\Delta\tau'')^2} \qquad (D.5)$$

The uncertainty associated with the time-lag is dependent on the sampling frequency [$\Delta\tau = 1/(2f_s) = \pm 0.0001$ s]. The uncertainty in positioning the hot wire sensor over the sensor port (Fig. D.1) was estimated to be on the order of the sensor port diameter ($\Delta x' = \pm D$,

where $\Delta x'$ is the uncertainty in the position and D is the sensor port diameter). Thus, a time-lag uncertainty associated with the positioning uncertainty could be estimated ($\Delta\tau' = U_c/\Delta x'$, where U_c is the convective velocity at a given x/c location estimated as half the edge velocity). Similarly, the uncertainty associated with positioning the hot wire sensor at the same x/c location as the sensor port as opposed to positioning the instruments at the same streamwise positions is illustrated in Fig. D.2. The time-lag uncertainty was calculated from the positioning uncertainty and the convective velocity ($\Delta\tau'' = U_c/\Delta x''$). The total root-mean-square uncertainty due to the time-lag uncertainty constituents is summarized in Table D.4. For both sets of flow parameters, it is evident that the uncertainty in the time-lag is comparable to the variability in the time-lag estimated from §4.2, and therefore, it is plausible that τ^* is actually zero.

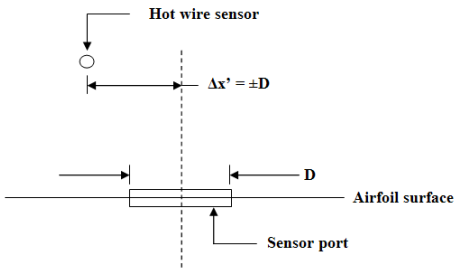

Figure D. 2: Misalignment of hotwire sensor probe over center of sensor port. Note that D is the sensor port diameter and Δx' is the positioning uncertainty.

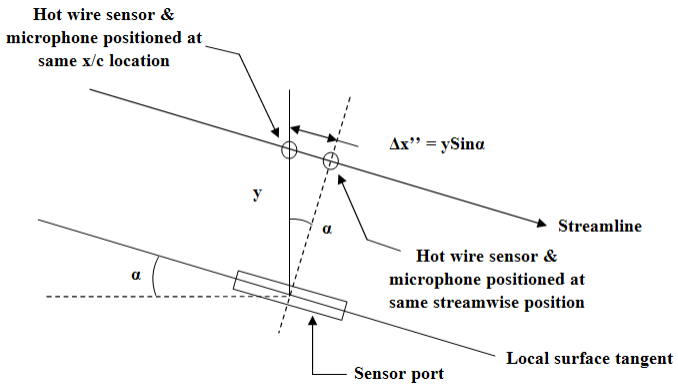

Figure D. 3: Alignment of microphone and hot wire sensor at the same x/c locations and the same streamwise locations. Note that α is the angle of attack, Δx'' is the positioning uncertainty, and y is the distance between the airfoil surface and the hot wire sensor.

Table D.4: Summary of time-lag uncertainties.

Re_c	α [deg]	$U_{0.95}$ [s]
$100x10^3$	8	0.0003
	12	0.0005

(vi) Time-Lag and Convection Velocity Uncertainty

The uncertainty in the time-lag ($\Delta\tau$) is due to discretization errors, which is governed by the sampling frequency [$\Delta\tau = 1/(2f_s) = \pm 5x10^{-5}$ s]. Accordingly, the computed time-lag (τ) deviates from the true time-lag (τ') according to Eq. D.6.

$$\tau = \tau' \pm \Delta\tau \qquad (D.6)$$

The uncertainty in the time-lag was estimated to be less than 8% within the separated flow region.

In order to estimate the uncertainty of the convective velocity, the time-lag uncertainty was added to the accumulated time-lag (τ^*), except at the reference x/c location since $\tau^* = 0$. A linear least-squares fit was applied to the data and the corresponding slope and convective velocity (U_c^+) were computed. The upper-limit of the uncertainty in the convective velocity [$UL(U_c)$] was estimated as the difference between U_c^+ and U_c [$UL(U_c) = U_c^+ - U_c$]. This process was repeated by subtracting the time-lag uncertainty from the accumulated time-lag (τ^*), computing a new convective velocity U_c^- and the corresponding lower-limit of the uncertainty [$LL(U_c) = U_c - U_c^-$]. Since the uncertainty in the convective velocity is dependent on the flow parameters, the uncertainty is depicted as error bars on the convective velocity plots in Fig. 5.11 and Fig. 5.12.